Software and hardware development for the next-generation liquid scintillator detectors JUNO and OSIRIS

Von der Fakultät für Mathematik, Informatik und Naturwissenschaften der RWTH Aachen University zur Erlangung des akademischen Grades eines Doktors der Naturwissenschaften genehmigte Dissertation

vorgelegt von

Christoph Genster, M.Sc.

aus Gummersbach

Berichter: Univ.-Prof. Dr. rer. nat. Livia Ludhova
Univ.-Prof. Dr. rer. nat. Achim Stahl

Tag der mündlichen Prüfung: 29.11.2019

Diese Dissertation ist auf den Internetseiten der Universitätsbibliothek verfügbar.

Just because you can't
figure something out
doesn't make it magic.

THE EXPANSE (S02E09)

Abstract

Large *liquid scintillator* (LS) detectors are acknowledged instruments in the field of neutrino physics. Based on various successful experiments, reporting the currently best limits on several parameters of neutrino flavor oscillations, a new generation of detectors with several tens of kilotons of LS are under consideration. The *Jiangmen Underground Neutrino Observatory* (JUNO) is a 20 kiloton LS detector, that is fully funded and under construction in China. Its main goal is the determination of the neutrino *mass ordering* (MO) through a precision measurement of the reactor electron anti-neutrino spectrum.

The first part of this thesis discusses the underlying theory of neutrino flavor oscillations, the JUNO detector design and how neutrinos of various sources can be detected with this instrument. The focus is laid on a correlated background for the *inverse beta decay* (IBD) measurement of reactor anti-neutrinos, which stems from cosmic muons. When they traverse the detector, the muons can create unstable radioisotopes, which decay after a short time in a $(\beta^- + n)$ channel. In order to identify and reject this background, it is paramount to know the track of the muon precisely. For this purpose, a novel muon reconstruction algorithm is developed and tested in this work. It is based on the geometric model of the intersection of the first-light front with the PMT array. The track parameters are optimized in a likelihood fit based on *probability density functions* produced with a detailed detector simulation. In addition, a simulation of the full readout electronics is performed to yield the best estimate of the performance on real data. Excluding the edge of the CD, the muon track's distance from the detector center ΔD can be determined with an uncertainty of 5 cm and its direction with 0.3 °. The impact on the detector's exposure by a muon veto based on this reconstruction was also studied. Compared to a perfect knowledge of each muon track, the developed method only creates an additional 4% of loss in exposure.

In the second part, a pre-detector for JUNO is investigated. OSIRIS is a standalone, 20 ton LS detector, that will be used to monitor the radiopurity of the cleaned LS before it is filled into JUNO. In the scope of this work, a detailed detector simulation based on `C++11` and `Geant4` is developed. It is then used to determine the sensitivity of the detector to its main physics goal: the identification of Bi-Po coincidences from the decay chains of ^{238}U and ^{232}Th in the LS. Furthermore, a calibration campaign for OSIRIS is studied. Under consideration of the available hardware, the decision is made to utilize an *automated calibration unit* (ACU) from the Daya Bay collaboration. The energy range of $0.5 - 3$ MeV will be calibrated by exposing the detector simultaneously to ^{137}Cs, ^{65}Zn, and ^{60}Co in a single capsule. With different vertical positions on a fixed radial distance $\rho = 120$ cm from the detector's center, its non-uniformity can be properly sampled. Timing calibration of the PMTs with an accuracy of $\sim$0.1 ns is realized with a 430 nm LED, that can be deployed along the same vertical axis.

Zusammenfassung

Große *Flüssigszintillator* (FSz)-Detektoren sind bewährte Instrumente auf dem Gebiet der Neutrino-Physik. Basierend auf verschiedenen erfolgreichen Experimenten, die die derzeit genausten Werte für mehrere Parameter von Neutrino-Oszillationen gemessen haben, wird eine neue Generation von Detektoren mit mehreren zehn Kilotonnen FSz entwickelt. Das *Jiangmen Underground Neutrino Observatory* (JUNO) ist ein 20-Kilotonnen-FSz-Detektor, der vollständig finanziert und in China gebaut wird. Sein Hauptziel ist die Bestimmung der *Neutrinomassenordnung* (MO) durch eine Präzisionsmessung des Spektrums von Elektron-Antineutrinos aus Kernreaktoren.
Der erste Teil dieser Arbeit behandelt die zugrundeliegende Theorie der Neutrino-Oszillationen, das JUNO-Detektordesign und wie Neutrinos aus verschiedenen Quellen mit diesem Instrument nachgewiesen werden können. Der Fokus liegt auf einem korrelierten Hintergrund für die Messung des *inversen Beta-Zerfall* (IBD) von Reaktor-Antineutrinos, der von kosmischen Myonen stammt. Wenn diese den Detektor passieren, können sie instabile Radioisotope erzeugen, die nach kurzer Zeit in einem $(\beta^- + n)$-Kanal zerfallen. Um diesen Hintergrund zu erkennen und zu unterdrücken, ist es von fundamentaler Bedeutung, die Spur des Myons genau zu kennen. Zu diesem Zweck wird in dieser Arbeit ein neuartiger Myon-Rekonstruktionsalgorithmus entwickelt und getestet. Es basiert auf dem geometrischen Modell der Schnittlinie des PMT-Arrays mit der Front des ersten Lichtes. Die Spurparameter werden in einem Likelihood-Fit optimiert, basierend auf *Wahrscheinlichkeitsdichtefunktionen*, die mit einer detaillierten Detektorsimulation erzeugt werden. Zusätzlich wird eine Simulation der Ausleseelektronik durchgeführt, um die bestmögliche Abschätzung der Genauigkeit mit realen Daten zu erhalten. Ausgenommen vom äußersten Rand des Detektors, kann der Abstand der Myonspur vom Detektorzentrum ΔD mit einer Unsicherheit von 5 cm und ihre Richtung mit $0.3\,^\circ$ bestimmt werden. Die Auswirkungen auf die sensitive Masse des Detektors durch ein Myon-Veto auf der Grundlage dieser Rekonstruktion wurden ebenfalls untersucht. Im Vergleich zur perfekten Kenntnis jeder Myonenspur, erzeugt die entwickelte Methode nur zusätzliche 4% Verlust an sensitiver Masse. Im zweiten Teil wird ein Vordetektor für JUNO untersucht. OSIRIS ist ein eigenständiger, 20 Tonnen-FSz-Detektor, der verwendet wird, um die Reinheit des FSz zu überwachen, bevor er in JUNO gefüllt wird. Im Rahmen dieser Arbeit wird eine detaillierte Detektorsimulation auf Basis von `C++11` und `Geant4` entwickelt. Diese wird dann verwendet, um die Sensitivität des Detektors für sein Hauptziel zu bestimmen - die Identifizierung von Bi-Po-Koinzidenzen aus den Zerfallsketten von ^{238}U und ^{232}Th im FSz. Darüber hinaus wird eine Kalibrierungskampagne für OSIRIS entwickelt. Unter Berücksichtigung der verfügbaren Hardware, wird die Entscheidung getroffen, eine *automatisierte Kalibriereinheit* (ACU) aus der Daya Bay Kollaboration einzusetzen. Der Energiebereich von $0.5 - 3$ MeV wird kalibriert, indem der Detektor gleichzeitig ^{137}Cs, ^{65}Zn und ^{60}Co in einer einzigen Kapsel ausgesetzt wird. Mit unterschiedlichen vertikalen Positionen in einem festen radialen Abstand $\rho = 120$ cm vom Zentrum des Detektors kann die Nicht-Uniformität des Ansprechverhaltens bestimmt werden. Die Zeitkalibrierung der PMTs mit einer Genauigkeit von $\sim$0.1 ns wird mit einer 430 nm LED realisiert, die entlang der gleichen vertikalen Achse eingesetzt werden kann.

Contents

Part I

Neutrino physics in LS detectors

Chapter 1

Neutrino Physics

The *Standard Model* (SM) describes neutrinos as elementary, spin-$\frac{1}{2}$ *Dirac fermions* with no mass [1]. They can only interact through the *charged current* (CC) and *neutral current* (NC) of the *weak force*, due to their lack of *electric* and *color* charge. Results from e^+e^--collider experiments suggest that there are three different, active neutrinos [1]. They are classified as counterparts to the three charged *leptons* e, μ, and τ and receive the definition of their *flavor* from there. In weak interactions, neutrinos ν and their antiparticles $\bar{\nu}$ are identified as $\nu_e(\bar{\nu}_e)$, $\nu_\mu(\bar{\nu}_\mu)$, and $\nu_\tau(\bar{\nu}_\tau)$. First experimental indications of neutrino physics beyond the standard model resulted from the *Homestake experiment* by R. Davis Jr. in the 1960s [2, 3]. The measurement of ν_e from the Sun via *inverse beta decay* (IBD) revealed an interaction rate of only one third of the ν_e flux predicted by the *Solar Standard Model* (SSM) [4]. This phenomenon is known as the *Solar Neutrino Deficit* and was confirmed by following experiments. Later it was complemented by discoveries of neutrino appearance at T2K [5], showing that neutrinos can change their flavor. The deficit was solved when the SNO [6] experiment provided evidence for a non-electron flavor component of the solar neutrino flux [7]. At the same, *Super-Kamiokande* (SK) [8] reported a consistent precision measurement of solar neutrinos [9].

1.1 Neutrino oscillations in vacuum

Neutrino flavor oscillations are an established theory to consistently explain the aforementioned observations. It was confirmed by several experiments in different energy ranges and with neutrinos from various sources [1]. This section will give a brief overview of the neutrino flavor oscillation in vacuum. The current state of the measurement of oscillation parameters is subject of Section 1.1.1. Sections 1.2 and 1.3 give some detail on neutrino interactions and their sources respectively. An outlook on future activities in the neutrino field is then sketched in Section 1.4.

The theory of three flavor neutrino oscillation describes the periodic changes of probabilities to measure a certain neutrino in a given flavor. It introduces three *mass eigenstates* (ν_1, ν_2, ν_3) in addition to the *flavor eigenstates* $(\nu_e, \nu_\mu, \nu_\tau)$ and each mass eigenstate

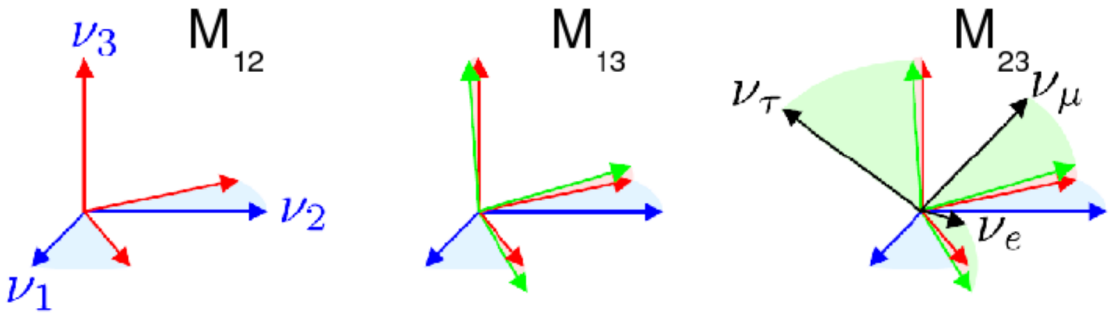

Figure 1.1 – Schematic illustration of the rotation of the mass eigensystem (blue) to the flavor eigensystem (black) via the three rotation matrices M_{ij} from Equation (1.3). The angles approximately match the measured values [12].

describes a neutrino with a slightly different mass. Neutrinos are observable when they interact through the weak force and manifest in a certain flavor state. These states can be described as a superposition of the three mass eigenstates. Both sets of states can formally be introduced as

$$|\nu_\alpha\rangle = \sum_i \mathcal{U}^*_{\alpha,i} \, |\nu_i\rangle \tag{1.1}$$

$$|\nu_i\rangle = \sum_\alpha \mathcal{U}_{\alpha,i} \, |\nu_\alpha\rangle \, . \tag{1.2}$$

Here, α denotes a flavor state and i a mass state while $\mathcal{U}_{\alpha,i}$ is the element of the neutrino mixing matrix. *Maki, Nakagawa*, and *Sakata* introduced this matrix [10] following the prediction of neutrino oscillations by *Bruno Pontecorvo* [11]. The *Pontecorvo-Maki-Nakagawa-Sakata matrix* (PMNS matrix) can formally be split up into three rotation matrices around one mass eigenstate each [1]. Choosing $c_{ij} \equiv \cos\theta_{ij}$ and $s_{ij} \equiv \sin\theta_{ij}$ for readability and θ_{ij} for the rotation angles of the mass eigenstates it can be written as

$$\begin{pmatrix} \nu_e \\ \nu_\mu \\ \nu_\tau \end{pmatrix} = \begin{pmatrix} 1 & 0 & 0 \\ 0 & c_{23} & s_{23} \\ 0 & -s_{23} & c_{23} \end{pmatrix} \begin{pmatrix} c_{13} & 0 & s_{13}e^{-i\delta} \\ 0 & 1 & 0 \\ -s_{13}e^{-i\delta} & 0 & c_{13} \end{pmatrix} \begin{pmatrix} c_{12} & s_{12} & 0 \\ -s_{12} & c_{12} & 0 \\ 0 & 0 & 1 \end{pmatrix} \begin{pmatrix} \nu_1 \\ \nu_2 \\ \nu_3 \end{pmatrix} \tag{1.3}$$

$$= \begin{pmatrix} c_{12}c_{13} & s_{12}c_{13} & s_{13}e^{-i\delta} \\ -s_{12}c_{23} - c_{12}s_{23}s_{13}e^{i\delta} & c_{12}c_{23} - s_{12}s_{23}s_{13}e^{i\delta} & s_{23}c_{13} \\ s_{12}s_{23} - c_{12}c_{23}s_{13}e^{i\delta} & -c_{12}s_{23} - s_{12}c_{23}s_{13}e^{i\delta} & c_{23}c_{13} \end{pmatrix} \begin{pmatrix} \nu_1 \\ \nu_2 \\ \nu_3 \end{pmatrix} . \tag{1.4}$$

The parameters of this relation are three mixing angles θ_{12}, θ_{13}, and θ_{23} and a CP-violating phase factor $\delta = \delta_{CP}$. This phase accounts for differences in the oscillation of neutrinos and anti-neutrinos and influences the flavor content of the mass states. Figure 1.1 illustrates the rotation of the *mass eigensystem* to the *flavor eigensystem* with approximately realistic angles.

For reasons of clarity Equation (1.3) omits one additional factor that accounts for neutrinos being *majorana* particles. If neutrinos are their own anti-particles the PMNS

matrix has to be multiplied with another diagonal matrix accounting for two *majorana* phases α_1 and α_2

$$\begin{pmatrix} e^{i\frac{\alpha_1}{2}} & 0 & 0 \\ 0 & e^{i\frac{\alpha_2}{2}} & 0 \\ 0 & 0 & 1 \end{pmatrix}. \tag{1.5}$$

Since the consideration of Majorana phases does not influence the physical behavior of neutrino oscillations it will be omitted going forward. Nevertheless, it is important for other aspects of neutrino physics like the $0\nu\beta\beta$ decay [1].

The neutrino propagation can be described with a plane wave approximation [1]. It describes the probability of detecting a neutrino in flavor state β after is was initially created in flavor α and traveled a certain distance L. Neutrinos are always measured at relativistic energies, allowing for the approximation of the traveled distance $\mathrm{L} \approx ct$ and $p \approx \mathrm{E}$. The time evolution of the neutrino state $|\nu_\alpha(t)\rangle$ is given by the plane wave solution of the time dependent Schrödinger Equation with no potentials

$$|\nu_\alpha(t)\rangle = e^{-i(E_\alpha t - p_\alpha x)} |\nu_\alpha(0)\rangle = e^{-iL\frac{m_\alpha^2}{2E}} |\nu_\alpha(0)\rangle . \tag{1.6}$$

Using Eqs. (1.6) and (1.1) one can express the general oscillation probability by

$$P_{\alpha\to\beta} = |\langle\nu_\beta|\nu_\alpha(t)\rangle|^2 = \left| \sum_i \mathcal{U}^*_{\alpha,i}\mathcal{U}_{\beta,i} e^{-i\frac{m_i^2}{2E}L} \right|^2 . \tag{1.7}$$

Eventually, this expression can be written as following with $(+)$ for neutrinos and $(-)$ for anti-neutrinos

$$P_{\alpha\to\beta} = \delta_{\alpha,\beta} - 4\sum_{i>j} \mathrm{Re}\left(\mathcal{U}^*_{\alpha,i}\mathcal{U}_{\beta,i}\mathcal{U}_{\alpha,j}\mathcal{U}^*_{\beta,j}\right) \sin^2\left(\frac{\Delta m^2_{ij}}{4\mathrm{E}}L\right) \tag{1.8}$$

$$\pm\, 2\sum_{i>j} \mathrm{Im}\left(\mathcal{U}^*_{\alpha,i}\mathcal{U}_{\beta,i}\mathcal{U}_{\alpha,j}\mathcal{U}^*_{\beta,j}\right) \sin\left(\frac{\Delta m^2_{ij}}{2\mathrm{E}}L\right). \tag{1.9}$$

Here, Re and Im describe the *real* and *imaginary* part of the matrix products and Δm^2_{ij} is the *squared mass difference* defined as

$$\Delta m^2_{ij} = m^2_i - m^2_j. \tag{1.10}$$

The same result could be achieved with a strict, but lengthy derivation using wave packets which would require much fewer assumptions. In general $P_{\alpha\to\alpha}$ is called the survival probability of a certain flavor $\alpha = e, \mu, \tau$ and $P_{\alpha\to\beta}$ is the appearance probability of the flavor β.
The theory of neutrino flavor oscillations builds on the assumption, that there is a mismatch of the flavor eigenstates and mass eigenstates of neutrinos. It implies different, non-zero masses for neutrinos, which is not foreseen in the SM. Thus, neutrino oscillations are a minimal extension of the SM. Apart from the non-zero mass of neutrinos, the theory is consistent with the SM.

1.1.1 Measurement of the oscillation parameters

As presented in Section 1.1 the three flavor neutrino mixing can be described with the parameters from the PMNS matrix and two independent mass splittings. By convention one usually chooses Δm^2_{21} together with either Δm^2_{32} or Δm^2_{31}. With regard to Equation (1.10), it is important to note, that neutrino oscillations do not allow for a direct measurement of the neutrino masses, but only the squared mass differences between them.

The different parameters can be grouped with respect to the channel and source they were first measured with. θ_{12} and Δm^2_{21} were first measured with neutrinos from the sun and are therefore called the *solar* parameters. The fission processes in the *Sun*'s core produce only electron neutrinos, which can then oscillate to the other two flavors along their way to *Earth*. As a consequence, the one main measurement channel is the ν_e disappearance. Substantial efforts in measuring these parameters were made by *KamLAND* [13], SNO, and SK [8]. While the experiments, that utilize neutrinos from the *Sun* give the best sensitivity on the mixing angle θ_{12}, KamLAND reported a precision measurement of Δm^2_{21} with reactor neutrinos.

The parameters θ_{23} and Δm^2_{23} can be accessed by measuring the disappearance of ν_μ and $\bar{\nu}_\mu$. They are created in large numbers when cosmic radiation interacts with Earth's atmosphere and thus, the parameters are called *atmospheric*. Important contributions in this sector were made by SK [14]. Another possibility to probe the disappearance of muon neutrinos is given by neutrino beams from accelerators over a baseline of several hundreds to thousands kilometers. Large contributions using neutrino beams were made by *Tokai-to-Kamioka* (T2K) [15] and the *Main Injector Neutrino Oscillation Search* (MINOS) [16].

The third mixing angle θ_{13} was measured by the liquid scintillator-based (LS) experiments Daya Bay [17], Double Chooz [18], and RENO [19]. They utilize electron anti-neutrinos from nuclear reactors and measure their disappearance at baselines between 1 km to 3 km. A non-zero value for θ_{13} was reported [20] and confirmed by the long-baseline experiments T2K and MINOS, which measured the appearance of ν_e in a muon neutrino beam [5].
A comprehensive review of the discoveries of the all experiments in the field can be found in Ref. [1].

The fact neutrino oscillations are governed by the squared mass differences introduces the issue of the unknown ordering of neutrino mass states. Following the convention to assort ν_1 to the state with the largest admixture of electron flavour, Δm^2_{21} is positive. For the atmospheric splitting Δm^2_{32} only its absolute value is measured yet, but the sign is unknown. Figure 1.2 pictures this issue and how the question of *mass ordering* (MO) emerges from this. Since Δm^2_{21} is measured > 0, the mass state m_2 is larger than m_1. The sign of Δm^2_{32} will determine if m_3 is the heaviest of the three mass states, which is called the *normal ordering* (NO), or if it is the lightest one, thus called the *inverted ordering* (IO).

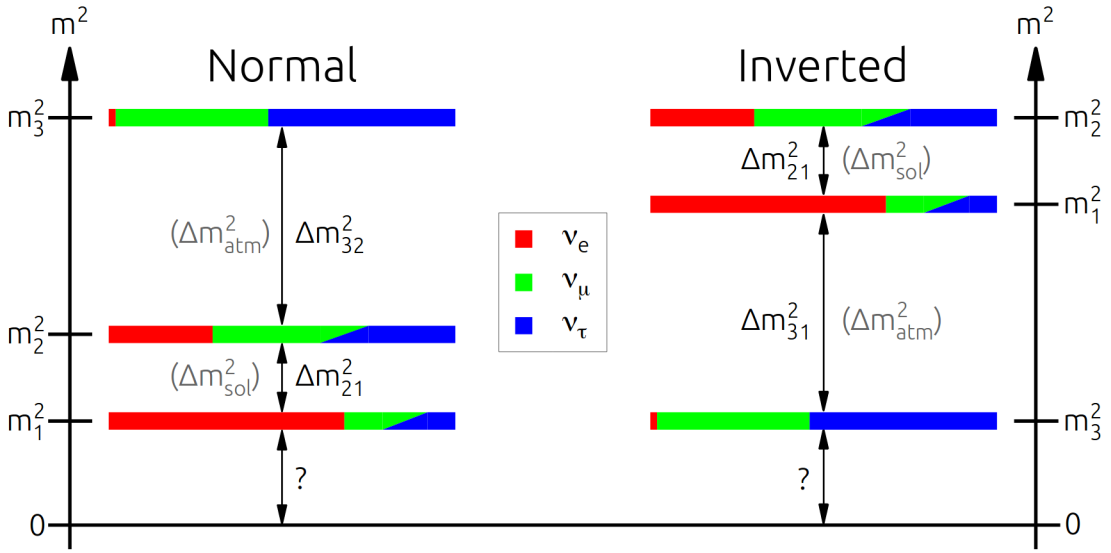

Figure 1.2 – Visualization of the normal and inverted neutrino mass ordering. Mass-squared states are color-coded with their flavor fraction due to the mixing angles. The shown magnitudes of the splitting are not drawn to scale. In normal hierarchy m_3 is the heaviest state and in the inverted hierarchy it is the lightest. Since the sign of Δm^2_{21} is known to be positive, m_2 is heavier than m_1 in both cases [30].

There are several experiments in different development stages, that will be able to probe the MO. While NOvA [21] can constrain the MO [22], the upcoming *Deep Underground Neutrino Experiment* (DUNE) [23] will try to determine it on a long baseline with accelerator neutrino beams [24]. Additionally, the MO is accessible through atmospheric neutrinos. Promising experiments in this channel are among others the deep-sea telescope ORCA [25], the IceCube extension PINGU [26], and Hyper-K [27]. JUNO is the only experiment so far, that will probe the MO via reactor neutrinos on a medium baseline. Thus, JUNO is complementary to the other future experiments, as it is the only one to determine the MO through vacuum oscillations, instead of matter effects.
Current results of long-baseline accelerator neutrino experiments like T2K [28] and NOνA [29] hint towards a NO with $\sim 2\sigma$, but are not decisive.

While Section 1.4 will go into more detail on the unknown characteristics of neutrino oscillations, the current best fit values for the measured parameters are presented in Table 1.1. They are based on a combined analysis of experimental results and takes into account the unknown mass ordering [31].

Table 1.1 – Overview of current global values for three-flavor neutrino mixing taken from Ref. [31]. Note the difference in $\sin^2(\theta_{23})$, Δm^2_{3l} and δ_{CP} for the two possible mass orderings. This also changes the definition of $\Delta m^2_{atm} = \Delta m^2_{3l}$ with $l = 1$ for normal ordering and $l = 2$ for inverted ordering.

Quantity	Value	Note
$\sin^2(\theta_{12})$	$0.310^{+0.013}_{-0.012}$	
$\sin^2(\theta_{23})$	$0.582^{+0.015}_{-0.019}$	normal ordering
$\sin^2(\theta_{23})$	$0.582^{+0.015}_{-0.018}$	inverted ordering
$\sin^2(\theta_{13})$	$0.02240^{+0.00065}_{-0.00066}$	normal ordering
$\sin^2(\theta_{13})$	$0.02263^{+0.00065}_{-0.00066}$	inverted ordering
Δm^2_{21}	$(7.39^{+0.21}_{-0.20}) \times 10^{-5}\,\mathrm{eV}^2$	
Δm^2_{31}	$(+2.525^{+0.033}_{-0.031}) \times 10^{-3}\,\mathrm{eV}^2$	normal ordering
Δm^2_{32}	$(-2.512^{+0.034}_{-0.031}) \times 10^{-3}\,\mathrm{eV}^2$	inverted ordering
δ_{CP}	$(217^{+40}_{-28}) \times 10^{-2}\,^\circ$	normal ordering
δ_{CP}	$(280^{+25}_{-28}) \times 10^{-2}\,^\circ$	inverted ordering

1.2 Neutrino interactions

Although neutrinos can only interact weakly and have a very small cross section, they are detectable through several different channels. This section will give an overview over the reactions relevant for neutrino detection in modern LS detectors, based on the theoretical background of Refs. [32, 1]. Typically, they observe neutrinos in the energy range of $\mathcal{O}(1\,\mathrm{MeV})$ and below, so that the notable reactions are *(quasi-) elastic scattering* and the *inverse beta decay*.

Neutrino-electron elastic scattering All neutrino and anti-neutrino flavors $l = e, \mu, \tau$ can partake in the scattering off electrons through NC interactions:

$$\nu_l + e^- \to \nu_l + e^- \quad \text{or} \quad \bar{\nu}_l + e^- \to \bar{\nu}_l + e^- \tag{1.11}$$

Since the initial and final state are the same, there is no energy threshold to this process. There is an additional CC process through the t-channel and s-channel respectively

$$\nu_l + e^- \to l^- + \nu_e. \tag{1.12}$$

Although this quasi-elastic scattering is possible for all three flavors, it is most often only observed for ν_e and $\bar{\nu}_e$ in LS detectors. This is due to the fact, that in the given energy range the neutrino energy is not sufficient to produce the rest mass of μ and τ. Nevertheless, atmospheric neutrinos and those from neutrino beams can have high enough energies to produce the heavier leptons in CC processes.

Table 1.2 – Cross-sections for elastic neutrino scattering on electrons and protons. Extracted from [33, 34]

Reaction	Current	Cross-section $[10^{-44}\text{cm}^2]$
$\nu_e + e^- \to \nu_e + e^-$	CC+NC	$0.95E_\nu$
$\bar{\nu}_e + e^- \to \bar{\nu}_e + e^-$	CC+NC	$0.45E_\nu$
$\nu_y + e^- \to \nu_y + e^-$	NC	$0.16E_\nu$
$\bar{\nu}_y + e^- \to \bar{\nu}_y + e^-$	NC	$0.13E_\nu$
$\nu_x + p \to \nu_x + p$	NC	$2.03E_\nu^2$
$\bar{\nu}_x + p \to \bar{\nu}_x + p$	NC	$2.03E_\nu^2$

Neutrino-nucleus scattering Similar to the case of electrons, neutrinos of all flavors can also scatter elastically on free protons [33] and nuclei through a NC process

$$\nu_l + p \to \nu_l + p \quad \text{or} \quad \bar{\nu}_l + p \to \bar{\nu}_l + p. \tag{1.13}$$

Among others, they can also undergo the same quasi elastic scattering CC interaction, which is relevant for many modern neutrino detectors as mentioned above

$$\nu_l(\bar{\nu}_l) + N \to l^-(l^+) + N'. \tag{1.14}$$

As for the process in Equation (1.12), this is only relevant for the electron flavor in the range of MeV energies. For the scattering processes on electrons and protons the cross sections are summarized in Table 1.2.

Inverse beta decay The IBD reaction is a CC process between a electron anti-neutrino and a proton

$$\bar{\nu}_e + p \to e^+ + n. \tag{1.15}$$

With its low energy threshold of $E_\nu \geq 1.806\,\text{MeV}$ and a coincidence signal it is a major detection channel for $\bar{\nu}_e$ in LS-based detectors. The cross section is energy dependent and can be approximated by [35, 36]

$$\sigma_{IBD}(E_\nu) = 9.61 \times 10^{-44} \times (E_\nu - 1.29\,\text{MeV}) \times \sqrt{(E_\nu - 1.29\,\text{MeV})^2 - 0.26\,\text{MeV}^2}\ \text{cm}^2\text{MeV}^{-2}.$$

The reactions of the resulting positron and neutron from Equation (1.15) form a delayed coincidence in the detector. A visualization of this process is shown in Figure 1.3. First, the positron deposits its energy in the LS and annihilates within nanoseconds into two 511 keV gammas. This part is called the prompt event and its energy release is proportional to the neutrino energy following $E_{prompt} \sim E_{\bar{\nu}_e} - 0.78\,\text{MeV}$ [30]. The much

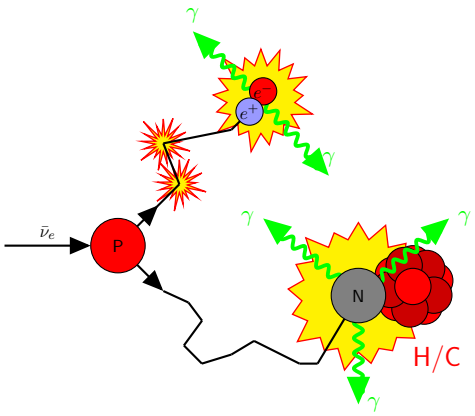

Figure 1.3 – Visualization of the principal IBD detection in LS. The incoming $\bar{\nu}_e$ interacts with the proton and creates a positron (top path) and a neutron. The kinetic energy of the positron is proportional to the neutrino energy and will be deposited quickly by elastic scattering before it annihilates under the emission of two 511 keV gammas with an electron. The neutron thermalizes for a short time and is then captured by Hydrogen (H) or Carbon (C) with an distinct energy release of 2.2 MeV or 4.9 MeV, respectively. Figure adapted from Ref. [37]

heavier neutron is recoiled with some tens of keV of kinetic energy and scatters around the LS until it is thermalized. It is then captured on Hydrogen or Carbon with a distinct energy of 2.2 MeV or 4.9 MeV, respectively. This capture happens on a time scale of about 250 μs and is thus called the delayed event. Both events are created at the same point in space and the neutron cannot travel very far until it is thermalized. Due to that, both the correlation in time and space can be utilized to identify the IBD reaction and to reject backgrounds. More details on the detection and rate of this reaction in JUNO will be given in Chapter 4.

1.3 Neutrino sources

Developing and probing the theoretical description of neutrinos requires well-understood neutrinos sources. In addition, the small cross-sections call for sources with a very high flux to achieve a meaningful measurement. Despite those demands, there is a variety of natural and man-made neutrino sources available to test and strengthen the neutrino theory in a large energy range.

The lower end of detected neutrino energies lies in the order of hundreds of keV with solar neutrinos as reported by e.g. Borexino [38], while the neutrino telescope IceCube measured neutrinos up to PeV [39].

Natural sources of neutrinos include among others the fusion processes in the Sun, core-collapse supernovae (SN), and cosmic rays as well as radioactive decays, especially inside the Earth. Those sources provide a large flux of neutrinos, but are not controllable and have to be understood to a certain extend in order to deduct neutrino properties from them.

Man-made sources are nuclear reactors, in which neutrinos are produced as a byproduct and particle accelerators. With the latter it is possible to create a dedicated neutrino beam aimed at a detector with a chosen baseline. An advantage of artificial neutrino sources is that they are localized and accessible. With the possibility to control their characteristics, it is possible to investigate neutrino (oscillation) properties systematically. On the other hand, the sources not only provide neutrinos to be studied, but their neutrinos can also give a unique insight into the processes happening in a source. Especially for natural sources and when electromagnetic channels are not sufficient, neutrinos can provide a complimentary picture on a source's state and evolution. As a *messenger particle*, neutrinos play an important role in understanding the mechanics of core-collapse SN and details of the fusion in the Sun. Also so-called geo-neutrinos, created by radioactive decays inside the Earth, are used to gather information about the Earth's radiogenic heat.

In the following, this section will give some more details on neutrinos from nuclear reactors, as this is the main source for JUNO. Reactor neutrinos are electron anti-neutrinos from β^--decays of unstable isotopes along the fission chains of nuclear reactors. Each core creates power by fission of mainly four isotopes: ^{235}U, ^{238}U, ^{239}Pu, and ^{241}Pu. Besides the released energy of about 200 MeV those reactions create on average six $\bar{\nu}_e$ per fission, that are radiated isotropically. A typical reactor core emits about $2 \times 10^{20} \bar{\nu}_e/s$ per GW of thermal power [36]. One of the aforementioned advantages of man-made neutrino sources, that applies to nuclear reactors, is the small and well defined size. This allows for a precise knowledge of where the anti-neutrinos were created. Since reactors typically have several cores, there is a small uncertainty on the position of creation of a few meters. This is small compared to the oscillation length of $\sim$3 km for $\bar{\nu}_e$ with the average energy of 3 MeV. Thus, a neutrino detector, that can resolve the energy spectrum of the reactor anti-neutrinos, can measure the full energy-dependent oscillation phase of those neutrinos. Although, the β^--decay of the fissile isotopes is well known, it is not trivial to precisely predict the neutrino spectrum emitted by a reactor core. One solution is to place a neutrino detector very close to the reactor in order to measure the un-oscillated spectrum in addition to the main measurement with a longer baseline. The reactor neutrino spectrum can also be modeled according to the core's fuel composition. In this case the neutrino flux reaching a detector at the baseline L is described by [36]

$$\Phi_\nu(E_\nu) = \frac{1}{4\pi L^2}\ N_{fis}\ N_\nu(E_\nu)\ P_{\bar{\nu}_e \to \bar{\nu}_e}(E_\nu, L). \tag{1.16}$$

The first term accounts for the solid angle, N_{fis} gives rate of fissions and N_ν the number of neutrinos per fission. The possible disappearance of neutrinos by oscillation is taken into account by the survival probability $P_{\bar{\nu}_e \to \bar{\nu}_e}$ (see Equation (4.1)). The fission rate can be expressed by the thermal power P_{th} of the core and the mean energy per fission $\langle E_f \rangle$ as $N_{fis} = {}^{P_{th}}/_{\langle E_f \rangle}$. Furthermore, the mean energy release per fission depends on the relative fraction of the four fuel components:

$$\langle E_f \rangle = \sum_k \alpha_k \langle E_f \rangle_k. \tag{1.17}$$

Here k sums over the four components mentioned above and α_k is the fission fraction, that gives their relative composition. Based on that, one can also define the power fraction, which describes the ratio of energy released by a fuel component

$$p_k = \frac{\alpha_k \langle E_f \rangle_k}{\langle E_f \rangle}. \tag{1.18}$$

Table 1.3 gives an overview of typical values for the fission fractions in a commercial reactor and the corresponding power fractions. In a similar fashion the number of

Table 1.3 – Overview of the mean energy release per fission, fission fraction and power fraction of a typical commercial reactor. The values for the mean energy release are taken from Ref. [40] and the fission fractions from Ref. [41], while the power fraction p_k was calculated from those values according to Equation (1.18).

Isotope	Energy release per fission $\langle E_f \rangle_k$ [MeV]	Fission fraction α_k	Power fraction p_k
^{235}U	201.7	0.58	0.57
^{238}U	205.0	0.07	0.07
^{239}Pu	210.0	0.30	0.31
^{241}Pu	212.4	0.05	0.05

neutrinos per fission $N_\nu(E_\nu)$ can be calculated using the neutrino spectra for each fuel component

$$N_\nu(E_\nu) = \sum_k \alpha_k N_{\nu,k}(E_\nu). \tag{1.19}$$

A phenomenological parameterization of the reactor anti-neutrino flux was first given in Ref. [40] by a polynomial of order 5

$$N_{\nu,k}(E_\nu) = \exp\left(\sum_{p=1}^{6} c_{k,p} E_\nu^{p-1}\right). \tag{1.20}$$

The coefficients $c_{k,p}$ for the four main fuel components were determined by a fit of the parameterization to precisely measured beta spectra of the isotopes [40]. A recent re-evaluation of this data in 2011 by *Huber* [42] and *Mueller et al.* [43] resulted in an increase of the total normalization by 3%, while the spectral shape stayed the same. Figure 1.4 shows an exemplary spectrum of emitted reactor anti-neutrinos following the re-evaluated parameterization coefficients, overlayed with the IBD cross-section and a spectrum measurable in a LS detector. The increase in the expected flux of anti-neutrinos lead to a tension between the theory expectation and the data of short-baseline reactor experiments. As a consequence of this re-evaluation, a signal deficit of ∼6% was reported, which is called the *reactor antineutrino anomaly* [44]. One possible explanation of this phenomenon could be a fourth, sterile neutrino, as discussed in Section 1.4.3.
In general, the resulting spectrum is time-dependent, because the relative fuel composition

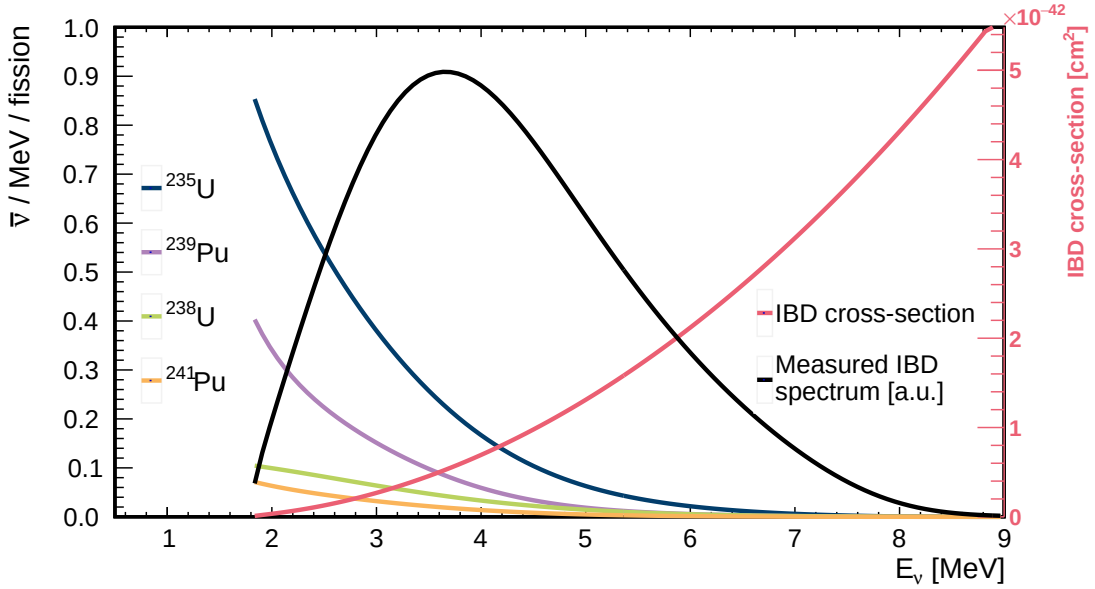

Figure 1.4 – The electron anti-neutrino spectrum emitted by a nuclear reactor. The contributions for the four main fissile isotopes ^{235}U (blue), ^{238}U (green), ^{239}Pu (violet) and ^{241}Pu (orange) are parameterized according to Ref. [43] and weighted as done in Ref. [41]. The corresponding values are presented in Table 1.3. Following Equation (1.15), the IBD cross-section (red) is overlayed. The resulting measurable IBD spectrum (black) assumes no oscillation and is a visualization of the shape in an arbitrary normalization.

changes over time. This effect is called burn-up and consists of the depletion of U and enrichment of Pu. More details on the reactor modeling in the context of current $\bar{\nu}_e$ oscillation experiments can be found in Ref. [36].
Another prominent case showing the complex issue of reactor modeling is a measured over-fluctuation of events in the energy range of 5-7 MeV. It was observed by Daya Bay [45], Double Chooz [46], and RENO [47] and correlates with the total thermal power of the reactors, but has yet to be explained. Figure 1.5 shows the extracted electron anti-neutrino spectrum of Daya Bay in comparison to the *Huber+Mueller* prediction [48]. The excess in the 5-7 MeV region is clearly visible, as is a deficit of the total flux, that is consistent with the reactor anomaly.

The focus on modeling the reactor spectrum triggered by the re-evaluation of the flux models [42, 43] led to more crucial insights for future reactor anti-neutrino experiments. First-principle calculations of the beta decay processes connected to the fission in nuclear reactors show a significant micro-structure of the electron anti-neutrino spectrum in the range of 50-100 keV [49]. While for current generation detectors with ∼8% energy resolution, the sawtooth-shaped substructure is smeared out, it was shown that for future experiments with better resolution, it will become visible [49]. Especially for JUNO, this is crucial, because this substructure is of the same scale as the effect introduced

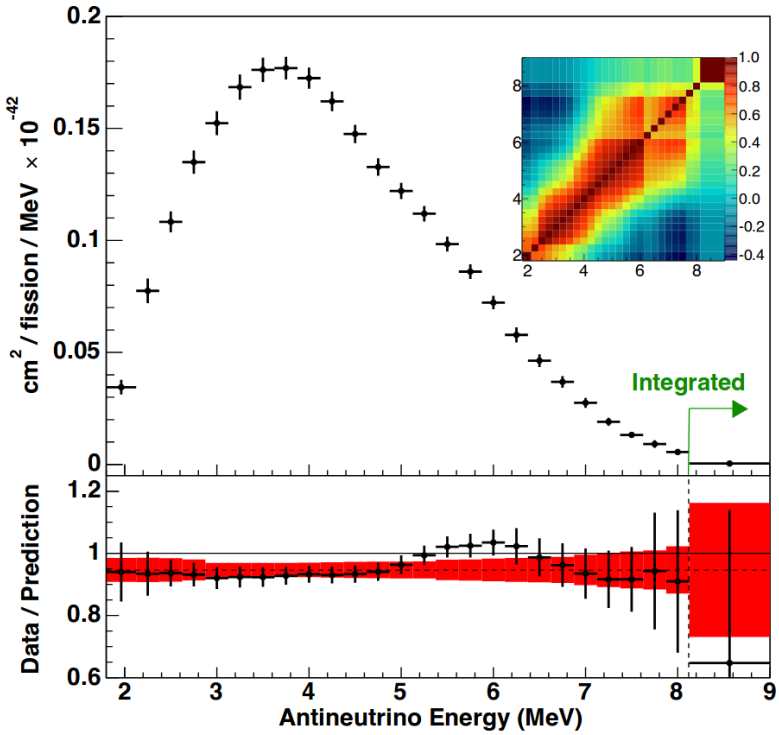

Figure 1.5 – Electron anti-neutrino spectrum extracted from DAYA BAY data. The bottom panel shows the ratio of the spectrum to the expectation from the Huber+Mueller model. Both the excess at 5-7 MeV and the deficit in the total flux are significantly visible. Reprinted figure from [48].

as fast wiggles by the MO, that is to be measured (see Section 4.1). It was estimated, that the fine-structure could significantly decrease JUNO's sensitivity to the MO [50]. A suggested solution to retain a good sensitivity is an independently measured reference spectrum of the reactor. Nevertheless, using an existing experiment like DAYA BAY is not sufficient, due to the lack of energy resolution to see the fine-structure [50]. For this reason, JUNO will employ a high-resolution detector very close to the detector to get a reference measurement of the reactor electron anti-neutrino spectrum [51]. The project is called *Taishan Antineutrino Observatory* (TAO) and will be presented in Section 3.2.5.

1.4 Open questions

Although large parts of the PMNS matrix and the mass splittings have been measured, there are still several neutrino properties unknown. The open issue about the neutrino mass ordering was already addressed in Section 1.1.1. In the following, Section 1.4.1 will discuss the absolute neutrino mass scale and Section 1.4.2 gives some information about the question whether or not the neutrino is its own antiparticle. Finally, Section 1.4.3 deals with the search of additional, sterile neutrino flavors.

1.4.1 Absolute neutrino mass scale

Flavor oscillations are only sensitive to the squared mass differences, but do not give any insight into the absolute mass scale of neutrinos. Due to that, other non-oscillation experiments have to be employed to determine the absolute neutrino mass.
Cosmology and astrophysics provide an upper limit on the sum of neutrino masses $\Sigma_\nu \equiv \sum_i m_{\nu_i}$. The Planck Collaboration has reported $\Sigma_\nu < 0.23\,\text{eV}$ at the 95% confidence level [52]. This result, obtained by a global analysis of current cosmological data gives the best sensitivity on this quantity yet, but is model dependent.
Another promising reaction for the neutrino mass is the neutrino-less double-β-decay $0\nu\beta\beta$ [1]. An observation of this decay would not only imply that neutrinos are Majorana particles (see Section 1.4.2), but also give access to the effective Majorana ν_e mass [53, 54]

$$m_{ee} \equiv \sum_i m_i U_{ei}^2. \tag{1.21}$$

Here, U is the PMNS-matrix including the Majorana phases explained in Section 1.1. They are relevant for this measurement, because it does not take the absolute value of matrix elements, but their direct value. Thus, the Majorana phases do not cancel out. Current experiments set an upper bound of 0.2 eV on m_{ee} and future $0\nu\beta\beta$ aim to reach the level of meV [54].

Another sensitive probe of the effective neutrino mass is the end point of the electron spectrum of β decays. It is possible to measure the average ν_e mass

$$\langle m \rangle_e \equiv \sqrt{\sum_i m_i^2 |U_{ei}|^2} \tag{1.22}$$

in the decay of tritium ${}^3_1He \rightarrow {}^3_2He + e^- + \bar{\nu}_e$. This was done in the *Mainz* [55] and *Troitsk* [56] experiments with upper limits of $\langle m \rangle_e < 2.3\,\text{eV}$ and $< 2.1\,\text{eV}$, respectively. Currently the *Karlsruhe Tritium Neutrino Experiment* (KATRIN) [57] is starting to measure the decay with a projected sensitivity to $\langle m \rangle_e$ of $\approx 0.2\,\text{eV}$. In addition, Project 8 will use *Cyclotron Radiation Emission Spectroscopy* (CRES) to probe the β-decay spectrum of tritium. Running parallel to KATRIN, the project follows a staged approach to finally reach a neutrino mass sensitivity of 40 meV [58]. Another current experiment searching for the neutrino mass is HOLMES. In contrast to the aforementioned projects, it uses the artificial isotope ^{163}Ho and will extract a limit on the neutrino mass by performing a calorimetric measurement of its *electron capture* decay [59].

1.4.2 Dirac or majorana particles

While the other leptons are Dirac particles, it is possible that neutrinos are Majorana particles and by that their own antiparticles. A direct consequence of this is the violation of lepton number conservation. Currently, the only feasible probe of the neutrinos nature is the aforementioned $0\nu\beta\beta$. This decay is expected to happen by exchange of a virtual Majorana neutrino between the two β decays in even-even nuclei according to $N(A,Z) \rightarrow N(A,Z+2)+2e^-$. Since the rate of this reaction is governed by m_{ee} according

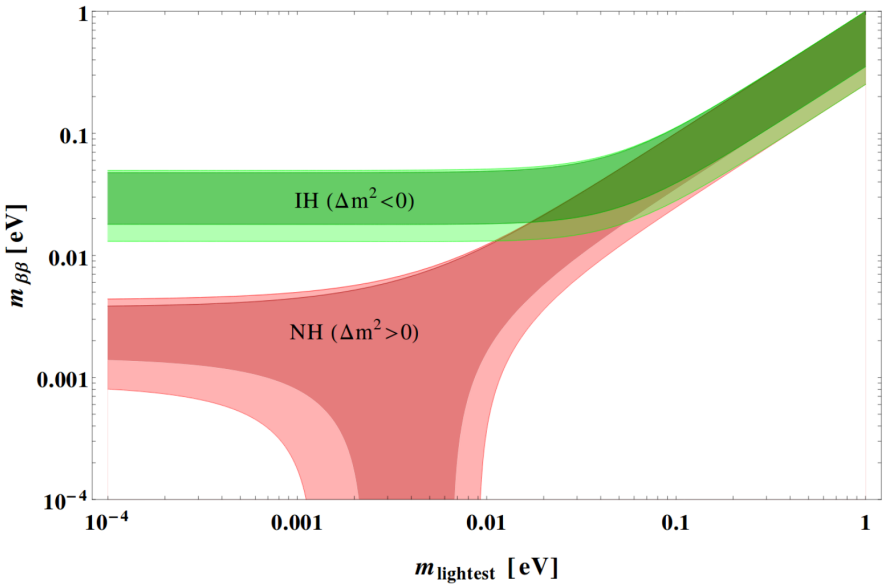

Figure 1.6 – Predictions of the effective Majorana mass m_{ee} as a function of the lightest neutrino mass m_{lightest}. Under the assumption that a Majorana neutrino is exchanged in the $0\nu\beta\beta$ decay, the shaded areas give the 3σ regions for the NO (red) and IO (green) of neutrino masses [54]. For $m_{\text{lightest}} < 0.01\,\text{eV}$ both mass orderings occupy a fully separated parameter space. Figure reprinted from Ref. [54].

to (1.21), its effect depends on the neutrino mass ordering among others. Figure 1.6 shows the possible parameter space for m_{ee} plotted as a function of the lightest neutrino mass m_{lightest}. With the given limits from Section 1.4.1, there are two separated areas for the normal and inverted ordering. Although so far no $0\nu\beta\beta$ has been detected [53], an external determination of the neutrino mass ordering could influence the design and sensitivity goal of future $0\nu\beta\beta$ experiments. Nevertheless, there are models to explain the $0\nu\beta\beta$ other than the exchange of a single light Majorana neutrino.

1.4.3 Sterile neutrinos

Another fundamental question in the neutrino sector is the number of species and the existence of additional neutrino flavors that do not interact through the standard weak force. The idea of so called sterile neutrinos is not only of theoretical nature, but also has some experimental motivation. Accelerator based short-baseline experiments and reactor anti-neutrino experiments have reported anomalies [60], that could be explained by oscillation of additional sterile neutrino species with a mass below 1 MeV. More details about this can be found in Refs. [36, 44]. Similarly, also the Gallium-based experiments GALLEX [61] and SAGE [62, 63] have reported anomalies in measurements of neutrinos from radioactive sources [64]. There was a dedicated experiment in planning with *Short distance neutrino oscillation with Borexino* (SOX) [65] to test a sterile neutrino hypothesis, but unfortunately it could not be realized. Nevertheless, future LS neutrino detectors like

JUNO will lower the uncertainty on the solar oscillation parameters below the percent level and help to test the three flavor hypothesis [30]. Furthermore, several *very short baseline* (VSBL) experiments are currently taking data to investigate the possibility of a fourth, sterile neutrino. A comprehensive overview and subsequent links can be found in Ref. [66].

Chapter 2

Liquid Scintillator Detectors

The use of scintillating materials is a standard method used in particle and nuclear physics, due to its favorable characteristics [67, 1]. In liquid form it can be cleaned and purified easily even in very large amounts, which allows for the construction of detectors with target masses in the range of tons and kilo-tons. In contrast to solid scintillators, it can also be maintained after initial deployment. Apart from only detecting the presence of particles, the properties of liquid scintillator enable calorimetry, since the amount of light is proportional to the energy, that particles deposit in the LS.
In neutrino experiments the bulk mass of LS builds the target for the neutrino to interact and is simultaneously used to detect the charged particles from said interactions. The same holds true for neutrino experiments that are based on water and ice like SK and IceCube, but they rely on the *Cherenkov effect* to render charged particles visible. New approaches investigate the possibility to combine LS materials and water to overcome limits on the attenuation length, which will be explained in more detail in Section 2.2.1. This is only important in the class of *unsegmented* detectors, which will be the focus of this chapter. A *segmented* detector has several smaller cells, that hold the target material and have a dedicated, but often single, readout. In an unsegmented detector the full target mass is hold within one vessel and observed from the outside by an array of readout-sensors, that detect the created light.
In the following Section 2.1 gives an overview over the ways light is produced in LS and Section 2.2 deals with the effects on the photons while propagating through the detector. The detection of the light and processing of a meaningful signal from it is covered in Section 2.3.

2.1 Light production

The process responsible for light emission of LS materials is luminescence, which is a form of cold-body radiation, since it does not result from heat [68]. Excited electron states in the luminescent material emit photons on de-excitation in the UV or visible spectrum. The process for this is different in organic and inorganic scintillators, but not of high

importance in this scope. In neutrino experiments often used representatives of aromatic, organic LS solvents are *linear alkylbenzenes* (LAB, $C_6H_5C_nH_{2n+1}, n = 10...16$), *phenyl-o-xylylethane* (PXE, $C_{16}H_{18}$), and *1,2,4-trimethylbenzene* (pseudocumene, C_9H_{12}).

Core aspects in particle detectors are the time profile of photon emission and the relation between deposited energy of a charged particle and the amount of emitted light. While the latter is a fundamental characteristic to extract an energy estimator for calorimetric measurements, the time profile carries information about the particle type and position of creation inside the detector.

It is important to note that charged particles will also produce photons via the *Cherenkov effect* when traversing LS. Although the intensity is much smaller than for scintillation light [1], it is measurable and influences the reconstruction of a particle's position and energy.

2.1.1 Scintillation light

When a charged particle moves through matter, it will lose energy by transferring it to the molecules that make up the material. This effect is well described as the mean energy loss per unit length $\langle {}^{dE}/_{dx} \rangle$ by the *Bethe-equation* for moderately relativistic particles heavier than electrons [1]. The equation holds for particles with $0.1 < \beta\gamma < 1000$ for intermediate-Z materials, with β being the particle's speed as a fraction of the speed of light in vacuum and γ its *Lorentz factor*. In order to describe particles in other energy ranges as well as electrons, some additional factors, like the *Bloch-correction* have to be added to the equation [1].
In LS this energy transfer leads to excitation of the electrons in the molecular shell. Their subsequent de-excitation to lower energy levels emits photons isotropically. Therefore, the emission spectrum is characteristic to the used LS material. Nevertheless, the emission spectrum is only shifted slightly against the absorption spectrum by the stokes shift. Thus, there is a high chance of the photon being absorbed by exciting another electron and hence, the LS is not as transparent to its own light as needed for large detectors. A solution to this was found by adding organic flours and wavelength shifters in small concentrations to the bulk of LS. Neutrino experiments often use *2,5-diphenyloxazole* (PPO, $C_{15}H_{11}NO$) or *1,4-Bis(2-methylstyryl)benzene* (bis-MSB, $C_{24}H_{22}$) to absorb the scintillation photons and re-emit them at a longer wavelength, that is also favorable for the photon detection modules.
The scintillation light yield is a crucial measure for neutrino detectors because it is the main energy estimator. About 3% of the transferred energy in a LS is released as photons, but the relation between deposited energy and light yield is not linear [1]. The ionization density along a particle track influences the light response. A very high ionization density, as created by heavy particles like protons or α-particles, produces less light than expected from a minimum-ionizing particle [1]. This effect is called *quenching* and is well-described by a semi-empirical model by Birks [1, 68]. With $\mathcal{L}_0$ being the luminescence at a low specific ionization density of about 1 photon per 100 eV deposited energy, Birks' formula

is [1]

$$\frac{d\mathcal{L}}{dx} = \mathcal{L}_0 \frac{{}^{dE}/_{dx}}{1 + k_B {}^{dE}/_{dx}}. \tag{2.1}$$

Here k_B is the Birks' constant, which is a material property and has to be measured for a given LS.

The second defining characteristic of a scintillator is the time profile of the light emission. This is caused by the fact that the decay of an excited electron state does not happen instantaneously, but after several nanoseconds to some hundreds of nanoseconds. With the decay rate of an excited state being proportional to its population, the process can be statistically described by an exponential function. Usually, there is a number of states with different decay times which amount to two or three components in the effective decay time distribution [68]. The probability density function for the emission time of a photon can be written as the weighted sum of exponential functions like

$$f(t, \tau, \omega) = \sum_{i=1}^{n} \frac{\omega_i}{\tau_i} e^{-\frac{t}{\tau_i}}. \tag{2.2}$$

Here $\tau = \{\tau_1, ..., \tau_n\}$ and $\omega = \{\omega_1, ..., \omega_n\}$ are the mean life times and weights of the different components and for a meaningful normalization $\sum_{i=1}^{n} \omega_i = 1$ must hold. Naively, the complicated delay in photon emission seems to be deteriorative to a reconstruction of the process by the photon timing, but in fact it gives power to particle discrimination. Different charged particles will create different populations in the excited state which lead to distinctive sets of effective decay times τ and weights ω. The discrimination of different particles like electrons and positrons as well as protons and α-particles is called pulse shape discrimination and is often used for background rejection [69].

2.1.2 Cherenkov light

When a charged particle passes through a dielectric medium at a speed greater than the local phase velocity of light, it will radiate Cherenkov light [70]. The mean energy loss $\langle \frac{dE}{dx} \rangle$ in condensed materials by Cherenkov radiation is only $\sim 10^{-3}\,\mathrm{MeV\ cm^2\ g^{-1}}$ and does not play a significant role [1]. Nevertheless, the emitted photons contribute to the full signal in a LS detector and are the main signal in water-based neutrino detectors. A distinctive feature of this effect is, that the photons are not emitted isotropically, but under a distinct Cherenkov angle θ_c to the particle's momentum direction. For a *dispersive medium* with refractive index $n(\lambda)$, the Cherenkov angle is defined as

$$\cos\theta_c = \frac{1}{\beta n(\lambda)}, \tag{2.3}$$

where β is the particle's speed as a fraction of the speed of light in vacuum. This definition implies a threshold velocity of particles depending on the medium of $\beta_t = {}^{1}/_{n(\lambda)}$. The group velocity of the radiated photons with wavelength λ in a medium with normal dispersion is given by [1, 70]

$$v_g = \frac{c_0}{n(\lambda) + \lambda \frac{dn}{d\lambda}}, \tag{2.4}$$

with c_0 being the speed of light in vacuum. Since this velocity is slower than the charged particle, the light travels behind the particle and there is constructive interference of the light waves that create a coherent wavefront [70]. As can be seen in Figure 2.1, this wavefront forms a cone with the opening half-angle η and has its vertex at the position of the moving particle. This directional light can be detected as rings in large Cherenkov detectors and holds information about the particles spatial orientation.

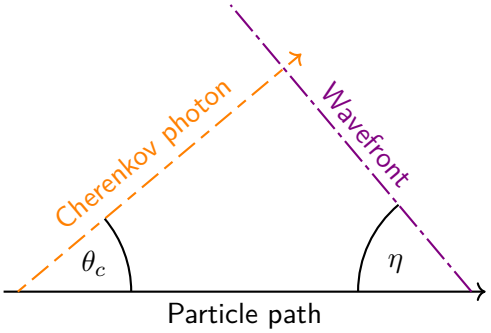

Figure 2.1 – While a charged particle (black) moves with $v = \beta c_0$, it will emit Cherenkov photons (orange) under the characteristic angle θ_c in every point of its path. In the dispersive medium the photons travel with $v_g < c_0$ and interfere constructively in the Cherenkov wavefront (purple). Together with the momentum direction of the particle this front builds a cone with opening half-angle η.

The number of emitted Cherenkov photons along a unit path length dx and an photon energy interval $d\epsilon$ for a particle with charge Ze is given by the *Frank-Tamm-formula* [1]

$$\frac{d^2N}{dxd\epsilon} = \frac{\alpha Z^2}{\hbar c}\sin^2\theta_c = \frac{\alpha Z^2}{\hbar c}\left(1 - \frac{1}{\beta^2 n^2(\epsilon)}\right) \tag{2.5}$$

$$\approx 370\sin^2\theta_c(\epsilon)\mathrm{eV}^{-1}\mathrm{cm}^{-1} \quad (Z=1). \tag{2.6}$$

In general, the Cherenkov effect only contributes a few percent to the total light yield of a LS detector. Nevertheless, its light carries directional information about the incident particle. Current design studies for very large future neutrino detectors consider a water-based LS, which would allow for a tuning between both scintillation and Cherenkov radiation. With a higher fraction of Cherenkov photons of the total light yield, it would be easier to extract its directionality information [71, 72].

2.2 Light propagation

After creation of the photons by an interaction, they have to traverse the LS and often other media before reaching the light detection modules. At the time of creation the photons carry all available information about the event they stem from, but several processes along the way can alter the signal before detection. For a good localization of an event in space and time, it is important to understand and model the effects that influence the time profile and actual number of detected photons. Section 2.2.1 deals

with the effects that are summarized as *light attenuation* and particular effects of certain detector designs are subject of Section 2.2.2.

2.2.1 Light attenuation

The main effects in photon propagation are *scattering* and *absorption*. Among others, most prominent are *Rayleigh scattering* on bound electrons in the medium and *Mie scattering* on impurities like dust as well as absorption of photons by molecules. The latter has a chance to either re-emit the photon, effectively changing its momentum direction or a conversion to an energy form that is invisible to the detector like infrared light or heat [73]. For the purpose of event reconstruction absorption with subsequent re-emission is identical to scattering, as it changes only the photons direction, but does not remove it completely. Nevertheless, any scattering means a loss of information about the photon's origin as it is impossible to recover the processes it went through at time of detection. The number of scattered photons follows an exponential distribution, so that the probability density function for a photon to be scattered or absorbed is [73]

$$f_{\text{att}}(x) = \frac{1}{L} e^{-\frac{x}{L}}. \tag{2.7}$$

The defining factors are the traveled path $x = |\vec{x} - \vec{x}_0|$ and the total *attenuation length* L. The latter is an effective value, but can be split with respect to the underlying processes

$$\frac{1}{L} = \frac{1}{l_A} + \frac{1}{l_S}; \qquad \frac{1}{l_S} = \frac{1}{l_{are}} + \frac{1}{l_{ray}} + \frac{1}{l_{mie}}. \tag{2.8}$$

The full attenuation is made up from the characteristic lengths for absorption (l_A) and scattering (l_S) respectively. The latter further consists of the three lengths for absorption/reemission (l_{are}), Rayleigh scattering (l_{ray}), and Mie scattering (l_{mie}) [73].

While those effects are not crucial for small or segmented detectors, light attenuation is a limiting factor for large LS experiments. At some point an increase in quantity of statistics by a larger target volume no longer justifies the associated deterioration of the data quality, due to growing attenuation effects. The attenuation length is a material property, that is influenced by the composition and purity of the LS. For this reason, it is a design parameter for future LS detectors and large R&D efforts are underway to increase the attenuation length of organic liquid scintillators. Another approach to this problem is solving the LS in water, as mentioned in Section 2.1. Although the absolute light yield decreases, the long attenuation length of water in the order of $\sim 100\,\text{m}$ would reduce the deteriorating effects on the available photon statistics.

2.2.2 Other effects

While the attenuation describes the light propagation inside the LS target well, there are more effects to take into account before the photons are detected. In most cases of neutrino experiments, the light detection modules are not submerged in the LS, but observe the volume from further outside. This implies that the photons will undergo transitions between media with different refractive indexes. Not only the light's group velocity (see

Section 2.1.2) is influenced by that, but there is also the possibility of refraction and reflection. Although those effects are not statistical, at the point of detection the photons have lost the information about their origin similar to being scattered. Nevertheless, it is often possible to predict and model those processes to minimize their effect on the event reconstruction.

2.3 Light detection

The second key element of LS detectors apart from the scintillating target are the light detection modules. They mark the last step of information collection about physical events happening inside the detector. After a charged particle created photons and they moved through the detector as explained in the two sections before, at some point this light has to be detected and converted into a meaningful and storable signal. Typically, this is done with photo-multiplier tubes [67], which is the topic of Section 2.3.1. Lastly, Section 2.3.2 outlines the basic choices of immediate electronics to digitize the analog signals.

2.3.1 Photo-multiplier tubes

Photo-multiplier tubes (PMT) are highly sensitive light detectors, that are able to measure light down to the level of single photons [74]. Although realized in different shapes and with different technology (see Ref. [74] for details), their working principle remains the same. An incoming photon is converted to an electron, which is then accelerated and multiplied in a cascade to a measurable signal. This mechanism is realized with mainly three parts shown in Figure 2.3. First, the transmission cathode allows for an incoming photon to be converted to an electron by the photoelectric effect [70]. Through an applied high voltage in the range of $\sim$1000 V this photoelectron (PE) is then accelerated towards the first dynode. Upon hitting it, the PE will knock out more electrons, which are subsequently accelerated to the next dynode. This cascade through an array of dynodes multiplies the number of electrons exponentially until they are collected as a measurable current at the anode. The variable number of dynodes and choice of potential gradient between them governs the amplification factor called *gain*, which typically ranges from 10^3 up to 10^8 [74]. All components of a PMT are enclosed within an evacuated glass housing to reduce disturbance of the electron trajectories. As can be seen in Figure 2.2, smaller PMTs are actual cylindrical tubes, while those that feature a large photocathode often have a bulb-like shape with an ellipsoid attached to the glass tube.

An alternative design of PMTs modifies the electron multiplication stage to utilize microchannel plates (MCP) in order to increase its efficiency. Instead of discrete dynodes, one or more MCPs are placed in the middle of the glass bulb. These are positively charged metallic plates, that are coated with a strongly resistive material, which is penetrated by many small tubes, the eponymous microchannels [74]. Due to some angle towards the charged plane, electrons that reach a channel are accelerated towards a wall, where they knock out more electrons and create an avalanche similar to the dynode array. With the diameter in the range of 2 µm to 6 µm per channel, MCP-PMTs are supposed to

Figure 2.2 – Range of dynode PMTs in different sizes and shapes from Hamamatsu [75]. LS neutrino experiments typically use the larger, bulb-shaped models.

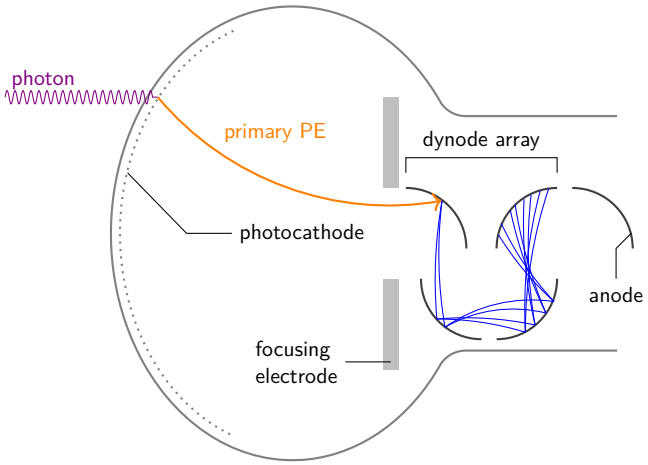

Figure 2.3 – Schematic working principle of a PMT. An incoming photon can knock out an electron in the photocathode. This electron is accelerated through the focusing electrode to the first dynode, where more electrons are released. Through the dynode array the electrons are multiplied in an avalanche to a measurable signal at the anode.

be less susceptible to magnetic fields than dynode PMTs [74]. For large area PMTs the use of MCPs at the electron multiplication stage allows for an increased size of the photocathode. As shown in Figure 2.4, the top half of the bulb consists of a transmission photocathode (PC) similar to a dynode PMT. In addition to that, the bottom half of the bulb can be covered with a reflection PC, which has two implications for incident photons. If in the first passing of the transmission PC, the photon was not converted

to a PE, this can still happen at the bottom of the PMT on the reflection PC. Finally, the photon has a chance to be reflected back towards the front of the PMT, hitting the transmission PC one more time.

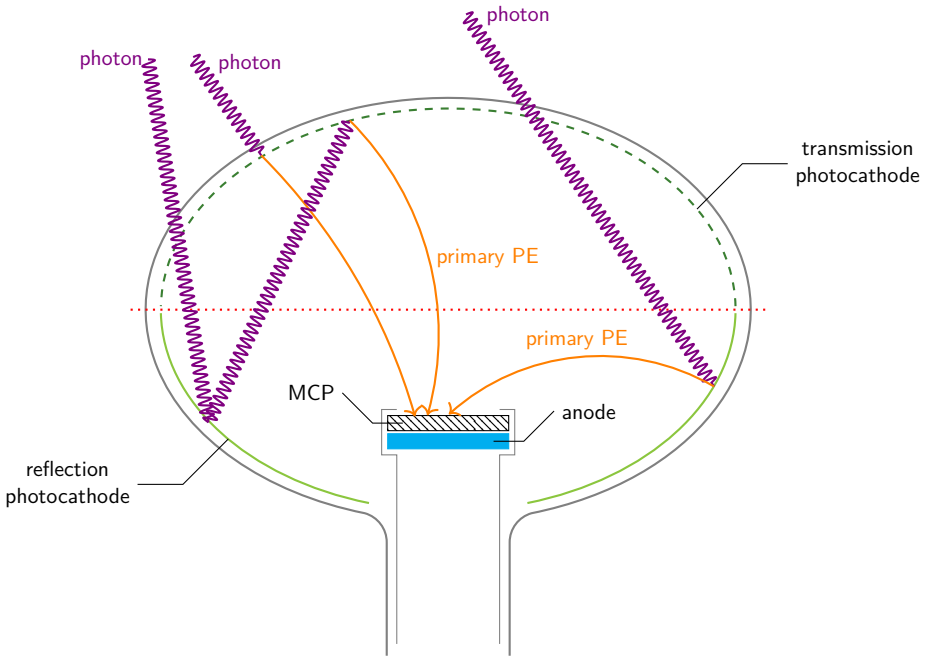

Figure 2.4 – Working principle of a MCP-PMT. If an incoming photon is converted to a PE in the transmission photo-cathode, the process is similar to a dynode PMT with the only difference being the MCP multiplying the electron avalanche. The unique feature is the reflection photo-cathode at the bottom part of the glass bulb. Photons that pass the first cathode have a second chance to be converted to a PE here. The geometry still allows electrons from those points to be accelerated towards the MCP.

Although different in technology, the performance of both kinds of PMTs is compared by the same parameters. The detection efficiency of a PMT ϵ_{det} is the number of output signals per incident photons N_γ. While this is influenced by many factors, it is mainly governed by the quantum efficiency ϵ_q of the PC and collection efficiency ϵ_c of the multiplication stage like

$$\epsilon_{det} = \epsilon_q \times \epsilon_c. \tag{2.9}$$

The quantum efficiency is the ratio of the number of created PE to the number of incident photons. It is a quantity of the PC can be tuned by the choice of material and its thickness among others. In MCP-PMTs ϵ_q is boosted by the fact, that a transmitted photon has another chance to create a PE at the back of PMT or to be reflected to the front again. Typical values for ϵ_q range between 10% and 40% [74]. Subsequently, the collection efficiency describes the fraction of PE, that are successfully focused and multiplied to a measurable current. It is possible that the trajectory of a PE is deflected, e.g. by magnetic fields, and thus it will not reach the dynode or MCP at the required

position. Although the inside of a MCP is much less vulnerable to magnetic field than a dynode array, the path of the primary PE to the middle of the bulb is comparably long for large area PMTs. Often this requires a magnetic shielding around the PMT even for the Earth magnetic field [74].

Directly connected to this is the second characterization parameter of PMTs, the *Transit Time Spread* (TTS). From the working principle of the PMT it is evident, that it takes a finite time between a photon reaching the PC and the output of the electric current. The total transit time T can be expressed as the sum of an average time $\bar{T}$, mainly governed by the path length and a fluctuation δT arising from the PMT geometry and the multiplication stage. The TTS describes the distribution of δT and is often expressed as FWHM, due to its generally asymmetric shape. Since the photon can only be detected through its PE, the reference point for determining the transit time has to be associated with the photon and not the PE. Due to that, the MCP-PMT tends to have a much larger TTS compared to a dynode PMT, because in a fraction of cases the photon travels through the PMT and only creates a PE on the back or after reflection. In the case of large PMTs in which the PC is not a perfect sphere, also the incident point of the photon on the cathode contributes to δT. Taking those effects into account, both $\bar{T}$ and δT increase with growing PMT size.
The photon statistics driven by ϵ_{det} are fundamental for the energy reconstruction of an event, but the localization heavily depends on its time structure. While the constant part of the transit time is easily accounted for as an offset, the TTS worsens the detectors time resolution and limits the accuracy of position or track reconstruction and particle identification.

Being highly sensitive detectors, PMTs are also subject to noise and other false signals. *Dark pulses* are signals that look like a PE, but actually stem from a different source, like thermionic emission of electrons in the cathode or dynode or leakage current. Typically, this rate is coupled to the operating temperature, the structure of the PC, and the applied high voltage [74].
Another effect are *pre-pulses*, that occur when the photon passes the PC and creates an electron directly at the multiplication stage. Compared to normal operation, this pulse is earlier and with lower intensity, due to skipping the first multiplication step. In a situation where several photons hit the PMT at the same time, a pre-pulse can be misidentified as a preceding, separate photon [74].
In the same fashion there are can be delayed pulses, called *afterpulses*. There are two different types to be distinguished that also happen on different time scales. The majority of afterpulses with a short delay of several nanoseconds to several tens of ns are caused by an electron scattering elastically from the first dynode [74]. In the context of LS detectors this type of afterpulse is often overshadowed by other time resolution effects. On the other hand, the long delayed afterpulses are much more prominent in this application. They appear when an electron ionizes the residual gas in the tube while moving to the dynode. The thereby created ion is accelerated back to the PC, where it produces several photoelectrons, which lead to the spurious signal. Depending on the high voltage

supplied to the PMT, the delay time lies between several hundred nanoseconds up to a few microseconds [74].

2.3.2 Electronics

As explained above, the PMT will create a current pulse for each photon that creates a PE. This has to be converted to a voltage signal, which is usually done by measuring the voltage drop at a load resistor. The distinction between noise and signal can then be done via a voltage threshold. Especially for single-photon hits this threshold has to be considered carefully in order not to lose actual hits.
For further information extraction from this signal many different approaches were tailored to each experiment's needs. The most simple approach is a *charge integration* for the signal's time over threshold. This solution is easy to implement, works fast and with full efficiency and the digitized value is proportional to the detected charge for low photon-hit densities.
For higher hit rates this proportionality gets disturbed, as overlapping PE are not guaranteed to result in a linear combination of several single PE pulses. This happens because after a high charge signal PMTs usually need a small amount of time to return to their *baseline*. Another downside of this direct charge integration is, that the timing pattern cannot be recorded, but only the start time of each integration. For detectors, that operate only in a low hit rate mode, this does not pose any problem, but LS detectors typically feature a large dynamic range of signals, which require a more detailed *data acquisition* (DAQ).
On the other end of the spectrum of PMT readouts stands the full waveform sampling. This involves recording the whole temporal evolution of the PMT voltage signal with an *analog-to-digital-converter* (ADC). The reconstruction of charges and hit time patterns is then outsourced to another step where more sophisticated methods can be applied. Main factors for the ADC electronics are the *dynamic range* and the *sampling rate*, typically expressed in *samples* (S) per second. The signal of a muon in a LS detector can induce a pulse that is up to 10^3 times higher than a typical low energy event. Resolving this with an ADC while maintaining a good resolution for small pulses is a challenge for the electronics design. It is governed by the number of bits provided by the ADC and their utilization for a dynamic range. Another important characteristic for the resolution of the recorded waveforms is the sampling rate. Typical values lay between 0.25 GS/s and 1 GS/s, which corresponds to one sample per 4 ns and 1 ns respectively. If feasible, the sampling rate is chosen to at least resolve the rising edge of the investigated signal.
Digitizing the full ADC trace gives the possibility to extract much more information from the signal, which in turn can be utilized by subsequent algorithms to better reconstruct the physics processes. An example of this is the muon track reconstruction discussed in Chapter 5. Nevertheless, this mode of operation needs more sophisticated electronics and produces more data to be processed and saved.

2.4 Particle identification

Any particle that interacts with the LS will produce light according to the mechanisms discussed in Section 2.1, which can then travel to the PMTs, where it is detected. Nevertheless, the topology of the signal depends on the interacting particle. Since not only the photon emission time profile is influenced by that, but also the total amount of visible light, particle identification is crucial for the energy reconstruction. Section 2.1.1 discussed that quenching stems from the ionization density of the traversing particle, so that the different categories correspond to the particle's masses. The classification discriminates gammas, electrons and positrons from the group of protons, and lastly the heaviest α-particles, as reflected in Table 3.1. In the following, the different categories will be discussed shortly.

Electrons, positrons, gammas The lightest particles are often taken as the reference, since they appear in energy ranges where they are minimum-ionizing and, thus, have the smallest quenching. Within this group, positrons have the shortest range, as they can directly annihilate with electrons into two 511 keV gammas. Therefore, the visible energy of a positron is not only its kinetic energy lost by ionization, but it is always shifted by 1.022 MeV from the annihilation. However, the positron can enter a short-lived, bound state with an electron called *positronium* before its annihilation. The configuration with parallel aligned spins is called *ortho-positronium* and has a lifetime of 142 ns [76]. This feature makes it distinguishable from electrons, which deposit their energy directly in one process. The discrimination of electrons and positrons is an important technique for background reduction in the IBD event selection (see Section 4.1.2). Electrons and gammas do not annihilate, but have a longer range, which increases with the energy. This is especially important for gammas, as they can penetrate the vessel and deposit a part of their energy outside of the LS. In that case, only the energy lost in the LS is visible and calorimetry of the full gamma is not possible. Chapter 8 goes into detail, how this so-called *gamma leakage* can worsen a detector's calibration.

Protons, Neutrons Being considerably heavier than electrons, protons have a higher ionization density and experience more quenching. The corresponding Birks' constant used in the OSIRIS simulation for this case is given in Table 6.5. In addition, their timing profile trends more towards the longer emission times (see Table 3.1). Hence, comparing the time-of-flight corrected hit time distribution of events, a proton is expected to have more hits in the tail region than an electron, with the same total number of detected photons. Depending on the time constants of a LS mixtures, this effect gives a handle for particle identification. Although the mentioned effects are not applicable to neutrons, due to them not having an electromagnetic charge, they also have a distinct topology. Fast neutrons can scatter of protons and are then visible through the secondary energy deposition of the said proton. Apart from that, they are invisible to the LS, until they are thermalized and captured on a Hydrogen or Carbon atom. This effect is also only visible through the secondary energy deposition of the gammas released in the capture process. Nevertheless, it is a mono-energetic process and paramount for the IBD event

selection (see Section 4.1.2).

α-particles Being the heaviest of the considered particles, αs have a similar topology to protons, but the effects are more pronounced. Their visible energy is even more quenched than that of protons. In addition, their time profile has longer lived components and a higher weight for the longest component. Thus, the discrimination power for α-particles from electrons and positrons is higher and even a distinction from protons is essentially possible.

Details on how the different topology of the particles can be exploited for background rejection in JUNO is discussed in Section 4.1.2.

Part II

JUNO

Chapter 3

Jiangmen Underground Neutrino Observatory

LS detectors have a long history in particle physics and were the instruments used to make the observations that started neutrino physics [77]. More than 60 years later, LS detectors are well established and successful in spectral analysis of ν and $\bar{\nu}_e$ in the range of some 100 keV up to several tens of MeV [67]. Essential features of LS detectors are a good energy resolution and no intrinsic energy threshold. The current generation of LS-based neutrino experiments features target masses of up to 1 kton of LS, like KamLAND [78]. Other leading experiments of this category are Borexino [79], Double Chooz, Daya Bay, and RENO. Collectively, they helped to provide the most precise description of neutrino oscillation physics today, as explained in Chapter 1.1.1. Similar in size, the SNO successor SNO+ [80] will be searching for neutrino-less double beta-decays and several VSBL reactor experiments are also LS based [66].
In the next generation of LS-neutrino detectors, a larger target mass and more dense instrumentation will lead to even better energy resolutions and push the boundaries of the LS-technique. The *Jiangmen Underground Neutrino Observatory* (JUNO) is set to be the first next-generation detector with a target mass of 20 kt. Being currently under construction, it is estimated to start data taking in 2021 and be part of the first experiments to determine the neutrino mass ordering [30]. In 2013 the project was approved by the *Chinese Academy of Science* and the formation of an international collaboration followed in 2014. As the name suggests, it is located close to *Kaiping*, which is part of the prefecture-level city *Jiangmen* in Southern China.

More information about the choice and features of the experimental site is given in Section 3.1. Section 3.2 gives a description of the JUNO detector systems, including a more detailed overview over the *OSIRIS* project for later reference. As important as the hardware is the software framework used to process and analyze the data, which is explained in Section 3.3.

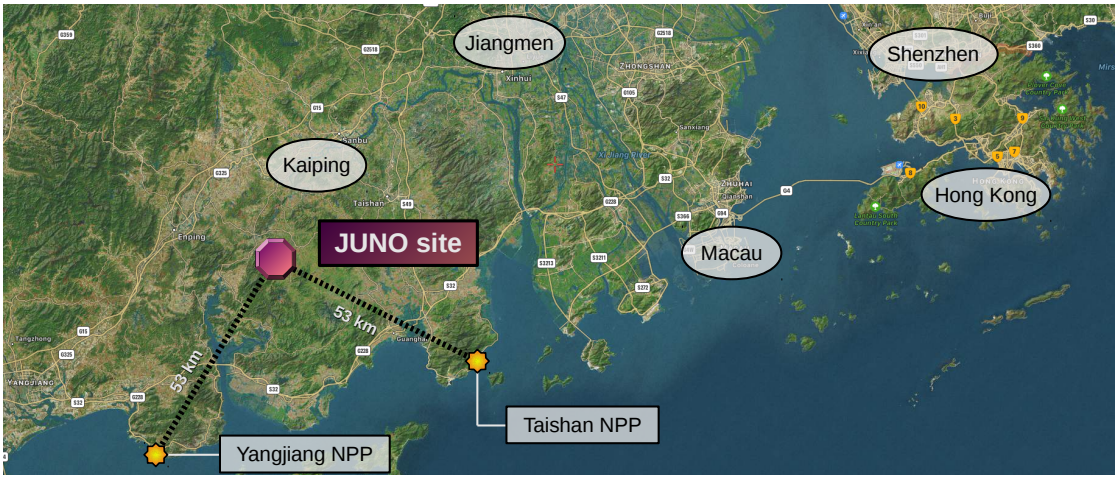

Figure 3.1 – Map of the JUNO experimental site and the two nuclear power plants Yiangjiang and Taishan. The largest surrounding cities are marked as well.

3.1 Experimental site

JUNO is designed as a reactor anti-neutrino experiment, which implies certain requirements on the location of its detector. The experimental site was chosen to be on a baseline of 53 km with regard to two *nuclear power plants* (NPP). The *Yianjiang* NPP will operate with six reactor cores of 2.9 GW thermal power each when JUNO starts data taking. Additionally there will be at least two 4.59 GW cores working in the *Taishan* NPP at this time with two more cores of equal power to be finished not long time later. Thus, the total thermal power will amount to $\approx 36\,\mathrm{GW_{th}}$, with $\approx 26.6\,\mathrm{GW_{th}}$ available when JUNO starts [30]. The next neutrino source is the Daya Bay complex being about 215 km away from JUNO. This will still make up for about 2.9% of the antineutrino reactor events, that JUNO will detect [30]. Other than two proposals for new NPP there is no strong neutrino source in a 500 km radius around JUNO to compromise a clean signal from the 53 km baseline. An overview for the distribution of NPP is given in Figure 3.1.

A second crucial requirement for JUNO is the achievable *overburden*, to shield the detector from cosmic backgrounds. With the limitation by the distance to the NPP, the ideal experimental site was chosen to be beneath Dashi Hill. It has an elevation of 268 m which provides much needed shielding against cosmic muons [30]. Additionally, the laboratory is placed in a cavity ~ 460 m underground. This amounts to a total overburden of more than 650 m or ~ 2000 m.w.e [30]. The laboratory will be accessible by two tunnels, a vertical shaft going straight down and an inclined slope tunnel of 1340 m length. Facilities of the underground lab include LS halls, that house the purification systems and OSIRIS, as well as storage areas and the main detector hall.

The surface facilities, shown in Figure 3.2, are mainly storage and assembly halls, but also include the first level of data processing and transfer.

Figure 3.2 – Surface facilities at the JUNO site include storage and assembly halls as well as accommodation for on-site workers.

3.2 Detector systems

In its role of an neutrino observatory, JUNO does not only consist of one single detector, but several sub-systems, that are designed to interact according to their individual strengths.

Nevertheless, the heart of the experiment is the Central Detector (CD) with 20 kt LS as the neutrino target. This volume is contained by a spherical acrylic vessel with 12 cm thickness and a diameter of 35.4 m. It is enclosed in a *Stainless Steel Truss* (SST), that holds the sphere into place. With a diameter of 40 m, the SST is also the holding frame for two independent PMT arrays for the light detection. Details on the chosen LS mixture and the PMTs are given in the Sections 3.2.1 and 3.2.2 respectively.

The CD is placed in a large, cylindrical *Water Pool* (WP), that acts as shield against external radioactivity. In addition to that, it is instrumented with PMTs to act as a water Cherenkov detector for muon veto purposes. On top of the WP, there will be a plastic scintillator tracker, to measure external radioactivity and the cosmic muon flux. Both systems are presented in Section 3.2.3 in more details.

Finally, Section 3.2.4 introduces OSIRIS, which is a fully functional smaller LS detector in its own. It will be placed within the filling line of the CD to monitor the cleanliness of the LS after purification. Over the course of at least 6 months, the CD will then be filled with its LS mixture. With such a large target mass, it is imperative not to spoil the total LS in the CD with a single batch of contaminated LS.

3.2.1 Liquid scintillator

The unprecedented size of the CD presents challenges especially to the LS, that is used. For good data quality it is crucial that the largest amount of light can travel through the 40 m-spherical vessel and be detected on the PMTs without being absorbed or scattered.

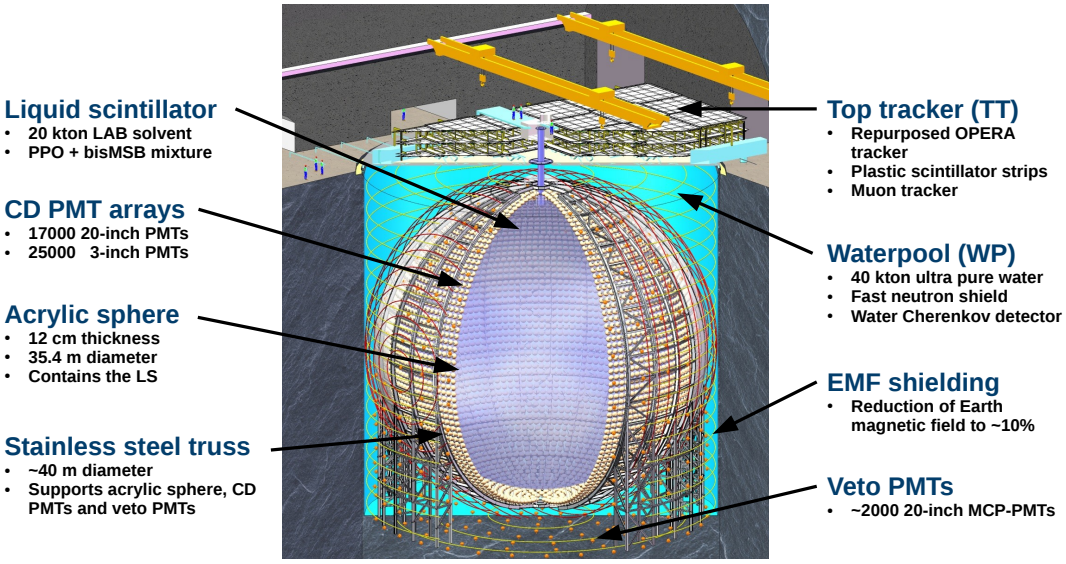

Figure 3.3 – Render of the main detector hall of JUNO.

Supposing an energy deposition in the center of the detector an attenuation length L (see Section 2.2) of at least 20 m is needed to detect direct scintillation light. Earlier designs of even bigger detectors like LENA chose a tube-like cylindrical shape to counter this problem [81]. The comparatively small radius would ensure short paths to many light detection modules, while the large height provides to total target mass. With the progress in increasing the attenuation length of commonly used LS, it is possible to realize JUNO in a spherical shape.
A second aspect of importance is the light yield. With the experiment's success depending largely on the energy resolution for depositions of a few MeV, a high light yield of ~ 10000 photons per MeV has to be achieved. In combination with the photon-detection systems discussed in the following section, a total of ~ 1300 detected *photo-electrons* (PE) per MeV deposited energy can be achieved.
JUNO will use LAB for its LS mixture. It will serve as a solvent for a two component system of scintillating flour and wavelength shifter. The flour was chosen to be PPO, while the wavelength shifter is Bis-MSB (see Section 2.1). With this mixture, the excitation of an ionizing particle is transferred to the PPO and shifted by the Bis-MSB to a wavelength of 430 nm. A higher concentration of PPO and Bis-MSB will increase the light yield, but with a higher chance of self-absorption decrease the attenuation length as well.
In order to find the mixture with the best balance between light yield and attenuation length, JUNO engaged in dedicated LS testing, using one antineutrino-detector of Daya Bay. The exact composition is not yet finalized, but about 2.5 g/l PPO is foreseen with Bis-MSB in the range of 1-3 mg/l [82]. Current reports quote an attenuation length of > 25 m [83], while maintaining the needed light yield level.
Following Equation (2.2), the JUNO simulation models the particle dependent emission times and yield fractions with three components. The expected values are summarized in

Table 3.1 and correspond to measurements of Daya Bay. As explained in Section 2.1.1, the light production in LS depends on the ionization density and is thus dependent on the particle type. Therefore, it is expected to measure different responses for the three groups: α particles, protons and neutrons, and gamma, electrons and positrons in the final mixture of PPO and Bis-MSB.

Table 3.1 – Particle dependent emission time constants and corresponding weights in the JUNO `Geant4` simulation. While the fast component has the same time constant and only varies in yield ratio for the three groups, the second and third time constant vary for the different particle categories.

Particles	Component 1		Component 2		Component 3	
	Value [ns]	Weight	Value [ns]	Weight	Value [ns]	Weight
$\gamma,\ e^+,\ e^-$	4.93	0.799	20.60	0.171	190.00	0.030
$n,\ p$	4.93	0.650	34.00	0.231	220.00	0.119
α	4.93	0.650	35.00	0.228	220.00	0.122

Another crucial consideration for the LS is its internal radioactivity. As an organic scintillator, there is a natural occurrence of uranium, thorium, and potassium in the LS. Along their natural decay chains, those isotopes produce decays in the sensitive energy range and by that pose a background for the measurements of JUNO. In addition, significant concentrations of ^{210}Bi, ^{210}Po and out-of-equilibrium ^{85}Kr can be found in organic LS [79]. While the energy spectrum is fixed, the rate is proportional to the abundances of the isotopes. Consequently, it is possible to reduce this contamination by purification of the LS.
In JUNO, this is done with a sophisticated purification plant. It includes a Al_2O_3 column, distillation, water extraction, and steam stripping stages in order to fulfill the requirements on the LS. A more detailed overview over this sub-system can be found in Ref. [84].
It has also to be noted that as an organic substance the LS contains a high natural abundance of ^{14}C. This isotope has a β^--decay with an endpoint at 156 keV. Although there is no intrinsic energy threshold in LS, some neutrino experiments tend to set their threshold above the ^{14}C range, because its high rate could overshadow other signals. Nevertheless, the very low energy range is important for fitting the spectra of solar neutrinos, so that Borexino has a threshold of 50 keV, and thus, detecting part of the ^{14}C spectrum. Currently there is no artificial way (e.g. purification) to reduce the amount of ^{14}C.

3.2.2 Photomultiplier tubes

Next to the LS discussed above, the second key element of the detector are its PMTs. JUNO's main feature is its unprecedented energy resolution, for which high photon statistics is a must. In order to achieve this, the CD is instrumented with two independent PMT systems, that provide a combined coverage of 77.5% [82]. While the pivotal

modules for the coverage are large PMTs (LPMT) with 20 inch diameter, there is an additional system of small PMTs (SPMT) with 3 inch diameter in place. Both systems are complementary and work in favor of the other as explained in the following [82, 85].

LPMT The LPMT array in the CD is made up of about 18000 modules in a distance $r = 20\,\text{m}$ from the detector center. About 5000 of them are conventional dynode PMTs by *Hamamatsu* (R12860-HQE) and the remaining 12000 modules are custom developed MCP-PMTs by *NNVT* in China. Photographs of both PMT types from the JUNO testing site can be found in Figure 3.4. They account for a coverage of 75% and do not feature any kind of light concentrator, due to their dense arrangement.
In order to reach the design goal of ~ 1300 PE per MeV, there are strict requirements on the PMT's performance. Most important is the photon detection efficiency, that has to be at least >24% at 420 nm for an individual PMT, but >27% averaged over the array [82]. Additionally, the dark count rate has to be less than 100 kHz for the MCP-PMTs and below 50 kHz for the dynode PMTs. Each individual high voltage supply will be calibrated to a gain of 10^7.
As presented in Section 2.3, the resolution of photon hit times is defined by the PMTs TTS and differs between MCP- and dynode-PMTs. This manifests in the specification for JUNO's modules as well. While the MCP-PMTs need to satisfy a TTS of better than 12 ns (FWHM), the dynode modules are able to achieve 3.5 ns.

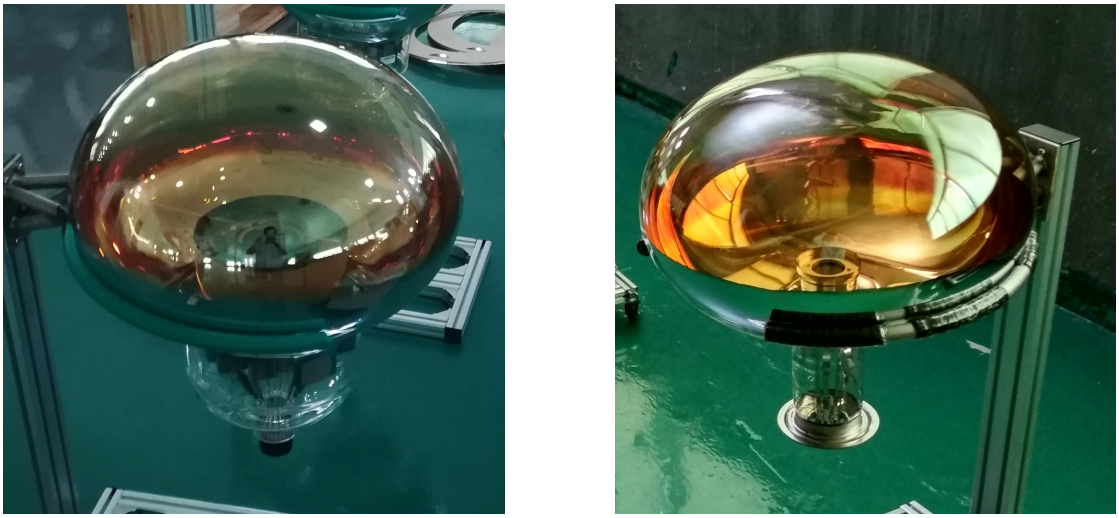

Figure 3.4 – Photographs of the two kinds of 20-inch PMTs that will be mounted in the JUNO CD. The *Hamamatsu* dynode PMT (left) has a bulkier bottom to accommodate the dynode array. The *NNVT* MCP-PMT (right) features the reflection photocathode on its bottom half.

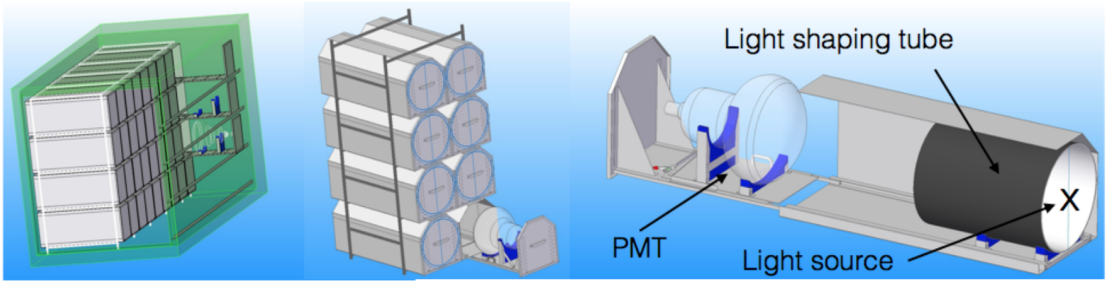

Figure 3.5 – PMT test-container schematic with the full container (left), detailed view of the drawer arrangement (middle), and a PMT mounted inside a drawer (right) [86].

SPMT The SPMT system is an independent readout system that consists of 25000 PMTs by *HZC* (XP72B22). However, it only contributes about 2.5 % to the total coverage, due to the very small size of the modules. This allows them to work in a pure *photon-counting* mode for events below 10 MeV, which is JUNO's focus. The combination of a large distance to most events and small surface area makes multiple hits on one module unlikely. Mounted in the spaces between the LPMT system, the SPMT array is designed to provide a second set of eyes with different and well understood systematics from the LPMT. While the 20 inch PMTs are new developments and need highly accurate characterization, small PMTs do not suffer from the effects introduced by the sheer size. A double calorimetry measurement can thus help to reduce systematic errors from the LPMT system [85]. The required specifications are a TTS <5 ns and an average quantum efficiency of >24 % with a dark count rate of <1.8 kHz.

LPMT Testing It is mandatory, that the LPMT system of JUNO is well understood and characterized to ensure a successful operation. For this purpose, a dedicated acceptance and testing facility was developed in the collaboration. As laid out in Ref. [86], all LPMTs have to undergo an acceptance test for the required performance and will later be characterized fully in a more sophisticated test procedure. Both steps are done in dedicated, custom-made test containers, that can take batches of up to 36 modules per run and work fully automated. The setup is completed by a scanning station, that is able to sample the whole photo-cathode of the PMTs. Currently about 8000 PMTs have went through the acceptance test and the preparation for the full characterization is well underway. More details can be found at Refs. [87, 88].

3.2.3 Shielding and veto systems

The CD is designed to be a highly sensitive detector to small energy deposition and by that susceptible for backgrounds induced from natural radioactivity and cosmic rays. For JUNO, the possibilities for natural shielding by e.g. mountains, is limited due to the restrictions set by the baselines to the NPP's reactor cores. In order to sustain the optimal sensitivity to the neutrino mass ordering, it is mandatory for JUNO to have the same distance to all reactors in both NPPs. A fixed baseline to two different NPPs

limits the possible location for JUNO to a small area. Nevertheless, the experimental site features $\approx 650\,\mathrm{m}$ total rock overburden, as explained in Section 3.1.

Waterpool A second layer of shielding is added by a large, cylindrical waterpool (WP), in which the CD is placed. With a diameter of 43.5 m and a total height of 44 m, it will give a minimum of 2 m water between the rock wall and the CD at the closest area. Since the SST, that holds the PMTs, is a frame and not a tank, also the space between the acrylic vessel and the PMT array is filled by the water. Typically, this area is called buffer and is needed to shield the LS from radioactivity in the PMT glass. The great importance of this system demands high standards of the water used. Impurities in the water can compromise the shielding effect by introducing radioactive elements to the PMTs and vessel. Furthermore the water will equate the PMT's and the electronic's heat loss and thus needs to circulate. JUNO addresses this with an on-site water production and purification circle with elements placed on the surface and underground.
In addition, the WP is instrumented with about 2400 MCP-PMTs to upgrade it from a pure shielding to an active water Cherenkov detector for vetoing cosmic muons. A good knowledge of the muon flux and their tracks' positions is important, as their background is manifold, which will be explained in Section 4.1.2. All muons that reach the CD will first cross the WP and thereby create Cherenkov light. This can be detected by the PMTs, that observe the water volume, in order to track the muon path. By that, the muon signal can be quantified an vetoed. A part of the muon flux traverses through the surrounding rock without hitting the WP and creates fast neutrons there. The WP provides shielding for the CD also from this kind of background. Details on background rates and veto efficiencies can be found in Section 4.1.2.

Top tracker The top tracker (TT) of JUNO will utilize the decommissioned target tracker of the *Oscillation Project with Emulsion-Tracking Apparatus* (OPERA) [89, 90]. It uses plastic scintillator strips with multichannel PMT readout to detect the passage of muons. In total there are 62 so called walls with an area of $6.7\,\mathrm{m} \times 6.7\,\mathrm{m}$ available for JUNO. Each wall consists of four vertical and four horizontal modules which allows for tracking in two dimensions in the wall's plane. According to its readout of 64 channels on each end, a module is divided into 64 strips of 26.4 mm width. Thus, each wall module is rasterized with 26.4 mm squares which leads to an extraordinary resolution [90].
The configuration of the TT in JUNO is subject to different circumstances than it was for OPERA. In its original setup, it was deeper underground with less radioactivity from the surrounding rock and also shielded by concrete walls. The noise level at the JUNO site for the TT is higher and for reliable tracking three layers of walls are stacked with a spacing of 1.7 m between each. Nevertheless, in this three layer layout it is not possible to cover the whole top area above the WP [82]. Consequential, it will be placed on top of the WP and cover about 50% of its area in one large bridge over the detector center as sketched in Figure 3.6. This allows for observing a full slice of the detector, including a large part of the CD and the WP. A detailed measurement of the flux through the TT area allows for an extrapolation over the whole area.

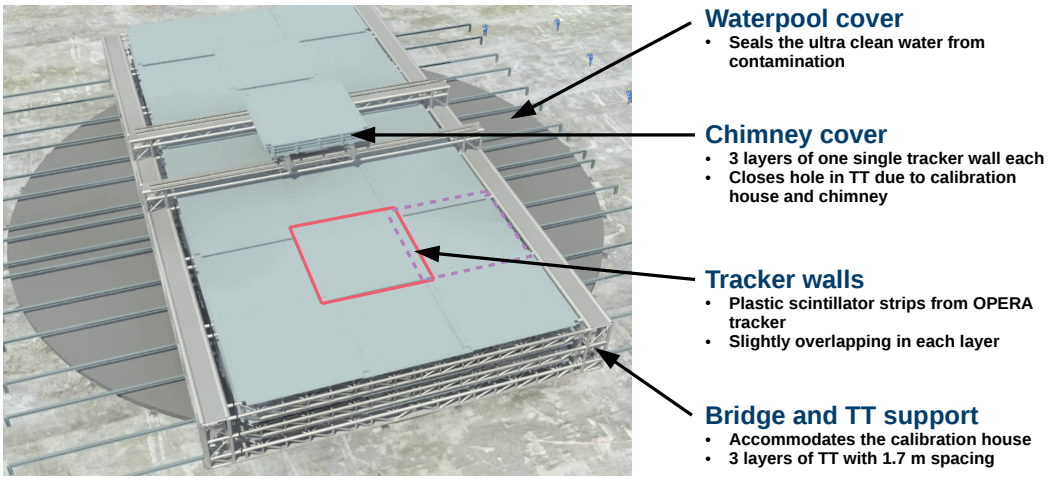

Figure 3.6 – Schematic of the bride over the WP. It will accommodate the TT holding structure as well as the calibration house, which gives access to the chimney into the CD. The individual plastic scintillator walls are placed slightly overlapping in three layers with 1.7 m spacing.

Both systems provide a powerful shielding and tracking potential for the CD in combination. Nevertheless, due to its highest information density, the CD has the largest reconstruction potential and is the main focus for the method presented in Chapter 5. In this context, the veto systems can provide a first guess track to seed a reconstruction based on the CD data and localize muons that traversed the WP without crossing the CD. In addition, the TT can be used to collect a sample of well-reconstructed muon tracks, that act as a calibration of reconstruction algorithms for the CD.

3.2.4 OSIRIS

A crucial aspect for the success of JUNO is the radiopurity of its LS [30]. The *Online Scintillator Internal Radioactivity Investigation System* (OSIRIS) is a standalone 20-ton pre-detector currently under development to ensure the cleanliness of the LS. It will be installed in the underground lab in the filling line close to the CD. There, it is supposed to act as an independent radiopurity test facility, that monitors the nominal operation of the purification plants. The fact that it will be taking data while the CD is being filled gives it also the possibility to act as a test bed for some JUNO subsystems.
Inspired by the Borexino CTF design [91], the central part of the detector is a transparent acrylic vessel (AV), that can hold a batch of about 21 m^3 LS. The volume is chosen to be as large as possible to reduce the required measurement time for the goal sensitivity. In contrast to the CTF, the AV of OSIRIS has a cylindrical shape similar to Daya Bay, with a wall strength of 3-4 cm. It is placed on a pedestal that consists of an acrylic footing and a mechanical support structure made of stainless steel.
The light created in the LS is detected by an array of PMTs on a stainless steel frame,

placed so that the photocathodes are at about 1 m distance to the AV. The LS will be observed by 76 of the same Hamamatsu 20-inch PMTs as used for JUNO. While four PMTs are placed in a ring on the bottom and the top each, cylinder mantle is covered by five rings of 16 modules each. The choice of fast, large area PMTs creates a coverage of ∼13.4% and yields a sufficient energy resolution of ∼5-6% at 1 MeV.
The space between the PMTs and the AV is filled by water to act as a shielding similar to the CD of JUNO. This water volume extends another 2 m beyond the PMTs to also shield the detector from the surrounding rock in the lab. The volume is contained by a cylindrical steel tank, that is both 9 m in diameter and height. It will be made from carbon steel and have an HDPE liner on the inside. In the same fashion as JUNO, the water shield will be instrumented with a secondary array of PMTs to as as a outer muon veto.
More details on the geometry, physics cases and their simulation will be given in Chapter 6 and the sensitivity study for U- and Th-contamination is presented in Chapter 7. A special focus is set on the development of the detector calibration campaign, including the hardware, as introduced in Chapter 8.

3.2.5 TAO

The *Taishan Antineutrino Observatory* (TAO) will be an additional standalone detector for JUNO to produce a high resolution reference spectrum of the electron anti-neutrinos emitted by one of the reactors in the Taishan NPP. As discussed in Section 1.3, modeling the reactor spectrum precisely is very difficult. With the improved energy resolution of JUNO, it is expected to measure the fine-structure of the reactor spectrum for the first time. In order to control for this effect in the context of the MO, which manifests itself in a similar looking way as wiggles on the spectrum, a reference spectrum with the same or better energy resolution is needed [50].
In order to achieve this, TAO is designed to provide a model-independent reactor anti-neutrino spectrum with a resolution better than $2\%/\sqrt{\mathrm{E[MeV]}}$. It will feature 2.6 tons of Gadolinium *doped* LS, hold in a spherical vessel with ∼1.8 m diameter. The acrylic vessel surrounded by a copper shell that holds the photon detection modules and is placed in a cylindrical steel tank filled with LAB as buffer material. Placed within the Taishan NPP, it will have a distance of ∼30-35 m from the reactor core in a 10 m deep laboratory. Photon detection will be realized by 10 m^2 of *silicon photo-multipliers* (SiPM) with a detection efficiency of 50%. The SiPM are operated at -50 °C to reduce their dark noise. With a resulting coverage of about 94%, a light yield of 4500 photo-electrons per MeV is expected, which translates to an energy resolution from photon statistics of $1.5\%/\sqrt{\mathrm{E[MeV]}}$. Considering the detection efficiency of the coincidence signal (see Section 4.1.2), a rate of 2000 IBD events per day is expected. This allows for a fast accumulation of a statistical significant sample. Currently, the detector design is under development and details are subject to change.

3.3 Software Framework and Data

A software framework for data processing and analysis is a substantial part of an experiment's development. The output of the *data acquisition* (DAQ) after event building are collections of either *waveforms* or hit times and charges, depending on the DAQ design outlined in Section 2.3.2. At this point, a two parted software is needed. First, low level reconstruction algorithms are used to process the raw data and determine actual physical events from them. In the second step follows the physics analysis of those events, that tests for theories and gives sensitivities or confidence levels.
JUNO implemented a framework called *Software for Non-collider Physics Experiments* (`SNiPER`), which is tailored to the needs of neutrino experiments, including the possibility to account for temporal relations between events. The software interfaces established standard libraries in particle physics like `ROOT` [92] and `BOOST` [93] to provide a foundation for simulation, reconstruction and analysis needs. It features a user friendly python interface to configure and execute tasks, while all performance critical parts are coded in `C++`. `SNiPER` is not a JUNO specific framework, as it mainly provides interfaces to libraries and manages tasks. The package of algorithms that are exclusive to JUNO is called *offline*. It includes the detector simulation based on `Geant4` [94] with generators for many physics cases as well as a full set of reconstruction algorithms to process the data. Although currently limited, it also provides means of data analysis for the reconstructed events. The reconstruction algorithm presented in Chapter 5 is fully implemented into the framework to guarantee a closed workflow and accessibility by the whole collaboration.

3.3.1 Simulation

The simulation of detectors is crucial in all stages of an experiment. Beginning by sensitivity studies and, based upon those, decisions of general detector design up to the development of reconstruction algorithms, *Monte Carlo* (MC) studies are the most important source of information before real data is available. The JUNO software uses the `Geant4` toolkit to simulate its detector systems and particle interactions within. In addition, it employs event generators to produce correct input positions, directions and momentum spectra for different particles and processes [82].
The first step in the simulation is the detector description. It includes the detailed geometry of all system and especially the characteristic properties of the LS and the PMTs. All LS processes mentioned in Section 2.2 are included in the simulation. Their modeling and values are based on the experience from Daya Bay, but modified to fit current R&D measurements for JUNO. For easy tracking and recovery of different setups, the simulation can export the full geometry in a GDML file [97].
In the second step, the particles of interest are placed somewhere in the geometry and propagated through the detector by `Geant4`. While doing so, all possible interactions are taken into account according to their energy- and position-dependent probabilities. The set of physics processes, that are considered, is defined in the so called *PhysicsList* beforehand. This allows for an efficient simulation by including or excluding certain processes from the simulation.

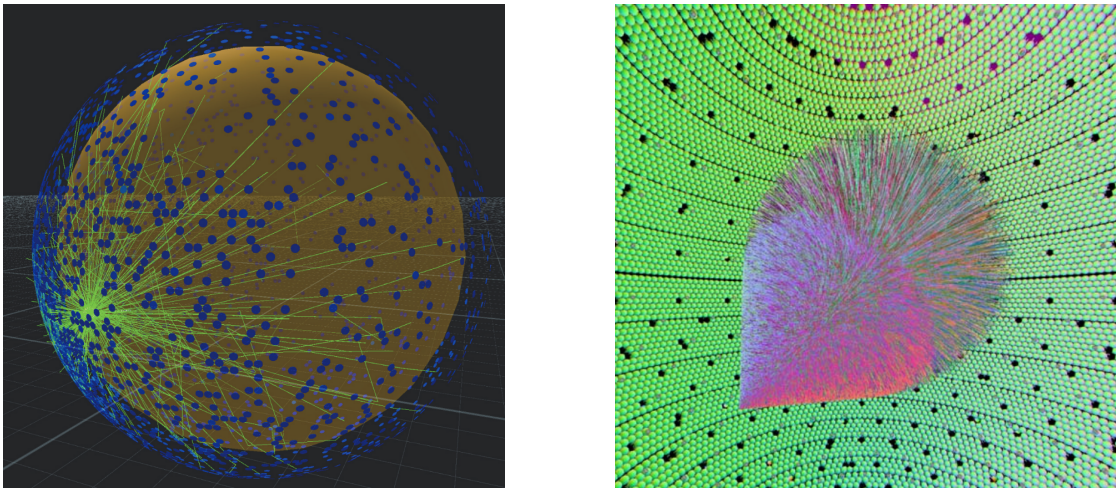

Figure 3.7 – Simulated events in the JUNO CD visualized with two different tools. *Left*: Point-like event close to the edge of the CD. Green lines show the true photon paths and the blue circles are hit PMTs. Figure reprinted from Ref. [95]. *Right*: Visualization of generated optical photons by a 100 GeV muon starting in the detector. The simulation was done with the *Opticks* package and the figure adapted from Ref. [96].

With its large size and number of readout channels, the CD is pushing the limits of what `Geant4` is intended to provide in regards of efficient simulation. The largest individual signals in JUNO are produced by cosmic muons, which can be in the order of $\mathcal{O}(10^8)$ optical photons. Sequential tracking of each individual photon through the whole detector usually takes several hours in the offline simulation. At this point, it can be beneficial to deactivate the scintillation process if, for example, only spallation effects are investigated. Another promising approach is the utilization of GPUs to process the optical photons. It is possible to extract information about generated optical photons from `Geant4`, track them fully in a dedicated framework and inject them back into the simulation. Details on this can be found in Ref. [96].
In general the simulation of a LS detector produces an array of photons that hit a PMT, including information about the time, ID of the PMT, and charge. In a second step, the detector response beyond the LS has to be simulated. The effects are mainly the PMT *response* and the subsequent *digitization*. Since JUNO will feature a DAQ, that can output the full waveform sampling of the PMTs, this is also done in the simulation within the package `ElecSim`. It includes all PMT effects discussed in Section 2.3.1 and also introduces a global time axis. This allows for mixing different events in a temporal relation and makes a *trigger* simulation possible.
When dealing with real data, the main source of information are the sampled PMT waveforms, which require some algorithm to extract hit times and charges. Since this will inevitably introduce some inaccuracy and efficiency, the input data of any event reconstruction is deteriorated by this step. Using the detector simulation allows to

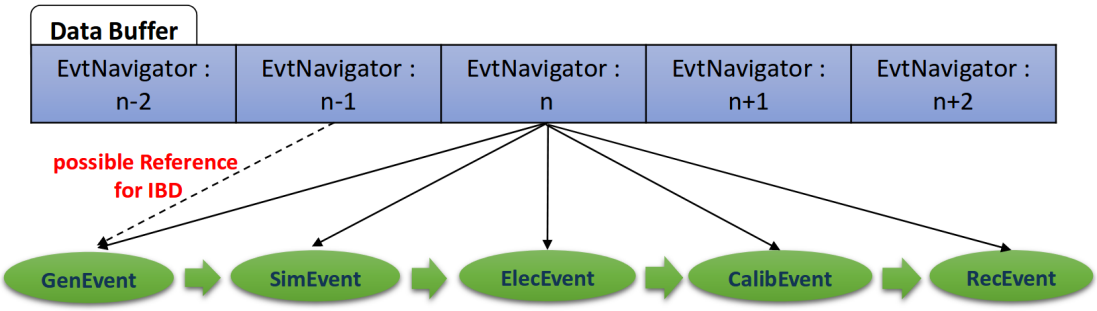

Figure 3.8 – Working principle of the `EvtNavigator` in `SNiPER`. Within the data buffer, the `EvtNavigator` can read all events and provide access to its full EDM. This functionality is crucial to create references to identify a temporal correlation between events. Figure adapted from Ref. [98].

circumvent this step and assume a perfect waveform reconstruction. This will be used in Chapter 5 to test the herein developed algorithm with and without electronics simulation in order to quantify its impact on the performance.

The *Event Data Model* (EDM) of JUNO will be used to save a large number of events and needs to be able to provide effective and fast browsing. Especially the identification of time coincidences stemming from correlated events is a challenge for the data model. In order to keep consistency, JUNO implements a static data model that discriminates between headers and actual events. The data in one event is divided into different categories with individual data substructure. The different stages of processing include the generator, followed by the simulation event, the calibration event as well as reconstruction and physics. When browsing an event defined by its *RunID* and *EventID*, only the headers are read in order to decide if the full data is needed. If that is the case, the data can be loaded in form of an *event object* that is derived from a `ROOT TObject`. The connection between the headers and their events is established by a `SmartRef`, which is an upgraded and optimized pointer based on `ROOT's TRef` [82].

For many of JUNO's physics cases, which will be discussed in Chapter 4, the signal consists of events with a temporal relation between each other. Analyzing the time correlation between events is a key requirement for neutrino LS detectors. To account for that need, `SNiPER` introduces the *EvtNavigator* [82]. Within a given buffer length, it can browse through many consecutive event headers to identify an event that satisfies certain cuts on time and energy. This concept is visualized in Figure 3.8. After finding a suitable event, it can load the full data of both correlated events and provide it for further analysis. More details on the simulation and event data model can be found in Refs. [82, 97].

Chapter 4

Physics Potential and Goals of JUNO

The JUNO detector systems presented above are a powerful instrument for a broad physics program. A key feature of LS detectors is the real-time detection of neutrinos, which in return allows to establish a temporal and spatial correlation between events. The main focus of JUNO is determining the neutrino mass ordering, presented in Section 4.1.1. Furthermore, the extended physics program includes improvements on the oscillation parameters and studies on neutrinos from other sources. An overview is given Section 4.2, while full details can be found in Ref. [30].

4.1 Neutrino mass ordering

As Section 1.1.1 introduced, the neutrino *mass ordering* (MO) is one of the open questions in the field of neutrino physics, that JUNO wants to answer. Section 4.1.1 will explain how the electron anti-neutrinos from nuclear reactors can be measured in LS detectors and how the information about the MO is extracted from the spectrum. After that, Section 4.1.2 sheds some light on the backgrounds for this measurement and quantifies the rates for the case of JUNO.

4.1.1 Measurement with $\bar{\nu}_e$ vacuum oscillations

Nuclear reactors produce a very large number of exclusively electron anti-neutrinos in the fission process as a byproduct of the energy release. In a LS detector, those $\bar{\nu}_e$ are detected via the IBD reaction given in Equation (1.15).
In the case of JUNO, the neutrino flux from 36 $\mathrm{GW_{th}}$ results in 83 IBD events per day in a 20 kilo-ton LS detector at 53 km distance [30].
The MO can be probed with the fine structure of the electron anti-neutrino's oscillation spectrum. According to Equation (1.8), the survival probability of $\bar{\nu}_e$ can be expressed

as

$$P_{\bar{\nu}_e \to \bar{\nu}_e} = 1 - \cos^4\theta_{13}\sin^2 2\theta_{12}\sin^2\Delta_{21} - \sin^2 2\theta_{13}(\cos^2\theta_{12}\sin^2\Delta_{31} + \sin^2\theta_{12}\sin^2\Delta_{32}) \tag{4.1}$$

with the conventional abbreviation of $\Delta_{ij} = 1.27\,\Delta m^2_{ij}[\mathrm{eV}^2]\,\mathrm{L[m]/E[MeV]}$, where L is the baseline and E the energy of the anti-neutrino [30, 99]. The first term is governed by $\sin^2\Delta_{21}$ and produces a slow oscillation over the IBD spectrum. The second term is suppressed by θ_{13}, but accessible through its non-zero value and has a faster oscillation frequency (see Table 1.1). In order to make the influence of the MO more visible, it can be rewritten as

$$\cos^2\theta_{12}\sin^2\Delta_{31} + \sin^2\theta_{12}\sin^2\Delta_{32} \tag{4.2}$$

$$= \frac{1}{2}[1 + \cos 2\theta_{12}\sin\Delta_{21}\sin(\Delta_{31}+\Delta_{32}) - \cos\Delta_{21}\cos(\Delta_{31}+\Delta_{32})], \tag{4.3}$$

with $\Delta_{31} - \Delta_{32} = const. \cdot (m^2_3 - m^2_1 - m^2_3 + m^2_2) = \Delta_{21}$. The MO creates an interference in this term in the E_ν spectrum, as $\Delta_{31} + \Delta_{32}$ is either positive for the normal ordering (NO) or negative for inverted ordering (IO). As can be seen in Figure 4.1, the effect is visible as a phase-factor of the fast oscillation on top of the slow one. Due to the fact that this effect is small, a very good energy resolution on the spectrum of $3\%/\sqrt{\mathrm{E[MeV]}}$ is needed as well as a energy scale uncertainty below 1%.

Small variations or uncertainties can shift the signature from one ordering to the other. JUNO is designed to resolve the spectrum with an excellent energy resolution of $3\%/\sqrt{\mathrm{E[MeV]}}$ by collecting $\sim$ 1200 PE per MeV deposited energy. With that unprecedented resolution JUNO would also be the first experiment to measure both the slow Δm^2_{sol} oscillation and the fast oscillation from Δm^2_{atm} simultaneously. The achievable sensitivity for JUNO with this resolution and the order of 100000 IBD events can be seen in Figure 4.2. Under the assumption of the NO being realized in nature, it plots the $\Delta\chi^2$ in dependence on $|\Delta m^2_{ee}|$. In order to account for the small absolute difference between Δm^2_{31} and Δm^2_{32} depending on the MO (see Table 1.1), a common combination is used here [30]

$$\Delta m^2_{ee} = \cos^2\theta_{12}\Delta m^2_{31} + \sin^2\theta_{12}\Delta m^2_{32}. \tag{4.4}$$

Using this formalism and $\Delta_{ee} = \Delta m^2_{ee} L/4E$, the survival probability can be rewritten as [100]

$$P_{\bar{\nu}_e \to \bar{\nu}_e} = 1 - \frac{1}{2}\sin^2 2\theta_{13}\left[1 - \sqrt{1 - \sin^2 2\theta_{12}\sin^2\Delta_{21}}\cos(2\Delta_{ee} \pm \phi)\right] - P_s. \tag{4.5}$$

Here, $P_s = \cos^4\theta_{13}\sin^2 2\theta_{12}\sin^2\Delta_{21}$ is the part of the survival probability that belongs to the solar mass splitting. Furthermore, the phase ϕ is defined via

$$\sin\phi = \frac{c^2_{12}\sin(2s^2_{12}\Delta_{21}) - s^2_{12}\sin(2c^2_{12}\Delta_{21})}{\sqrt{1 - \sin^2 2\theta_{12}\sin^2\Delta_{21}}}, \tag{4.6}$$

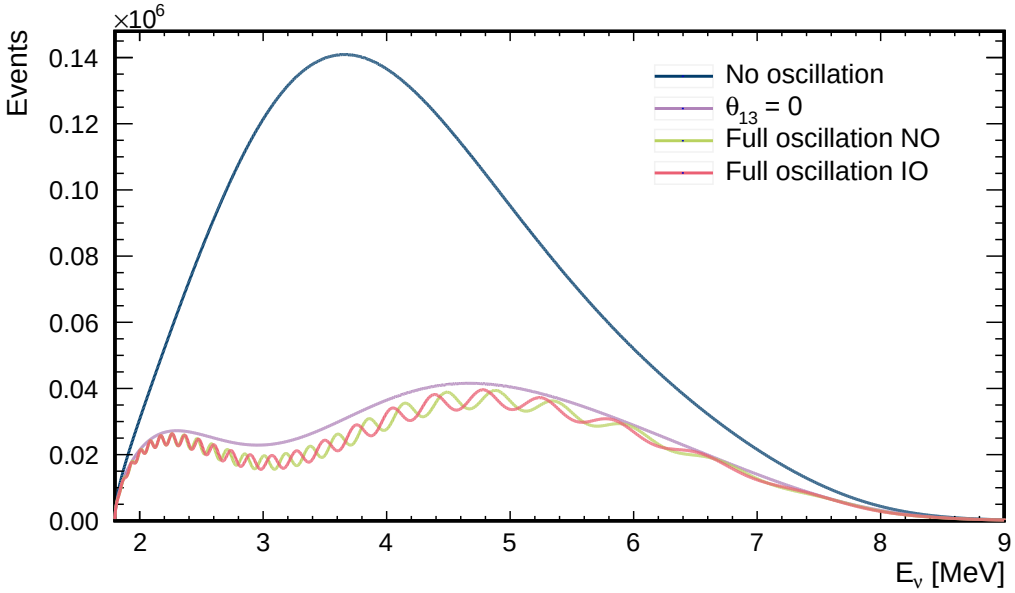

Figure 4.1 – Expected neutrino spectrum at a JUNO-like detector. Based on Figure 1.4 the IBD spectrum was scaled with $1.5 \cdot 10^{33}$ free protons in 20 kton on a baseline of L = 53 km. A NPP with 36 GW thermal power and six years of 300 days per year data taking were assumed. No efficiencies or detector resolutions were assumed, as the true neutrino energy is plotted. The un-oscillated spectrum ($P_{\bar{\nu}_e \to \bar{\nu}_e} = 1$) (blue) is identical to the one shown in Figure 1.4. The violet spectrum shows mainly the influence of the atmospheric oscillation. Under the assumption that $\theta_{13} = 0$, the two different mass orderings would not be visible in this spectrum. Assuming full oscillation with current best fit values from Table 1.1, the NO (green) and IO (red) are distinguishable by their phase difference, most prominent between 3 MeV and 5 MeV.

$$\cos\phi = \frac{c_{12}^2 \cos(2s_{12}^2\Delta_{21}) + s_{12}^2 \cos(2c_{12}^2\Delta_{21})}{\sqrt{1 - \sin^2 2\theta_{12} \sin^2 \Delta_{21}}}. \tag{4.7}$$

The positive sign in Equation (4.5) corresponds to the NO, while the negative sign denotes the case of IO. Consequently, the mass ordering manifests itself only in the sign of this phase, if Δm^2_{ee} is determined precisely. The dashed lines in Figure 4.2 give the sensitivity for the case of only using reactor neutrinos. A $\Delta\chi^2 > 10$ can be achieved, which corresponds to a 3σ confirmation of the assumed MO.
Similarly to Δm^2_{ee}, $\Delta m^2_{\mu\mu}$ can be defined as [101]

$$\Delta m^2_{\mu\mu} = \sin^2\theta_{12}\Delta m^2_{31} + \cos^2\theta_{12}\Delta m^2_{32} + \sin^2 2\theta_{12} \sin\theta_{13} \tan\theta_{23} \cos\delta \Delta m^2_{21}. \tag{4.8}$$

The precision of this effective mass-squared difference can be improved by the long-baseline accelerator neutrino experiments T2K [102] and NOνA [29]. Including such an external precision measurement of $\Delta m^2_{\mu\mu}$ with 1% precision, the combined result can

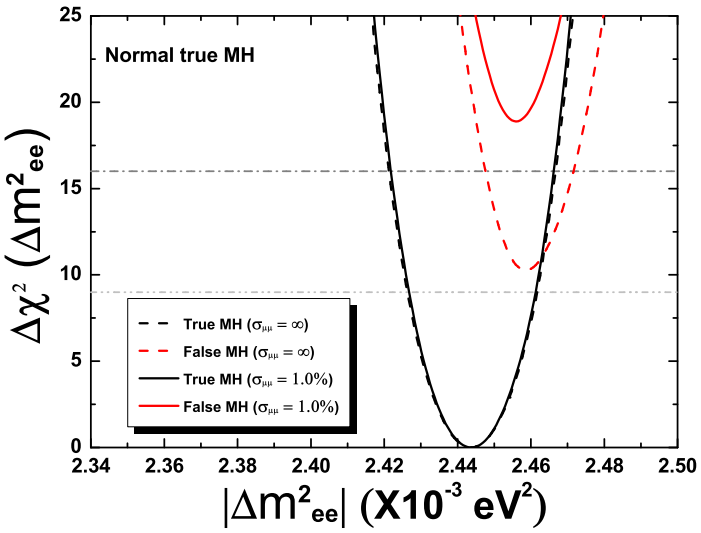

Figure 4.2 – $\Delta\chi^2$ distributions in dependence on $|\Delta m^2_{ee}|$ with the NO being true [30]. The dashed lines give the reactor-only measurement and the solid lines the combination with a 1 % measurement of $\Delta m^2_{\mu\mu}$. Black lines are for the true hierarchy while red lines indicate the values for the inverted hierarchy. The CP-phase was set to correspond to $\cos\delta = 0$ [30].

yield $16\Delta\chi^2$ sensitivity. This case is shown in the figure by the solid lines and would correspond to a 4σ measurement.

4.1.2 Backgrounds for the IBD measurement

When trying to identify the IBD signature there are a lot of backgrounds to considers, that either mimic the prompt or delayed event or even the correlated signal. The following paragraphs will give an overview over the *raw* rates and physical processes that are responsible for the backgrounds. It is shown, that without any cuts, the raw background rates are very high. Additionally, a choice of cuts is presented to efficiently create a data set with optimal signal-to-background ratio.

Accidental background When two uncorrelated signals are falsely identified as prompt and delayed event of an IBD, it is called an accidental coincidence. Most dominant for this are so called singles, which are single energy depositions in the energy range, that is considered for the IBD selection. Ranging typically between 0.7 MeV and 10 MeV the coinciding events can stem from different sources. Although radio-purity is a focus in the development of JUNO to keep singles rates small, all detector components show some level of radioactivity. Especially the surrounding rock and the glass bulbs of the PMTs are a dominant source of radioactivity. The rate of accidental coincidences

can be calculated directly from the rate of singles and the coincidence time [103], if no further cuts are considered. Given the rate of single events in the prompt energy range R_p and the rate for delayed-like events R_d, the accidental coincidence rate R_a within a time window Δt is $R_a = R_p \cdot R_d \cdot \Delta t$. The gammas from external radioactivity are mainly absorbed by the buffer around the LS, but a residual rate still reaches the outermost part of the LS. For this reason, a so called fiducial volume cut is often applied to remove those events close to the edge of the vessel. Taking events with $r < 17\,\mathrm{m}$, the resulting raw coincidence rate in $\Delta t = 1\,\mathrm{ms}$ of radioactive energy deposits would be 7.6 Hz. Only about 8% of the those events are in the neutron-like energy range. Under the consideration of energy windows, the rate of actual IBD background is ∼480 $^{\mathrm{events}}/_{\mathrm{day}}$ without any other cuts [30].
The singles from radioactivity can also coincide with events from products of cosmic muons traveling through the detector. Details on their production will be given in the next paragraph, but the main contribution to the accidental background are cosmogenic isotopes and spallation neutrons. The rate of emitted neutrons by cosmogenic isotopes is about 340 per day [30]. Combined with the singles from radioactivity this amounts to a rate of 2.4 coincidences per day for the given time window. In contrast, the rate of neutrons from spallation is much higher with ∼1.8 Hz. When this is considered with prompt-like event from radioactivity, the resulting raw background rate is about 1100 events per day [30]. Nevertheless, this background can be controlled with further cuts explained below.

Cosmogenic background An important background for the reactor neutrino measurement stems from cosmic muons. Due to its characteristics to produce correlated events that look like IBD, it is also complicated to identify.
Generally the best reduction in cosmogenic muon background is a large rock overburden, that shields the detector from a large part of the muon flux. Similar to the processes described in Chapter 1, the energy loss of muons traversing matter can also be described by the *Bethe-Bloch-equation* [1]. With increasing overburden, more muons lose energy until they are stopped in the rock before reaching the detector. Although the strict baseline restrictions for JUNO limit the possible overburden, the underground lab is shielded by ∼650 m of granite. Under the assumption of a constant average density of $2.60\,^{\mathrm{g}}/_{\mathrm{cm}^3}$ and a detailed topological map of the hill atop the experimental site, the muon propagation through the rock was simulated [82]. The residual muon rate at the detector was reported as $0.003\,^{\mathrm{Hz}}/_{\mathrm{m}^2}$ with a mean energy of $< \mathrm{E}_\mu > = 215\,\mathrm{GeV}$. This results to a muon rate in the CD of 3.5 Hz and for the water pool of about 1.0 Hz [82].
An important feature of cosmic muons reaching the CD is the production of *muon bundles*. They are created in an interaction of the parent muon within the rock above the detector and were estimated to be parallel within 0.2∘ by MC studies. Current generation LS detectors do not have to account for muon bundles explicitly, because the mean distance between the parallel muon tracks is larger than the detector dimensions. Nevertheless, the CD of JUNO is large enough to identify bundles. Taking into account the detector geometry, about 90% of the muon flux are single tracks and 7.7% are bundles of two

Table 4.1 – The multiplicity of muons going through JUNO detector [30, 104].

Multiplicity	1	2	3	4	5	6
Fraction	89.6%	7.7%	1.8%	0.6%	0.3%	0.07%

muons. The remaining part are bundles of three and more muons as Table 4.1 shows in detail.

Generally, three categories of muons reaching the detector can be distinguished: (a) Muons, that cross the WP and the CD, (b) muons that will only traverse the WP, but not the CD, and (c) muons that miss the WP and only cross the surrounding rock. Figure 4.3 shows some exemplary muon paths for those categories.

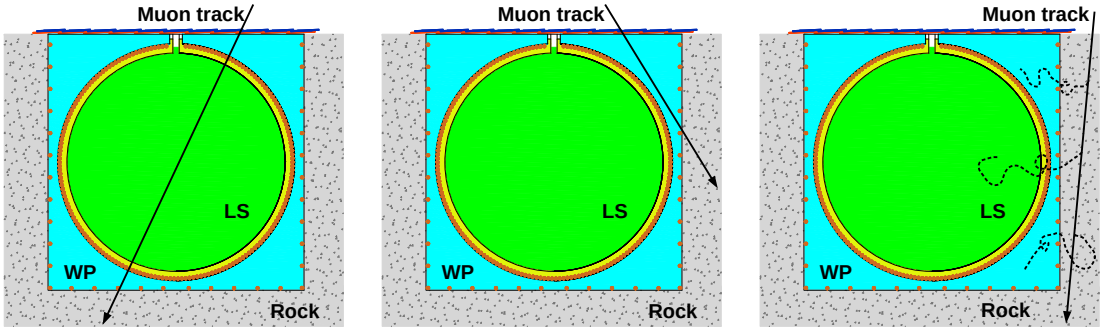

(a) WP and LS crossed **(b)** WP crossed **(c)** Rock crossed

Figure 4.3 – Three distinguishable categories of muons crossing the detector. Case (a): The muon first crosses the WP and then enters the CD. It traverses the LS and leaves the detector again through the WP. Case (b) shows a muon track that moves through the WP but misses the LS. Only Cherenkov light in the water produced. Events shown in case (c) are not directly visible because the track traverses only the surrounding rock. Nevertheless, by that free neutrons are produced which can enter the detector and produce background, shown by the dotted lines.

When the muons move through the LS (a) they will always ionize it and create a track. In some cases they can also interact electromagnetically or hadronically with the carbon in LAB and create a shower of unstable isotopes. There is a wide range of those accordingly called *cosmogenic isotopes* from ^{3}He to ^{18}N and free neutrons [82]. The largest part of cosmogenic isotopes decay in a way that creates singles, which can mimic delayed-like events between 1.9 MeV and 2.2 Mev and lead to an accidental coincidence as explained above. A more challenging kind of background stems from the (β^- + n) emitters of the cosmogenic isotopes. Along their decay chain they release a β electron followed shortly by a neutron. This is a correlated event with a signature that mimics IBD events. Since it emerges from the same isotope, this background usually survives time and distance cuts and is thus very hard to distinguish from an actual IBD event. The dominant

contribution in this category comes from ^{9}Li and ^{8}He with half-lifes of 0.178 s and 0.119 s, respectively [105]. Under the assumption of a production cross section of these isotopes from KamLAND [106] and the branching ratios of the decay chains 77 coincidence events per day are expected from those isotopes. This is the same rate as signal IBD events and thus makes it a dominant background.
In spite of having a very similar signature to the IBD reaction, it is possible to identify and reject those events. An efficient rejection can be achieved by exploiting the isotope's correlation to the their parent muon in time and space. They are created along or very close to the track of the muon through the LS. Driven by the isotopes' lifetime, a cylindrical veto around the muon track can be introduced to remove IBD-like events from the data sample. Furthermore, it would also be possible to identify the points of spallation more accurately by an increased neutron capture rate or with a reconstruction of the energy deposits along the track. If that is the case, a spherical veto around those points could further reduce the introduced dead time of partial volumes. The introduction of a simple cylindrical veto would result in a residual background rate from ^{8}He/^{9}Li of 1.6 events per day. With a sophisticated particle identification, it is possible to distinguish the prompt electron created by the β^{-}-decay from the positron of an IBD event to further reduce this background.
Independent of the actual veto strategy, an efficient and high accuracy muon tracking is a fundamental requirement for a successful reduction of this background. In general, the muons in case (a) can be further distinguished by their track in the LS. Approximated by a straight line, most muons are *through-going*, meaning that they were produced outside of the detector, travel through it and exit at some point. If a muon loses all its kinetic energy in the LS, it can stop within the detector. The endpoint of the track lies in the LS and the muon is called a *stopping muon*. Similarly, a *starting muon* can be created by neutrino interaction in the LS (see Section 1.2). The combination of both aforementioned cases is called a *fully contained muon*, since both, its starting and endpoint are contained within the LS.
The muons in cases (b) and (c) do not create scintillation light, but fast neutrons in the water or rock. It is possible that they can reach the LS, where they scatter off a proton, which looks like a prompt event, and are then captured. Despite being a correlated background, that can look like an IBD event, it is negligible as the estimate rate for JUNO is ∼0.1 events per day [30].

Geo-neutrinos The natural abundance of radioactive isotopes inside the Earth is another source of background events for the MO measurement. Along the decay chains of ^{238}U and ^{232}Th electron anti-neutrinos are produced, which are accordingly called geo-neutrinos. Their flux is measurable with JUNO and highly dependent on the local environment. Since the incident particle is the same as for the reactor measurement, the signature is a real IBD and not distinguishable on the event basis. Thus, it is a irremovable background and its estimated rate is ∼1.2 events per day [30], based on the assumed abundance of U and Th in the Earth's crust and mantle. Since the endpoint of the geo-neutrino spectrum at ∼2.6 MeV [30] is much lower than the one from reactor anti-

neutrinos, a large part of it is not influenced by the background. Although geo-neutrinos are considered a background for the MO measurement, their detailed study is a part of the extended physics program, as JUNO is well equipped to reduce the uncertainty of current measurements.

^{13}C$(\alpha, n)^{16}$O background This background stems from the α-particle decays in the LS and the acrylic vessel that holds the LS in place. They can interact with the ^{12}C and ^{13}C and thereby create a fast neutron or a gamma from the de-excitation of ^{16}O. The rate of this correlated (α, n) background was estimated to be 0.05 events per day [30] for ^{238}U and ^{232}Th levels of 10^{-15}g/g. In addition, the out-of-equilibrium concentration of ^{210}Po in the LS has to be controlled, as its α-decay can increase this background.

Event selection So far the only constraints considered were a fiducial volume of $r < 17\,\text{m}$ and coincidence time of 1 ms. The calculated background rates are almost raw and heavily outweigh the signal rate. Due to that, an extended set of cuts is needed to guarantee an efficient signal selection and a high background rejection. The well known characteristics of the process can be utilized to set a preliminary choices of cuts to be refined in future with real data. For the prompt event an energy window from 0.7 MeV to 12 MeV is set and for the delayed neutron capture a more narrow energy of 1.9 MeV to 2.5 MeV is required. Another powerful criterion against accidentals is the spatial correlation of prompt and delayed events. Taking the precision of the localization into account, a distance of less than 1.5 m between both events is demanded. Finally, the cosmogenic background has to be eliminated with an efficient veto strategy. As a baseline, a muon track reconstruction efficiency of 99% was assumed with the following veto scheme [30]:

- Well tracked muons in the CD receive a cylindrical volume veto around the track with $R = 3\,\text{m}$ and 1.2 s to reduce the Li and He background.
- Muons tagged only in the WP, but no track in the CD cause a full veto of the whole detector for 1.5 ms. This can veto the events caused by fast neutrons entering the detector.
- Muons that were tagged in the LS but failed to be reconstructed cause a full detector veto for 1.2 s, as a safety measure against the Li and He background.

The total IBD signal selection efficiency is about 73%, with 60 signal events surviving all cuts from the total of 83 initial IBD events per day. At the same time the total residual background rate is only 3.8 per day. A detailed overview over all selection- and rejection efficiencies for the several cuts is shown in Table 4.2.

Table 4.2 – Overview of rate reduction and efficiency per cut [30]. Free cells indicate combined cuts e.g. energy, time, and vertex cuts reduce the IBD rate from 76 to 73. The rates are given as events per day.

Selection	IBD eff.	IBD	Geo-νs	Accidental	^{9}Li/^{8}He	Fast n	(α, n)
No cut		83	1.5	$\sim 5.7 \times 10^4$	84		
Fiducial volume	91.8%	76	1.4		77	0.1	0.05
Energy cut	97.8%			410			
Time cut	99.1%	73	1.3		71		
Vertex cut	98.7%			1.1			
Muon veto	83%	60	1.1	0.9	1.6		
Combined	73%	60		3.8			

4.2 Extended physics program

Although JUNO focuses on the MO, it is not limit to only this measurement. The large target mass in combination with an unprecedented energy resolution enables a broader physics program. This is based on detection of neutrinos from various different sources. The analysis of the energy spectra and time distributions of those events can give insights into physics, that could not be probed otherwise (see Chapter 1). Since this thesis is focused on low level reconstructed methods instead of data analysis, only a choice of the extended physics program is motivated and referenced for detailed information. A comprehensive overview can be found in Ref. [30].

4.2.1 Precision measurement of oscillation parameters

As mentioned in Section 4.1.1, the high statistics measurement of reactor anti-neutrinos will simultaneously map multiple oscillation cycles of the atmospheric mass-splitting together with the oscillation driven by the solar Δm^2_{21}. This allows to measure $\sin^2\theta_{12}$, Δm^2_{21}, and the effective mass-squared difference $|\Delta m^2_{ee}|$ (see Equation (4.4)). JUNO's energy resolution will increase the precision of this measurement to an uncertainty of less than 1% on those parameters of neutrino oscillations. Table 4.3 gives the current and estimated uncertainties with the nominal data from JUNO.

Table 4.3 – Overview of the improvement on the oscillation parameters achievable with JUNO [30].

Parameter	Current best-fit	With JUNO
$\sin^2\theta_{12}$	4.1%	0.67%
Δm^2_{21}	2.6%	0.59%
Δm^2_{ee}	1.9%	0.44%

4.2.2 Solar neutrinos

The fusion processes in the sun create mainly electron neutrinos, called solar neutrinos according to their source. While the reactor anti-neutrinos are detectable via a correlated IBD signature, electron neutrinos are only detectable through elastic scattering off electrons. In a LS detector this is only visible as one single, low energy event. Since only a fraction of the neutrino's energy is transferred to the electron, the spectrum of visible energy is continuous even for mono-energetic neutrinos. The point-like events are not distinguishable from background on an event-by-event basis, so that a statistical analysis of the spectrum is needed. The fusion of four protons to a ^{4}He nucleus can happen via two reactions, the *pp* chain and the CNO cycle. About 99% of the sun's neutrino flux stems from the *pp* chain, in which the neutrinos are categorized into *pp* neutrinos, *pep* neutrinos, and *hep* neutrinos as well as ^{7}Be neutrinos and ^{8}B neutrinos. The naming is based on the reaction that produces the neutrinos within the chain. In the CNO cycle, nucleon decays of e.g. ^{13}N, ^{15}O and ^{17}F create the accordingly called CNO neutrinos.
Since the largest part of the solar neutrino spectrum lays well below 1.5 MeV, it is important to have a very low energy threshold. While sophisticated trigger schemes were developed for JUNO to push the threshold in the range of hundreds of keV, it is limited by physical background events. Intrinsically, all organic LS contains considerable amounts of ^{14}C, which has a β-decay with an endpoint at 156 keV. Even in extremely clean LS like the one Borexino uses, its rate overshadows any other physical process in that energy range. Nevertheless, Borexino is still clean enough to use the spectra starting at their 50 keV-threshold for spectral fits of solar neutrinos [79].
Within the accessible energy range of JUNO, the main consideration is the internal radioactivity of the LS. Thus, a deciding factor for the successful measurement of solar neutrinos is the radiopurity. The baseline requirement for the JUNO LS is a concentration for ^{238}U and ^{232}Th of 10^{-16}g/g and less than 10^{-17}g/g for ^{40}K [30]. In addition, the possible non-equilibrium concentration of ^{210}Pb and its daughter ^{210}Bi has to be less than 5×10^{-24}g/g. The rate of ^{85}Kr should also not exceed 500 counts per day and kton. If this requirement is fulfilled, the estimated rate of signal to background events is 1 : 3. This would enable the measurement, but in an ideal case with the concentrations being one order of magnitude lower, a ratio of 2 : 1 could be reached. Figure 4.4 shows a simulated spectrum of singles in JUNO in the low energy range for the baseline radiopurity assumption. It becomes evident, that the detection of most solar neutrinos is difficult. The *pep* and CNO neutrinos are overshadowed by ^{210}Bi in the lower energy region and by the cosmogenic ^{11}C at energies above 1 MeV, because of JUNO's shallow depth. Furthermore, the *pp* signal is dominated by the ^{14}C background at the lowest energies and by ^{210}Bi beyond that. Only the spectrum of ^{7}Be is visible in the total spectrum by a small edge at ∼665 keV. If the ^{210}Bi spectrum is well determined, JUNO can measure the ^{7}Be neutrino spectrum. In the case of ideal radiopurity, the ^{7}Be spectrum will rise well above the background. In addition, even *pp* neutrinos could be measured as a falling edge between the ^{14}C spectrum and the ^{7}Be in the range from 160 keV to 230 keV [30]. The independent and precise measurement of the ^{7}Be neutrino spectrum could test the vacuum oscillation region of the *Mikheyev-Smirnov-Wolfenstein*

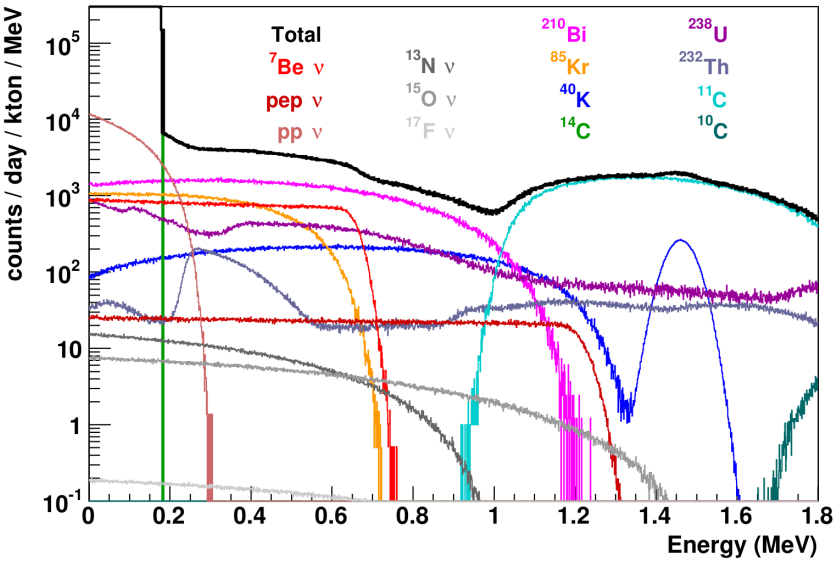

Figure 4.4 – Simulated singles spectrum for JUNO with baseline radiopurity assumptions defined in the text. The plot was taken from Ref. [30].

(MSW) matter effect [107, 108] and help solving the solar metallicity problem [109, 110]. Furthermore, JUNO is well equipped to measure the spectrum of ^{8}B neutrinos, which reaches up to 12 MeV [30]. Its large target mass can increase the counting statistics compared to current LS experiments and the high light yield allows for a lower energy threshold. Similar to the other solar neutrinos, the ^{8}B neutrinos are only visible as single events from neutrino-electron elastic scattering. Given the small overburden, the main background for this measurement are the long-lived cosmogenic isotopes ^{10}C, ^{11}C, and ^{11}Be [30]. Nevertheless, with sophisticated veto schemes like the *Three-Fold Coincidence* [79], this background can be heavily reduced. A measurement of the ^{8}B spectrum could further aid the solution of the solar metallicity problem. It is also relevant for testing the *large mixing angle* (LMA)-MSW effect. Especially the region around 3 MeV is important, as it corresponds to the transition between matter dominated and vacuum dominated regions of the LMA-MSW solution [30].

OSIRIS will play a crucial role in the endeavor to have a radiopure LS in the CD. Along the filling process of the CD, it will be the only independent measure to quantify the residual contamination of the LS after all purification stages before a spectral fit. A failure in this stage could spoil all LS, that was already filled into the CD, with a batch of highly contaminated scintillator and make a measurement of solar neutrinos impossible. JUNO has the principle capabilities to improve measurements of the solar neutrino flux, but there are much higher demands on background control than for the reactor neutrino measurement [30].

4.2.3 Supernova neutrinos

One premier goal of JUNO is the ability to detect the burst of neutrinos from a nearby supernova (SN). For that purpose, a dedicated hardware development is underway with a buffer and specialized DAQ. It is designed to record several seconds of continuous full detector readout to collect as much data as possible. Thus, a typical SN at 10 kpc distance could yield 5000 IBD events in JUNO, with another 2000 neutrino-proton scattering events as well as 300 neutrino-electron scattering events [30]. This high statistics signal would give much more insight into the SN process than the sparse SN1987A data. In addition, there is high potential for synergy with other astrophysical detectors to produce a mulit-messenger recording of a SN. Theoretically a SN detection with JUNO could lead to a direct measurement of the neutrino mass and also shed light on the MO. Nevertheless, it is not guaranteed, that a SN will happen close enough within the projected lifetime of JUNO.

Another species of SN neutrinos are those from all past core-collapse SN in the visible universe. They make up the *diffuse supernova neutrino background* (DSNB) and carry information about the star formation rate and the average neutrino spectrum from core-collapse SN among others. It has not yet been discovered, but a 10 year measurement with JUNO could yield a 3σ signal or in the case of non-detection set stricter limits on the DSNB parameter space [30]. The main detection channel is the IBD signature and the sensitive energy range is limited by reactor neutrinos in the lower edge and by atmospheric neutrinos beyond $\sim$30 MeV.

4.2.4 Geo-neutrinos

Geo-neutrinos are electron anti-neutrinos that are produced along the decay chains of natural U and Th in the Earth. Although previously introduced as a background to the MO measurement, they are a unique way to probe the Earth's composition and a physics case for JUNO on their own. Since they are also detectable via the IBD, their signature is identical to the reactor neutrino signal, but with an estimate of 300 to 500 events per year, the rate is very small in comparison [30]. Nevertheless, it is a significant contribution to the studies of geo-neutrinos, since JUNO could double the world data sample within one year with the given rate.

Geo-neutrinos allow to study the amount of radiogenic heat production in the mantle. Additionally, a high statistics sample could help to measure the ratio of thorium to uranium in the Earth's composition and by that give information about its origin and evolution.

Chapter 5

A Novel Muon Track Reconstruction in Liquid Scintillator

A novel track reconstruction method based on studies of the muon signal in the detectors of JUNO is presented in this chapter. It utilizes a geometrical model that describes the intersection of the emitted light front with an arbitrary PMT array. The use of pre-calculated *probability density functions* (PDFs) allows for a fast algorithm. At the same time, it has to be fast and adaptable to different signal topologies. Section 5.1 will motivate the importance of localizing muon tracks in LS experiments, while Section 5.2 sheds some light on typically used approaches in muon track reconstruction. The algorithm developed in this work is explained in detail in Section 5.3 and possible improvements in the final usage with real data are motivated in Section 5.4. Furthermore, it was published in form of an article in the *Journal of Instrumentation* in March 2018 [111].

5.1 Motivation

In LS detectors, localizing the tracks of muons is typically used to veto *cosmogenics*. As described in Section 4.1.2, the radioisotopes are correlated in space and time to their parent muon. Due to that, knowledge of the muon's tracks makes it possible to identify point-like events that stem from the decay of the previously created cosmogenic isotopes. Most current LS detector's sizes are on the same scale as the travel path of the radioisotopes created by a muon, which still makes a full detector veto necessary. Nevertheless, with increasing dimensions, it becomes viable and relevant to veto only a confined volume around a track, while keeping the rest of the volume active. One exemplary implementation of this is the so-called *three-fold coincidence* in Borexino to tag long-lived ^{11}C [79]. In the JUNO CD, the longest possible straight muon track of 35.4 m would only cause a veto of $\sim$4% of the total volume for a cylinder with a radius of 3 m. Given the muon rate of 3.5 Hz in the CD, a full detector veto would not be feasible. Thus, a spatial veto

around the muon track is crucial for JUNO.
The same argument is valid for *muon bundles*. Current LS detectors often only see one muon of a bundle, due to its spatial extend, and consequently are not equipped to resolve those bundles. As explained in Section 4.1.2, about 10% of muons in the JUNO CD will be bundles and they are visible as such, due to the detector's dimensions. Although this often calls for a veto of the full detector, due to the difficulty of resolving two overlapping muon signals, sophisticated algorithms can succeed in finding two tracks when they are separated by some meters. Studies in KamLAND have shown, that the production of cosmogenics is strongly correlated with particle cascades along the track [106]. Those muons are called *showering muons* and stand out by large energy depositions along their way through the LS. Recent *Monte Carlo* simulations have confirmed this correlation [104]. In order to identify points of high energy deposition on the track, it is mandatory to utilize all information of the CD. When those showers are well localized, the veto volume can be shrunk further to allow for a larger data taking efficiency. Using only a straight line defined by an entry- and exit-point could not yield such information. Additionally, the full light information is important when reconstructing starting, stopping or fully contained tracks in the LS.

5.2 Muon Reconstruction Approaches

In general, one can distinguish fast and simple reconstruction algorithms from those that process the largest amount of data to yield the most precise result. While the best possible reconstruction is obviously desirable, it often requires high computing power and is not feasible for all situations. A high muon rate like in JUNO calls for a quick tracking algorithm to define a veto. For most, non-showering muon events this is also sufficient and only a fraction of incident events are showering muons that can profit from a more sophisticated reconstruction. In the following, examples from both approaches are shortly introduced and referenced for detailed information.

Fast reconstructions This category of reconstruction algorithms is not inaccurate by definition, but focuses on providing fast information about the event. Usually this is used to make a decision whether or not a more sophisticated algorithm is called and can provide a seeding track for subsequent minimization approaches.
The *center-of-gravity* method is adapted from reconstructing point-like events. It disregards any timing information of the received photons, but takes only the total amount of detected light per PMT into account. All PMT positions $\vec{p}_{PMT}$ are weighted by their total detected charge and summed over

$$\vec{x}_{\mathrm{COG}} = \sum_{i=0}^{\mathrm{nPMT}} w_i \cdot \vec{p}_i. \tag{5.1}$$

The resulting point lays on or very close to the track. A second point, which is needed to define a straight track can be found by averaging the positions of the PMTs that saw the

first light. Those modules have the earliest hit times and can be selected either by taking a fixed number of earliest PMTs or all modules in a fixed time window after the first one. This is a tuning parameter and depends on the application and detector geometry. The approach is deterministic and fast, but not very accurate since it only uses the charge information and not the detailed timing pattern on the PMTs.
Another typical approach is the *minimization of time residuals* via a χ^2 formalism. For a given track hypothesis and each PMT, it is possible to calculate the fastest time to receive a signal. This time consists of two parts, of which the first is the path that the muon traveled under the assumption of $\beta \approx 1$ along its track until the photon was emitted at $\vec{x}_{em}$. The second part is the path of the photon from this point to the PMT position $\vec{p}_{PMT}$. For this, it is important to take the refractive indexes n_j of the different crossed media into account and in some cases also refraction at transition points. The point of emission is deterministic and can be found as a minimum of the hit time modeling as shown in Ref. [112]. The predicted hit times $t_{i,pre}$ on each PMT are then compared to the observed first hit times $t_{i,obs}$ under consideration of the uncertainty of the measured time σ_i like

$$\chi^2 = \sum_{i=0}^{\text{nPMT}} \left(\frac{t_{i,obs} - t_{i,pre}}{\sigma_i} \right). \tag{5.2}$$

Minimizing this quantity will yield the best fitting set of track parameters. The performance in regard of speed and precision mainly depends on the level of detail with which the point $\vec{x}_{em}$ is calculated and the description of the photon path. A successful and very precise implementation of this approach in JUNO is reported in Ref. [112].

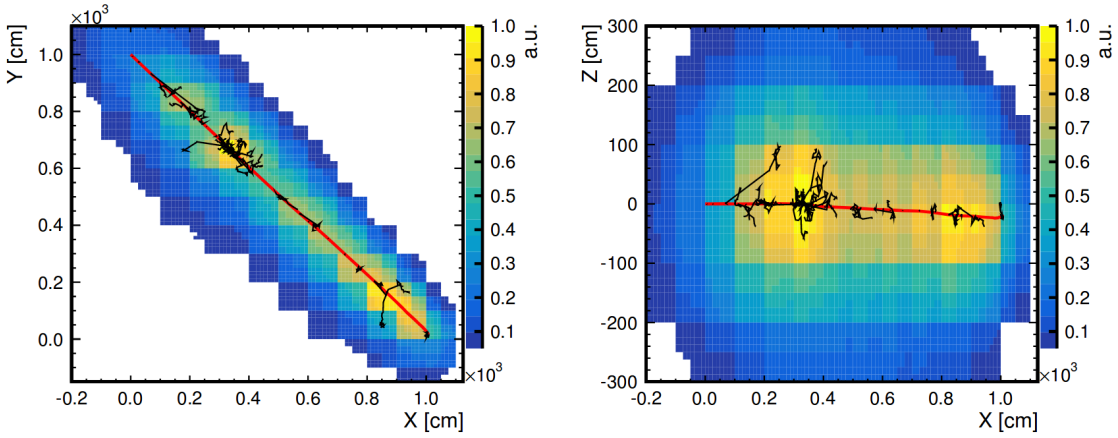

Figure 5.1 – Result of the *topological reconstruction* of a muon with 3 GeV initial kinetic energy in LENA after 21 iterations. The left plot is a projection along the symmetry axis of the detector and the right plots shows a projection along the radial y-axis. The true primary track (red) and the tracks of secondary particles (black) are overlayed in both projections [113]. The arbitrarily scaled probability of light emission clearly coincides with the creation of secondary particles along the track.

Detailed reconstructions This class of algorithms focuses solely on providing the largest amount of information about the traversing muon while the computational time is only of secondary importance.
A prominent example for this is the *topological reconstruction* [113]. The following rough sketch of the method is based on Ref. [113], in which all details can be found. With help of an adaptive grid inside an arbitrary LS volume, it takes the full PMT hit profile of times and charges to assign a probability of light emission to each grid point. In an iterative process which takes the latest result as prior for new iteration, the grid is refined around the region of interest and the accuracy is improved. The result of the reconstruction is a 3-D probability map of energy depositions in the detector. This method's performance stems from the inclusion of all known effects of photon creation and propagation, called the *optical model* and effects on the PMT, where the photon detection happens. In pre-calculated PDFs, those effects are taken into account with respect to the geometry's symmetry. The resulting probability map can not only be used to define a straight muon track, but also to identify energy depositions along the track for through-going, starting, and stopping muons. An example of this is shown in Figure 5.1. Furthermore, it was shown that this method can also be used for point-like low energy events and particle discrimination [114].

Geometrical reconstruction The geometrical model developed in this thesis belongs to the group of fast reconstructions, but tries to be more adaptable to different muon event topologies. A visualization of the muon signal in the CD of JUNO shows exploitable features, that give rise to a different description from the time residuals. Studying the PMT hit patterns in different slices along the temporal evolution of the muon signal shows the intersection between the muon light cone (see Figure 3.7) and the PMT array. An example of the time evolution is shown in Figure 5.2, where at four different time slices of 5 ns those PMTs are marked that received their first light withing that time. The resulting shape is an ellipse on the sphere surface which, in the case of a central muon, becomes a circle. With progressing time, it is moving in direction of muon. When the muon exits, a second ring will move in the opposite direction until both rings meet. The algorithm introduced in next chapters uses this feature to find the most probable muon track parameters with a likelihood approach.

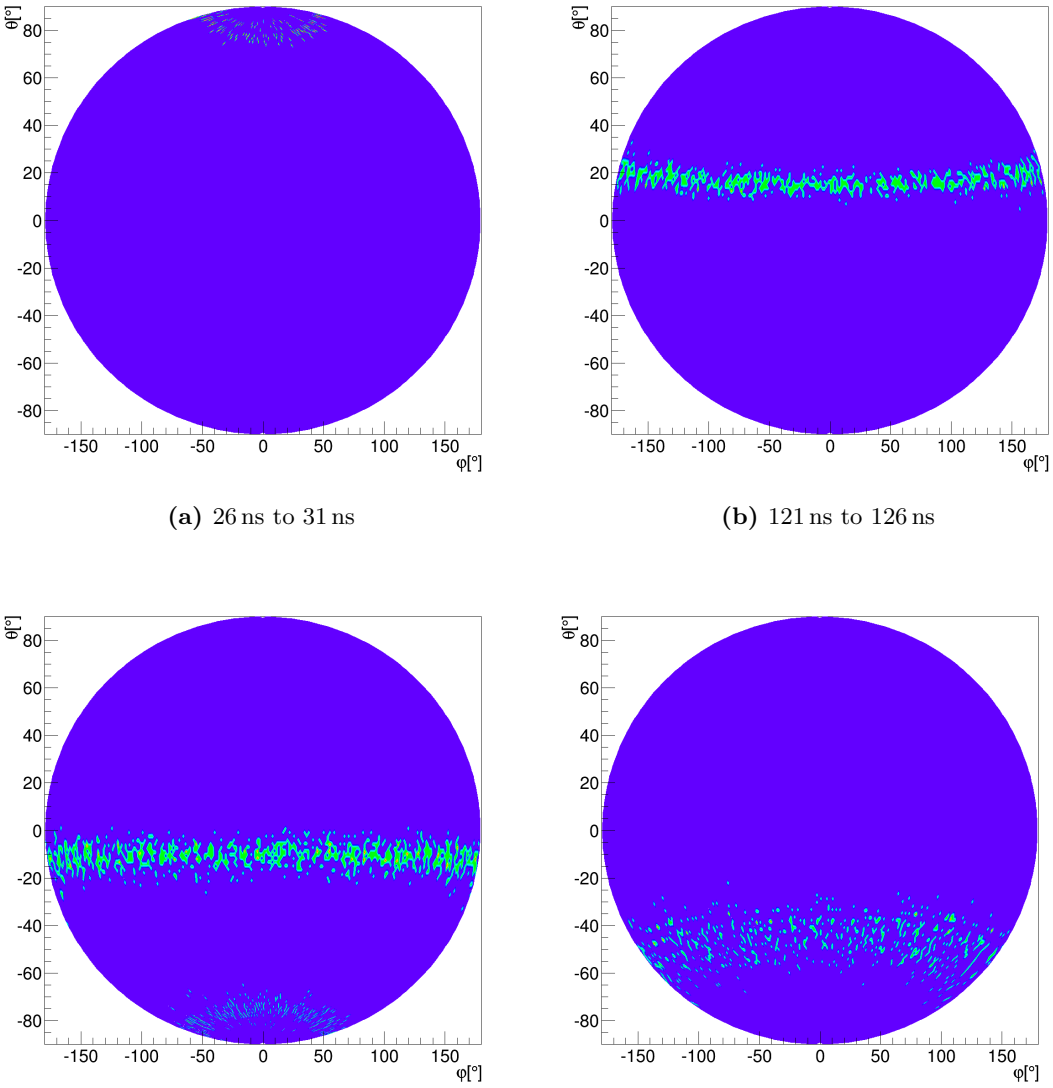

(a) 26 ns to 31 ns

(b) 121 ns to 126 ns

(c) 146 ns to 151 ns

(d) 166 ns to 171 ns

Figure 5.2 – First hit time event display of a 100 GeV muon in four time intervals. The CD sphere projection is shown in purple while bins with PMT first hit times in the denoted time are marked in cyan. The muon started above the CD on the vertical, central axis at $(0, 0, 20\,\mathrm{m})$ with a direction vector $\vec{d} = (0, 0, -1)$. Tiles (a)-(d) are characteristic segments of the event's chronology. The earliest PMTs are marked in (a), followed by a downward moving circle in (b). The exit point of the muon is depicted in (c) from where a second circle travels upward and meets the downward moving circle in (d).

5.3 Muon reconstruction with a geometrical model in JUNO

5.3.1 Characteristics of muon events

Muon tracks are the brightest events expected in JUNO, which gives them a distinct signature. Nevertheless, the detailed characteristics depend mainly on the muon's tracklength in liquid scintillator and in water. Before reaching the CD, a muon will travel through a part of the cylindrical waterpool and create Cherenkov light. Due to the optical seperation of the WP from the CD, this light will only be detected by the waterpool PMTs. Whether or not it crosses the CD can then be distinguished by the CD signal. Given the energy loss only by ionization of 1.43 MeV/cm [104], even a *corner-clipping* muon with 1 m track length in LS would produce more than $1.5 \cdot 10^5$ p.e. This amount of light is sufficient to tag muons. For the purpose of background rejection, the muons travelling through the CD are the most important. When entering the CD, the muon will first traverse the waterbuffer between the PMT array and the acrylic sphere. On this path, it will create Cherenkov light just like in the waterpool. After that, the acrylic sphere is entered and the LS is crossed. When exiting the detector, the muon will traverse the waterbuffer once more. Since the light production in water and LS is very different, the tracklength in each medium has a large impact on the *event characteristics*. Under the assumption of a straight line track and with a given track's minimal distance from the detector's center D, the tracklength in the CD can be expressed as $l_{\mathrm{CD}} = 2\sqrt{R_{\mathrm{CD}}^2 - D^2}$. With the tracklength in liquid scintillator $l_{\mathrm{LS}} = 2\sqrt{R_{\mathrm{LS}}^2 - D^2}$, also the length in water is defined as $l_{\mathrm{buffer}} = l_{\mathrm{CD}} - l_{\mathrm{LS}}$. Figure 5.3 shows the construction and the influence of D on the track lengths in LS and water. With JUNO being a spherical detector, a track's orientation in the spherical coordinates θ and ϕ has a smaller impact on its characteristics than the parameter D.

Tracking in liquid scintillator is a challenge, because the light emission is isotropic and not directional. For an extensive track it can be used that all isotropic light emissions along the track add up. Since the travel speed of photons is reduced by the refractive index of the LS $v_g = c_0/n_{\mathrm{LS}}$, a forward-moving light front in shape of a cone is formed (compare to Section 2.1.2). As shown in Figure 5.4, the construction is similar to a Cherenkov-light cone depictured in Figure 2.1 and carries information about the track's position and direction. The muon track is the central axis of the cone and encloses the opening angle θ_α with the light front, which is the mantle of the cone. The opposite angle θ_c is the angle under which the photons were emitted that add up to the fastest light front. The scintillator in JUNO is expected to have a refractive index $n = 1.485$. According to Figure 5.4, the expected opening angle of the cone is then $\theta_\alpha = \arccos(\frac{1}{\beta n_{\mathrm{LS}}}) = 47.7°$. This assumes a through-going muon with $\beta = 1$.

5.3.2 The cone model

Description of light propagation

The focus for the light propagation model is on the scintillation light, which is dominant for all events that hit the CD. This was already explained in Section 2.1. According to

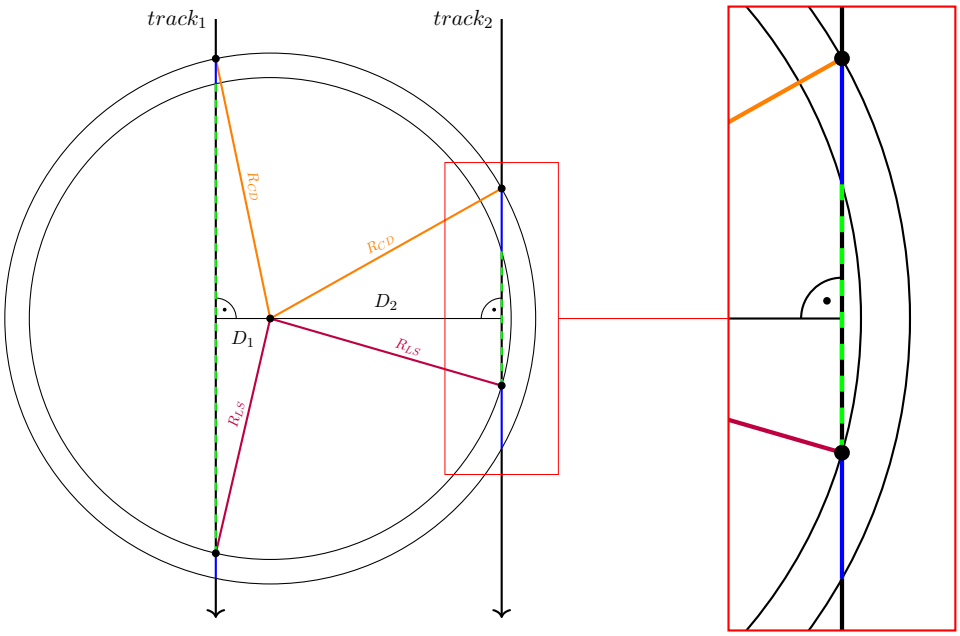

Figure 5.3 – Track lengths in different media in the JUNO CD. Track 1 has a distance from center $D_1 = 4\,\mathrm{m}$, while track 2 is closer to the edge with $D_2 = 17\,\mathrm{m}$. For both tracks the length in the waterbuffer is marked in blue and the track length in LS is given by the green dashed line. The inset gives a magnified view on the track close to edge to show that almost equal lengths in LS and waterbuffer are traversed.

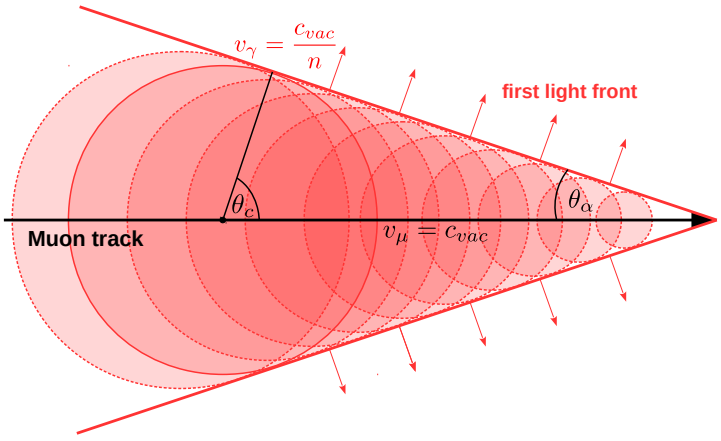

Figure 5.4 – Build up of the first-light surface by isotropic emission of photons along a muon track in liquid scintillator. The opening angle θ_α depends on the photons group velocity and by that on the refractive index n of the traversed medium.

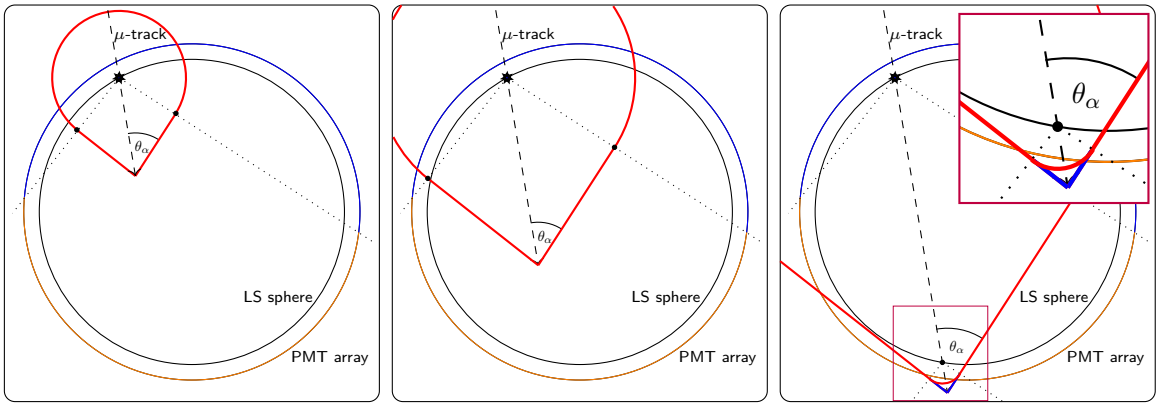

Figure 5.5 – The evolution of the first light front for a muon traveling through the central detector of JUNO. The muon track is represented by a dashed line and the entry point into the LS with a black star. The left plot shows the light front after about 1/3 of the track length. The dotted lines separate the PMT array into an area that was or will be hit by the sphere-part and the one that will see light from the cone-part of the model. The transitions between the two categories of light fronts are marked with black dots. The middle plot depicts the evolution of the light front after the muon travelled about 2/3 of its track. On the right, the muon already left the CD, but some PMTs are yet to be struck by the light front. In addition, the spherical scintillation around the exit point is marked. At this time, the cone's apex consists of Cherenkov light from traversing the waterbuffer. The insert is a zoomed-in view on the exit point. The circle segment models the fastest scintillation photons from the exit point out of the LS.

Figures 5.4 and 5.5, the first photons traveling behind the muon can be described with a *conical* shape. The model has to be extended, when it is applied to a real detector. The track starts when the muon enters the LS and builds the cone in the *forward direction*. Due to that, the PMTs behind the muon around the entry point cannot receive light from the cone. They collect photons from the isotropic emission along the very first bit of track inside the LS. In order to model the signal, the cone model is extended with a *backward sphere*. The same effect is present on the apex of the cone, when the muon exits the acrylic sphere. After leaving the LS, no more scintillation light is produced by the muon and the apex of the cone is smoothed out by a sphere around the last bit of tracklength in the LS. In contrast to the entry point, the Cherenkov light, created after the muon leaves the LS, is directed towards the PMTs. This allows to continue the conical model for the PMTs close to the muon's exit point, but with an *opening angle* according to the refraction in water instead of that in LS. For some track orientations with large D, it is also possible that PMTs around the entry point see light directly from the Cherenkov light produced in the waterbuffer before the muon enters the liquid scintillator. Thus, their hit time is much earlier than predicted with the scintillation model. Instead of including this effect in the model, the PMTs are removed from the fit as described in Section 5.3.3. Cherenkov light is also produced in the LS together with the scintillation light. A separation of Cherenkov- and scintillation-photons from

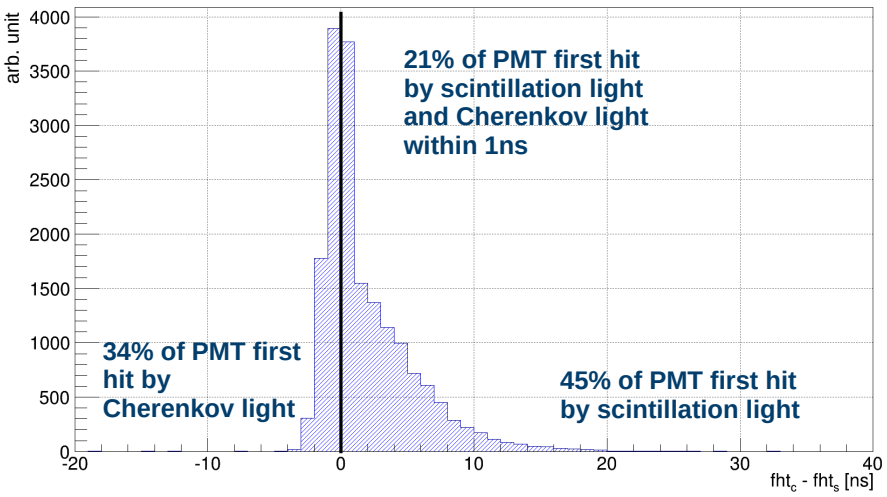

Figure 5.6 – Time difference between the first hits by scintillation and Cherenkov light on each PMT of an exemplary muon event. While the largest part of PMTs receive their first hit from scintillation light, the time difference between scintillation and Cherenkov first-hits is mostly below the achievable time resolution of 3.5 ns.

inside the LS is not needed with the cone model. Most PMTs receive their first hit from scintillation photons and in those cases, where Cherenkov hits are earlier, they are only separated from scintillation hits by less than 3 ns. Figure 5.6 shows the time between the first hits from scintillation and Cherenkov light on each PMT for a typical muon event. In the part of PMTs, that received their absolute first hit from Cherenkov light, the time difference to the first scintillation hit is less than 3 ns. Section 5.3.3 will show in detail that this is on the same order of magnitude as the reconstructed hit times from the expected waveforms.

Implementation of the model

In contrast to other fastest-light-based muon track reconstructions [115, 116], this approach implements the geometrical models of the *light cone* and *-sphere*. Thus, the figure of merit in the fit is not a time residual, but the opening angle θ_α of the first light cone. Incorporating the physical dependencies of light propagation, also the sphere that models backward moving light can be defined distinctly by this angle, as constructed in Figure 5.7. In the following, four signal categories are introduced that model different aspects of light propagation in the detector:

(1) Forward Cone. The track parameters are the entry point into the LS, the time of entry, and the muon's direction $\vec{d}$. This information is transformed into a description of the time dependent position of the muon in the detector. According to Figure 5.7, this

also coincides with the apex of the cone

$$\vec{r}(t) = \vec{r}_0 - c(t - t_0)\vec{a}, \tag{5.3}$$

with $\vec{r}_0$ being the entry point into the LS, t_0 the entry time, and $\vec{a} = -\vec{d}$ a unit vector of the inverted direction of the muon. This allows to track the muon through the detector and to build the model of the first photons forming a conical surface. Every point $\vec{x}$ on the surface of a cone around the track with opening angle θ_α can be described by

$$\frac{\vec{x} - \vec{r}(t)}{|\vec{x} - \vec{r}(t)|} \cdot \vec{a} = \cos(\theta_\alpha). \tag{5.4}$$

The available data are the static PMT positions $\mathbf{P} = \{\vec{p_1}, \vec{p_2}, ..., \vec{p_n}\}$ and their set of first hit times $\mathbf{T} = \{t_1, t_2, ..., t_n\}$ for each event. Under the assumption that the PMT was hit by the earliest photons possible, the first light cone can be constructed with an opening angle of

$$\theta_{\alpha,i} = \arccos\left(\frac{\vec{p}_i - \vec{r}(t_i)}{|\vec{p}_i - \vec{r}(t_i)|} \cdot \vec{a}\right). \tag{5.5}$$

Thus, the opening angle is defined as the angle between the track direction and the connection between the position of the muon $\vec{r}(t_i)$ at hit time t_i and the PMT at position $\vec{p}_i$. Since both vectors of the product are normalized, this function will always yield an angle between 0 and 180 °, even for track parameters far off the true values. Figure 5.7 gives an example of the cone construction. It shows an event at a time t_i, when a PMT at position $\vec{p}_i$ is first hit. The track hypothesis $\vec{q}$ contains $\vec{r}_0$, t_0, and $\vec{a}$. The position of the muon at the apex of the cone $\vec{r}(t_i)$ can be calculated with the track hypothesis. The cone according to the hit times data t_i and the track $\vec{q}$ is then calculated. Its opening angle θ_α is enclosed by the link vector between $\vec{r}(t_i)$ and $\vec{p}_i$ and the inverse direction $\vec{a}$.

(2) Backward Sphere. The sphere model to describe light moving behind the muon is described in a similar fashion. It has to merge continuously with the cone and is centered around the entry point $\vec{r}_0$. The radius of this light sphere depends on the opening angle θ_α via

$$\rho(t) = c(t - t_0) \cdot \sin(\theta_\alpha). \tag{5.6}$$

If a PMT was hit by this sphere, the radius is specified and the corresponding opening angle is calculated by

$$\theta_{\alpha,i} = \arcsin\left(\frac{|\vec{r}_0 - \vec{p}_i|}{c(t_i - t_0)}\right). \tag{5.7}$$

For certain arguments, the arcsin can run out of bounds. This happens if the track parameters are too far from the true values or when the scintillation model is not sufficient. In those cases, the arcsin is extended to return the value of π or 0, respectively, to reflect the low probability, while maintaining a smooth function. This model is very idealized because it assumes that exactly at the entry point into the LS, enough light is produced to reach all PMTs crossed by the sphere-front. According to Figure 5.5, this can be a

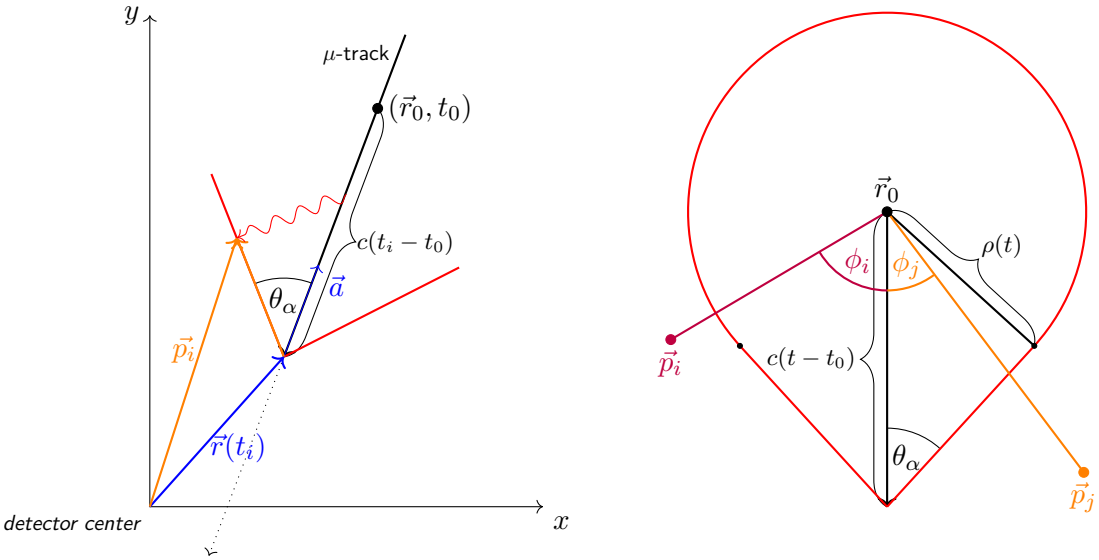

Figure 5.7 – *Left:* Implementation of the cone model with a vector that points to the apex of the cone $\vec{r}(t)$ and an inverse muon-track direction unit vector $\vec{a}$. The detector center is at $(0, 0)$ and $\vec{r}_0$ corresponds to t_0, giving the entry point into the LS and its time. A PMT at position $\vec{p}_i$ would be struck by the photons depicted that were emitted at a certain point along the track. According to Equation (5.5), the corresponding cone would have an opening angle θ_α between the muon direction and light front. The plot shows a snapshot at the time t_i when the PMT at position $\vec{p}_i$ first detected light and the muon was at position $\vec{r}(t_i)$. In this fashion, a cone with a certain opening angle θ_α can be constructed from the muon track hypothesis for every PMT. *Right:* Implementation of the sphere around the entry point to close the bottom of the cone. It can be derived from the opening angle θ_α as well. A PMT, struck at time t_i by the spherical light front around the entry point into the LS $(\vec{r}_0, t_0)$, defines the radius $\rho(t_i)$. With the track length $c(t_i - t_0)$ to the apex of the continuously merging cone the opening angle can be calculated. For two arbitrary PMT positions $\vec{p}_i$ and $\vec{p}_j$ the angles ϕ_i and ϕ_j, respectively, for category-weighting are also shown.

substantial part of the whole signal. One possibility to take the finite tracklength for production of enough photons into account, is to shift the effective point of emission along the track. The reconstruction takes $\vec{\tilde{r}}_0 = \vec{r}_0 - l \cdot \vec{a}$ with $l = 20\,\text{cm}$ as the effective center of the backwards sphere.

(3) Cherenkov Cone and (4) Forward Sphere. In addition, two more categories of signal are introduced in the algorithm. Around the last point of the track in LS, another sphere is built to model the scintillation light on the cone's apex when it enters the waterbuffer again. It is implemented like the backward sphere. The forth category of signal models the Cherenkov cone in the waterbuffer after the muon exited the LS. Its implementation is identical to the normal cone explained above and it is only applied to those PMTs that fall into category (3).

Likelihood function. The actual fit is performed with a *likelihood function* minimized by `MINUIT` [117]. For each function evaluation, all selected PMTs have to be assigned to one of the four categories explained above. For each PMT, the angle between the muon-track direction and the connection between PMT and entry point $\vec{r}_0$ can be used to assign it either to the cone (1) or the backward sphere (2) category. The same calculation is done with the exit point $\vec{r}_{exit}$ to further categorize PMTs from the cone part to case (3) or (4). In order to achieve a smooth likelihood function, the transitions between categories have to be continuous. In addition to that, the track's distance from center heavily influences the share of PMTs that fall into the different categories. For this reason, the opening angle and its probability for all four categories are calculated and weighted by a transition function. In the algorithm, the weighting function was chosen to be a normalized error function. For example, the weight for the i-th PMT for category (2) is given by

$$w_{2,i} = \frac{1}{2}\left(1 + \mathrm{erf}\left(s \cdot \Delta\phi_i\right)\right), \tag{5.8}$$

where $\Delta\phi_i = \phi_i - \Phi_{\mathrm{LS}}$, ϕ_i being the angle enclosed by the direction of the track and the link between the PMT and the LS entry point $\vec{r}_0$. Two examples for ϕ_i are shown in the right panel of Figure 5.7. $\Phi_{\mathrm{LS}} = \arccos\left(\frac{1}{n_{\mathrm{LS}}}\right)$ is the constructed transition angle in LS and s is a constant factor to scale the transition width. The scaling factor s has only a negligible effect on the reconstruction and was chosen to be $s = 25$ for all weights. If $\phi_i = \Phi_{\mathrm{LS}}$, the PMT is exactly at the transition between the cone-part and the sphere-part and will receive a weight of 0.5 for both categories. For $\phi_i > \Phi_{\mathrm{LS}}$, the weight $w_{2,i}$ for the sphere-part increases up to 1. In the same fashion, the weight for category (3) is defined and the weight for (1) is given by $w_1 = 1 - w_2 - w_3$. Category (4) is a subclass that can only be applied to the selection of PMTs in (3). The transition is also modeled by an error function and increases the weight of the Cherenkov model when the PMT hit time is significantly earlier than predicted by the scintillation model (3). The complete log-likelihood function sums over all n_{PMT} PMTs that detected light and were selected for the fit. For each PMT a cone and a sphere is calculated according to its data $(\vec{p}, t)$ and the track hypothesis $\vec{q}$ as explained before. The complete function is given by

$$-2\log\mathcal{L} = -2\sum_{i=0}^{n_{\mathrm{PMT}}} \ln f_i(\theta_{\alpha,i}; \vec{q}), \tag{5.9}$$

with the probability function

$$\begin{aligned} f_i(\theta_{\alpha,i}; \vec{q}) &= w_{2,i}(\vec{q}) P_2(\theta_{\alpha,i}|\vec{q}) \\ &+ w_{3,i}(\vec{q})\left[w_{4,i} P_4(\theta_{\alpha,i}|\vec{q}) + (1 - w_{4,i}(\vec{q})) P_3(\theta_{\alpha,i}|\vec{q})\right] \\ &+ (1 - w_{2,i} - w_{3,i}) P_1(\theta_{\alpha,i}|\vec{q}). \end{aligned} \tag{5.10}$$

The probabilities P_j are evaluated from the *pre-calculated*, normalized angle distributions. For each of the four categories, there are 18 probability functions for each 1 m step in the distance from center D. For a given set of track parameters $\vec{q}$, the probability is linearly interpolated between the values of the functions of the two enclosing values for D. An

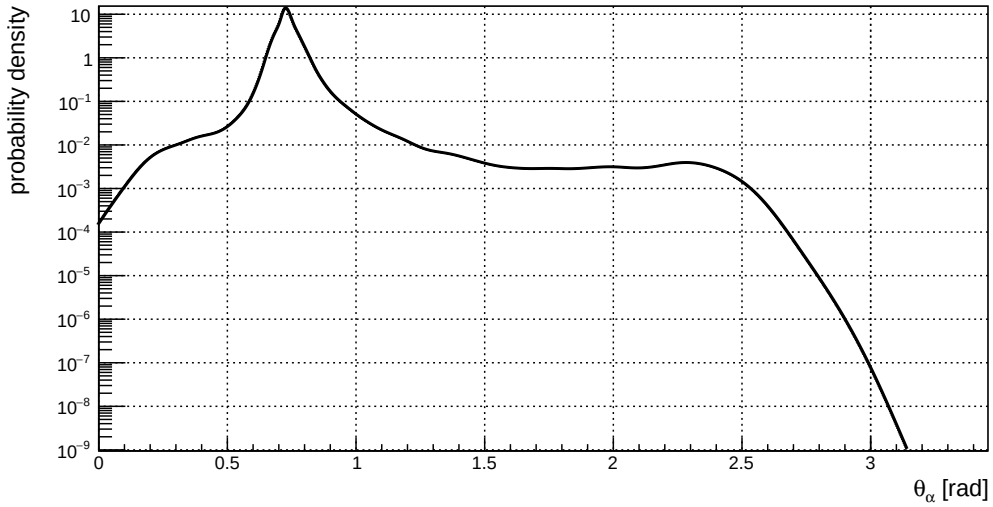

Figure 5.8 – Probability density function of θ_α for $D = 0\,\mathrm{m}$ for the LPMT cone-part of the model. It is produced by plugging-in the first hit times from the Monte Carlo simulation of muon tracks into the reconstruction model. It was smoothed over the whole domain of definition with adaptive kernel density estimators [118].

example of a probability density function for the cone-part can be seen in Figure 5.8. To account for the difference in light collection and geometrical placement there are two dedicated sets of PDFs for the LPMT and the SPMT systems. The performance differences within the LPMT array between dynode- and MCP-PMTs are sufficiently small to justify using the average PDF for the full LPMT system. The functions were obtained by plugging the Monte Carlo truth track parameters of simulated events into the model and extracting the distribution of θ_α. For this purpose a set of 3000 muons was simulated. They are set to penetrate the central detector at distances from center $D = 0\,\mathrm{m}$ to $17\,\mathrm{m}$ in $1\,\mathrm{m}$-steps, with inclinations between $\theta = 180\,^\circ$ (straight down) to $100\,^\circ$ and at 10 orientations in spherical ϕ. The true hit times were smeared according to the PMT time resolution in order to include those effects in the probability distributions. Incorporating *adaptive kernel density estimators* (KDE) [118], the distributions were smoothed over the full range of possible angles to increase the stability of the fit. An example of the raw data PDF featuring a frayed tail overlaid with the smooth function obtained with KDEs is shown in Figure 5.9. The fit has 5 parameters in total. Two define the track entry point on the LS sphere, one the corresponding entry time t_0, and two more the muon track's direction unit vector. The starting parameters for the fit are provided by a fast and simple tracking algorithm. In the first step, the distance from center D is extracted from the event's first hit time distribution. The time from the first PMT being hit until the last PMT being hit is linearly correlated with the track's distance from center. According to Section 5.3.1, one can directly get the track length in the CD from D via $l_{CD} = \sqrt{R_{CD}^2 - D^2}$. The starting point of the track is the charge

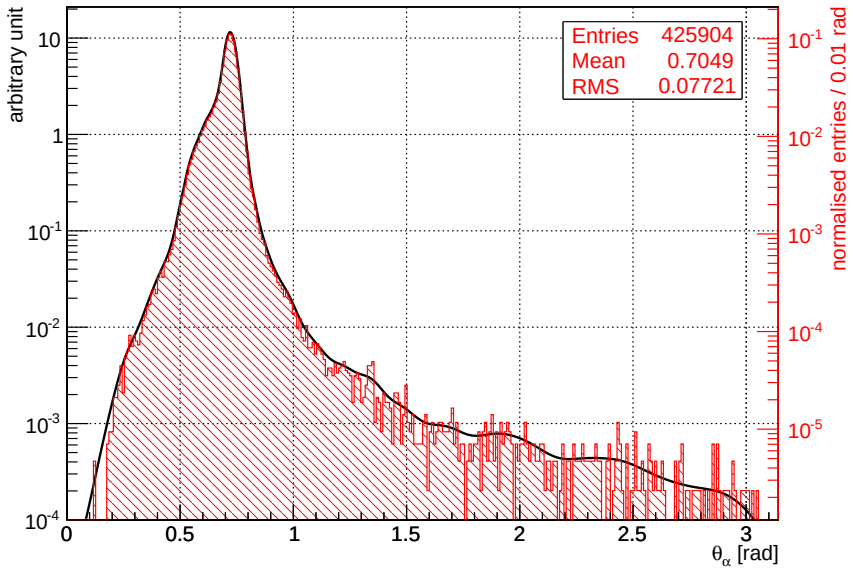

Figure 5.9 – Exemplary distribution of opening angles for the cone part from raw simulation data (red) overlaid with the smooth PDF over the whole domain of definition by adaptive kernel density estimators [118].

weighted sum of positions of fired PMTs within 2.5 ns of the first fired PMT. The starting point and track length confine a window in space and time on the PMT array for the exit point. The window is gradually increased until a group of 6 PMTs is inside, in order to charge-weight their positions to obtain an exit point. The entry- and exit-points define a straight track from which the seeding parameters for the fit are calculated.

5.3.3 Test procedure

The reconstruction algorithm has to be tested with simulated data, because JUNO is currently under construction and data taking has not yet started. This allows to study the model for a perfect detector and the impact of different stages of the detector response.

Detector simulation In the first step, a full `GEANT4` [119] simulation of the muon events is performed. The detector geometry includes a fully detailed model of the central detector submerged in the waterpool. The forseen PMT placement with all holding structures is modeled, as well as the 12 cm thick acrylic sphere that holds the liquid scintillator (see Section 3.2.2). The optical model is build according to the proposed detector design [82] as described in Section 3.2.1. In addition, also the quantum efficiency and collection efficiency of the PMTs is modeled. The collection of registered photoelectrons of an average muon event contains about 10^6 entries.

Electronics simulation The second step of simulation models the LPMT *response* and their FADC electronics. The LPMT simulation adds an estimated darknoise of 20 kHz to the signal. In a readout window of 1250 ns with a 1 GHz sampling, a pulse is added for every simulated hit according to its arrival time and charge. According to the different kinds of PMT explained in Section 3.2.2, a TTS is assigned to every LPMT. Every hit time is smeared according to the LPMT's TTS and the charge is varied according to the LPMT resolution. For each hit, a pulse is created with the shape of a single p.e. log-normal function scaled by the hit's charge. The parameters for this function are extracted from PMT measurements at Daya Bay [120] and dedicated measurements on 20-inch PMTs. Afterwards, all pulses on one LPMT are added to build its raw waveform. Finally, the simulation samples the *raw waveform* with a 3x8bit FADC that can provide a dynamic range of 1600 photoelectrons. It is built in a way, that it can keep approximately the same relative resolution over the whole dynamic range. In Figure 5.10 the simulated effect can be seen by the coarser ADC trace in the high signal range and the much smoother curve in the mid and lower range. The output is expected to be of the same format as the real data will be. For the SPMT-array the main factor is the TTS. Since they will not produce waveforms, but deliver hit times and charge directly, their simulation consists of a Gaussian hit-time smearing according to their TTS.

Signal reconstruction When working with waveforms, the concept of the first-hit times translates to the starting time of the waveform. In order to reconstruct this time consistently over the large dynamic range of the muon signals, the principle of a *constant-fraction discriminator* was used, as shown in Figure 5.10. This approach correlates the first-hit time to the time, when the rising edge of the waveform passes a threshold that is determined as a relative fraction of the signal height. A study of the simulated waveforms showed that a 6% threshold gives the most stable results. The time is linearly interpolated between the two waveform samples below and above the threshold. The achieved first hit-time resolution over all 20 inch PMTs is 3.5 ns. This is better than the average TTS of the LPMT system. While the TTS describes the resolution for a single hit, the rising edge consists of hundreds of hits within a few nanoseconds. Due to the high statistics of hits at the same time, it is possible to extract the first hit time with a better resolution than the PMT's TTS. Additionally, the *rise time* of the waveform is extracted to aid the PMT selection in the fit. It is defined by the time difference between the muon waveform exceeding 10% and 90% of height of the rising edge. Those times are also extracted by linear interpolation between the two samples around each threshold. The charge reconstruction is performed by integration of the waveform over the entire readout time after baseline correction.

Signal cleaning The aforementioned high PMT coverage of (75 + 2.5)% is due to the dense PMT array. The mean distance between neighbouring LPMTs is less than 60 cm center-to-center and it is even lower, when taking both LPMT and the interlaced SPMT into account. The very high number of channels allows for a strict removal of PMTs with a high uncertainty on the reconstructed first hit time, while maintaining sufficient

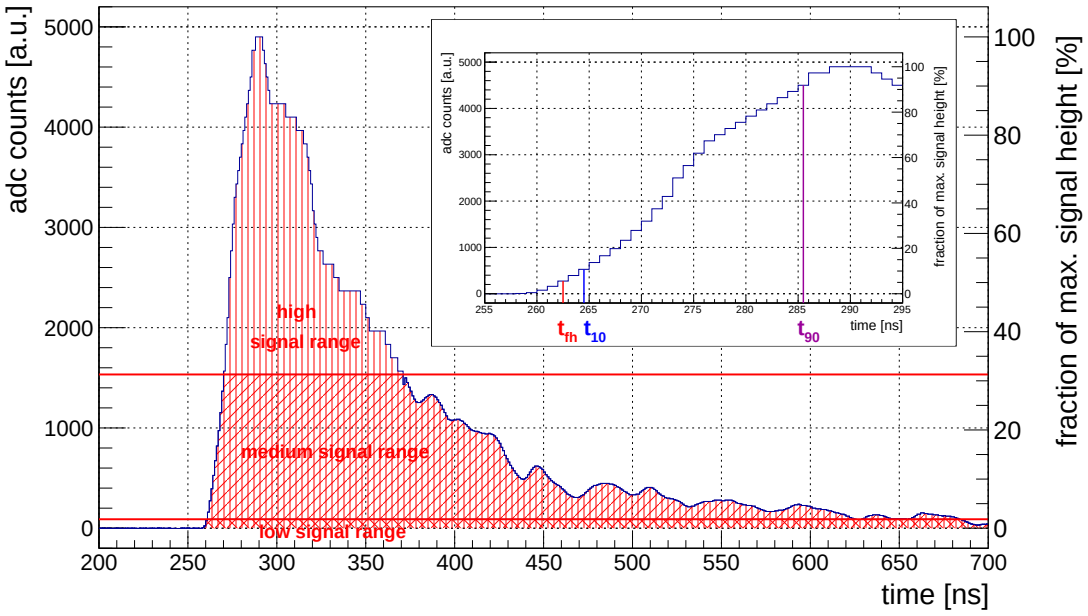

Figure 5.10 – Simulated waveform of one LPMT for a muon event. The first hit time t_{fh} is defined as the time when the rising edge crosses the threshold of 6% of the total signal height. Additionally, the t_{10} and t_{90} points are marked, which are used to define the signal's rise time. The different ranges of the 3x8bit FADC are visible through the change of resolution for the high, medium and low signal regions.

information for precise tracking. The information of rise time and charge is used to remove some PMTs from the selection the fit will run on. The rise time and charge are arranged in a two dimensional table that was created with the truth information from a sample of through-going muons. Cherenkov light produced in the LS will travel slightly in front of the scintillation light front but it is considerably less intense. This effect can lengthen the rise time and by that also worsen the accuracy of the first hit time reconstruction. Due to that, PMTs with a rise time longer than 150 ns are removed from the selection directly. Low charge PMTs have an increased probability to have a first-hit time from reflected or otherwise *indirect* light. Those photons do not fit the model described above. A general low-charge cut removes PMTs with a charge of less than 50 p.e. After those two loose cuts, the two dimensional table, shown in Figure 5.11, is used to further remove PMTs. High-charge PMTs have to feature a faster rise time, while lower-charge PMTs have a wider window of allowed rise times. The high density of PMTs also gives a handle on outlier PMTs that show a reconstructed first hit time due to dark noise or reflected light. According to the cone model, the surface of first light intersects the PMT array continuously. If a PMT was fired by this light front, its hit time cannot deviate much from its direct neighbour's hit times. For each PMT, the mean hit time of its six neighbours is calculated and it is removed, if the difference to its

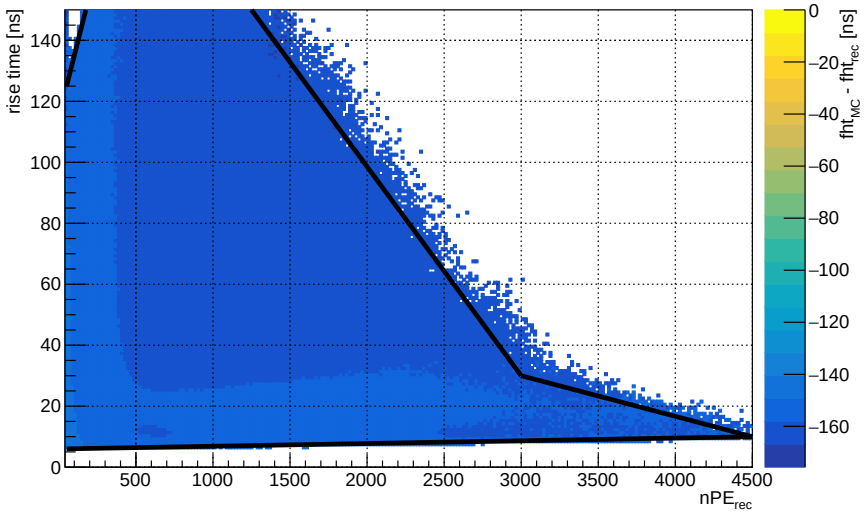

Figure 5.11 – The difference between simulated and reconstructed first hit time, in dependence of the reconstructed number of photoelectrons and the rise time. Only the region is shown where the analysis is performed. The black lines indicate a two-dimensional cut to further remove PMTs with a less reliable reconstructed first hit time. The PMTs within the black lines all feature a very similar shift in first hit time, which reflects the good waveform reconstruction performance.

own hit time is more than 5 ns.

Test sample In order to get a clear picture of the algorithms characteristics, it is tested with a synthetic sample of 5900 simulated muon events. They were simulated according to the procedure explained in Section 5.3.2. In this fashion, it is possible to identify areas of the detector where the reconstruction performs worse and to improve it accordingly. The mean energy of muon events in the central detector is expected to be 215 GeV [30]. In this energy range they will traverse the whole detector and exit again at the bottom. Thus, the muons in the test sample were simulated with this energy. In order to test the impact of the detector response, the algorithm is evaluated both with and without electronics simulation.

5.3.4 Tracking performance

As explained in Section 5.3.1, the track's distance from center D has the main influence on the event characteristics. For this reason, the performance of the reconstruction algorithm is presented against the track's true distance from the center. The benchmark quantities are the deviation in distance from center $\Delta D = D_{\text{sim}} - D_{\text{rec}}$ and the angle α between the true and the reconstructed track.

Figure 5.12 shows the algorithm's performance for the different PMT systems. In this

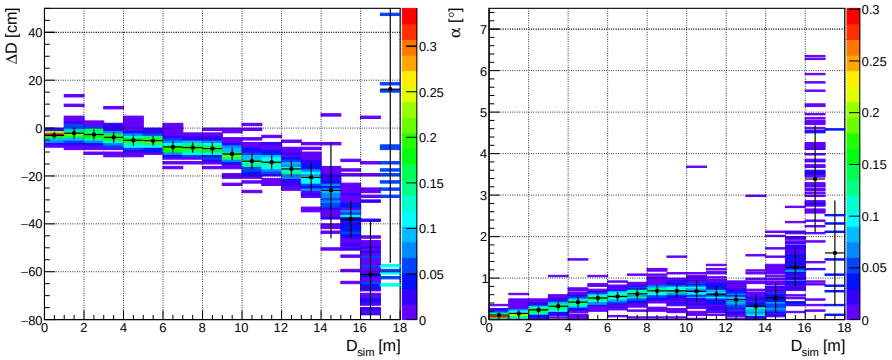

LPMT ΔD

LPMT α

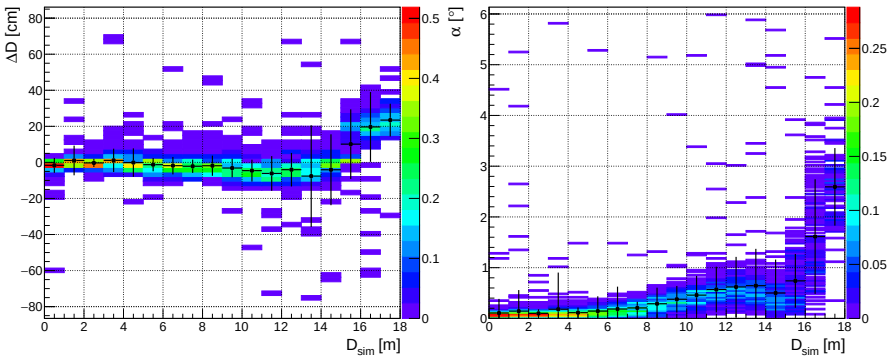

SPMT ΔD

SPMT α

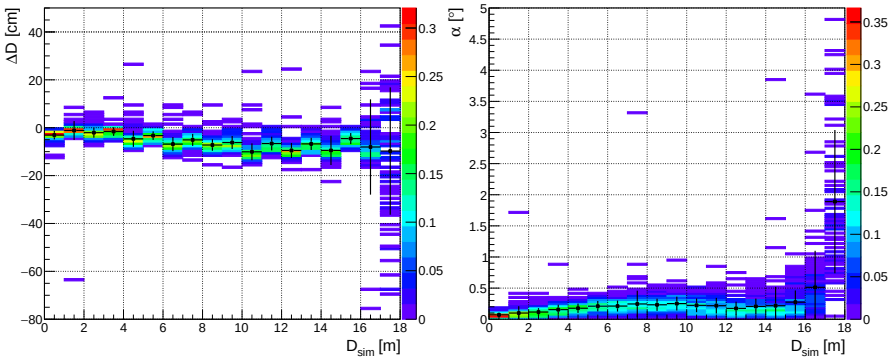

LPMT+SPMT ΔD

LPMT+SPMT α

Figure 5.12 – Reconstruction results for a sample of 5900 simulated muon tracks with smeared hit times according to the PMT's TTS. The first row shows results when using only the LPMT's array. In the second row only the SPMT's system was used and the third row presents the combination of both systems into one fit. In this case, the deviation in distance from center ΔD shows a small mean bias of less than 10 cm. The bias in angular reconstruction is better than 0.5 ° for the largest part of the detector. On the very edge of the sphere, the reconstruction performance declines because the muon travels only a short distance through the LS.

mode, the PMT's quantum efficiency and collection efficiency is simulated and the hit times are smeared by a Gaussian distribution according to their respective transit time spread as explained in Section 5.3.3. The first row shows the performance that can be achieved with only the LPMT system. There is a strong increase in bias for ΔD for increasing D. This bias development can be explained with taking the amount of collected light into account. When collecting a lot of light within a short period of time, the extracted first hit time tends to be systematically earlier. PMTs that have an earlier hit time pull the track towards themselves. This effect increases towards the detector edge, when the tracks comes closer to the PMTs and they collect even more light. The second row displays the results for the isolated SPMT system. The bias develops in the opposite direction as with the LPMTs, but stays below 20 cm. Nevertheless, it has a larger spread around the mean values. Since the SPMTs are much smaller and also slightly shadowed by the LPMT, they do not suffer from the effect of pulling tracks towards the edge, as explained above. In this case the bias only significantly increases for values of $D > 15$ m, where the influence of refraction on the acrylic sphere increases. In the bottom row, both PMT systems, 20 inch and 3 inch, are used in a combined fit. The reconstruction runs stable with a small mean bias in ΔD of less than 10 cm for most of the tracks. Both PMT systems isolated exhibit a bias that pulls the tracks in opposite directions when increasing the track's true distance from center. In the combined fit, the effects of the complementary systems cancel out. In the same region, also the angular bias stays below 0.5 °. Only the last bin for tracks with $D \geq 17$ m features a worse resolution due to the very short tracklength. The tracking efficiency is calculated by the ratio of well reconstructed tracks to all tracks. A track is considered well reconstructed if the deviation of each parameter is less then five times their standard deviation. The overall efficiency is better than 96%. As shown in Figure 5.13, reconstruction in the inner 13 m has an efficiency around 97%, while for edge tracks the efficiency declines to 91%.

In a second step, the method was verified when using the additional step of the waveform reconstruction. The results are shown in Figure 5.14. In this mode, only for the large 20 inch PMT the waveform reconstruction is done explicitly. The SPMT system is not designed to output waveforms, but direct counts for charges and hit times. Due to that, there is no need for a waveform reconstruction for SPMT. The largest uncertainty of this system is described by smearing the first hit times according to their TTS. However, for the LPMT system more distortion is introduced to the signal through another reconstruction step from waveforms to first hit times and charges. Accordingly, the performance is worsened. With increasing distance D from center, the bias in ΔD increases as well up to the mean value of 40 cm. Also the angular bias is increased to value up to 1.5 °. Both modes have in common that the last bins for $D \geq 17$ m show no reliable results for corner-clipping tracks. For comparison the LPMT profile without waveform reconstruction is shown in red.

This performance can compare to established experiments, which are currently taking data. Borexino reports a muon tracking algorithm with a lateral resolution between 35-50 cm and an angular resolution of 3-5 ° [116]. Around the detector center, Borexino

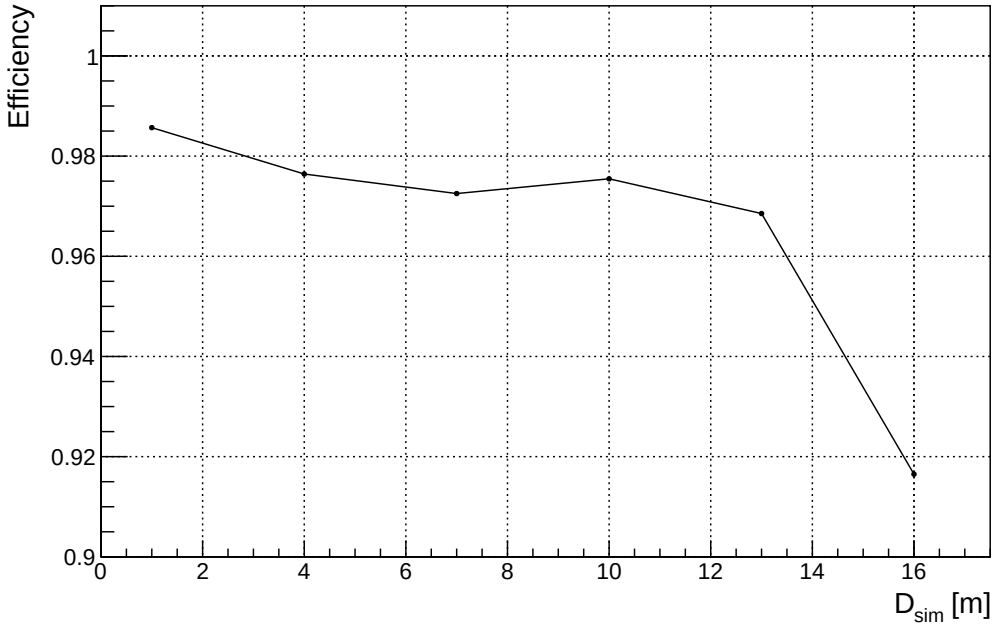

Figure 5.13 – The reconstruction efficiency when using the combined system of LPMT and SPMT.

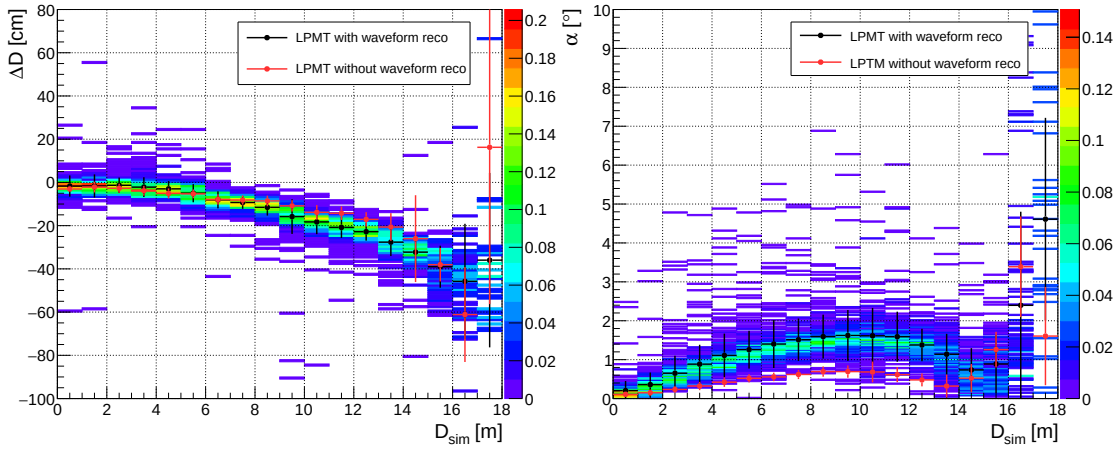

Figure 5.14 – Reconstruction results for a sample of 5940 simulated muon tracks with waveform reconstruction. Here the deviation in the muon track's distance from the detector center ΔD has an increasing mean bias of less than 50 cm. The bias in angular reconstruction is better than 2 ° for the largest part of the detector. Tracks at the very edge of the detector have a significantly larger spread similar to the case without waveform reconstruction.

can reach a spatial resolution of 30 cm. The high precision muon tracking in Double Chooz can even reach a spatial resolution of 4 cm in each transverse direction for tracks close to the center of the detector [115], while the shortest tracks are reconstructed with a spatial resolution of 10-15 cm. Within this context, the introduced cone algorithm promises an improvement in resolution compared to Borexino and being on about the same level as the muon tracking in Double Chooz. Nevertheless, a direct comparison by those numbers is not straightforward, since several other aspects like PMT coverage as well as detector geometry and size have to be taken into account. In order to compare JUNO to other multi-kiloton LS detectors, there are only Monte Carlo based studies available. The studies for the LENA detector [121] included a muon tracking algorithm which is also based on PMT hit times [122]. This reconstruction was tested on the simulation of contained lower energy muons between 0.2 GeV and 1 GeV. The reached resolution on the vertex is better than 10 cm, while the angular resolution could reach 1.7 °. Although the test sample features muons with shorter track lengths, it is also compatible with the results of 5 cm spatial resolution and 0.3 ° angular resolution obtained here for high energy through-going muons.

5.3.5 Deadtime estimation

As explained in Section 4.1.2, muons are responsible for a substantial amount of detector dead time due to the need to veto cosmogenic isotopes. With a partial veto of a volume around the muon track, this loss of *exposure* can be reduced significantly.
Using a coarse numerical volume integration, two veto cylinders of reconstructed muon tracks are drawn in Figure 5.15. The cylindrical volume around the true track is shown in blue, while the cylinder around the reconstructed track is drawn in red. In addition the volume overlap is represented by the green area. In the case of a bad reconstruction, the difference is clearly visible in the projections of the top row of Figure 5.15. The bottom row shows a well reconstructed event, in which the overlap is close 100%.

The effect of this muon veto on detector deadtime is quantified with help of a toy *Monte Carlo* simulation. As input, a simulated muon flux of 75000 tracks was used, which was generated as presented in [30]. This spectrum is considering the energy and angular distribution of muons arriving at the central detector. The baseline veto strategy is a cylindrical volume with $r_v = 3\,\mathrm{m}$ for 1.2 s after a muon along its track through the CD. This veto can reduce the cosmogenic background by 98% [30]. In accordance with a muon rate of $3\,\mathrm{s}^{-1}$, the vetoed and sensitive detector volume is numerically determined whenever a new muon enters the CD or an existing veto cylinder is released. The *volume integration* is done with a grid of $\sim 4.2 \cdot 10^9$ points, which corresponds to a volume of $5.5\,\mathrm{cm}^3$ per point. This approach takes into account that several veto cylinders are present in the detector at the same time and that they can overlap. In order to quantify the reconstruction efficiency, the cylinder radius $r_v = 3\,\mathrm{m}$ is increased in proportion to the biases in ΔD and α given above. The resulting effective veto radius is estimated as

$$r_{v,\mathrm{eff}} = r_v + \Delta D + \sin(\alpha) l, \tag{5.11}$$

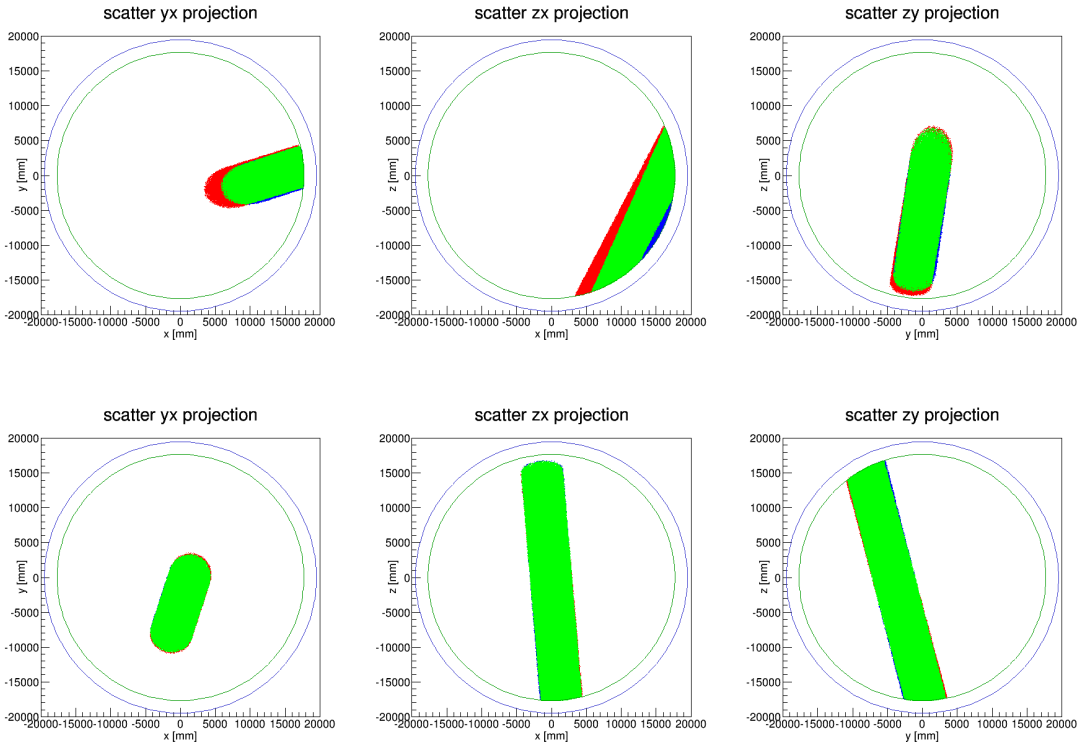

Figure 5.15 – Visualization of veto cylinders with $r_v = 3\,\mathrm{m}$ around the true and reconstructed track. The blue area shows the projection of the cylinder around the true track, while the cylindrical volume around the reconstructed track is red. The overlap of both volumes is colored in green. In the top row three projections of a badly reconstructed track are shown and the difference between the volumes is clearly visible. The bottom row shows the same projections for a well reconstructed track, where both cylinders overlap almost completely.

with $l = \sqrt{R_{LS}^2 - D^2}$ being the half track length in LS. The results are summarized in Table 5.1. The loss of 14% exposure with perfect tracking is unavoidable with the applied veto strategy and acts as a benchmark value for the developed reconstruction algorithm. With full simulation and waveform reconstruction the loss of exposure increases only to 18% in total when using only the LPMTs. Thus, the imperfection of the reconstruction algorithm adds only 4% of exposure-loss. According to the improved performance of the combined LPMT+SPMT system the loss of 4% is a conservative estimate.

Table 5.1 – Summary of deadtime estimation in terms of exposure ratio. The efficiency of 86% for a perfect tracking is in accordance with the reported muon veto efficiency for IBD events [30]. The results for the reconstruction with the cone model are seperated as explained in Section 5.3.4.

Veto strategy	Exposure ratio
No veto	100%
Perfect tracking	86%
ConeReco LPMT+SPMT	85%
ConeReco LPMT with waveform reconstruction	82%

5.4 Conclusions and Outlook

A sophisticated implementation of the fastest-light approach for muon tracking was developed and tested for JUNO. It is based on the universally applicable geometrical model of fastest light propagation and its intersection with an arbitrary shape of a PMT array. It was shown that in the largest part of the detector, the algorithm can reconstruct muon tracks with a bias of less than 45 cm in D and 1.5 ° in direction. A resolution better than 5 cm in D and 0.3 ° in direction can be reported in this region. Given the proposed veto scheme [30], a reduction of only 4% in exposure is expected due to the waveform and track reconstruction itself for a realistic muon flux. Without the effects of waveform reconstruction the exposure loss introduced by the reconstruction is only 1% with both LPMTs and SPMTs combined. The geometrical approach models the scintillation light front that develops in any liquid scintillator. It fits the timing signal of the PMTs to the intersection of two geometrical shapes — the light cone and an arbitrarily shaped PMT array. Therefore it can be applied also in other liquid scintillator detectors.

One major difference between the categories of *fast* and *detailed* reconstruction approaches is the number of effects that is accounted for and their implementation. This is also the case for the presented reconstruction, which only explicitly models the major effects of the formation of the first light front. Several other light propagation effects are only included implicitly through the PDFs, which were generated with the *Monte Carlo* simulation. While this simulation takes effects of light attenuation individually into account, the PDFs only reflect the sum of all effects. This allows for a much faster reconstruction with the cost of some precision.
When the photons travel from the acrylic sphere into the water buffer towards the PMTs, the difference in refractive indexes of the two media leads to refraction of the photon path. This causes a change in the light path, which will distort the shape of the light front. With increasing path length after refraction, this effect creates a larger deviation from the idealized assumption. In application to the construction, this effect is contributing to the increasing bias towards the detector edge. The presented reconstruction approximates this shape to be perfectly conical. Due to the complicated calculation of this effect and its translation into an opening angle of the produced cone, this simplification is justified.

Nevertheless, the explicit inclusion of refraction could improve the achieved results.
Another approximation was made in the binning of the used PDFs. Along the axis of the opening angle θ, the PDFs were modeled using *adaptive kernel density estimators* , but in the dimension of D, it is binned in 1 m-steps. Although the algorithm interpolates linearly between two PDFs, the binning is rather rough. This was done with regard to the limited sample size of simulated events to create the PDFs. With help of larger sample, a more finely granulated PDF map could improve the resolution of the reconstruction further. Since this is a single time effort of high computational cost, it would not impair the speed of the actual reconstruction.
Finally, the reconstruction could be improved upon by introducing a bias correction. Similar to the method used in the time residual fit implemented for JUNO [112], biases in this kind of reconstruction can be corrected for. The basis for this is finding a set of variables that can represent the bias unambiguously to build a correction map.
For actual use in the data taking of JUNO, there are different ways possible. As tested in this case, the algorithm can be used purely for through-going muons, that do not yet indicate a showering feature. With the track result, the total deposited energy could be re-evaluated to make a decision whether or not it was a showering muon that needs further reconstruction. In this case, there is additional need for specialized algorithms for starting and stopping tracks. The second approach would foresee the starting and stopping points to float in the fit in order to reconstruct also those kinds of tracks. To benefit from just having one main reconstruction algorithm for the CD, an external input from other subsystems is crucial. This could be a track hypothesis from the TT or the WP combined with an energy estimator from the CD. In addition, the TT can be used to measure a precisely tracked muon sample to calibrate muon reconstruction algorithms in the CD.

Part III

OSIRIS

Chapter 6

The OSIRIS Simulation

The development of a detector typically involves several stages of designing its layout with increasing level of detail taken into account. Initially, many fundamental parameters like the target mass and in case of a LS detector, the needed coverage or light yield can be estimated by scaling parameters of existing experiments. Geometric coverage of PMTs and achievable resolutions from photon statistics can also be easily approximated with simple calculations. Nevertheless, at some point the required level of detail makes *Monte Carlo* (MC) simulations inevitable. Including many effects of light propagation and detection as described in Sections 2.2 and 2.3 requires a statistical analysis with a large number of events. The achievable sensitivity to the main physics questions of an experiment is a key aspect, that has to be evaluated with extensive MC simulations. In the case of OSIRIS, this question prompted the development of the first version of the simulation code. Developed by *Paul Hackspacher*[1], the first version of the OSIRIS simulation was designed as a single-purpose application to simulate different background rates from internal and external sources. The code was based on `Geant4` 10.02 [119, 123] and did not include an optical model or a scintillation process. Based on this, the first decisions regarding detector design were made.
In an effort to accommodate the dynamic nature of studies with developing detector systems, a more versatile framework was developed by a cooperation of *Sebatian Lorenz*[1] and myself in the scope of this thesis. It adapts core functionality of the first simulation and thus, is also based on `Geant4` 10.02 and written in `C++11`. The goal of this software is to provide a fast and easy-to-use tool, that can perform a full detector simulation for different physics studies with OSIRIS.
Although the framework has gone through several iterations of refactoring to accommodate new requirements from changes in the design, this chapter will focus on the most recent version and its features. Section 6.1.1 will introduce the physics program that is envisioned for OSIRIS and that the simulation has to satisfy. Details of the detector layout and its representation as slightly simplified geometry objects are explained in Section 6.2. This

[1] *Institute of Physics* of *Johannes Gutenberg-Universität Mainz*

is followed by an explanation of how the software was designed to be easily adaptable to changing requirements while allowing parallel development and fast simulations in Section 6.3. A core aspect in the simulation of LS detectors is the proper description of scintillation process and the optical model, which simulates the propagation of photons through the detector. Section 6.4 gives details on how this was implemented in the presented software. Finally, Section 6.5 discusses the key features of geometric biasing in the simulation, that allows for efficient simulation of highly attenuated background fluxes.

6.1 The OSIRIS Facility

As introduced in Section 3.2.4, OSIRIS first goal is monitoring the radiopurity of the LS while the JUNO CD is filled. It is the only system to test the nominal operation of the purification plants and will guarantee that the concentrations of U and Th in the LS do not exceed the given limits. In the following the physics program of OSIRIS will be introduces, as well as the general detector design and its modes of operation within JUNO.

6.1.1 Physical Motivation

For JUNO's main goal, determining the neutrino MO, its ability to detect a high purity sample of IBD events is of paramount importance. One large background for that are accidental coincidences, which are mainly driven by single events happening in the CD, as explained in Section 4.1.2. A large part of those events stem from the decay of radioactive isotopes in the LS itself (*internal background*) and in the surrounding materials (*external background*). If for any reason the purification plants decline in performance or an air leak happens anywhere along the filling line, the whole LS of JUNO could be spoiled. The danger of this happening is amplified by the long time it takes the fill the CD, which is estimated to a minimum of 6 months. In order to prevent this, OSIRIS will be placed between the purification plants and the CD, where it can constantly measure a part of the purified LS to ensure the final LS target is within its specifications. The estimation of backgrounds for the IBD measurement discussed in Section 4.1.2 is based on a contamination of less than $10^{-15}{}^{\mathrm{g}}/_{\mathrm{g}}$ for ^{238}U and ^{232}Th. Table 6.1 gives a full overview on the LS radiopurity requirements from JUNO.

For a significant measurement of solar neutrinos (see Section 4.2) even stricter limits of $10^{-16}{}^{\mathrm{g}}/_{\mathrm{g}}$ for ^{238}U and ^{232}Th are required. Furthermore, the amount of ^{85}Kr has to be less than 0.5 counts/day/ton for this measurement.
In order to determine the concentrations of Uranium and Thorium OSIRIS can exploit a coincidence signal of two subsequent decays, that happen within a short time window towards the lower end of the decay chains. The decay of the pairs ^{214}Bi $-^{214}$ Po and ^{212}Bi $-^{212}$ Po in the chain of ^{238}U and ^{232}Th, respectively, can be tagged efficiently. Figures 6.1 and 6.2 give an overview over the full decay chains of both, ^{238}U and ^{232}Th. As can be seen from the diagrams, both coincidences happen close to the end-point of the chains. Thus, both coincidence signals are the progeny of a preceding Radon

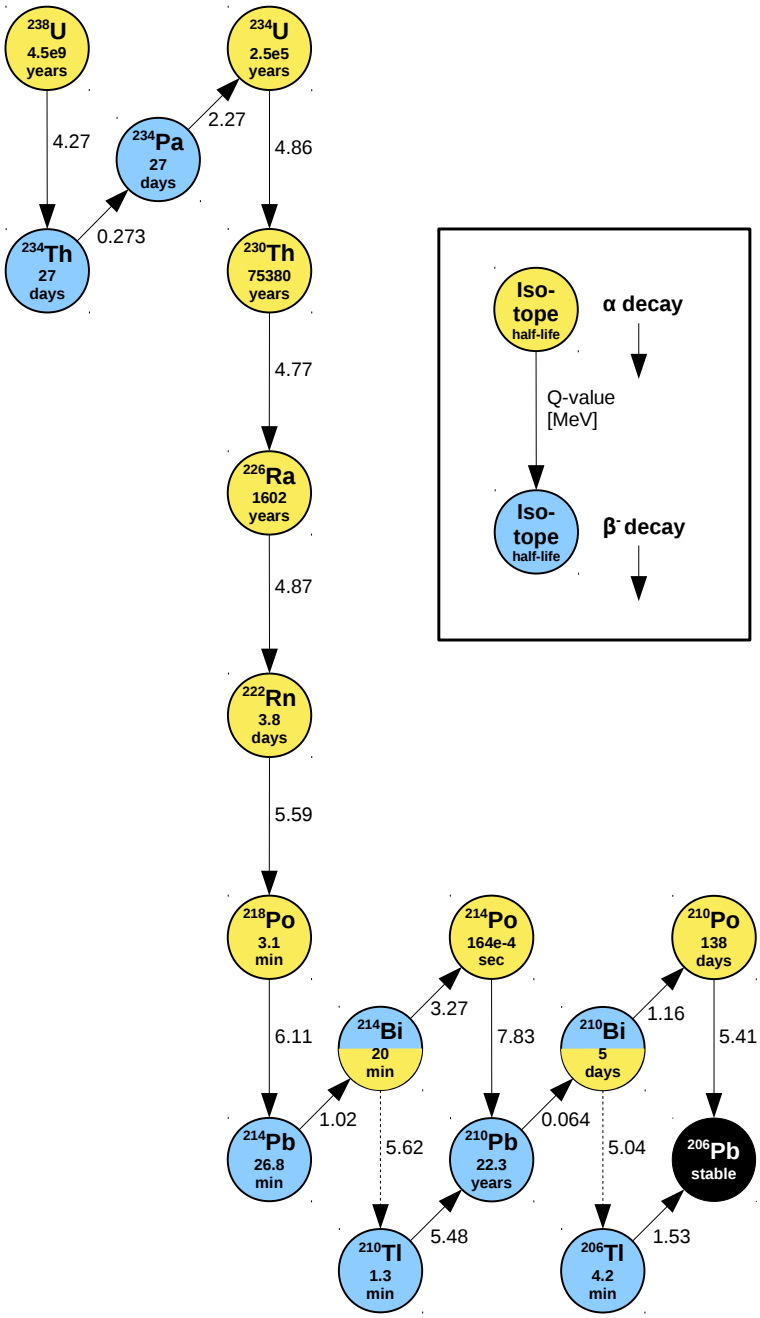

Figure 6.1 – Full decay chain of ^{238}U. For every isotope, the half-life and Q-value in MeV are given and the α decays are marked with yellow, while isotopes that decay via β^- are blue. The decays of Bi to Tl have a negligible branching ratio ($<2 \cdot 10^{-4}$), but are shown for completeness. Some decays are accompanied by gammas from excited states of the daughter isotope, which are not shown here. All data was taken from Ref. [124].

Table 6.1 – Baseline radiopurity requierements for JUNO [30], divided into the minimal demand for the MO measurement and the tighter limits needed for solar neutrinos. For comparison the experimentally achieved values of Borexino are added [79].

Chain/Isotope	JUNO IBD [g/g]	JUNO solar [g/g]	Borexino [g/g]
^{238}U chain	1×10^{-15}	1×10^{-16}	$< 1 \times 10^{-18}$
^{232}Th chain	1×10^{-15}	1×10^{-16}	$< 1 \times 10^{-18}$
^{210}Po	—	5×10^{-24}	$< 1 \times 10^{-25}$
^{40}K	1×10^{-16}	1×10^{-17}	$< 1 \times 10^{-19}$
^{14}C	1×10^{-17}	1×10^{-17}	$< 3 \times 10^{-18}$

decay, namely ^{222}Rn in the ^{238}U chain and ^{220}Rn in the ^{232}Th chain, respectively. Due to the fact, that one cannot measure a further coincidence of the Bi-Po-decay with an isotope earlier in the chain, the detection of a Bi-Po coincidence equals a detection of Radon. Under the assumption of secular equilibrium, the Radon rate is a measure of the corresponding ^{238}U or ^{232}Th contamination, respectively. Nevertheless, if the chains are not in equilibrium and Radon is introduced from another source, this inference is not directly possible anymore. Due to its long life-time, ^{222}Rn can emanate into other volumes and decay there, possibly increasing background rate. An example of this will be discussed in Section 7.2.
The Bi decays into Po are β-decays with an endpoint of $\sim$2.25 MeV for ^{212}Bi and $\sim$3.27 MeV for ^{214}Bi. Subsequently, the ^{212}Po and ^{214}Po decay via an α-decay and are thus mono-energetic with an Q-value of 8.95 MeV and 7.83 MeV, respectively. The data is taken from on the `RadioactiveDecay` package [125] in `Geant4`, which is based on the ENSDF (Evaluated Nuclear Structure Data File) data library [126]. A comprehensive overview of the decays including the life times and related branching ratios can be found in Table 6.2.

Table 6.2 – Overview of the decays of relevant isotopes to identify the Rn contamination through Bi-Po coincidences. The Q-values are rounded to keV and only the dominant decay modes are shown.

Isotope	Mean life	Decay	Branching ratio [%]	Q-value [keV]
^{212}Bi	87.4 min	β^-	64.06	2254
		α	35.94	6207
^{212}Po	0.431 μs	α	100	8954
^{214}Bi	28.7 min	β^-	99.98	3272
		α	0.02	5617
^{214}Po	237 μs	α	100	7833

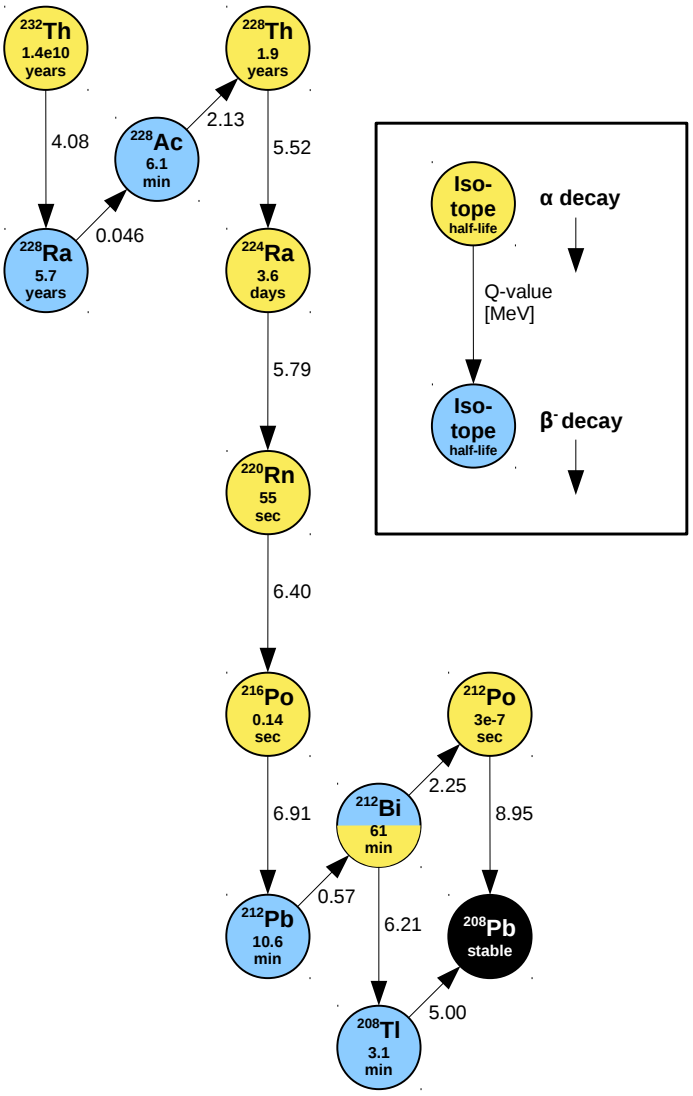

Figure 6.2 – Full decay chain of ^{232}Th. For every isotope, the half-life and Q-value in MeV are given and the α decays are marked with yellow, while isotopes that decay via β^- are blue. Some decays are accompanied by gammas from excited states of the daughter isotope, which are not shown here. All data was taken from Ref. [124].

Details on the event selection to identify the coincidence signal will be given in Chapter 7. Apart from identifying U/Th contamination in the LS, OSIRIS has the potential to be able to measure further internal backgrounds of the LS. In the decay chain of ^{238}U also the isotope ^{210}Po appears. As Borexino reported [79], this can be severely out of secular equilibrium and highly influence the ^{13}C$(\alpha, n)^{16}$O background for the IBD detection, which was shortly discussed in Section 4.1.2. If in secular eqilibrium, ^{210}Po is also the decay product of ^{210}Bi and, by that, gives a measure of this isotope, which is a

dominant background in the search for CNO neutrinos (see Section 4.2.2) [79]. Under consideration of quenching effects in the LS, the α-decay of ^{210}Po is a single-event with a visible energy of $\sim$500 keV. Depending on the background levels in this region and the ability to discriminate α and β particles, a sensitive measurement could give feedback to the purification plants during commissioning.
Another disturbing factor in JUNO is the naturally abundant ^{14}C in organic scintillators. It cannot be removed from the LS and appears as a high-rate β-decay with an endpoint of 156 keV. While it cannot cause triggers in JUNO, the decay of ^{14}C can pile-up with positron events and by that distort the energy scale for the anti-neutrino events. With sufficient photo-coverage OSIRIS could measure the spectrum and determine the rate of ^{14}C.
Lastly, the detector can be used to study the rates of cosmic muons as well as fast neutrons and radioisotopes produced by those muons. This would act as an independent background study before JUNO starts operation.

6.1.2 Modes of Operation

The baseline design of OSIRIS foresees a continuous measurement to reach the design level of sensitivity over the course of one day. Nevertheless, the facility will be used in several modes of operation through its lifetime. After its own entry into service, the first task of OSIRIS will be to aid in the commissioning of the JUNO purification system. The first batch of LS produced by the system will be studied in detail with the detector for the residual U/Th contamination and initial radon content. By cycling the same LS through the purification system and OSIRIS, the efficiency of the system can be determined and deficiencies in both system be found. The time schedule foresees enough time to measure batches of LS for days and weeks in order for both facilities to reach their design goals.
Followed by that, OSIRIS can start its operation as a radiopurity monitor for the filling of JUNO. About 13% of the produced LS ($\sim$900 liters per hour) will be diverted from the main filling line into OSIRIS. Before being filled into the vessel through a diffuser, it will be slightly warmed up above ambient temperature. By that, a temperature gradient over the whole height of the vessel allows for a continuous flow without mixing newly added LS with already present one. Combined with the filling speed, the gradient will be adjusted so that within 24 h the full vessel volume of $\sim$19 t of LS will be exchanged. In this mode, the facility's operation is two-fold. On the one hand, a live analysis of the Bi-Po coincidence rate and global event rate acts as an *early warning system* for any catastrophic failure. A sudden rise in the rate would indicate an increase in radioactivity of the LS either through an air leak or failure of the purification plant. Accordingly, OSIRIS could issue a warning to pause the filling of the CD. On the other hand, the *integrated sensitivity* is build up over time. Thus, OSIRIS can reach the design sensitivity over the course of a day by accumulating and analyzing data. It is important to note that in this mode the sensitivity is mainly limited by the measurement time. Thus, a longer duration with averaging over more LS samples could yield an even better sensitivity. Additionally, the long term stability of the filling is tracked.

After the JUNO CD filling is concluded, OSIRIS can enter its third mode of operation. In order to aid JUNO, the detector is available for long-term LS studies. If any need for dedicated LS measurements arises in the operation of JUNO, OSIRIS can be used without interfering with the nominal operation of the CD.
Moreover, the facility provides an excellent test bed for hardware to be used in subsystems of JUNO. This is not directly bound to the other modes of operation. In the commissioning phase the *liquid handling system* will be used and tested before it is operated with the main detector. Since the detector will be equipped with the *intelligent PMT* (iPMT) design [127], this will be the first real-life application of this PMT concept. After the filling of JUNO, this system can be tested and developed to maturity. Equally, a laser-based *light injection system* developed at the *Universität Tübingen* [128] for JUNO will be implemented in OSIRIS. It is intended to be used for regular timing calibration of the PMT system and thus further discussed in Chapter 8.

6.2 Geometry Implementation

Conceptually the detector geometry implemented in the simulation can be separated into three parts: concentrically placed cylindrical volumes that represent the different vessels, the PMT system including its holding frame, and structural details added to either one of them. The early versions of the software omitted many structural details and made many approximations. With progression of the design of the detector the description became more detailed. In the current state, all elements of importance are included according to their final or baseline design.

6.2.1 Vessels

The origin of the chosen coordinate system is placed in the center of the outermost volume, the so called *world volume*. It has no direct impact on the simulation other than limiting the maximum volume of the simulation. All subsequent vessel-like volumes are placed as concentric cylinders into each other starting from the outermost *rock* up the *scint* volume that represents the LS target. Their symmetry axis is aligned along the z-axis of the coordinate system. While it is common practice for modeling detectors like this to place solid cylinders from the largest and thus outermost volume to the innermost, the dimensions are typically calculated the other way round. In the development of OSIRIS the size of the outer steel tank limiting the real-life extent of the detector is fixed by the available space in the underground hall. Additionally, the maximum size of the *acrylic vessel* (AV) that holds the LS is limited by the practicability of transporting it underground. Thus, those two volumes are defined by radius and total height and all other volumes are calculated based on their thickness and available space.
At the center of the detector, the LS is placed as a cylinder with radius $r_{LS} = 150\,\text{cm}$ and height $h_{LS} = 300\,\text{cm}$. This volume is surrounded by the AV with a wall thickness of $t_{AV} = 3\,\text{cm}$. The steel tank on the outside has its maximum allowed measures of $r_{tank} = 450\,\text{cm}$ and $h_{tank} = 900\,\text{cm}$ with a wall thickness of $t_{tank} = 0.6\,\text{cm}$. Since the design of OSIRIS foresees a frame holding the PMTs, there is no separation between a buffer- and a shielding-volume. Thus, the space between the AV and the steel tank

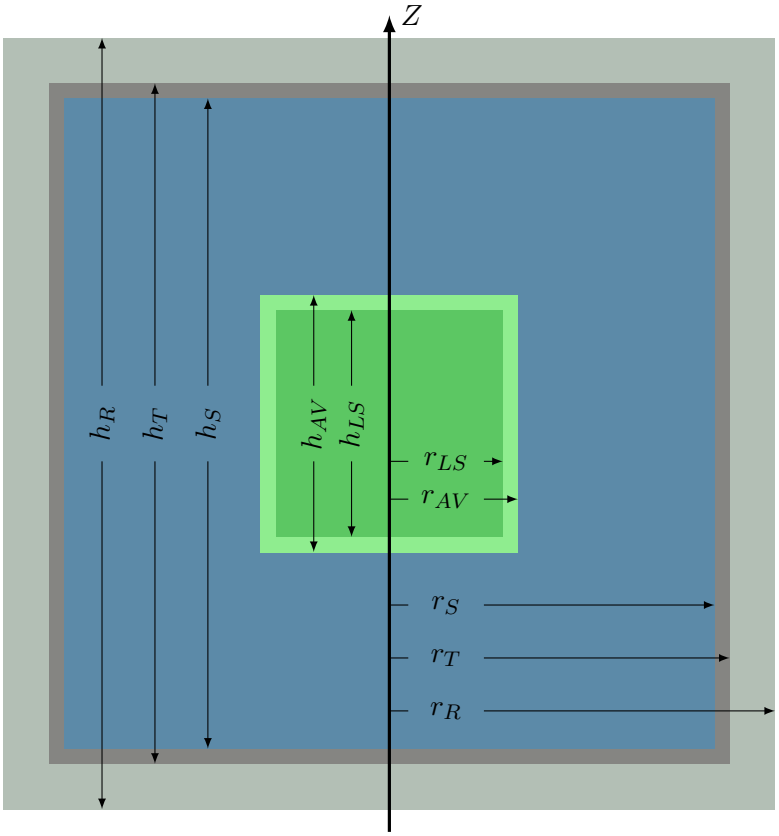

Figure 6.3 – Schematic of the cylindrical vessels that are placed concentrically in the simulation to describe the detector geometry. The wall thicknesses of the acrylic vessel and steel tank are increased for visibility, while the rest of the sketch is to scale. Set values for the introduced heights and radii are given in Table 6.3.

is filled with cylindrical water volume. Finally, the experimental underground hall is simulated as a rock volume surrounding the steel tank with a thickness of $t_{rock} = 60\,\text{cm}$.

A comprehensive overview of the vessel placement is shown in Figure 6.3 and the resulting measures of the volumes are summarized in Table 6.3.

6.2.2 PMT systems

In the development of the detector, several different types and sizes of PMT were considered, including the possibility of having a mixed system of different PMTs. The simulation software was designed to accommodate this requirement by introducing a *PMT system* class which manages a number of *subsystems*. An arbitrary number of PMT systems can be registered to be placed in the geometry with the ability to detect *optical photons*. In order to do so, a pointer to a PMT geometry implementation is created and added as a subsystem through a member function of the detector's PMT system. For

Table 6.3 – Parameters of the concentric cylindrical volumes that describe the OSIRIS geometry. The LS target in the center is full cylinder and thus, has no thickness. All radii are describing the outer radius of the volume. The parameters are also depicted in Figure 6.3.

Volume	ID i	radius r_i[mm]	height h_i[mm]	thickness t_i[mm]
LS target	LS	1500	3000	—
Acrylic vessel	AV	1530	3060	30
Water shield	S	4494	8988	2964
Steel tank	T	4500	9000	6
Rock	R	5100	10200	600

background studies this is often sufficient. If this subsystem is supposed to detect optical photons it also has to be registered to the *sensitive detector* (SD), which can be done via a member function of the PMT implementation. Subsequently, the placement of PMTs in the detector geometry is done. While a setup in rings is prepared in the code, the user is free to define an arbitrary number of PMTs and their placement. Any PMT subsystem, that was registered to the SD is automatically considered in the output of PMT data and does not need further setup.
The same pattern is realized for the veto PMTs that are supposed to be placed so that they observe the water-shield instead of the AV.
In the current state three different PMT geometries are implemented to chose from:

- **Hamamatsu R7081** is a 10-inch PMT, that was used in DoubleChooz [129]. Early designs considered using those PMTs after DoubleChooz stops data taking. They feature a very low radioactivity glass, which would allow a placement close to the vessel. Thereby, a good photo-coverage could be reached with the small number of ∼110 modules.
- **Hamamatsu R15343 / R12860** is a high-quantum-efficiency 20-inch dynode PMT. While both models feature the same geometry, the model R12860 will be used in JUNO (see Section 3.2.2) and R15343 is the production for OSIRIS. In March 2019 it was decided to use this model, so that it is the implemented PMT system in the current software version. The glass has a higher activity, which requires a larger water buffer between the PMTs and the vessel. Nevertheless, the much larger area not only compensates, but increases the total achievable light yield.
- **SimpleDisk** is an extremely simplified geometry, that can represent the effective aperture of an arbitrary PMT. The simplicity allows for a fast simulation. In the early stages it was used to investigate the viability of adding light concentrators to the PMTs in order to increase their effective area.

Table 6.4 summarizes the final PMT setup for the OSIRIS detector. The AV is monitored by a total number of $N_{PMT} = 76$ Hamamatsu R12860 20-inch PMTs. 60 of those are

Table 6.4 – Parameters of the PMT array as implemented in the OSIRIS simulation. A choice of parameters is depicted in Figure 6.4.

Description	Parameter	Value
Total number of PMTs	n_{PMT}	76
PMTs on lateral area	$n_{PMT,lat}$	60
PMTs on caps area	$n_{PMT,caps}$	16
Lateral PMT rings	$n_{ring,lat}$	5
PMTs per lateral ring	$n_{PMT,ring,lat}$	12
Cap PMT rings	$n_{ring,cap}$	1
PMTs per cap ring	$n_{PMT,ring,cap}$	8
Distance of lateral rings	Δz_{rings}	60 cm
Distance PMT cathode to AV wall	$d_{PC,AV}$	130 cm

arranged on 5 rings with $N_{PMT,ring,lat} = 12$ each, in planes parallel to the x-y-plane around the cylinder mantle of the AV. The middle ring is placed around the detectors equator at $z = 0$ and the distance between adjacent rings $\Delta z_{rings} = 60\,\text{cm}$ is constant. In order to increase the uniformity, neighboring rings are shifted against each other in the cylindrical ϕ coordinate. This shift is set to be half the angle between two modules in one ring, $\delta\phi = \pi/N_{PMT,ring}$. Thereby, PMTs on an adjacent ring are in the middle between the PMTs of that ring. Due to the fact, that the PMT glass itself is a source of radioactive background, the distance between the photo-cathode and the vessel is a tuning parameter in the placement. Background estimations in the scope of the sensitivity studies yielded an optimal distance $d_{PC,AV} = 130\,\text{cm}$. Taking into account, that the reference point for PMT placement in the simulation is the center of the ellipsoid of the PMT bulb, the ring radius is thus $r_{ring,mant} = 297\,\text{cm}$. All PMTs in the rings are facing parallel to their plane towards the z-axis.
The remaining 16 modules are split into two rings of which one is placed above the AV and one below. With 8 PMTs per ring, their angular distance is $\pi/4$ on a ring with $r_{ring,cap} = 100\,\text{cm}$. In order to preserve a uniform coverage, the rings are also aligned in the x-y-plane and centered around the z-axis. The modules face towards the AV parallel to the z-axis and have the same $d_{PC,AV} = 130\,\text{cm}$ as the mantle PMTs.

A holding frame is then inserted into the simulated geometry depending on the placement of PMTs. While it does omit details like connectors and screws, it properly represents the octagonal shape and correct mass of the frame that will be installed. Given the octagonal shape, the frame stands on 8 vertical struts and features one ring of 8 supporting struts for each of the 5 mantle-PMT rings. The rings that hold the PMTs on the cylinder caps are supported by 8 additional beams each at the top and bottom. Figure 6.4 shows a complete visualization of the implemented geometry.

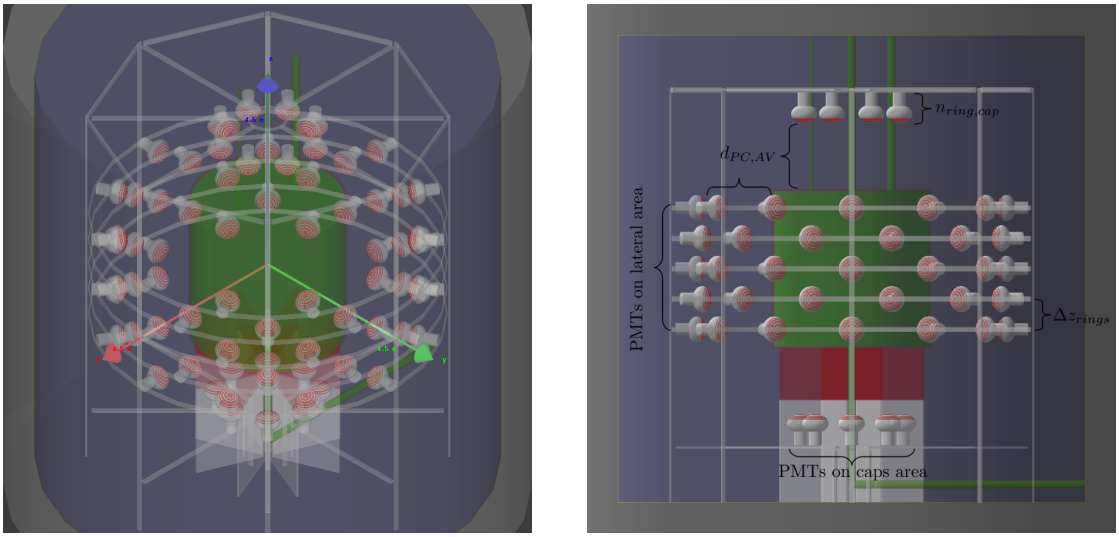

Figure 6.4 – Visualization of the full detector geometry currently implemented in the simulation from an angled top view and a side view. Details on the PMT array can be found in Table 6.4.

6.2.3 Structural details

In addition to the vessels and the PMT systems, also several other structural details were added to the simulated geometry. This is important especially for structures that can influence the light collection or introduce radioactive backgrounds to the measurement. As already shown in Figure 6.4, this encompasses mainly two kinds of geometries:

- **Piping** There are three pipes planned that enter the AV from the top and one more exits at the bottom. The central inlet at the top and the outlet at the bottom are straight-forward for providing the continuous flow in the detector. Additionally, there is a 1-inch pipe to lower a calibration source into the detector and a 4-inch pipe for level measurement of the LS. The inclusion of those pipes filled with LS is important, as particles can produce light also in there and thus might introduce high background rates. If an absorbing material is chosen for the pipes, a possible shadowing effect of the PMTs by those pipes can be studied.

- **Pedestal** The support structure of the AV is per definition in touch with the AV and thus very close to the LS. Therefore, its material and design choice can have a large influence on the background rates. In order to quantify the effect, the conclusive design for the pedestal is included in the geometry. It consists of 8 legs with two parts each that are arranged in a star-like shape. The lower part is made out of stainless steel, while the upper part, that comes in contact with the AV, is made from acrylic as well.

6.3 Software layout

With the general detector design introduced, this section will shed some light on the actual implementation and layout of the framework. It is written in single threaded `C++11` and heavily builds on the simulation library `Geant4` and the analysis framework `ROOT` [92]. The decision to not implement multi-threading was made, due to the comparably lower simulation effort in contrast to JUNO. With less than 100 PMTs as sensitive detectors and readout channels, needed MC samples in the order of $10^6 - 10^7$ events can be simulated in a reasonable amount of time. *Version-control* and *deployment* is realized with a `git` repository managed through a *GitLab* instance[2]. The *build* process is managed through *cmake* [130] and thus very user-friendly.
In general, the simulation framework was developed for fast but accurate studies of the OSIRIS detector from interaction of particles inside the detector up to the detection of light on the PMTs. Since a key requirement is the ability to accommodate often changing detector designs and setups, the design goal of the software was to be a versatile and dynamic framework with a high level of abstraction. Through stringent adherence to the *single responsibility principle* most classes and modules are easy to expand or to exchange. This manifests in separate class structures for PMTs (see Section 6.2.2), material properties, I/O, detector construction, and physics processes. Interfaced through abstract classes, the actual implementation of a PMT object, modules to describe physical processes or materials warrant touching only a single point in the framework. The management of data input and especially output is realized with the use of *singleton* classes. This provides consistency in data handling by ensuring that only one instance of each manager can exists and they can be accessed globally.
Typically, `Geant4` simulations are configured with the help of *macro files*, to allow the user a powerful but neat way of defining geometries and particles to be simulated. For the use of the *general particle source* (GPS) in `Geant4` the interface is straight-forward. On the other hand, manipulating the detector geometry is not. Due to the way that the toolkit handles geometries, they cannot be changed after initialization and changes of the geometry need to be communicated to other classes, like the *output manager* for example. Our framework makes use of the *observer* design pattern and *messenger* classes to tackle this challenge. The detector geometry is implemented as an *observable detector*, to which an arbitrary number of *observers* can be registered. Using messenger classes, the *detector construction* can then be modified through macro files and any *(re-)construction* of the geometry is broadcast through a dedicated *observer* class to all registered observers. Each observer can than query parts of the geometry's state, that are of interest for this particular observer. Examples for this would be the number of PMTs for the *output manager* or the variable placement of a calibration capsule in the geometry.
The output of the simulation is manifold and heavily depends on the *simulation mode*, which will be explained in the next section. Whenever the detected photons on the PMTs are written out, this is done in the form of nested vectors like `vector<vector<double>>`. While the outer vector has the length of the number of PMTs, each nested vector holds the

[2] `https://gitlab.rlp.net/OSIRIS/simulation_v2` (password protected)

times of each registered photon hit on this particular PMT as a *double* in the dimension of nanoseconds. Thus, the output is directly converted from an array of hits to an array of PMTs. It holds the same information, but the structure is more favorable for subsequent studies of this output. Every other MC truth output is not standardized, due to the vast differences in requirements of different studies.

6.3.1 Simulation Modes

The concept of different *simulation modes* was introduced to the software to keep the simulation fast while providing an extensive range of setups. This layout ensures, that fundamental inputs like the detector geometry and the physics list are the same, while different pre-configured scenarios are simulated. By that, the design leads to consistent assumptions and inputs among all studies. Each mode is tailored to one aspect if interest and thus, reduces overhead and allows for a fast simulation As mentioned before, the outputs are customized for each mode to provide exactly the data needed.
Another advantage of this design is the support for parallel development. Each mode can be developed independently of the others and the core functionality. Additionally, all changes in the fundamentals are directly available in each mode by their implementation through abstract classes. Any mode has to implement and output container, a detector geometry, a physics list, and the `Geant4` `G4RunManager`. Furthermore, all needed *user actions* have to be implemented and set in the *run mananger*. Those user actions, like e.g. *event action*, *track action*, and *step action* are periodically called functions in `Geant4`, that allow the user to access detailed information along the particle transportation through the detector. If one of those actions of a certain mode is suitable for another mode, it can just be implemented. Thereby, only user actions that are unique to a mode have to be developed and code duplication is avoided. Currently there are 10 modes available in the framework:

- **GeneralPS:** This is the default simulation mode and utilizes the *general particle source* (GPS) of `Geant4`. It is highly modifiable through macros. The GPS allows distributions of single or multiple particles in points and volumes as well as pre-defined and user-defined energy distributions. The output is divided into *data*, which is the photon hit times on the PMTs and *MC truth*, which stores information about the primary vertexes of generated particles.
- **ScintDiag/OptDiag:** Two diagnosis modes are implemented to independently test the custom scintillation process and the implementation of light propagation effects. Both modes write out extensive truth information, which is needed to verify proper functionality, but would be useless overhead for general simulation purposes. Details on the processes will be given in Section 6.4.
- **PhtBomb:** Another level of parallel development is enabled by the *photon bomb* mode. It is used to circumvent the complicated light creation processes and directly place a number of optical photons in the detector. Thereby, properties of light propagation and detection can be studied, while the detailed description of the LS is ignored. This mode was heavily used for early resolution studies.

- **Calib:** In order to study ways to calibrate the detector response, a dedicated mode was introduced. It is the only mode that modifies the detector geometry by adding a small capsule inside the LS volume. Then, the user can chose from a range of available γ-emitting isotopes that will be simulated inside the capsule. This mode is used to study the capsule design, orientation of the calibration axis, choice of isotopes, and response mapping. Details are presented in Chapter 8.

- **ParaDump:** The often changing setup during detector development requires a way of keeping track of simulation parameters. For this purpose the *para(meter) dump* mode is available. It works without inputs from the user and will write the full information about the current simulation setup to disk. One ASCII file contains a table of all PMT information, including not only their position, but also an ID and their facing-vector. Additionally, all optical parameters of all materials are saved in a `ROOT` file in the form of `TGraphs`. It is suggested to run this mode once for each large simulation production for further algorithms, like a reconstruction that depends on the PMT positions.

- **HepEvt:** The *HepEvt* format is a widely used format in physics event generators. It provides information about generated particles and their position and momentum in a simple format. The simulation provides this mode to easily interface with such generators.

- **BkgEdep:** The first version of the simulation did not include an optical model or sensitive detectors in form of PMTs. Instead, all energy depositions along the *steps* in the LS were saved. This is an important feature, that was re-implemented in the current version as the *background energy deposition* mode. It circumvents elements of the simulation that are sensitive to errors and makes a very fast simulation possible. Resolution effects of the setup can later be studied by application of effective smearings to the data without re-simulation. An in-depth discussion of this approach follows in Chapter 7.
  In the current implementation, radioactivity events from all volumes can be studied. While for the intrinsic radioactivity of the LS and AV, 29 relevant isotopes can be simulated, the outer volumes only allow the simulation of the γ spectra of the ^{238}U- and ^{232}Th-chains and from ^{40}K. α- and β-decays in those volumes are not simulated, since their mean free path does not allow them to reach into the LS. The output are all true positions and amounts of energy depositions in the LS. Additionally, the total energy is saved as the sum of all step-wise energy depositions and for the event position the center-of-gravity is saved. In order to allow detailed studies, also the position and energy of the originating particle is saved.

- **BiasSim/BiasTune:** Two modes for the use of the *geometrical biasing* are implemented. The method itself and its use in OSIRIS will be explained in Section 6.5. While the *tuning* mode is used to find the best parameters for the algorithm, actual productions are done with the dedicated *bias simulation* mode. The output is defined to act as a possible input for the *BkgEdep* mode.

Some of the available modes, like the diagnosis modes, might only be useful in development and when the MC is tuned with calibration data, but other modes can easily be added for future studies.

6.3.2 Generators

In the context of simulations, physics generators typically simulate particles and processes in the surrounding that lead to the interactions of interest in the actual detector. Examples for this include, but are not limited to, neutrino interactions inside the LS or cosmic muon backgrounds. Often the details of those are complicated but not subject to the detector investigation, so that a complicated brute-force simulation is prone to error and not efficient. For neutrino interactions the extremely small cross-section makes a direct simulation especially inefficient. Instead, validated effective spectra of neutrino interactions are used in generators to determine the positions, directions, and energies of detectable particles, that stem from said interactions. Those events can then be placed in the detector through an interface (e.g. the *HepEvt* mode) and their rate can be scaled with the cross-section and flux.
A similar approach is used for the simulation of cosmic muons. Their creation in cosmic showers in the atmosphere can be simulated with dedicated frameworks and then propagated to the Earth's surface [30]. In another step, the propagation through the rock to the underground lab can be simulated with another package like `MUSIC` [131, 30]. The resulting spectra of angular- and energy distributions are used by the generator to generate arbitrary numbers of realistically distributed muon events at the detector very quickly. For the OSIRIS simulation, the muon generator of JUNO [30] was adapted and implemented by *Axel Müller*[3].

6.4 Optical model

Modeling the creation of light and the physical effects related to its propagation (see Sections 2.1 and 2.2) is done in the *optical model*. It is extremely important in the simulation of LS detectors, due to the significant influence on the event topology and thus the particle discrimination abilities. The optical model consists of several modules. Each simulate single physical effects. While many modules are already available in `Geant4`, some of them do not satisfy the need of the OSIRIS simulation and have to be re-implemented. In the context of light creation, the Cherenkov process is well described by `Geant4` and used out-of-the-box, but the scintillation needs a custom module. Similarly, for the light propagation the absorption with subsequent re-emission is implemented by the framework, while for refraction, Rayleigh scattering, and absorption the provided modules are used. Since OSIRIS is a monitor for the JUNO LS, its simulation has to be in sync with the JUNO *offline* software to use the same models and parameters.

Scintillation process The internal scintillation module of `Geant4` does not provide *quenching* and only the possibility of two time constants for the emission spectrum.

[3]Physikalisches Institut, Universität Tübingen

Therefore, a custom module was implemented to properly model the LS as JUNO does. It is important to note, that in the geometry only the bulk material of LAB is modeled, but not the molecules of the flour PPO or the wavelength-shifter bis-MSB. Nevertheless, their effect is modeled with an effective spectrum for emission through the scintillation process. Using former experience, the code is based on the scintillation process implemented in LENA [132], but further developed for OSIRIS. The general parameters are fully defined in the material definition and queried by the process. An overview is given in Tables 6.5 and 3.1 and the main components are the scintillation light yield of $\mathcal{L} = 11522$ photons per MeV and the use of three particle-dependent time constants $\tau_{p,i}$ with respective particle-dependent weights $w_{p,i}$.
Using those values, the scintillation process will be called for each tracking step of a charged particle in the LS. First, the total energy deposit of this step is calculated in order to compute the corresponding mean number of photons μ_{op}. If *quenching* is activated (see Section 2.1.1), the *visible energy deposit* is calculated via Equation (2.1). The quenching discriminates between three groups of particles: α-particles, protons and the group of electrons, positrons, and gammas. The actual number of photons N_{op} is then sampled from a Poisson distribution $P(\mu_{op})$ if $\mu_{op} < 10$ and otherwise from a normal distribution $N\left(\mu_{op}, \sqrt{\mu_{op}}\right)$. Under consideration of N_{op} and the *yield ratios* of the three components, the optical photons are placed on uniformly distributed points along the track of this step. They are assigned isotropic directions and random linear polarization and their energy is sampled from the effective emission spectrum taken from the JUNO software. Finally, the time of emission after the energy deposition is sampled according to Equation (2.2) under consideration of the time constants. In addition, the default `Geant4` scintillation module is also setup with proper values, but is only supposed to act as a backup solution.

Table 6.5 – General parameters of the LAB scintillator used in the simulation. For the wavelength-dependent properties, the value at 430 nm is quoted.

Description		Parameter	Value
Mass density		ρ_m	$0.86\,\mathrm{g/cm^3}$
Light yield		$\mathcal{L}$	$11522\,\mathrm{MeV^{-1}}$
Birks constant	$\gamma,\ e^+,\ e^-$	$k_{B,e}$	$1.306 \cdot 10^{-2}\,\mathrm{g/cm^2MeV}$
	Proton	$k_{B,p}$	$8.428 \cdot 10^{-3}\,\mathrm{g/cm^2MeV}$
	α	$k_{B,\alpha}$	$6.106 \cdot 10^{-3}\,\mathrm{g/cm^2MeV}$
Wavelength-dependent	Refractive index	n	1.495
	Rayleigh scat. length	l_r	30 m
	Absorption length	l_{abs}	85 m
	Re-emission probability	p_{rem}	0.30
Re-emission time constant		τ_{rem}	1.5 ns

Light propagation The physical processes of light propagation (as described in Section 2.2) and their wavelength dependencies are also in line with the JUNO *offline*. One special process in LS, that is not accounted for in `Geant4` by default is the absorption with subsequent re-emission. This mechanism was shown to be the main contribution for isotropic scattering in LAB [73]. It is implemented by the class `OSIRISOpAbsReemission`, which is combined with the general absorption and replaces that module. Thus, it is only called when a photon is actually absorbed, but gives it another chance to be re-emitted. As for the scintillation process, all properties are queried from the materials property table. If the material has a *reemission probability*, the decision to re-emit is diced accordingly. If successful, a new optical photon is created with an isotropic direction and random linear polarization in the same position. In order to ensure energy conservation, the emission spectrum is limited by the energy of the absorbed photon such that $\lambda_{out} \leq \lambda_{in}$ holds for the outgoing photon. The time difference between absorption and re-emission is then sampled from an exponential function with a time constant $\tau_{re} = 1.5\,\text{ns}$.

6.5 Geometrical biasing

In general, the simulation of backgrounds for detectors is often time consuming and highly inefficient. This is inherent to the nature of their design, that is optimized to shield sensitive areas from said backgrounds. Thus, the largest parts of those simulated events only interact in the regions that are not of interest for the user and absorbed or stopped before reaching the target. While this is the expected and needed behavior in the real application, studies need to quantify the residual background rate, that can overcome the shielding. For this purpose, *biasing* methods can be employed. While conventional simulations are based on *real* PDFs, biasing methods introduce artificial distributions to enhance the event rate in interesting regions. Thereby, the efficiency of the simulation is increased, but the use of modified PDFs distorts the physical meaning of those events. In order to reconstruct the physical distributions and their fluctuations from the biased simulation results, detailed bookkeeping about the modification is needed. Typically, this is achieved by adding weights to each biased event, representing its proportion to the real event rate. Simulation toolkits like `Geant4` provide different kinds of methods that can be categorized in two groups. *Geometrical/acceptance biasing* modifies the detector geometry or introduces modifications based on the particles position and direction. The second approach, *physical biasing* influences production rates through modified cross-sections and branching-ratios. In the case of OSIRIS, an application of geometrical biasing was implemented and will be presented in the following.
The ambient radioactivity in the underground lab, where OSIRIS is situated, is dominated by the gamma flux from the surrounding rock. Although the large water buffer reduces the incoming gamma flux by a factor of 10^8, it is still the largest contribution to the background, due to the huge mass and relatively high activity of rock. Using a low statistics spectrum and scaling it to the real flux will blow up its errors and might even not give the true spectrum in the case of zero-content bins. Thus, the simulation of a statistical relevant and continuous spectrum of external gammas reaching the LS is crucial for determining the experiment's sensitivity. At the same time it is computational

expensive due to the high inefficiency of conventional brute-force methods. In order to tackle this challenge, an application of *geometric importance sampling* was implemented in the simulation framework in the scope of this thesis. It utilizes methods and interfaces provided by `Geant4` for this purpose, that are explained and validated in Ref. [133].

6.5.1 Biasing model

The basic idea of this biasing model is to shift the distribution of simulated events towards those, that happen in the regions of interest. In the case of OSIRIS, the LS target is the sensitive area for detecting particles and by that, the region of interest. Thus, gammas that move towards that region should be sampled more often, while those that move away from the target are samples less often. This can be achieved by introducing a second, parallel geometry called the *ghost world*. It is a copy of the original geometry, but holds no material information at all. Instead, it is just used to record volumes and particle's transitions between them. The volume in which the biasing will be applied is then divided into a large number of *shells*, according to their geometry. While the general implementation is heavily based on the experiment at hand, it is in general favorable to design the shells equidistant to the region of interest. In the ideal case of a spherical detector, the shells would be concentric spheres with fixed distances Δr. Given the shape of the OSIRIS AV, concentric cylinders around the LS were chosen to divide the buffer volume into shells. An importance value I_n is assigned to each volume V_n, with the outermost volume being the least important and the LS the most important. Whenever a particle moves from one volume to another, it has the chance to either be *split* or *killed*. Going from V_a to V_b, the particle moves from a volume with I_a to one with I_b. In order to simplify the formalism, we define the importance ratio $r = {}^{I_b}/_{I_a}$ and resolve the following cases:

$r = 1$ Both shells have the same importance and the transport is continued as if there was no boundary.

$r < 1$ The particle moves away from the region of interest. *Russian roulette* is played where the particle is killed with the probability $p = 1 - r$. Thereby, no more resources are spent on tracking a particle that will probably not reach the region of interest.

$r > 1$ The particle moves towards the region of interest and will be split into N tracks with a probability p:

- If r is an *integer*, the track is split into $N = r$ tracks with $p = 1$.
- Otherwise, the track is either split into $N = int(r) + 1$ particles with $p = r - int(r)$,
- Or into $N = int(r)$ particles with the residual probability $p = 1 - (r - int(r))$.

This decision tree is easily understood with a descriptive example for moderate importance steps that result in $1 < r < 2$. In this case the particle is either split into two tracks with a probability $p = r - int(r)$, or no additional track is generated. Finally, all resulting

tracks get an updated weight $w' = {}^{w}/_{r}$ in order to conserve their physical meaning. It is important to note, that in the aforementioned example the result of *no splitting* is an outcome of the biasing and thus needs an updated weight, although no additional track was added. A visualization of the mechanism in OSIRIS and an exemplary splitting process is shown in Figure 6.5. The number of shells, that define the average path

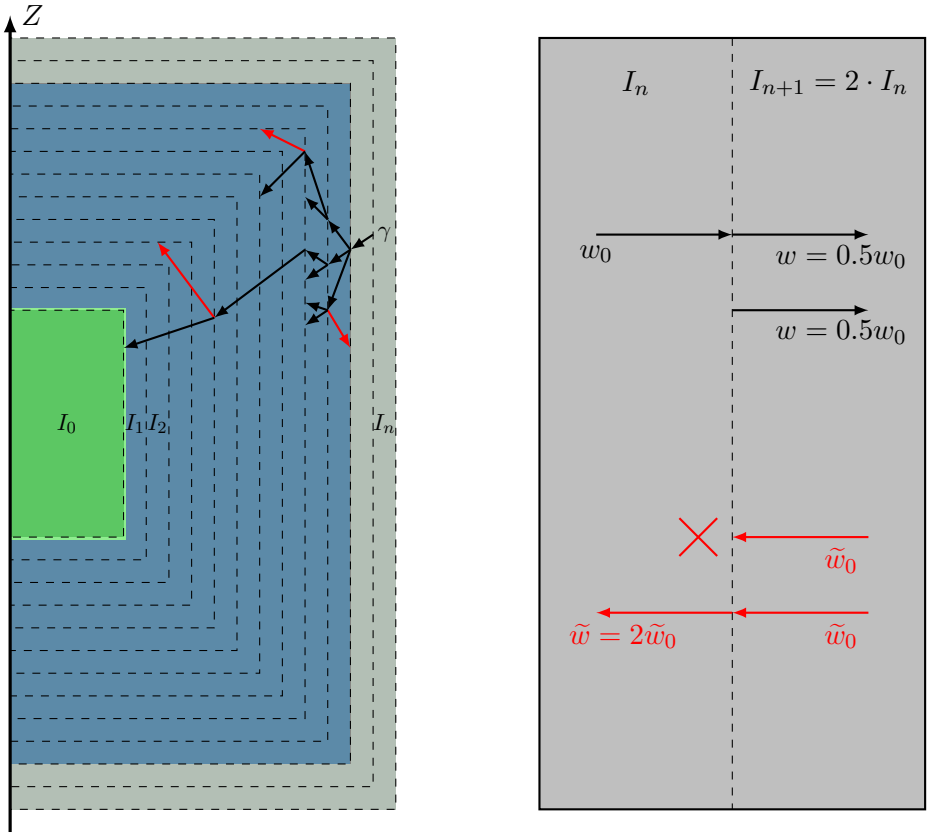

Figure 6.5 – *Left:* Principal visualization of the parallel geometry implemented in the detector simulation. The LS target is assigned the largest importance value $I_0 = \alpha^{N_s}$, while the outward going shells follow $I_i = \alpha^{N_s - i}$ for their importance value. An exemplary γ-track starting in the rock is shown. Black tracks move towards a higher importance shell, while red tracks enter a shell with lower importance. *Right:* Working principle of the splitting and killing of tracks in the biasing algorithm for an importance ratio $r = {}^{I_{n+1}}/_{I_n} = 2$.

between shells and the importance values are tuning parameters of the algorithm. They are not physical parameters, but need to be optimized to run the simulation efficiently. A typical starting point is a choice of shells so that the path between shells is similar to the mean free path of the biased particle and an importance ratio of 2. Nevertheless, the tuning is highly dependent on the scenario and can differ significantly from this basis. Similar to results achieved in Borexino [134, 135], the OSIRIS biasing uses a larger number of shells with an accordingly lower importance ratio. Details about the implementation of this model follow in the next subsection.

6.5.2 Implementation in OSIRIS

In OSIRIS the geometrical biasing is only used for the simulation of γs from external sources far from the LS, namely the *rock* and *steel tank*. The dedicated modes (see Section 6.3) implement the parallel geometry and the `Geant4` interface class `G4VSampler`. This allows easy setup of and access to classes that store the importance values of volumes and weights of tracked particles. In addition, a so called *particle filter* is introduced to ensure that only γs experience biasing, but not secondary particles. As the implementation of different modes suggests, a staged approach is utilized in OSIRIS:

1. In the first step the biasing parameters are tuned by simulation with the *BiasTune* mode and analysis of its output.

2. After optimized values for the number of shells N_s and their importance I_n, the simulation is run in the *BiasSim* mode with less diagnostics output. The output is a sample of γs that originated from the set volume and reached the edge of the LS. Their position, direction and energy are saved as well as their weight.

3. The full unbiased simulation of the previously produced sample is done via the *BkgEdep* mode.

Since the modes for tuning and simulation only differ in the form of their MC truth output and the initial direction of γs, they can be treated together in the following. The required tuning of the shell count and importance ratios is dependent on the energy of the tracked particles. One can either identify the most important peaks from the total γ-spectrum and simulate those mono-energetically or split the full spectrum into reasonable ranges and tune for those. In OSIRIS the choice was made for the second option. The energy spectra of ^{238}U and ^{232}Th are split into the ranges 0-1 Mev, 1-2 Mev, and 2-3 Mev to take the full spectrum into account without assumptions.
With the water shield being a homogenous medium, the choice was made to have a constant importance ratio α between neighboring shells. Thus, the importance is defined as $I_i = \alpha^{N_s - i}$, with N_s being the total number of shells and i the shell index counted from the inside towards the rock. In the process of tuning the two parameters N_s and α for each energy range, a strong correlation between the two parameters was found. Furthermore, already small variations in α could accommodate the energy dependency. For that reason, N_s was fixed to 400 shells and based on that only α tuned. The figure or merit to quantify the goodness of the tuning was defined as the ratio of γs that reached the LS to the total number of primary γs. The respective goal of the tuning is then to keep the density of γs more or less constant along the volumes towards the LS. If the importance values or the number of shells are too low, the particles are absorbed before splitting is possible and the simulation is still inefficient. On the other side, too high importance values or too many shells will lead to an exponential increase of particles to track. This can cause an endless simulation and a great amplification of the initial distribution's fluctuations. Those two examples of *bad* tuning are visualized in Figure 6.6. A good efficiency was reached when the number $n_{\gamma,LS}$ of γs that reached the LS, is approximately the same as the total number of primary γs $n_{\gamma,tot}$. Figure 6.7 shows an

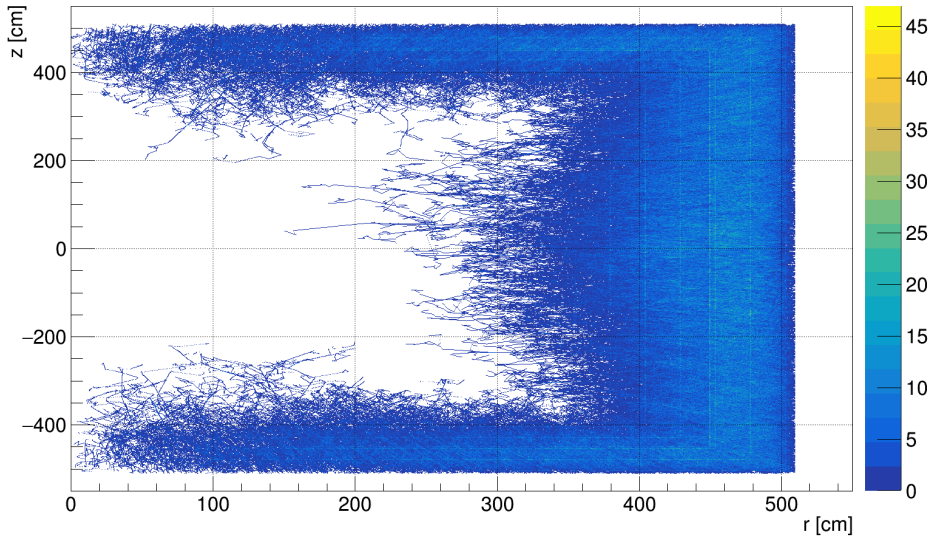

(a) $N_s = 800$ and $\alpha = 1.01$

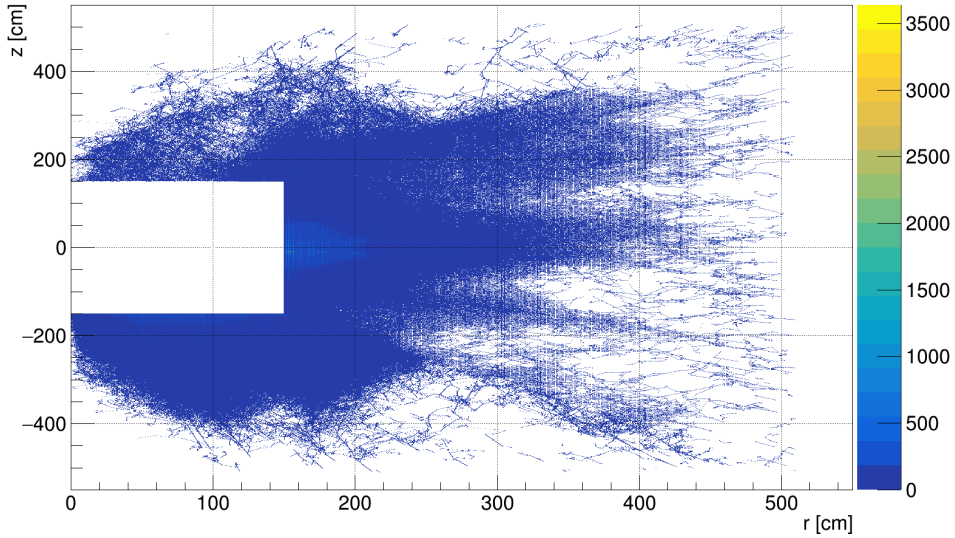

(b) $N_s = 400$ and $\alpha = 1.07$

Figure 6.6 – Visualization of the position of every step of a *gamma* in the *BiasTune* mode for two sets of bad tuning. Through correct tracking of the assigned weights, both results can still yield the proper physical distributions, but the algorithm lacks efficiency with those settings. If the importance is too low, as shown in the top panel, most γs still cannot reach the target and thus, there is no significant increase in efficiency compared to an unbiased simulation. The bottom plot shows an example of an exponential increase of tracks, because of a too large importance factor. Although it produces a great number of γs, that reach the LS, they stem only from a few primary vertexes. In order to sample the full initial distribution an unproportionally large number of particles have to be tracked and stored. This also reduces the efficiency of the simulation and can even lead to crashes for extremely large importance factors.

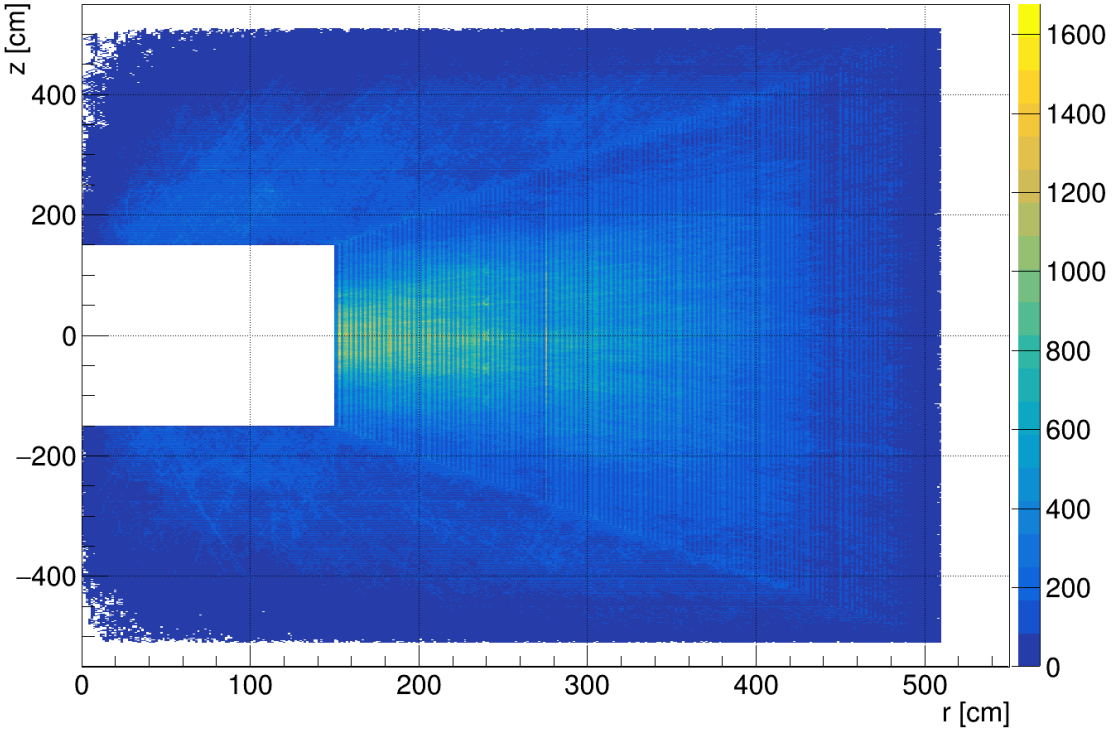

Figure 6.7 – Positions of all tracking steps of γ particles in the *BiasTune* mode with optimized parameters. The number of particles in the water volume is almost constant and the ratio of γs that reached the LS to the number of primary vertexes is ~ 1. Hence, the distribution of original positions and energies can be sampled efficiently while producing a similar number of particles in the region of interest. Nevertheless, the tuning of the parameters and their chosen values have no physical meaning or impact. They are set to maximize the efficiency of the simulation, but through bookkeeping of the assigned weights, the physical distributions can be recovered from any set of tuning parameters.

example of the resulting γ-density in the water volume. It is important to note, that in the tuning mode the primary particles were started with their direction pointing towards the detector. This removes the inefficiency that the detector only covers a small solid angle of particles emitted isotropically from the rock and speeds up the tuning process. In the simulation mode this option is deactivated, as this additional biasing would require adding another weight to the events. The full tuning results display values for α between 1.0333 and 1.0659 and are summarized in Table 6.6.

Since the detector is still in development, the simulation cannot be verified with data. Nevertheless, the method itself can be tested by comparison to the results from an unbiased, brute-force simulation. For this purpose, a very large sample of $2 \cdot 10^{11}$ primary γ events of the ^{232}Th spectrum were simulated in the rock volume with the *BkgEdep* mode. Only $\sim$2600 of those reached the LS at all and much fewer were detected in the inner region of the target. With an identical initial setup, 10^7 biased primary events

Table 6.6 – Optimized importance factors α used in the geometric biasing simulation. The corresponding number of shells N_s was set to 400 for all isotopes and ranges.

Isotope	Range [MeV]	Importance α rock	tank	PMT
^{40}K	mono	1.0500	1.0450	1.0318
^{232}Th	$0-1$	1.0643	1.0586	1.0436
	$1-2$	1.0479	1.0430	1.0304
	$2-3$	1.0372	1.0333	1.0232
^{238}U	$0-1$	1.0659	1.0602	1.0456
	$1-2$	1.0481	1.0434	1.0316
	$2-3$	1.0401	1.0359	1.0251

resulted in $\sim 3.5 \cdot 10^5$ γs, that deposited energy in the LS. Thus, the geometric biasing increased the simulation efficiency by a factor of more than 10^6. The validation, that the energy spectrum is properly reproduced is shown in Figure 6.8. With the red histogram retrieved from biased events and their weights, the shape of the unbiased simulation is perfectly reproduced. Additionally, the result from biasing yields a much smoother, high-statistics spectrum with significantly lower simulation time. It is also important to note, that the red histogram was scaled to the same number of initial events as the blue one and not the same total integral. This means, that both, the shape and rate are reproduced exactly as expected. The samples simulated with this method are the basis for the sensitivity study presented in Chapter 7.

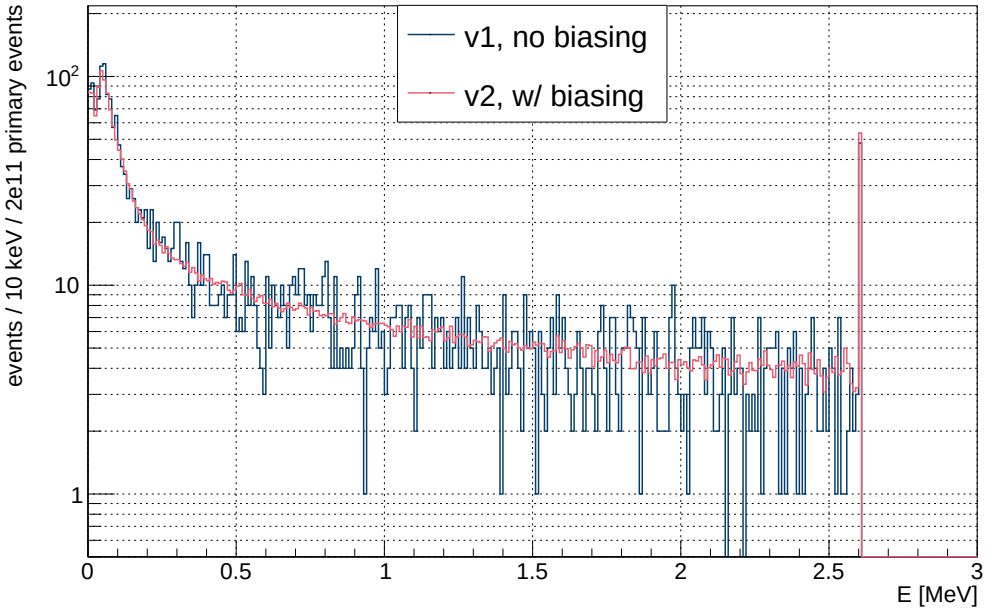

Figure 6.8 – Spectrum of γ events in the LS from ^{232}Th decays in the surrounding rock volume. The blue plot shows results from an unbiased simulation with $2 \cdot 10^{11}$ primary events. Of those, only $\sim$2600 events reached the LS, so that the spectrum shows large fluctuations and holes. The red spectrum was created with identical parameters, but using the geometric biasing method with 10^7 primary vertexes. It is scaled to the same number of primary events and is in full agreement with the unbiased spectrum.

Chapter 7

OSIRIS Sensitivity to U/Th-Contamination

This chapter presents how the sensitivity of OSIRIS to radioactive contamination of its LS is determined. The focus lays on a statistical analysis of the sensitivity to a Rn contamination, that stems from residual ^{238}U and ^{232}Th. It is based on the detector simulation presented in Chapter 6 and a subsequent post-processing of the data. Details on how this step is used to introduce effects from reconstruction to the data are given in Section 7.1. Following that, Section 7.2 explains the expected levels of radiopurity the study is based on and Section 7.3 discusses the applied cuts to select events stemming from the Bi-Po-coincidence. Finally, the statistical analysis and the achievable sensitivity is presented in Section 7.4.

7.1 Simulation and Reconstruction

The BiPo sensitivity is based on the `Geant4` simulation fully described in Chapter 6. Although it includes a full optical model and sensitive PMTs in its current state, this was still being validated when the sensitivity was estimated. In addition, a simulation of the electronics response and a subsequent waveform reconstruction are under development, but not yet available. This lead to the decision to use the `BkgEdep` mode instead of the full optical simulation. In this mode, the MC truth position and value of every energy deposition in the LS is stored to a file. All resolution effects due to e.g. photo coverage or reconstruction algorithms are then included in a post-processing step. This approach has the advantages that one can easily estimate the impact of different setups on the sensitivity without simulating new data samples.
The post-processing is done in several steps to properly model the effects introduces by reconstruction. The event position $\vec{r}_{evt}$ is computed as the energy-weighted barycenter $\vec{r}_{bar}$ of all corresponding energy depositions

$$\vec{r}_{bar} = \frac{\sum_i \epsilon_i \vec{r}_i}{\sum_i \epsilon_i}, \tag{7.1}$$

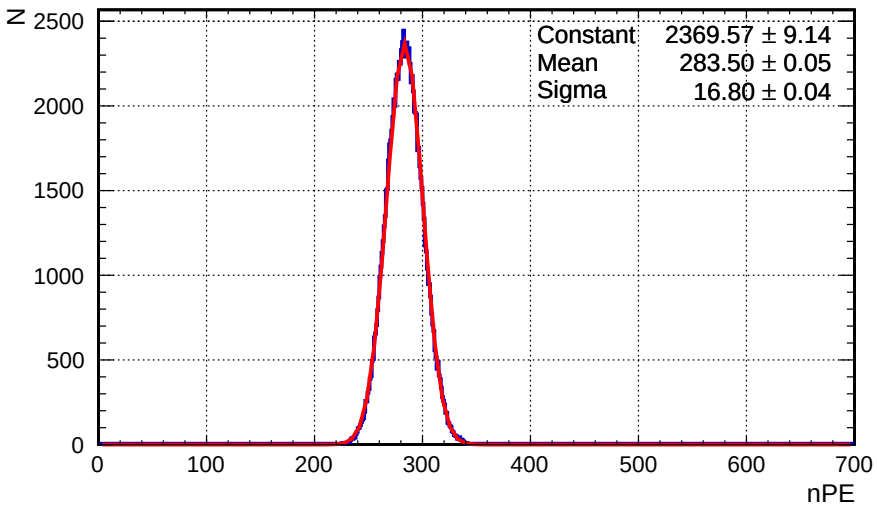

Figure 7.1 – Estimation of the baseline energy resolution $\sigma_{0,E}$ with 10^5 1 MeV electron events in the detector center. The driving effect on the resolution are photon-statistics.

with ϵ_i being the deposited energy of the i-th step at position $\vec{r}_i$. Accordingly, the event energy is defined as the sum of all energy depositions $E_{evt} = \sum_i \epsilon_i$. In the subsequent step, the true event position is smeared coordinate-wise in x, y, and z. A position-independent shift for each coordinate is sampled from a Gaussian distribution centered around zero with an energy-dependent standard deviation of

$$\sigma = \frac{\sigma_0}{\sqrt{E_{evt}/1\,\mathrm{MeV}}}. \tag{7.2}$$

Here, E_{evt} is the true energy and σ_0 was chosen to be 14 cm based on a scaling from established experiments [79] and the expected photon statistics. Thus, the resulting three-dimensional position smearing amounts to ∼24 cm.
In a similar fashion, the true energy is also smeared using Equation (7.2) with a baseline resolution of $\sigma_{0,E}$ that corresponds to a relative resolution of ∼6% at 1 MeV. This was estimated with help of the detector simulation. A sample of 10^5 electron events with $E_{evt} = 1\,\mathrm{MeV}$ in the detector center was simulated and the detected number of photo electrons is shown in Figure 7.1. Based on the assumption, that the dominating effect is the photon statistics, the relative energy resolution is determined via

$$\frac{\sigma_E}{E_{evt}} = \frac{\sqrt{nPE}}{nPE} = \frac{1}{\sqrt{nPE}}. \tag{7.3}$$

For the value of $283\,\mathrm{pe/MeV}$, the baseline resolution is set to $\sigma_{0,E} = 1/\sqrt{283} \cdot E_{evt} \approx 6\% \cdot E_{evt}$.

7.2 Radiopurity Assumptions

OSIRIS's mission is to measure residual radioactivity in the LS after its purification and to detect a re-contamination by Rn from possible air leaks in the filling system. The small expected contamination *signal* is not isolated, but has to be detected in the presence of background events induced by other radioactivity. Those decays are visible in the detector as single events in the same energy range as the signal events. As discussed in Section 4.1.2, also the coincidence signal of Bi-Po decays can be mimiced by two unrelated single events. This accidental background depends on the rate of singles and the coincidence time.

The radioactive decays from all detector volumes, that are not the LS are called *external* background. For this, the isotopes under consideration are ^{40}K and the decay chains of ^{238}U and ^{232}Th. Taking their range into account, α and β-decays are not simulated in external volumes, as they cannot penetrate the AV to reach the LS. Thus, only the γ spectra of ^{40}K and the two decay chains are taken into account for all volumes except for the AV. Since the acrylic comes into direct contact with the LS, it is mandatory to take all decays along the chains into account for this volume.

The spectrum for ^{40}K consists of a single 1.46 MeV γ-ray that accompanies its *electron capture* decay with a *branching ratio* (BR) of 10.72% [124]. The primary β^--decay to ^{40}Ca with a BR of 89.28% does not emit a gamma. For ^{232}Th and ^{238}U, all daughter nuclides of their chains are sources of γ-background. Under the assumption of secular equilibrium, only gamma emissions above 250 keV are taken into account. Thus, the four isotopes ^{228}Ac, ^{212}Pb, ^{212}Bi, and ^{208}Tl contribute from the ^{232}Th chains. Accordingly, the background considered from the ^{238}U chain consists of the three isotopes ^{234}Pa, ^{214}Pb, and ^{214}Bi [136]. The input spectra used in the simulation can be found in Appendix A.

The *internal* background on the other hand, is caused by residual radioactivity in the LS itself. Therefore, all decays of the two chains have to be considered, as they will deposit visible energy. In addition, the naturally abundant ^{14}C as well as the cosmogenic ^{10}C and ^{11}C have to be accounted for in this case.

The simulation framework is used to simulate a certain number of events which is needed to create a spectrum of each background source with sufficient statistics. Those event numbers have then to be translated into single event *rates* with the assumption of radiopurity levels and masses for the used materials. The contamination levels refer to the amount of ^{40}K, ^{238}U, and ^{232}Th in the materials. In order to properly estimate the decays of all isotopes along the chains, secular equilibrium is assumed and all branching ratios are taken into account. For the acrylic and stainless steel structures, the collaboration's requirements are assumed[1]. The values for the surrounding rock and the PMT glass are taken from an JUNO-internal database [137] and based on dedicated measurements of recent material samples. Finally, the assumptions regarding the water shield are based on the water purification system used for the Borexino CTF [138]. All values and the corresponding rates inside the LS volumes are summarized in Table 7.1. The internal contamination is based on the *JUNO solar* requirement of 10^{-16}g/g for ^{238}U and ^{232}Th

[1]Not yet published, taken from: J. Zhao, "Requirement to CD radioactive background." Dec. 2017, available at JUNO DocDB-3057v1 (password protected)

Table 7.1 – Assumed contamination of the materials used for the AV, the stainless steel frame, the water shield, the carbon steel tank, and the surrounding rock as well as the PMT glass. All values are based on sample measurements done in the JUNO collaboration [137] or their requirements, except for the ultra-pure water, which is based on Ref. [138]. The total γ production rates were calculated under assumption of secular equilibrium and based on the input spectra described in the text. The total mass and the resulting rate in the LS are determined with the detector simulation (see Chapter 6).

Component	Contamination [Bq/kg]			Total mass	Gammas	Rate in LS
	^{40}K	^{232}Th	^{238}U	[kg]	[s^{-1}]	[s^{-1}]
AV	2.70×10^{-4}	4×10^{-6}	1.2×10^{-5}	1.53×10^{3}	0.12	7.4×10^{-2}
Shield	1.60×10^{-6}	3×10^{-7}	3.0×10^{-7}	5.41×10^{5}	1.23	8.4×10^{-3}
PMT glass	1.89	1.72	4.77	6.00×10^{2}	1.28×10^{4}	1.5
Frame	1.34×10^{-2}	8×10^{-3}	1.2×10^{-3}	2.20×10^{3}	82	9.0×10^{-4}
Tank	2.60×10^{-1}	4×10^{-2}	7.0×10^{-2}	1.20×10^{4}	444	3.7×10^{-5}
Rock	220	123	142	6.18×10^{5}	5.82×10^{8}	4.5
Total	–	–	–	–	–	6.15

and less than 10^{-17}g/g for ^{40}K (see Section 4.2.2). Studies in Borexino have shown that not all isotopes in the LS are in secular equilibrium [79]. Therefore, the assumptions for ^{210}Bi, ^{210}Po of the ^{238}U chain and ^{85}Kr were artificially increased in the study. Since the general contamination levels of the JUNO LS are expected to be a factor 10 higher than in Borexino, the same factor was applied to the values from Ref. [79] for the activity of the three isotopes. Considering the carbon isotopes, the abundancies of cosmogenic ^{10}C and ^{11}C are based on the production rates from Ref. [30]. For ^{14}C a contamination of 3.710^{-3} Bq/kg is assumed [30]. This corresponds to a ^{14}C/^{12}C-ratio of 10^{-17} and is in agreement with the assumption of 10 times the value from Borexino [79]. All used values and the resulting rates in the LS are given in Table 7.2. For the spectra of the internal background all 31 relevant isotopes were simulated with 10^7 events each. As explained above, also for the AV all decays along the U- and Th-chain have to be simulated. Thus, the AV sample consists of 27 relevant isotopes, each simulated with 10^8 primary events to account for those that will not reach the LS due to the isotropic directions. For all other external background volumes, only γs from the spectra of the U- and Th-chains and ^{40}K were sampled. The number of simulated primary events depends on the thickness of shielding, that has be crossed and thus, on the volume's distance to the LS. For the PMT glass, its support frame and the water shield itself 10^9 events per spectrum were simulated each. The outermost volumes required simulation using the biasing method presented in Section 6.5. With 3×10^9 biased events per chain and for ^{40}K, an equivalent of 10^{16} primary events were simulated for the tank and rock volumes each.

Table 7.2 – Assumptions of the most significant internal LS rates from radioactive and cosmogenic isotopes. The production rates of ^{10}C and ^{11}C, and the concentration of ^{14}C, ^{40}K, ^{232}Th, and ^{238}U are taken from Ref. [30]. While the decay chains were assumed to be in secular equilibrium for the largest part, the rates for ^{85}Kr, ^{210}Bi and ^{210}Po are increased by a factor of ten in regard to the values that were reported by Borexino [79].

Isotope / Chain	Contamination	Rate in LS [s^{-1}]
^{10}C	0.035 [cpd/t]	7.4×10^{-6}
^{11}C	1.9 [cpd/t]	4.0×10^{-4}
^{14}C	$^{14}C/^{12}C = 1 \times 10^{-17}$	29.6
^{40}K	1×10^{-17} g/g	4.7×10^{-5}
^{232}Th	1×10^{-16} g/g	7.4×10^{-6}
^{238}U	1×10^{-16} g/g	2.3×10^{-5}
^{85}Kr	3.12 [cpd/t]	6.6×10^{-4}
^{210}Bi	4.1 [cpd/t]	8.7×10^{-4}
^{210}Po	8×10^{2} [cpd/t]	1.7×10^{-1}
Total (w/o ^{14}C)	–	0.17

The resulting background spectra are shown in Figures 7.2 and 7.3. While Figure 7.2 gives a detailed picture of the internal background with the contributions from the out-of-equilibrium isotopes, Figure 7.3 shows how the internal and external background contribute to the total spectrum.

Apart from the contamination with naturally abundant radioisotopes, that is inherent to the materials and their production, further radioactive isotopes can be introduced in some materials of the detector. One significant background source can stem from *radon emanation* into the water shield. The ^{220}Rn from the ^{232}Th chain, as well as ^{222}Rn from the ^{238}U chain can emanate from all surrounding materials and volumes into the water. Under the assumption of some convection, the isotopes could then move with the water closer to the vessel and thus, the LS is less effectively shielded from the high energy gammas of their progeny. In OSIRIS, the inner side walls of the tank and its bottom and top lid will be covered by an HDPE liner, which largely prevents contamination of the water by the steel tank. In addition, the stainless steel frame, that supports the PMT array is in direct contact with the water as well as the nitrogen blanket at the top of the tank. Taking the material contamination and their contact surface with the water into account, the radon emanation can be estimated to a rate of 550 $^{\mathrm{mBq}}/_{\mathrm{m}^3}$ for ^{222}Rn and about 3.9 $^{\mathrm{mBq}}/_{\mathrm{m}^3}$ for ^{220}Rn [139]. In order to estimate the effect of this Radon contamination on the sensitivity of OSIRIS to Bi-Po-coincidences, the background spectra of the shield were extended by ^{220}Rn and ^{222}Rn. Since both elements appear in

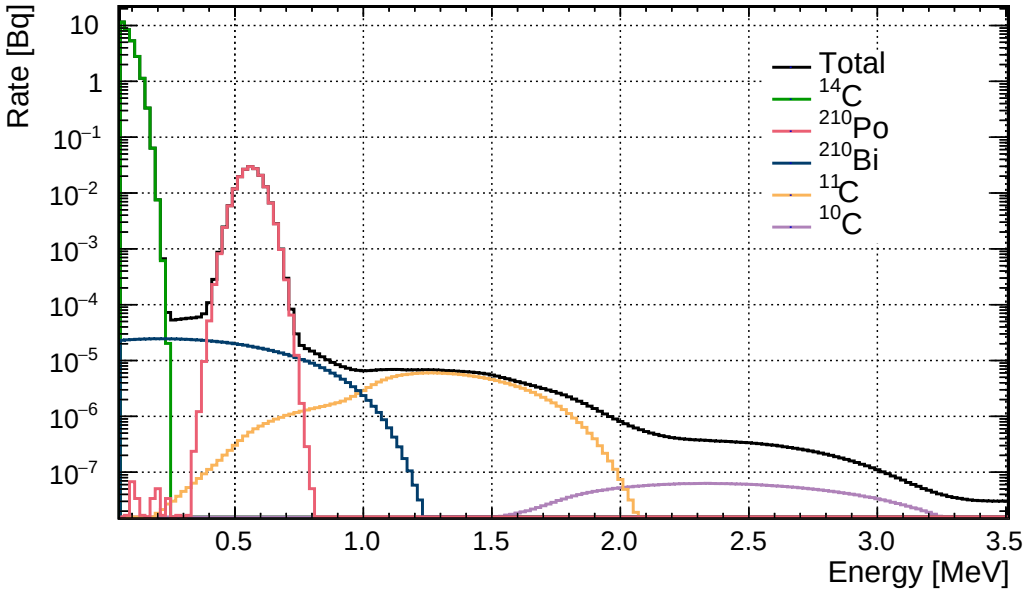

Figure 7.2 – Energy spectrum of the internal background rate expected in the full LS volume. Only the contributions that define the shape are overlayed to show their influence in the different energy regions. All internal isotopes were simulated with 10^7 events each and smeared with the baseline energy resolution of 6%.

the decay chains, that were already considered, their γ-spectra are sub-spectra of the ones used for the equilibrium states of ^{232}Th and ^{238}U. The input γ-spectra are shown in Appendix A. Assuming conservatively a uniform distribution of both elements in the water, gammas from their decay chains were simulated in the full shield volume and tracked to the LS. In the same fashion as for the other background sources, the spectra were scaled to the singles rate by using the mass of the corresponding volume and the specific activity. The maximum influence on the sensitivity was studied by using the worst case contamination of 550 $^{\mathrm{mBq}/\mathrm{m}^3}$ for ^{222}Rn and 3.9 $^{\mathrm{mBq}/\mathrm{m}^3}$ for ^{220}Rn.

The resulting rates in the LS are presented in Table 7.3 and show that ^{222}Rn has to be considered a significant background source together with the rock and the PMT glass, while ^{220}Rn lays way below the dominant sources. Figure 7.4 visualizes the impact of the additional radon on the energy spectrum. While the general shape is still dominated by ^{232}Th from the rock, the peaks at 1 MeV and 1.6 MeV of the ^{222}Rn chain are visible in the total spectrum. The ^{208}Tl peak around 2.5 MeV is not heavily pronounced, due to the low rate of ^{220}Rn, which is the result of its short half-life.

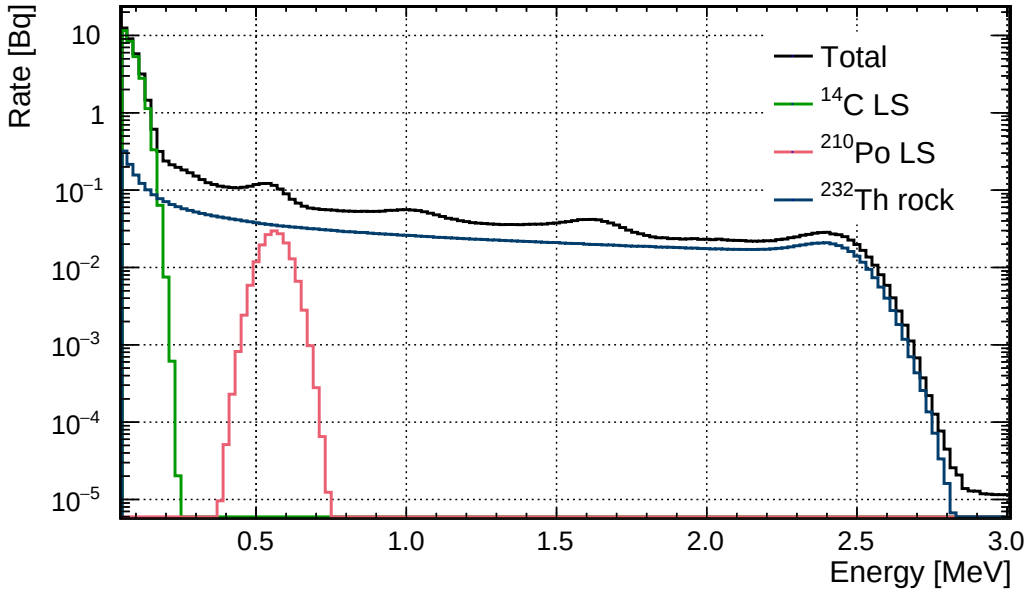

Figure 7.3 – Energy spectrum of the total background rate expected in the full LS volume. Similarly to Figure 7.2, the significant contributions are overlayed. Details about the number of simulated events with the biasing method can be found in the text. The true energy depositions were smeared with 6% according to Equation (7.3). While the γ background from the decays along the ^{232}Th chain in the rock are defining the overall shape, the peaks of ^{210}Po and ^{14}C are clearly visible in their energy regions.

Table 7.3 – Singles rates in the LS caused by additional contamination of the water shield by Radon in comparison with the main contributions from the regular external background presented in Table 7.1. While the rate from ^{220}Rn is two order of magnitude lower than the dominating ^{232}Th from the rock, the ^{222}Rn decays produce a considerable rate of singles in the LS on a similar level.

Component	Isotope	Contamination [Bg/kg]	Rate in LS [s^{-1}]
Water shield	^{220}Rn	3.9×10^{-6}	4.9×10^{-2}
	^{222}Rn	5.5×10^{-4}	3.4
Rock	^{40}K	220	1.5×10^{-2}
	^{232}Th	123	4.2
	^{238}U	142	3.3×10^{-1}
PMT glass	^{40}K	1.89	2.0×10^{-2}
	^{232}Th	1.72	9.0×10^{-1}
	^{238}U	4.77	6.1×10^{-1}

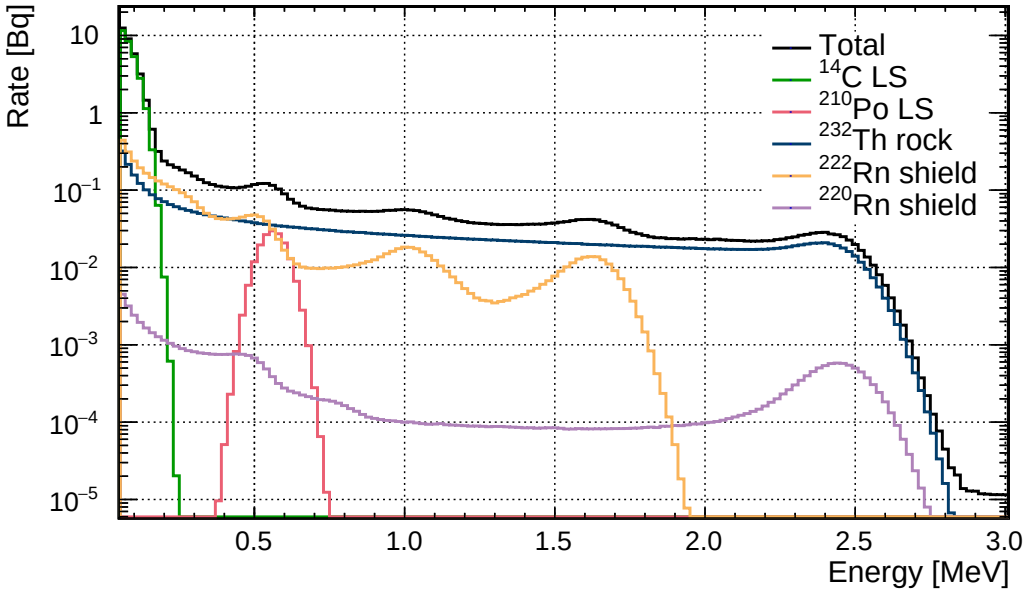

Figure 7.4 – Energy spectrum of the total background rate expected in the full LS volume including Radon contamination of ther water shield. Similarly to Figure 7.3, the significant contributions are overlayed. While the γ background from the decays along the ^{220}Rn chain in the water are always one to two order of magnitude below the dominant ^{232}Th background from the rock, the peaks of the ^{222}Rn spectrum are at a comparable level. The total influence can be seen as slightly increased total singles rate and additional peaks around 1 MeV and 1.6 MeV.

7.3 Event Selection

Similar to the identification of IBD events in JUNO, the Bi-Po-coincidence identification in OSIRIS is based on a sequence of cuts. Selecting Bi- and Po-candidates according to their energy and correlating both in space and time can increase the sensitivity, due to an improved signal-to-background ratio. Since the infrastructure and event reconstruction are still in development, the analysis is not done on event-by-event basis, but with statistical considerations. Nevertheless, the efficiencies of all cuts are computed with the simulated position and energy distributions of all background event rates. In the following, the cuts are presented and explained in the order in which they are applied to the background spectra to determine the residual background event rate.

Fiducial volume (FV) cut All external γs, that reach the LS have to overcome a certain amount of shielding, but in order to reach far into the LS, they have to penetrate even more material. Due to that, the event rate close to the AV edge is significantly higher than in the central part of the target. This is also visualized in Figure 7.5, which shows the total external background event rate in the LS. The total event rate including the uniformly distributed internal background from ^{14}C and ^{210}Po is shown in Figure 7.6. Its high rate, which is independent of the position, smears out the features of the external rate distribution. A cylindrical cut around the center of the LS can reduce the number of accidental coincidences. Thus, events with a reconstructed position below a given distance to the AV surface are excluded from the coincidence selection. Gammas with a higher energy can penetrate deeper into the LS. Therefore, the energy spectrum of the remaining single background events is dependent on the FV cut and in reverse, also the rejection efficiency depends on the energy. In order to estimate its impact, the cut is applied on all events prior to building their energy spectra and scaling them to event rates.

Energy cuts The beta decays of Bi feature a broad energy spectrum with endpoints around 2.3 MeV and 3.5 MeV for ^{212}Bi and ^{214}Bi, respectively (see Section 6.1.1). In contrast to that, the Po-decay emits mono-energetic α particles. Although they have a large Q-value, their energy is quenched in the LS to about one tenth of this amount. Thus, the Po is visible as a sharp peak broadened by the detectors energy resolution. Figure 7.7 shows the spectra of the decays for the Bi-Po-coincidences of both chains and the optimal energy windows for the selection. The noticeable large range of accepted energies will be explained in the following section. While the plot shows the spectrum for no FV cut, in general the selection efficiencies are computed with respect to the preceding FV cut. This is due to the fact, that the gammas with a higher energy can penetrate further into the inner volume of the LS. Thus, the spectra of energy depositions of all backgrounds change slightly for different FV cuts.

Delay time cut Given the lifetimes of 431 ns and 237 μs for ^{212}Po and ^{214}Po respectively [124], their decays happen quickly after the Bi-decay. This yields a large rejection power against accidental coincidences by accepting only Po candidates with a delay Δt

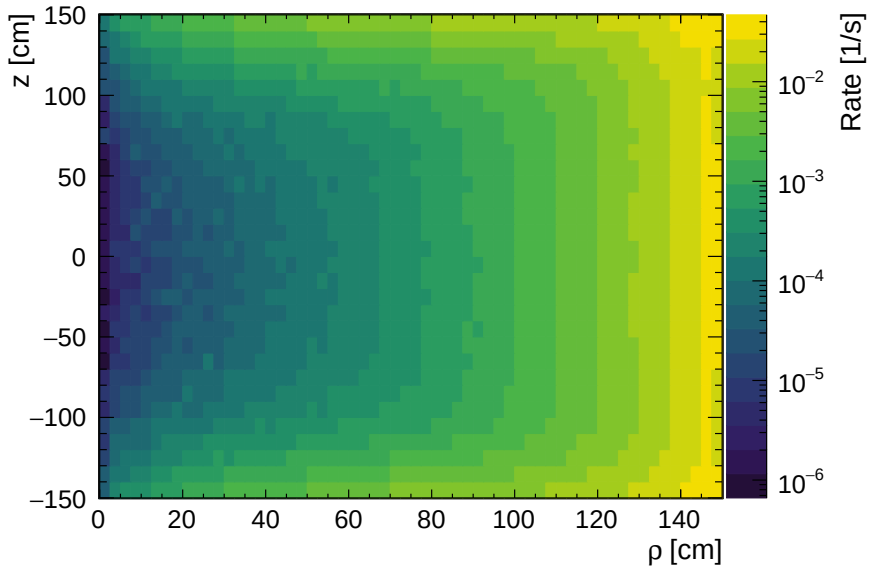

Figure 7.5 – Distribution of single event rates in the full LS volume from external background sources. The vessel is centered at $\rho = 0$ and $z = 0$ and extends to $\rho = 150\,\text{cm}$ and $z = -150...150\,\text{cm}$. Details about the rates are given in Table 7.1. The rate decreases over several orders of magnitude from the AV edge towards the center, giving rise to the application of a fiducial volume cut.

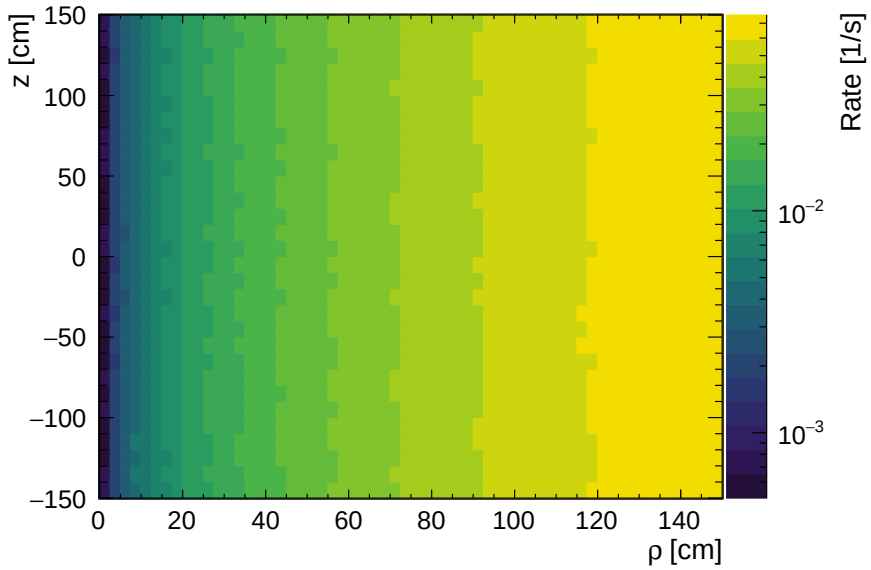

Figure 7.6 – Distribution of single event rates in the full LS volume from intern background sources. The vessel is centered at $\rho = 0$ and $z = 0$ and extends to $\rho = 150\,\text{cm}$ and $z = -150...150\,\text{cm}$. Details about the rates are given in Table 7.1. The rate is uniform over the volume and dominated by ^{14}C and ^{210}Po.

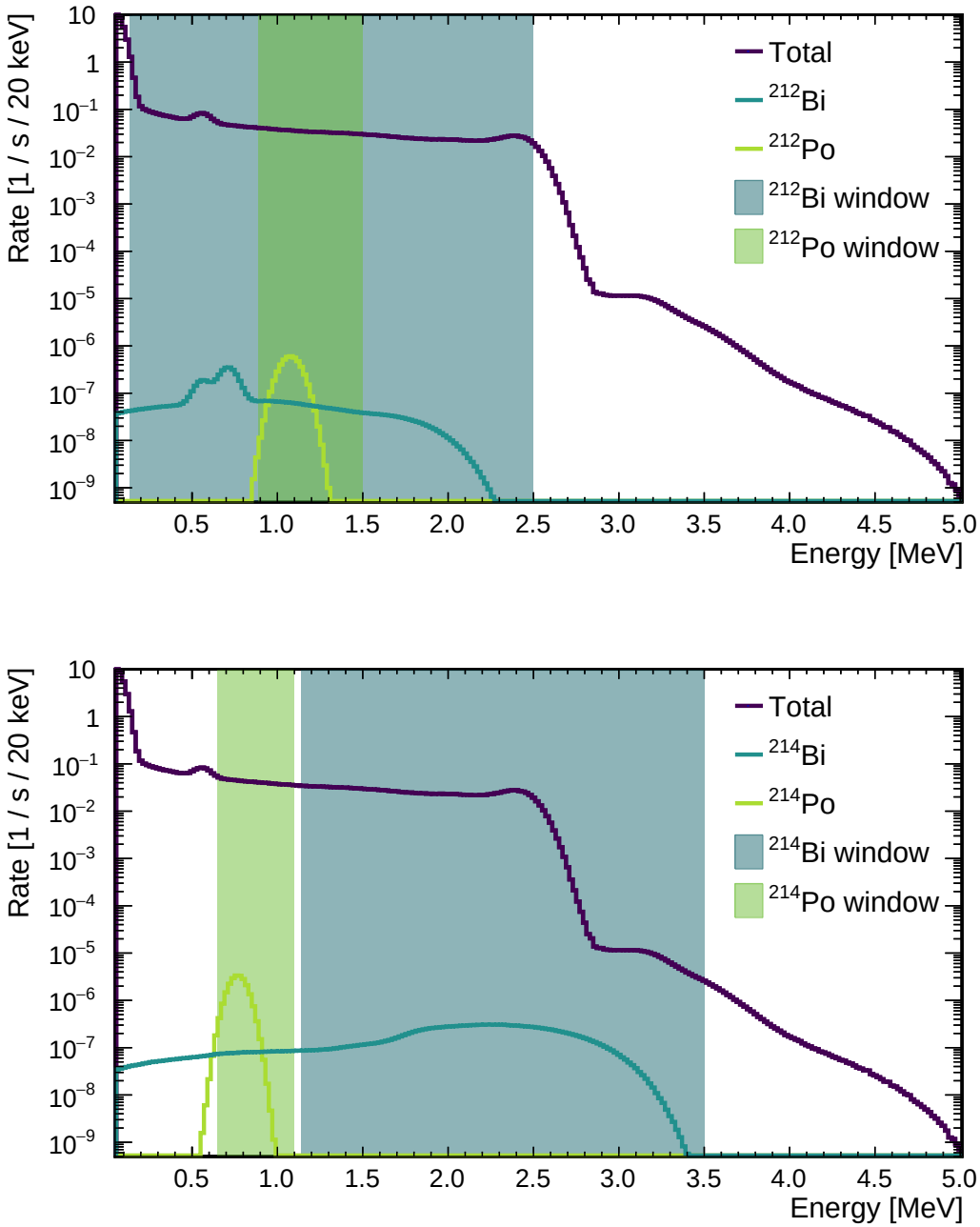

Figure 7.7 – Energy spectra of the ^{212}Bi-^{212}Po (*top*) and ^{214}Bi-^{214}Po (*bottom*) decays in comparison to the total singles rate. The optimized energy cut windows are drawn in green for the α decay of Po and in blue for the β spectrum of Bi.

and a certain time window after the Bi event. With regard to the readout electronics, it is important to note the very fast ^{212}Po decay is on the level of a single readout window. Although the electronics are designed to be deadtime-less, the study assumes a minimum of 200 ns between two events to separate and reconstruct them properly. Thus, the lower end of the energy window Δt_{low} cannot be smaller than 200 ns. After choosing the upper end of the time window Δt_{up}, the selection efficiencies are calculated analytically from the *probability density function* (PDF) of the respective Po decay. The development of sophisticated algorithms that can separate two clustered events in one readout window could push the limit Δt_{low} further down and increase the selection efficiency for ^{212}Po. Furthermore, the estimated 200 ns to separate clusters is based on studies done in the JUNO CD and mainly driven by the photons time of flight. Given the much smaller OSIRIS detector and thus, shorter travel times of the photons, a decrease of this time is likely.

Distance cut Due to the kinematics that follow from the large mass of Bi and Po and the short time between their decays, real Bi-Po events occur at practically the same position. Accordingly, a distance cut is introduced for the event selection, that only considers Po candidates with $\Delta r = |\vec{r}_{Bi} - \vec{r}_{Po}| < r_{cut}$. The perceived distance between real events emerges mostly due to the imperfect resolution of the position reconstruction. Thus, the selection efficiency $\epsilon_{\Delta r}$ can easily be estimated with help of a toy MC. Two events at the same initial position with energies corresponding to the respective Bi and Po decays are smeared with a σ according to Equation (7.2). Events with a distance $\Delta r < r_{cut}$ are counted towards the selection efficiency. The background rejection efficiency $\epsilon'_{\Delta r}$ is computed with a more detailed toy MC: first, Bi-candidates according to the FV and energy cut are sampled from the full single event energy and position distribution. Then, a second event is randomly sampled from the same distribution with regard to the Po energy window. The distance between both events is calculated and it is evaluated whether or not the two unrelated events survived the distance cut.

The process to find the optimal set of correlated cuts is presented in Section 7.4, followed by the resulting values and efficiencies with and without additional Radon contamination in the water in Tables 7.4 and 7.5, respectively.

7.4 Results

The sensitivity of OSIRIS to a Rn contamination in the LS is defined as the rate of Bi decays for which the selected Bi-Po-coincidence events N_{BiPo} exceed a background fluctuation from accidental coincidences N_{BG} on a 90% *confidence level* (CL) within the measurement time T. This seemingly low value is typically used in the context of live monitoring, where a false positive is more acceptable than triggering an alarm too late. In the case of high count rates, this can be expressed via Gaussian distribution like

$$N_{BiPo}(T) \leq 1.645 \cdot \sqrt{N_{BG}(T)}. \tag{7.4}$$

In the case of application in OSIRIS, the low contamination requirement of 10^{-16}g/g for U and Th has to be taken into account. It translates into a Bi-Po-signal rate in the order of 10^{-9}Bq/kg, which yields only $\sim$2 *counts per day* (cpd) of Bi-Po-events in the total volume of 19 tons LS. Considering a reduction of volume by the FV cut and a not perfect selection efficiency, the expected count rate approaches less than one count in the baseline measurement time of 24 h.
The classical calculation of a sensitivity or upper limit collapses in the case of a *null result*. Nevertheless, a meaningful sensitivity can be formulated by using well-established *Feldman-Cousins limits*. In 1997 *G. Feldman* and *R. Cousins* introduced a method to construct confidence intervals with an ordering principle that is based on likelihood ratios [140]. It unifies the treatment of upper limits and two-sided confidence intervals and is heavily used by experiments in the neutrino field, that expect no or only a very small signal like $0\nu\beta\beta$ searches [141].
Based on the original publication, one can define the function $\mathcal{U}(n|b)$ that gives the upper limit using the unified approach for observing n events and a mean predicted background b of a given CL. This function is implemented in several libraries for statistical analysis like for example the class `TFeldmanCousins` in `ROOT`. Following Ref. [141], the sensitivity $\mathcal{S}(b)$ of an experiment expecting b background events can then be calculated by averaging the upper limits from $\mathcal{U}(n|b)$ with their Poisson distributed probability of n observations like

$$\mathcal{S}(b) = \sum_{n=0}^{\infty} \mathcal{P}(n|b)\mathcal{U}(n|b). \tag{7.5}$$

The returned value for $\mathcal{S}(b)$ gives the number of counts that need to be observed in order to reach the desired CL.
The first step of the sensitivity analysis for OSIRIS is to define a full set of cuts and estimate their efficiencies as discussed in Section 7.3. After selecting only events in the FV, the single event rates $R_{BG,i}$ in the energy ranges for Bi and Po are extracted from the full background spectrum. In addition, the selection efficiency for real Bi and Po events are determined by integration over the individual spectra of the isotopes. The background rate amounts to

$$R_{BG} = R_{BG,Bi} \cdot R_{BG,Po} \cdot \Delta T \cdot (1 - \epsilon'_{\Delta r}), \tag{7.6}$$

with $\Delta T = \Delta t_{up} - \Delta t_{low}$ being the coincidence time window and $\epsilon'_{\Delta r}$ the rejection efficiency of the distance cut. Given the baseline measurement time $T = 24$ h, the total expected number of background events is estimated in cpd:

$$N_{BG}(T) = R_{BG} \cdot T. \tag{7.7}$$

If this value is larger than 100 cpd, the limit $N_l = 1.645 \cdot \sqrt{N_{BG}(24\,\mathrm{h})}$ is calculated in the classical way using Equation (7.4). Otherwise, Equation (7.5) is employed to yield an upper limit $N_l = \mathcal{S}(N_{BG}(24\,\mathrm{h}))$ of required counts per day to exclude a statistical fluctuation at a certain CL. Finally, the counts have to be set in relation with the chosen

fiducial mass m_{FV} to retrieve a rate limit and all cut efficiencies have to be accounted for

$$R_{Bi} = \frac{N_l}{m_{FV} \cdot \epsilon_{tot}}. \tag{7.8}$$

Here, ϵ_{tot} is the total selection efficiency, calculated from the correlated single-cut efficiencies ϵ_{Bi}, ϵ_{Po}, $\epsilon_{\Delta t}$, and $\epsilon_{\Delta r}$ (see Table 7.4). The detectable activity limit in $^{Bq}/_{kg}$ can then be translated into a mass limit for ^{238}U and ^{232}Th.

The application of four consecutive cuts with each at least one or more parameters results in a large and multi-dimensional parameter space for cut optimization. The needed CPU time for calculating the Feldman-Cousins limits and cut efficiencies renders a full and detailed sampling of the parameter space not feasible. Instead, a simple yet effective *grid search* algorithm was used to find the set of cuts that yields the best sensitivity. It was developed in the collaboration [142] and features a grid point cache to reduce multiple calculations of the same point. Starting at a given point in a defined grid through the parameter space, the algorithm calculates the sensitivity for all directly neighboring points. It will then move towards the best found value and start a new iteration. If no improvement can be achieved by moving to a neighboring grid point, because the current point has the minimal value, the grid size refined and the process repeated. The search goes on until a pre-defined minimal grid step size is reached for all parameters. When a candidate for the final minimum is found, one more iteration is run with the original grid size. By that, the algorithm tries to ensure that it in fact found the global minimum instead of being trapped in a local minimum. After termination, the user is able to retrace the path along the grid and verify its validity.
In the case of this study, the outermost grid was defined by reasonable assumptions for the different cuts: The FV can run from a "no cut" setting to $r < 75\,\text{cm}$ and $|z| < 75\,\text{cm}$, while keeping the volume symmetric in r and z around the center. Due to the detector's symmetry, there is no reason to assume an asymmetric FV and thus the dimension of the parameter space can be reduced from two to one for this cut.
For the energy windows, the low expected signal rate is taken into account by allowing very relaxed cuts. Given the dominant ^{210}Po peak in the lower energy range, the lower end of the Po-selection window $E_{Po,min}$ is left to float, while the upper end is fixed to the endpoint of the expected energy spectrum. Thus, the algorithm may take only a part of the respective Po-peak in order to avoid the high accidental background rate caused by ^{210}Po. For the selection of Bi candidates the upper end of the energy window $E_{Bi,max}$ is fixed to the endpoint of its respective spectrum. Hence, the cut is reduced from four parameters to only the lower limits of the Bi and Po energy windows $E_{Bi,min}$ and $E_{Po,min}$.
The distance cut is one dimensional by definition and is allowed to float between 40 cm and 150 cm, considering the reconstruction resolution and detector size.
Finally, the delay time cut is treated differently for the two decay chains. The selection of ^{212}Po is already inefficient because of the assumed minimal delay time $\Delta t_{low} = 200\,\text{ns}$. For that reason, the value is fixed and the upper time limit Δt_{up} is also fixed to maximize the selection of the remaining signal. In the case of ^{214}Po, the decay time is much longer,

Table 7.4 – Cut values and resulting efficiencies for the Bi-Po event selection. Details about all cuts are given in Section 7.3. The energy and distance cuts are correlated with the fiducial volume and thus optimized with respect to the preceding FV cut. Accordingly, the efficiencies are also quoted with regard to the preceding cuts.

		^{212}Bi-^{212}Po			^{214}Bi-^{214}Po		
Cut		Values	Efficiencies		Values	Efficiencies	
FV	ρ	$\leq 150\,\mathrm{cm}$	–		$\leq 145\,\mathrm{cm}$	–	
	$\lvert z\rvert$	$\leq 150\,\mathrm{cm}$			$\leq 145\,\mathrm{cm}$		
Energy	E_{Bi}	$[0.1375, 2.50]\,\mathrm{MeV}$	$\varepsilon_{\mathrm{Bi}}$:	0.98	$[1.1375, 3.50]\,\mathrm{MeV}$	$\varepsilon_{\mathrm{Bi}}$:	0.87
	E_{Po}	$[0.8875, 1.50]\,\mathrm{MeV}$	$\varepsilon_{\mathrm{Po}}$:	1.00	$[0.65, 1.10]\,\mathrm{MeV}$	$\varepsilon_{\mathrm{Po}}$:	0.99
Delay	Δt	$[0.2, 2]\,\mu\mathrm{s}$	$\varepsilon_{\Delta t}$:	0.62	$[0.2, 711]\,\mu\mathrm{s}$	$\varepsilon_{\Delta t}$:	0.95
Distance	Δr	$72.5\,\mathrm{cm}$	$\varepsilon_{\Delta r}$:	1.00	$45\,\mathrm{cm}$	$\varepsilon_{\Delta r}$:	0.90
			$\varepsilon'_{\Delta r}$:	0.95		$\varepsilon'_{\Delta r}$:	0.98
Total selection efficiency				0.61			0.74

so that both ends of the delay time window are allowed to float. Nevertheless, the lower bound was fixed to 200 ns in the final analysis, as it did not lead to any improvement, but instead to longer and less stable minimizations. The best set of cuts found with help of this grid search is given in Table 7.4 for no Radon contamination of the water and in Table 7.5 for the case of Radon contamination discussed in Section 7.2.
As shown in Section 7.3, the energy selection windows of both Bi and Po are concerned by the increased singles rate in presence of additional Radon in the water. Most notable is the smaller energy selection window, that has to be considered for ^{214}Bi in order to reduce the accidental rate from the enhanced total singles rate. Plots for the optimized energy windows in this case are shown in Appendix B for reference. The coincidence selection of ^{212}Bi-^{212}Po is almost not affected due to its much shorter coincidence time window.

The optimized cuts yield an activity limit for ^{214}Bi-^{214}Po (^{212}Bi-^{212}Po) of $3.4 \times 10^{-9}\,\mathrm{Bq/kg}$ ($2.9 \times 10^{-9}\,\mathrm{Bq/kg}$) after 24 h. This can be translated into a mass limit of $2.8 \times 10^{-16}\,\mathrm{g/g}$ for ^{238}U and $7.3 \times 10^{-16}\,\mathrm{g/g}$ for ^{232}Th under the assumption of considerable Radon contamination of the water shield. Figure 7.8 shows the sensitivities in terms of the activity limit as a function of the measurement time.

Although the much shorter coincidence time window for ^{212}Bi-^{212}Po yields a better background rejection, the limit cannot improve much, because the background rate is already minimal. The sensitivity was also evaluated with changed relative energy resolutions by ±2%, but it did not show any significant change in sensitivity. This loosened energy dependency is also reflected in the maximal relaxed energy window cuts. Nevertheless, the JUNO IBD requirement can be confirmed within a few hours of measurement. Reaching a sensitivity to probe the solar requirement takes a longer

Table 7.5 – Cut values and resulting efficiencies for the Bi-Po event selection including additional Radon contamination in the water shield. Details about all cuts are given in Section 7.3. The energy and distance cuts are defined with respect to the preceding fiducial volume cut.

		^{212}Bi-^{212}Po			^{214}Bi-^{214}Po		
Cut		Values	Efficiencies		Values	Efficiencies	
FV	ρ	$\leq 145\,\mathrm{cm}$	–		$\leq 145\,\mathrm{cm}$	–	
	$\lvert z\rvert$	$\leq 145\,\mathrm{cm}$			$\leq 145\,\mathrm{cm}$		
Energy	E_{Bi}	$[0.1375, 2.50]\,\mathrm{MeV}$	$\varepsilon_{\mathrm{Bi}}$:	0.98	$[1.4, 3.50]\,\mathrm{MeV}$	$\varepsilon_{\mathrm{Bi}}$:	0.83
	E_{Po}	$[0.8625, 1.50]\,\mathrm{MeV}$	$\varepsilon_{\mathrm{Po}}$:	1.00	$[0.65, 1.10]\,\mathrm{MeV}$	$\varepsilon_{\mathrm{Po}}$:	0.99
Delay	Δt	$[0.2, 2]\,\mu\mathrm{s}$	$\varepsilon_{\Delta t}$:	0.62	$[0.2, 711]\,\mu\mathrm{s}$	$\varepsilon_{\Delta t}$:	0.95
Distance	Δr	$72.5\,\mathrm{cm}$	$\varepsilon_{\Delta r}$:	1.00	$45\,\mathrm{cm}$	$\varepsilon_{\Delta r}$:	0.90
			$\varepsilon'_{\Delta r}$:	0.95		$\varepsilon'_{\Delta r}$:	0.98
Total selection efficiency				0.61			0.70

measurement time than 24 h, but is still possible when a larger amount of LS is averaged. The relaxed cuts and low background levels show, that this measurement is not background limited, but rate limited. Hence, the sensitivity can only be further improved by increasing the measurement time or the observed mass. Unfortunately, both the tank and AV dimensions are fixed at their possible maximum, due to the available space in the underground lab and especially its access tunnel. Nevertheless, OSIRIS can fulfill its purpose in validating the nominal purification power in the commissioning phase of the purification plant by measuring a batch for an extended amount of time. In the filling process, it is able to detect critical increases in contamination almost in real-time and ensure stricter limits over the course of a few days.

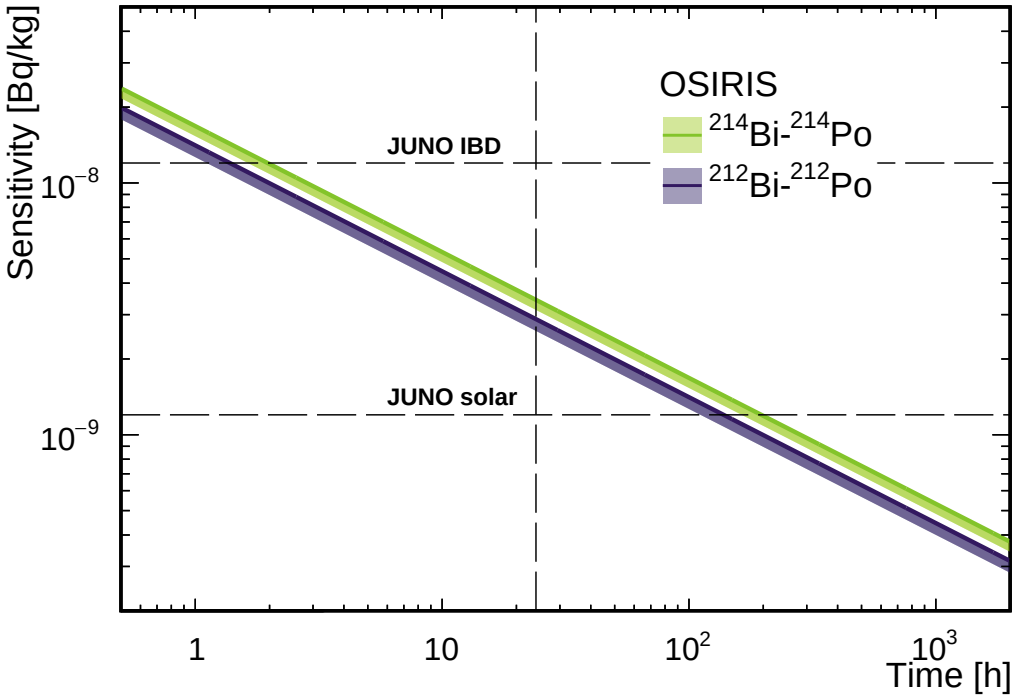

Figure 7.8 – Sensitivity of OSIRIS as a function of the measurement time for the ^{212}Bi-^{212}Po (purple) and ^{214}Bi-^{214}Po (green) coincidence searches. The sensitivity is given as a 90% CL upper limit on the contamination. While the line at the upper end of the band gives the sensitivity with maximal estimated Radon contamination, the band shows the improvement of the sensitivity up to no additional Radon contamination in the water shield. Within a few hours, OSIRIS can verify the JUNO IBD requirement. In order to confirm a contamination of 1×10^{-9}Bq/kg required for solar neutrinos, a measurement longer than one day is needed.

Chapter 8

Calibration Studies for OSIRIS

In all experiments some kind of calibration is needed to translate the recorded response of a detector into physical quantities. One prevalent example in LS detectors is the conversion of estimators like the detected amount of light to actual deposited energy. The goodness of a detector's calibration has direct influence on the capability to determine precise results. Typically it is done by injection of a well known signal into the detector and measuring its corresponding response. Depending on the complexity of the underlying projection, a number of one or more calibration points are measured like this in the range of interest. Interpolation between those points then allows for a general translation of arbitrary measured quantities to physical ones. Additionally, the calibration is not guaranteed to be constant over time, due to changing conditions and properties of the detector. Therefore, it must be possible to repeat the procedure on a regular basis, while the detector is in nominal operation.
From a perspective of calibration, OSIRIS is a typical LS neutrino detector, whose calibration goals are motivated in Section 8.1. After that, the possibilities of needed and available hardware to reach those goals are explored in Section 8.2. Based on those considerations, Section 8.3 presents the simulation studies carried out to assess the viability of the systems and to fine tune their parameters. The resulting decisions and suggestions for a general calibration campaign are discussed in Section 8.4.

8.1 Goals of calibration

The calibration need for OSIRIS is manifold and interdependent, because it takes several steps to reconstruct a physical event from the signals in the PMT channels.
The first important point in this chain is the *charge calibration* of the PMTs. It is a fundamental conversion of the measured charge in a PMT, represented by an integral over ADC counts of the voltage drop, to the *number of detected photo-electrons* (npe). Under the assumption of a linear behavior in the region of interest, this is typically done by precise measurement of the single photoelectron (SPE) charge response. Thus, a system needs to be in place, that can illuminate the PMTs on the level of single photoelectrons.

In order to keep the contamination of multiple hits below 1%, the system should be tuneable to a expected occupancy of $\mu \leq 0.05$ for all PMTs.
The translation of the PMT signal into a number of detected photoelectrons in this channel gives access to the total number of detected photoelectrons of one event. It is a fundamental energy estimator and can be used in OSIRIS to define the energy of an detected event. The definition of the *energy scale* in the range of 500 keV to 3 MeV is the focus for the detection of Bi-Po-coincidences (see Chapter 7). With a well measured response in this region, it would be possible to extrapolate down to ∼50-100 keV for the measurement of the ^{14}C β-spectrum. Although, in general, the response is not linear due to quenching (see Section 2.1.1), the effect is small and the scale can be fitted with linearly. Subsequently, the non-linearity can be modeled from detailed measurements and MC studies. The OSIRIS calibration aims to provide an energy calibration, that is considerably better than the resolution effects from photon statistics. The *detector response mapping* is inextricably linked with the energy scale, because the energy response has a position dependency. Calibrating the energy scale in only one arbitrary point in the LS volume is possible, but does not necessarily reflect the response in every point. This effect is predominantly introduced by the geometry of the AV and the PMT array. In order to account for it, several points in the LS have to be sampled, that allow for an extrapolation to the full volume. Determining a sufficient number and positions of those points is another goal of the study presented here.
Given the inhomogeneous response and a limited number of accessible points in the LS, usually the MC simulation is used to extrapolate the response map over the whole detector. To do this, the MC simulation has to be validated by comparison of the calibration data with the equivalent simulation. If in agreement, the simulation can be further tuned to reproduce the measured data in the calibration points and then be used to predict the response in every point of the target. It is crucial to define a set of points, that represent the full amplitude of fluctuations in the response introduced by geometric effects.
Lastly, the individually read-out PMTs need a *time alignment* on a global time scale. Due to different cable lengths and runtime in the internal electronics, each PMT channel has a different time offset t_0 to a global reference point. The timing profile of the emitted light carries information about an events position and time and can be used for particle identification (seeSection 2.4). Hence, a precisely calibrated alignment of the PMTs is crucial for time-based reconstruction algorithms. In addition, pulse-shape discrimination techniques often rely on a well known event position to do a time-of-flight subtraction. Usually one can use the same system for timing calibration, that is used for the charge calibration. Furthermore, it is also possible to do the charge calibration on ^{14}C events. A well defined point of light emission in space and time with tuneable intensity can be used for this purpose. The calibration is expected to be more precise than the intrinsic TTS of the PMTs.

The employment of OSIRIS in the continuous filling of JUNO creates the need for a fast and efficient calibration. In addition, the observed LS is constantly changing, which also allows for unforeseen changes in the detector response. The following study investigates

a calibration scenario, that schedules a full calibration at the beginning of data taking followed by the regular, small re-calibrations on a weekly basis for fine tuning. It also foresees the constant deployment of a source to monitor a steady signal, that could trigger another full calibration upon significant change of the detector response.

8.2 Hardware considerations

There are two general approaches to realize the injection of a known signal into the detector in LS experiments. One is the deployment of a radioactive source along one or more axis into the LS, called a *source injection system* (SIS). The sources are typically γ or neutron sources with a well understood event topology placed at a known position in the detector. In OSIRIS, such a system could be used for energy calibration with a set of different sources and for detector response mapping with different positions. The choice of available isotopes is based on the γ-sources that will be ordered for JUNO: ^{40}K, ^{60}Co, ^{22}Na, ^{54}Mn, and ^{137}Cs. Their maximum activity is limited from the perspective of procurability to 10 kBq. Other factors like the maximum trigger rate of the DAQ system and possible pile-up effects are expected to give tighter limits on the useable activity.
A special requirement for general SIS is the need to precisely locate the source position. While a simple *fishing rod* design can keep track of the position by mechanical means, more complex deployment systems often rely on an additional system for source location, like a CCD camera setup [143].
The second widely used method is a *light injection system* (LIS). Instead of injecting a source, that will induce light emission in the LS by energy deposition, a LIS circumvents the LS by directly emitting photons. By that, the emission delaying decay time of the LS is suppressed and thus a light signal with a precisely known start time is available. LIS are often used for SPE charge calibration and timing alignment of PMTs, due to the easy adjustability of light intensity.
For OSIRIS different approaches are under investigation: a direct deployment of a LED into the LS with a 4π light-diffusor or an injection through fibers shooting light from outside through the LS on the opposite PMTs.

Either way, cleanliness of the calibration system is paramount. Any contamination introduced by OSIRIS would be transported into JUNO and also contaminate the LS there. Thus, it is vitally important to keep the contact of the LS with surfaces and materials minimal and to use the most radio-pure materials available. A calibration system, that is sealed and does not need any outside access for maintenance or the exchange of sources would be favorable.

Furthermore, the strategy to operate in a continuous flow mode sets OSIRIS apart from other LS detectors also in aspects of detector design. In order to avoid turbulence in the LS, an acrylic diffusor is placed underneath the central inlet. While it will ensure a proper flow according to the temperature gradient in the vessel, it prevents access to the central z-axis for calibration. Usually, the central axis is favored in calibration, because of its symmetry in regard to the LS and the PMT array. The absolute detector center is also not accessible by a vertical axis with the diffusor in the way. The implications

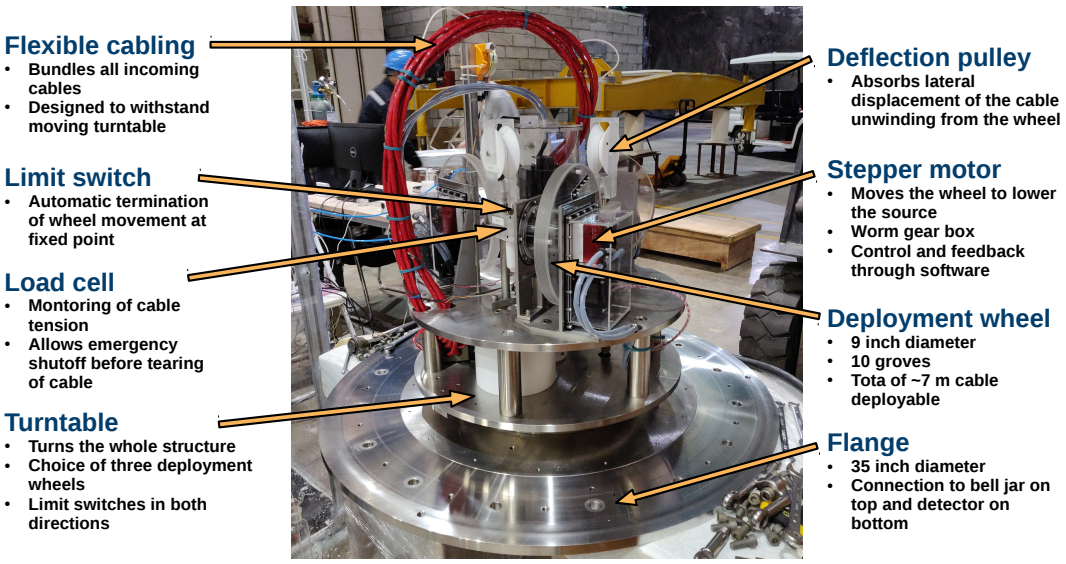

Figure 8.1 – Overview of the inner design of the *automated calibration unit* of Daya Bay to be used in OSIRIS. The key features are expanded in the text and all details can be found in Ref. [144].

of an off-axis calibrations include an asymmetric response of the PMT array and the possibility of so-called *gamma leakage*. The latter describes the effect of γs leaving the LS and depositing a part of their energy outside of the target. In this case, a distortion in the calibration accuracy is introduced, since the real deposited energy is only known when the γ is fully absorbed. Section 8.3 aims to investigate and answer the question if an off-axis calibration is sufficient and how many axis at which positions are necessary. Finally, another point to consider for the calibration systems of OSIRIS is its time schedule. The detector has to be ready for operation before JUNO is filled, ideally also the same time of commission of the purification plant. Additionally, the underground space is limited, so that OSIRIS has to be transported underground and set up before the purification plants. The tight schedule does not allow for extensive hardware R&D or the development of new designs. Instead, options are explored to adapt existing systems originally developed for Daya Bay and JUNO.

8.2.1 The Automated Calibration Unit

The Daya Bay collaboration developed a fully automated calibration unit (ACU) for the calibration needs of their antineutrino-detectors [144]. Based on its specifications and design, it fulfills several requirements of OSIRIS as well: it can deploy a calibration source along one vertical axis in an automated and fast way with minimal user interaction. In addition, the system is fixed and sealed on top of the detector, providing a closed system, that cannot introduce contamination into the detector if it in installed cleanly. Finally, the ACU is established and proven to work in years of Daya Bay operation.
The Daya Bay collaboration kindly offered to provide a spare ACU for the use in OSIRIS,

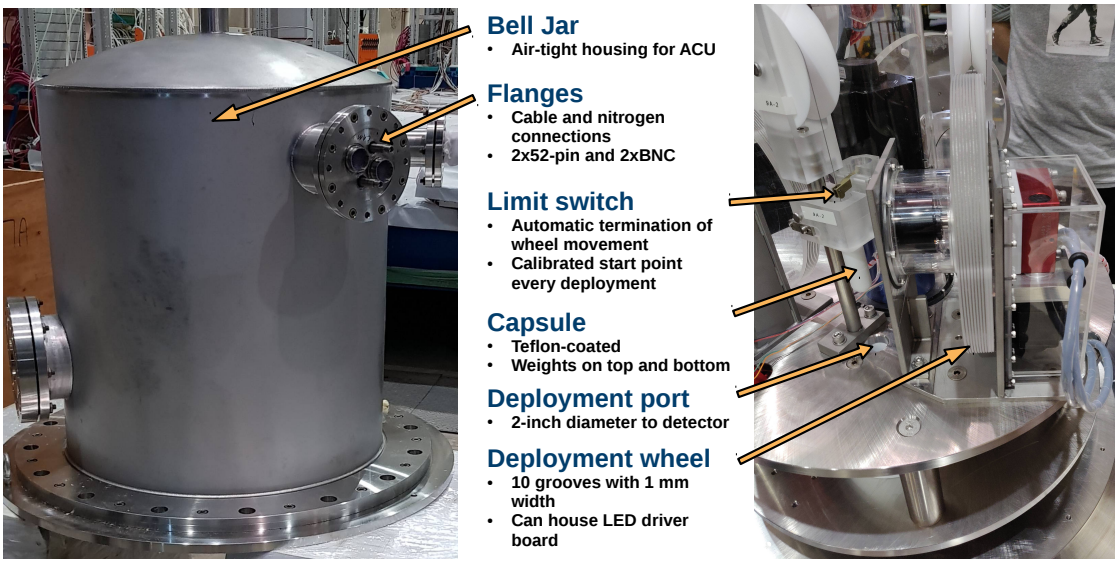

Figure 8.2 – Details of the ACU design. *(Left:)* The ball jar housing of the ACU features several flanges to connect all electronics through 2 ports with 52 pins each and two BNC ports. In addition there is a flange with two ports for nitrogen supply and outlet as well as a window-flange to observe the unit by eye, even if closed. *(Right:)* Close-up of one deployment wheel, including its limit switch, a capsule, and the deployment port in the bottom of the unit.

if the system can be fitted for use with the OSIRIS detector. In January 2019, an on-site visit at Daya Bay was undertaken to investigate the possibility of using an ACU and to identify what modifications would be needed. The following description of the ACU is limited to crucial points for OSIRIS and is based on Ref. [144], which holds all detailed information and hands-on experience with the unit. An overview of the system's main components is shown in Figure 8.1. While Daya Bay used three ACUs per detector, OSIRIS considers only one, due to its design and limitations. A single ACU has one port and is therefore providing a single vertical axis, as can be seen in Figure 8.2. Nevertheless, it features a *turntable* with three positions and wheels for source deployment. Thus, it can house three different calibration sources and they can be selected and lowered into the detector automatically without the need to touch the system. The ACU at hand is fitted in a way that two of those positions can be used as SIS for capsules with arbitrary radioactive sources on a teflon coated stainless-steel rope. The third wheel is prepared to be used as an LIS, with a teflon coated coax cable to deploy an LED with a light diffusor. All three deployment systems are also equipped with load cells to monitor the load on each cable in order to stop the motors before a cable would break if it is stuck somewhere. Hence, it is perfectly suited for the use in OSIRIS with regard to being a closed system and the variety of options for source deployment. One crucial mechanical aspect are the unit's size and weight. With an outer diameter of 61 cm, a height of 76 cm, and a weight of 320 kg it is considerably heavier than similar single-axis systems of other

experiments. Nevertheless, the top-lid of OSIRIS is designed to support the weight, due to the fact that it has to accommodate the DAQ system as well.
When lowering a source into the detector, the inside volume of the ACU comes into contact with the LS through the 1 inch port for the capsule. Since the LS would be highly contaminated with Rn upon contact with air, the system needs to be constantly flushed with ultra-pure nitrogen. The ACU provides two ports, a supply and return, that allow for the unit to be easily integrated into the general nitrogen system of OSIRIS.
For remote operation of the ACU, a working LabView software is available. Its core functionality of controlling the motor motions, reading of the load cells and all security checks, as well as logging and plots of the source position can be adapted. Only the communication with other systems like the DAQ and *runcontrol* has to be rewritten to accommodate what OSIRIS will use.
Apart from the nitrogen cycle, the ACU is connected by two 48-pin connectors and two RG58 coaxial cables. One of the coaxial cables is used to send a TTL signal directly to the LIS of the ACU to pulse the LED, while the other is used as a signal cable for an internally mounted CCD camera to visually monitor the inside of the ACU. The other two large cables are connected to a *control box*. This box acts as a power- and signal distribution box and hosts the motor drivers, several independent power supplies, and interface boards. It is connected to three *National Instruments* PCI cards in a control computer (or server) running the LabView software package.
All auxiliary systems needed to operate the ACU were kindly provided to be used for JUNO in OSIRIS by the Daya Bay collaboration.
In conclusion, the ACU hardware unit can be integrated into OSIRIS as it is. It does not need any major modification and can act as the main device for the calibration needs of the detector. Naturally, all source deployment cables will be replaced and the unit has to be fully cleaned before mounting. In addition, the control software has to be adapted to the new infrastructure.

8.2.2 Light injection systems

With regard to a LIS, OSIRIS considers two available systems as mentioned above. The ACU provides the possibility to lower an LED along its axis into the LS, that can illuminate the PMT array from arbitrary points along this axis. Due to the fact, that the system was used successfully and regularly used in Daya Bay, a good characterization of the installed LED is available to study the system's performance in OSIRIS. Especially the timing profile of light emission is important, since a narrow peak is needed to accurately calibrate the PMT timing. In addition, it is not trivial to build a light diffusor with perfectly isotropic emission in the full 4π solid angle.
The simulation study also has to take into account, that the distance between the point of light emission and each PMT is not constant. Thus, a time-of-flight correction has to be done, which introduces another uncertainty to the calibration, due to the spatial extent of the PMTs. Nevertheless, this challenge is not introduced by the off-axis calibration alone, but also the geometry of the detector. In contrast to the spherical JUNO, there is no point of equal distance to all PMTs in a cylindrical array.

The second investigated LIS is based on a much faster laser system developed at the *Physics Institute* of *Universität Tübingen* by *Tobias Sterr*. There was no dedicated study done on this system in the scope of this thesis, but it is shortly presented to give a full overview on the OSIRIS calibration hardware.
The laser system features a very fast laser with 420 nm wavelength and a pulse width of only 60 ps. Its light can be fed into fibers by a custom-made 1:4 beam splitter, that allows each light path to be blocked independently by beam shutters. Thus, it allows for 4 independent light injection groups which can easily be extended to 8 groups with the addition of another module. In contrast to the ACU, this LIS is foreseen to inject the light from outside of the LS. The fibers can be mounted on the PMT holding frame or the PMTs itself to shoot the light through the LS onto the PMTs on the opposite side. The advantages of this system are that no possible contamination is introduced into the LS and the fixed fiber positions can be determined to a very high accuracy. Additionally, the much more narrow pulse width in contrast to a LED, allows for a fast calibration, that can be repeated regularly without prolonged interruption of the nominal operation. The details of integration into OSIRIS like number and position of light injection points and the design of the diffusors at the end of the fibers are still under investigation.

8.3 Simulation studies

Extensive simulations of the calibration systems under consideration were done to provide a solid foundation for the hardware decisions to be made. The simulation runs were carried out with the software framework described in Chapter 6 by using its dedicated calibration modes. For the SIS, the *Calib* mode was used to study the impact of adding introducing a capsule geometry in the LS on the light propagation. Furthermore, it was used to study the detector's response to different combinations of several isotopes as well as the number and orientation of deployment axes.
Investigations on the LIS are based on the *photon bomb* mode, due its ability to shoot optical photons sampled from a given wavelength spectrum from any point of interest.
The studies were done in close collaboration with *Alexandre Göttel* (A.G.) in our working group. While the simulation software was developed independently, the analysis of the produced data sets was a joint effort. Plots and conclusions based on his work are denoted accordingly in the following.

8.3.1 SIS studies

The *Calib* mode of the OSIRIS simulation was explicitly developed to accommodate the needs of this study. It places a representation of the foreseen calibration capsule at any set point inside the LS and allows for the full decay of chosen isotopes in the inside. While the lifetime of the unstable isotopes were set to zero in order to force a direct decay, no other modification was applied. This is important, because the capsule is also designed to contain secondary particles from other decay branches, so that only γ particles of known energy are detected in the LS. A comparison between the technical drawing and its implementation in `Geant4` is shown in Figure 8.3. The capsule has a total diameter of 12 mm and a height of 22 mm, while the innermost volume holding the

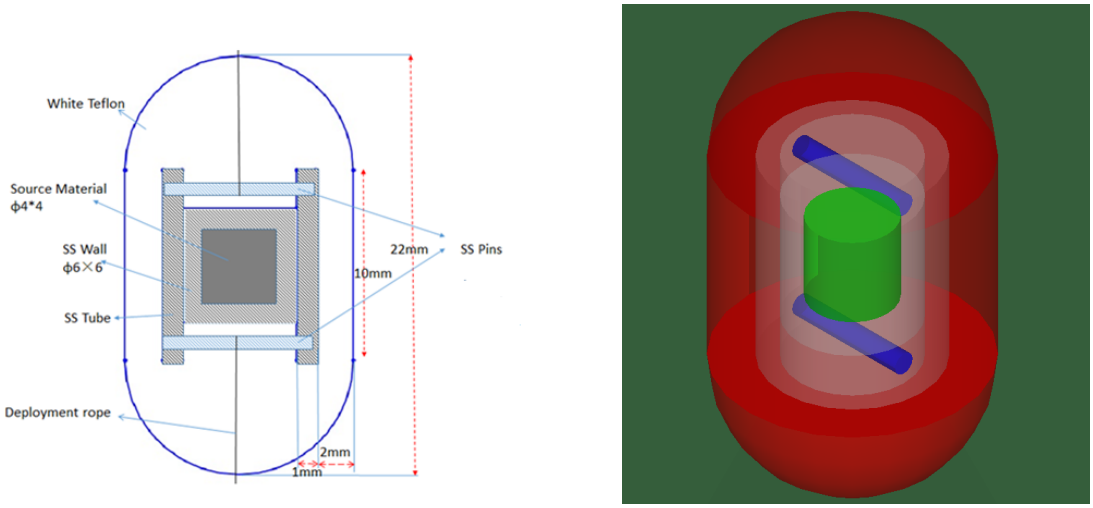

Figure 8.3 – *Left:* Technical drawing of a calibration capsule prototype for JUNO (internal design by collaboration). *Right:* Visualization of the implemented geometry in the OSIRIS simulation.

radioactive material is a cube with 4 mm side length. In order to avoid any loss of light by shadowing effects from the capsule, it is designed with a reflective teflon surface on the outside.
The simulation output is twofold: the full PMT hit time data is written to file to study the detector response. In addition, the full MC output of position, volume, value, and creator process of each energy deposition is saved. This allows for a detailed investigation of the energy losses in the capsule, its ability to stop unwanted, secondary particles, and of possible gamma leakage.

In order to decide whether or not a single off-axis calibration axis is sufficient for OSIRIS and at what radial distance it has to be placed, a response map was simulated. Figure 8.4 shows the average number of detected photo electrons per MeV of deposited energy for a sample of $5 \cdot 10^6$ electrons with a uniform energy distribution between 50 keV and 5 MeV. Along the radial direction fluctuations of up to 26% can be seen, while the fluctuations along the vertical axis are about 20% at the most extreme positions. For the choice of a calibration axis, vertical slices along the z-axis have to be considered. From a perspective of verifying the MC simulation, the ideal candidate for a calibration axis would feature the largest variation in detector response. A high non-uniformity is easier to identify and gives a large handle on cross-checking the simulation. In combination with the region of interest being inside a certain FV cut that excludes the regions very close to the AV, a choice of calibration axis candidates between $\rho_a = 100$ cm and 140 cm can be made. Following that, a more detailed simulation with the actual isotopes was carried out along points on those axis. At each point, the peak of the spectrum of detected photo-electrons was fitted with a Gaussian function to estimate its mean value. The variation of the

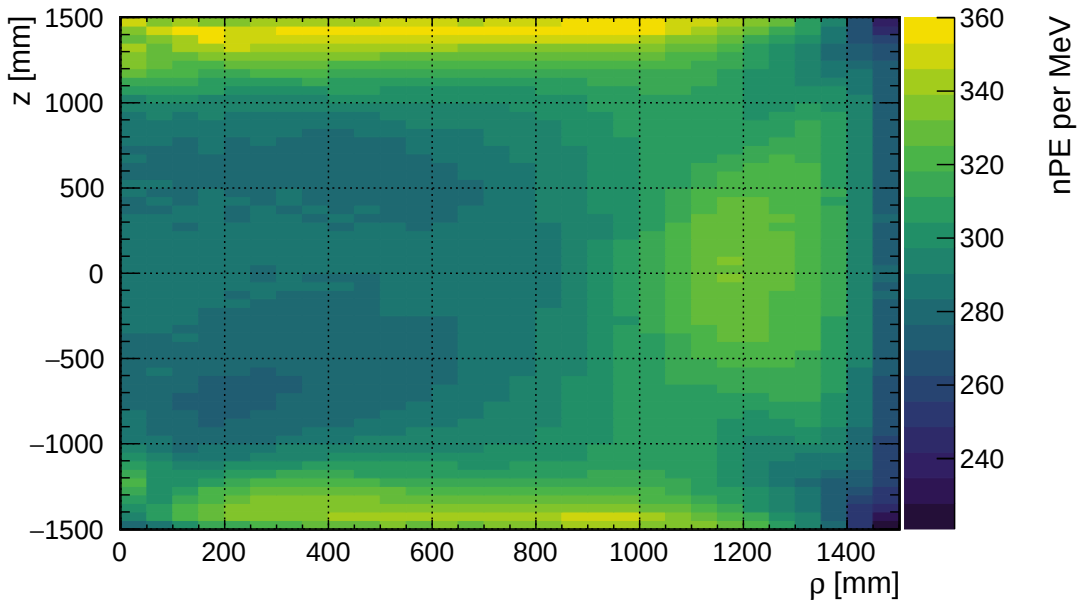

Figure 8.4 – 2D response map of the LS volume giving the mean light yield in number of photo-electrons per MeV deposited energy. It was determined using the detector simulation with $5 \cdot 10^6$ electron events distributed uniformly in space and an energy range of $[0.05 - -5]$MeV.

mean value along each axis is plotted in Figure 8.5. While the points give the mean light yield per axis at a given radial distance, the bars indicate the extend of the variation in response.

A second aspect to take into consideration is gamma leakage. The isotopes used for calibration emit γs with a fixed energy in their decay. When traveling through matter, they can have a track length of several tens of centimeters depending on their energy. Thus, the amount of γs that can leave the AV and deposit a part of their energy outside of the LS increases with the calibration axis moving closer to the AV edge. Utilizing the full MC truth output, the amount of leaked γs and their contribution to the measured spectrum can be evaluated. Figure 8.6 shows the mean fraction of γ-events, that leaked out of the LS over a range of radial positions between 90 cm and 130 cm. Even moving the calibration axis to $\rho = 90$ cm, close towards the LS diffusor, still results in a leakage rate of $\sim$15%. Thus, some leakage is unavoidable, but the full extend in shifting the measured energy peak has to be checked. The full measured spectrum of three isotopes can be divided into the sub-spectra of events, that deposited some energy either in the capsule or outside of the LS. The resulting spectra are presented in Figure 8.7 for a calibration axis at $\rho = 120$ cm and $z = 120$ cm close to the top of the AV. It can be seen, that the measured spectrum is shifted slightly to lower energies than the *full absorption* peak. Both, the measurable peak and its corresponding full absorption peak were fitted by a Gaussian function to estimate the energy shift. Table 8.1 shows, that the shift

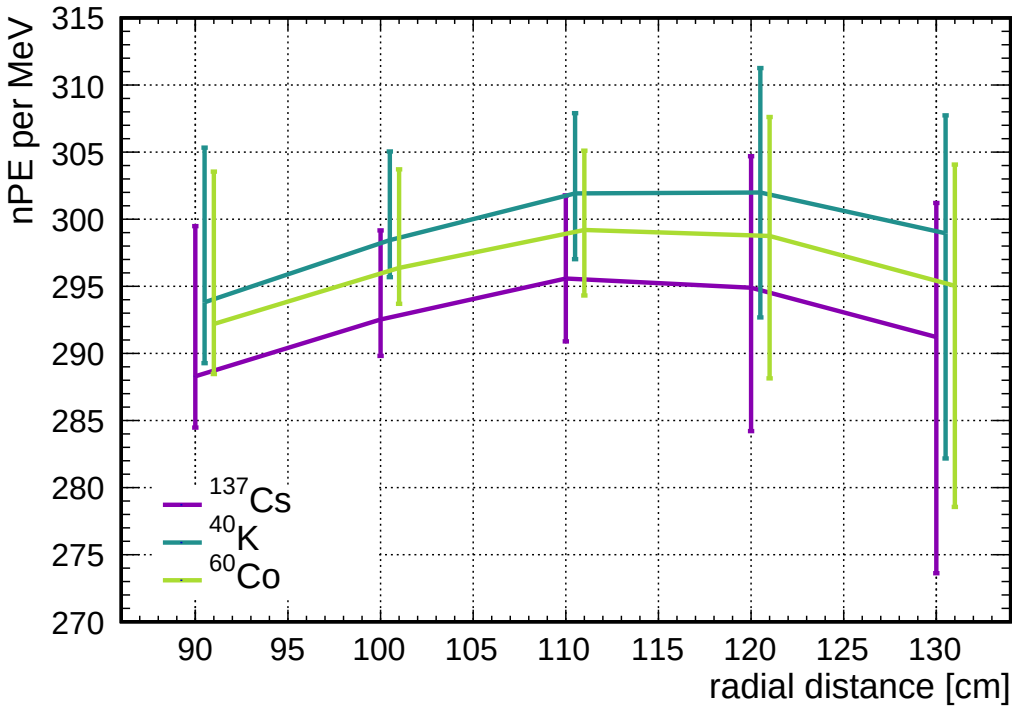

Figure 8.5 – Mean light yield in number of photo-electrons (nPE) per MeV deposited energy as a function of the calibration axis' radial distance to the detector center. The lines give the mean value along the z-axis, while the bars indicate the minimum and maximum value along this axis. The graphs for ^{40}K and ^{60}Co are shifted for readability, but were determined at the same positions as ^{137}Cs.

towards lower energies is a percent-level effect and thus much smaller than the achievable resolution, due to photon statistics. If the detector simulation can be verified with the calibration data, it can be used in this way to correct for the introduced bias in the energy calibration. Considering both the amplitude of light yield variation along the axis and the bias introduced by γ-leakage, the calibration axis was chosen to be at $\rho = 120\,\mathrm{cm}$ as a compromise.
From this follows also the conclusion that one axis for energy scale calibration and non-uniformity mapping is sufficient for OSIRIS. The chosen axis can model the maximal variation of the expected non-uniformity and while providing energy spectra close to the full absorption peak of the respective isotopes. In the worst case of incompatibility between the simulation and the calibration data in terms of non-uniformity mapping, there is no sound reason why an additional axis would improve the result.

The ability of the calibration capsule to hold the radioactive isotopes without interfering with the detector response was already mentioned shortly above. Most of the isotopes to choose from feature not only the single γ decay of interest, but also other decay modes.

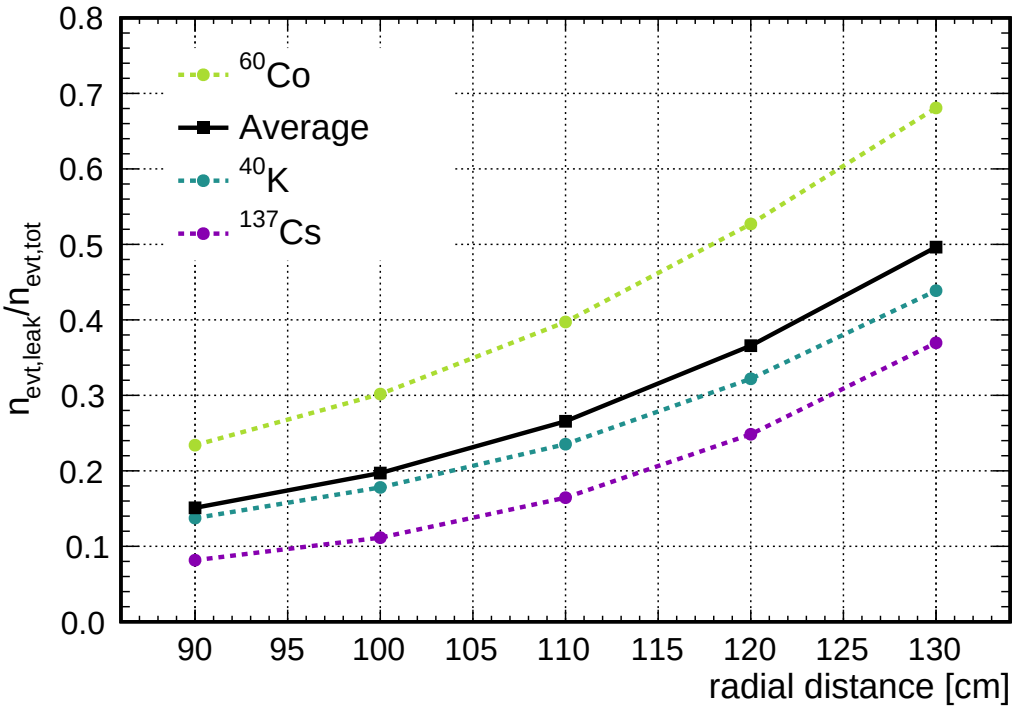

Figure 8.6 – Mean ratio of the number of events with γ-rays that deposited energy outside of the LS to the total number of events as a function of the calibration axis' radial distance to the center. Since the capsules distance to the AV wall changes with its position on the z-axis, the values are averaged for a given ρ. The dotted lines give the ratio per isotope and show an expected increase in the ratio for higher energy γs. Since all three isotopes are supposed to be contained in one capsule, the average over the isotopes is overlayed as a black line.

The concentric, cylindrical capsule design is chosen to absorb electrons and positrons from β-decay channels, so that they cannot produce a visible event in the LS. By that, the capsule ensures a clean γ sample released into the LS. Nevertheless, it is possible that those γs also interact with the capsule material and lose a part of their energy invisibly before entering the LS. An exemplary spectrum of the events that have losses in the capsule was shown in Figure 8.7. Only a small fraction of events is affected and a shift of the peak position is not present. Figure 8.8 shows the spectrum of ^{137}Cs including all events, as they would be measured and overlayed the spectrum without events in which the primary γ-ray lost any energy in the capsule. No shift in the peak position can be identified. Since the energy loss is caused by the capsule alone, it has no dependency on the position of the calibration axis.

The composition of isotopes inside one capsule is another aspect, that was investigated in the scope of this study. In order to fit a linear energy scale, a minimum of three

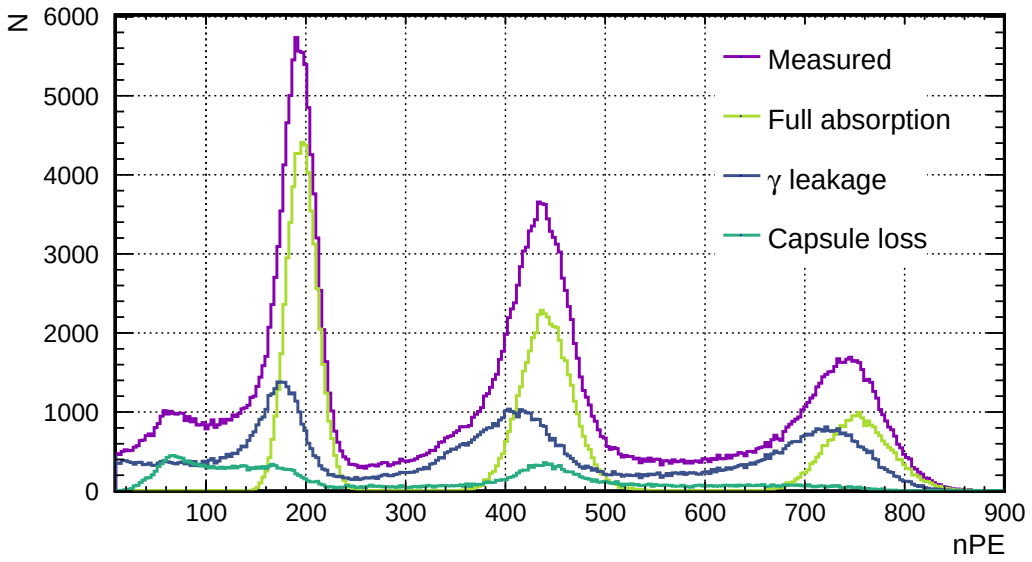

Figure 8.7 – Measured energy spectrum in nPE for the combination of ^{137}Cs, ^{40}K, and ^{60}Co in one capsule at $\rho = 120\,\text{cm}$ and $z = 120\,\text{cm}$. The measurable spectrum is divided into the sub-spectra of events with full γ-absorption and events with either losses by γ-leakage or effects in the capsule. Here, energy loss in the capsule refers to events where the primary γ-ray with known energy from the decay, interacts inside the capsule and loses energy by that. It can be seen, that the events affected by γ-leakage create a smaller signal and thus, the total measured peak is slightly shifted to lower energies in comparison to the full absorption peak.

calibration points need to be recorded. Ideally, this should be done via the deployment of one capsule housing three different isotopes to reduce the number of positions that have to be scanned in each calibration run. This is only feasible, if the isotopes can be chosen in a way that the overlay of their spectra is minimal. It is crucial, that the peak positions of the individual γ-spectra are not distorted by the presence of the other two isotopes. Given the choice of available calibration isotopes (see Section 8.2), the ideal setup would consist of ^{137}Cs, ^{40}K, and ^{60}Co. With the γ energies of 0.66 MeV, 1.4 MeV, and 2.5 MeV respectively, they could cover the needed energy range without any overlap as shown in Figure 8.9. Despite its favorable peak position, ^{40}K is not a viable option for the main calibration because of its low natural activity. One usually uses natural potassium, because it is easily purchasable. Nevertheless, the natural abundance of ^{40}K is only $1.17 \cdot 10^{-4}$ [145], so that in the given capsule volume a maximum total activity of $\sim$0.1 Bq could be reached. Hence, it is not possible to collect sufficient statistics on several points in the detector in a reasonable time.
Alternative isotopes in this energy region from the choice of JUNO calibration sources are ^{22}Na and ^{54}Mn. Nevertheless, ^{22}Na has a double peaked spectrum, due to the annihilation of the positron produced in its β^+-decay, which is not ideal for fitting a well

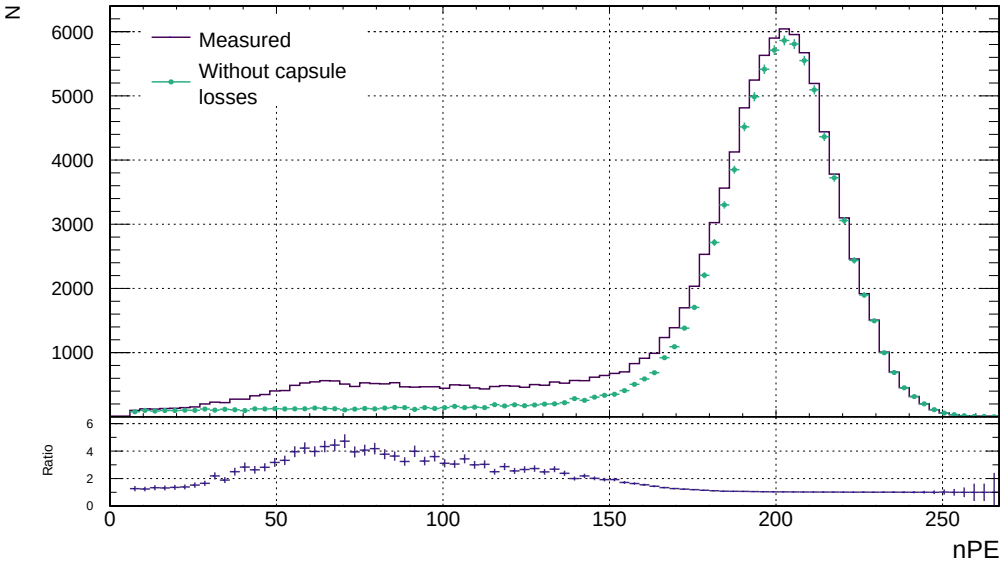

Figure 8.8 – Histogram of the measurable nPE spectrum of ^{137}Cs at $\rho = 120\,\text{cm}$ and $z = 0\,\text{cm}$. The overlayed points with error bars show the corresponding spectrum of all events except those with energy losses in the capsule. At the bottom the ratio of both spectra is plotted. It shows, that the peak region is not affected by losses in the capsule.

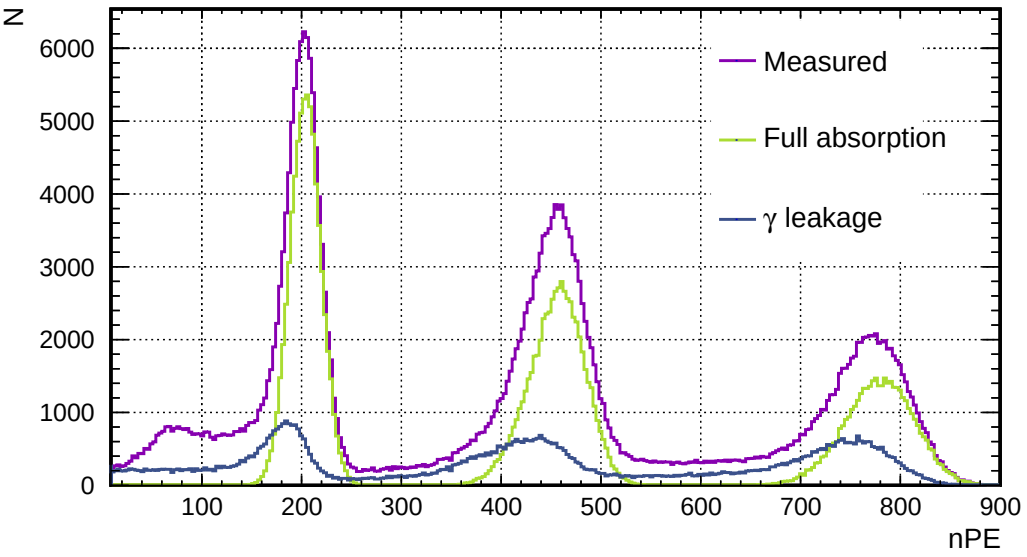

Figure 8.9 – Energy spectrum of ^{137}Cs, ^{40}K, and ^{60}Co in one capsule at $\rho = 120\,\text{cm}$ and $z = 0\,\text{cm}$ in the central detector plane. The sub-spectra of full absorption and γ-leakage show, that the effect is smaller in the middle of the axis in comparison to the extreme point of $z = 120\,\text{cm}$ in Figure 8.7. All three peaks are well separated and do not interfere.

Table 8.1 – Shift between the fitted mean of the measurable energy spectrum and the full absorption spectrum for ^{137}Cs, ^{40}K, and ^{60}Co. All peaks were fitted with a Gaussian function limited to the peak region. In the actual energy calibration are more sophisticated fitting would be used to account for the low-energy tail. As expected, the measured peak is slightly shifted to smaller energies, due to gamma leakage. For all three isotopes, the shift is below or at the 2% level.

Isotope	Measureable [nPE]		Full absorption [nPE]		relative shift [%]
	Mean	Sigma	Mean	Sigma	
^{137}Cs	192	18	196	15	2.0
^{40}K	435	32	441	26	1.4
^{60}Co	741	40	753	33	1.6

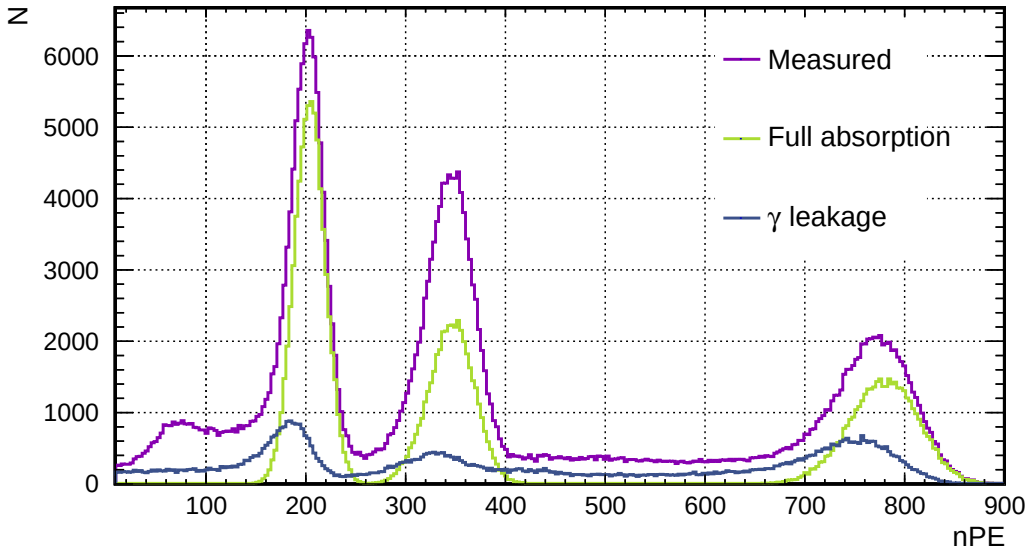

Figure 8.10 – Energy spectrum of ^{137}Cs, ^{65}Zn, and ^{60}Co in one capsule at $\rho = 120\,\text{cm}$ and $z = 0\,\text{cm}$ in the central detector plane. Although the ^{65}Zn peak is closer to the one of ^{137}Cs, they are still sufficiently separated.

defined energy. The decay of ^{54}Mn emits a 0.83 MeV gamma, that produces a considerable overlap with the ^{137}Cs peak in the spectrum.
Instead of ^{40}K, the isotope ^{65}Zn can be used to cover the energy range of 1-2 MeV, as shown in the combined spectrum in Figure 8.10. In order to define the energy scale, three pairs of real deposited energy and corresponding response of the detector in number of photo-electrons are needed. The direct way of obtaining those points is fitting the peaks of the spectrum with Gaussian functions and taking their mean value μ. This method is the most basic approach and does not rely on any other input than the measured

spectrum. Therefore, it is robust, but the shift in the spectra due to energy losses in the capsule or γ-leakage is invisible to this method. With help of the MC truth information, the amplitude of this effect can be estimated. The three extracted points can be fitted using a linear energy scale model

$$E_\gamma = a \cdot n_{PE} + b \tag{8.1}$$

with n_{PE} being the number of detected photo electrons and E_γ the corresponding γ energy. The extracted slope $a \pm \sigma_a$ and y-intercept $b \pm \sigma_b$ can than be compared to the values obtained from the MC truth. In order to do this, the full absorption peak without any losses is fitted in the same way to extract $a_{MC} \pm \sigma_{a,MC}$ and $b_{MC} \pm \sigma_{b,MC}$. Then, the bias introduced by the losses is included to the uncertainty by adding the squares

$$\sigma^2_{a,tot} = \sigma^2_a + (a - a_{MC})^2, \quad \sigma^2_{b,tot} = \sigma^2_b + (b - b_{MC})^2. \tag{8.2}$$

Under consideration of the covariance, the energy dependent uncertainty on the translated energy from the number of photo-electrons can be propagated. Figure 8.11 shows that this energy uncertainty including the bias from the Gaussian fit is significantly smaller than the statistical uncertainty from photon statistics[1]. Once the MC is validated using the calibration data, it could be used to model the shift due to energy losses and thus provide an even more accurate energy scale. This approach and an simulation-independent, empirical modeling of the energy losses are currently under investigation by A.G. Using only the fit of Gaussian functions to the peaks, an energy scale uncertainty of $\sim$1% can be achieved.

For an optimal use of the calibration time, the composition of the isotopes should be chosen in a way, that all three peaks are recorded with roughly the same statistics. Therefore ^{137}Cs, ^{65}Zn, and ^{60}Co have to be mixed in a ratio of 1.174 : 1.976 : 1 in the capsule. The absolute activity can be limited by three factors: the regulations of buying high activity sources, the maximum trigger rate of the DAQ, and pile-up of consecutive events. From an administrative point of view the acquisition of sources with an activity of up to 10 kBq is possible. Internal studies of the PMT readout electronics predict an estimated maximum trigger rate of 500 Hz to 1 kHz. This rate is in agreement with the trigger rate of other similar detectors like Double Chooz [146].
The pile-up effects can be estimated by a toy simulation using fully simulated events as an input. Choosing a realistic total capsule activity of 500 Hz signal events and a readout window of 512 ns, the pile-up rate can be estimated to

$$R_p = 500\,\text{Hz} \cdot 500\,\text{Hz} \cdot 512\,\text{ns} = 0.128\,\text{Hz}. \tag{8.3}$$

Compared to the full rate of 500 Hz, which is equally distributed for the three γ-sources, the pile-up is a per-mil level effect. By randomly sampling events from the three-source spectrum, pile-up events were constructed and scaled according to the rate. The resulting spectrum is drawn together with the measured singles spectrum in Figure 8.12. For

[1] The extraction of the parameters a and b by fitting, Equation (8.2) and the data for Figure 8.11 were produced by A.G.

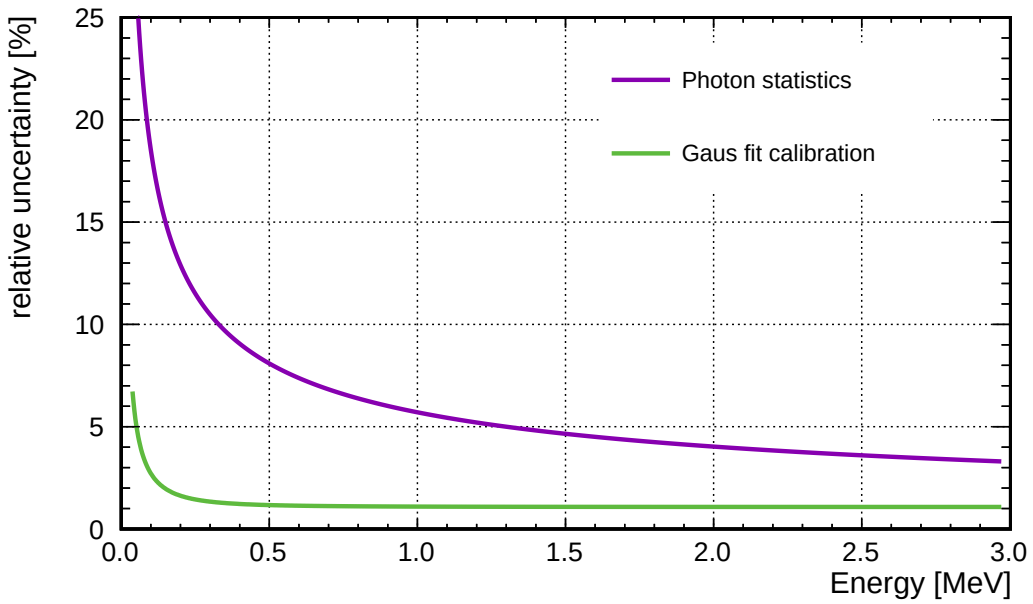

Figure 8.11 – Relative energy uncertainty from pure photon statistics and introduced by simple Gaussian fitting of the calibration spectrum peaks. The bias introduced by losses in the capsule and through gamma leakage are included through Equation (8.2). The data for this plot was provided by A.G.

realistic assumptions concerning the DAQ system, the pile-up spectrum is not a limiting factor for the source activity. Thus, the limitation of the absolute rate for the calibration sources is set by the DAQ and pile-up can be disregarded in this activity range. It is important to note, that this limit is set for the total activity of the capsule including all three isotopes.

8.3.2 LIS studies

Due to the fact, that this work is focused on the ACU, the LIS studies were only carried out for the LED deployable via the ACU. For the simulation, the *photon bomb* mode was used, as it resembles the operating principle of the LED by direct emission of a set number of optical photons into the detector. The LED under investigation is of the model BL-LBVB5N15C from *Brite-LED* and is provided with the ACU. Its emission spectrum was extracted from the data-sheet [147] and implemented into the simulation mode. In addition, the pulse time spectrum of the LED was modeled according to characterization measurements of Daya Bay [144]. Both spectra are shown in Figure 8.13 for reference. Since the ACU provides one axis of deployment, the LED is also lowered at a radial distance of 120 cm. An off-axis light injection point results in different solid angles for each PMT in regard to the event. Therefore, the intensity of the LED pulses for SPE measurements have to be tuned to the PMT that receives the most light, while the data collection time is set by the PMT that receives the least light in order to acquire enough

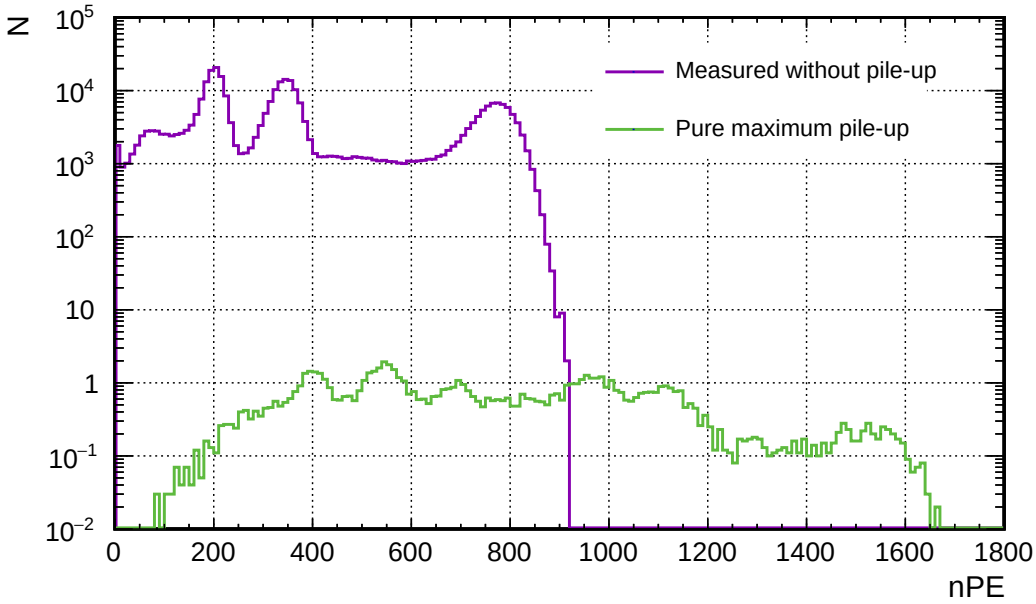

Figure 8.12 – Measurable energy spectrum of ^{137}Cs, ^{65}Zn, and ^{60}Co and the corresponding pile-up spectrum under the assumption of a total event rate of 500 Hz and a maximum readout window of 512 ns. The pile-up spectrum lies three order of magnitude below the singles spectrum and is, thus, negligible for the consideration of source activities. The data for this plot was provided by A.G.

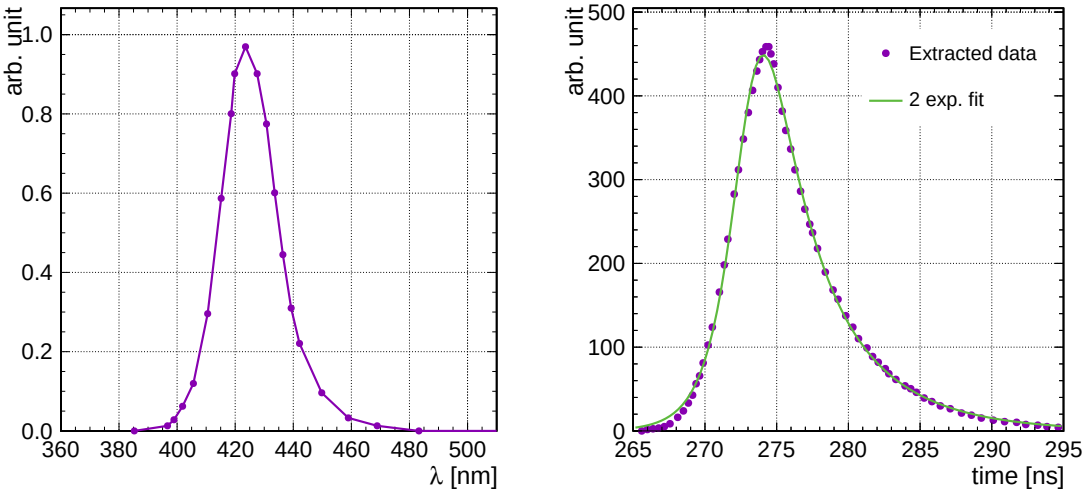

Figure 8.13 – *Left:* Emission spectrum of the LED used in the simulation. The values were extracted from the data sheet [147]. *Right:* Pulse time spectrum used for the simulation. It was determined using a characterization measurement of the LED by Daya Bay [144].

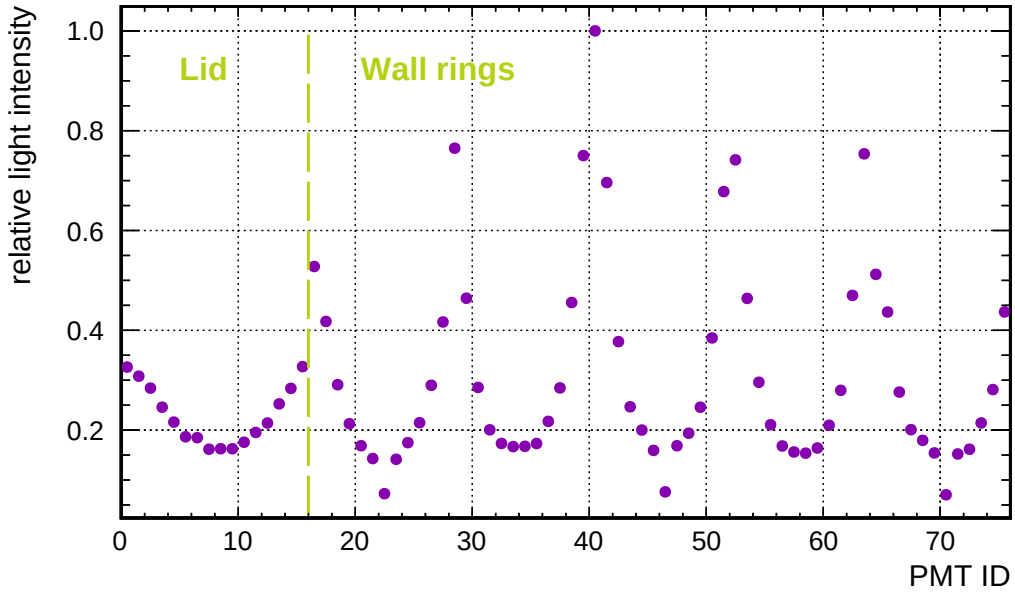

Figure 8.14 – Relative light intensity on the PMT array as a function of the PMT ID for a LED deployed at $\rho = 120\,\text{cm}$ and $z = 0\,\text{cm}$. The dashed line indicates the PMTs belonging to the tank lids and walls, respectively. As can be seen from the projection of the ring structure, the driving factor for the light intensity is the PMT's distance to the emission point. The lowest intensity on a PMT amount to <10% of the highest intensity. The data for this plot was provided by A.G..

statistics. BOREXINO has reported that the measured *first hit time* of photons on a PMT depends on the total charge received in this pulse [143]. Given the large variation in received light over the PMT array in the case of OSIRIS, two scenarios are possible. Either it has to be ensured, that all PMTs receive light only at the SPE level, or the illumination has to be high enough to saturate this effect. The latter approach could introduce systematic effects like PMT non-linearity, so that a SPE level illumination is favored. Simulations at $z = 0\,\text{cm}$ were conducted to estimate the relative difference in light intensity over the PMT array. Figure 8.14 shows the resulting distribution normalized to the PMT that received the highest intensity. One can identify the first 16 PMTs on the top and bottom lid and five rings of PMTs on the side walls by the different received intensities. While the largest factor is their individual solid angle corresponding to the event position, also refraction by the vessel and attenuation by the LS influence the result. The furthest PMT sees ∼10% of the light intensity of the one with highest illumination. If an average expected illumination level of $\mu = 0.05$ is set for the closest PMT, its contamination of multiple hit events is less than 1%. At the same time, the PMT with the smallest solid angle has an expected occupancy of $\mu_{min} \approx 0.005$.

The residual uncertainty of the PMT time alignment was estimated by simulating the timing calibration procedure with a toy MC. In order to do this, one compares the

measured hit time on a PMT to the expected hit time from a model and averages over many events. In reference to some arbitrary global time t_{ref}, the measured signal time $t_{hit,mes}$ can be defined as

$$t_{hit,mes} = (t'_0 + t_{LED} + t_{tof} + t_{PMT} + t_{elec}) - t_{ref}. \tag{8.4}$$

Here, t_{LED} describes the emission time of the LED, t_{tof} the time-of-flight it takes the photon to reach the PMT cathode, and t_{PMT} is the time it takes for the photo-electron to reach the anode and to create a signal. The signal processing including cable lengths is represented by t_{elec}. Except for the term t'_0, that accounts for undefined shifts, all elements of the sum are statistical distributions with a mean value and some shape. While for most of the mentioned effects, the uncertainty is known through measurements or simulation, their expectation value depends on the individual PMT. Therefore, the mean values, that are independent of the event position are absorbed into the effective time offset

$$t_0 = t'_0 + \sum_i \bar{t}_i \tag{8.5}$$

with i iterating over the time contributions. This is defined as the position independent time alignment of the PMT signal in reference to a global time. It can be determined through the calibration measurement by subtracting the modeled hit time, which only accounts for event position by time-of-flight subtraction:

$$t_0 = t_{hit,mes} - t_{hit,mod} = t_{hit,mes} - \bar{t}_{tof}. \tag{8.6}$$

The modeled hit time assumes the position of the injected light to be known as well as a hit on the middle of the PMTs cathode and no refraction at the AV. In order to estimate the accuracy with which t_0 can be determined, the *measured* hit time $t_{hit,mes}$ has to be simulated as detailed as possible. Regarding effects of photon propagation in the detector, the simulation framework was used. Events in a small spherical volume around the set position were generated to account for the uncertainty in the light source position. In addition the simulation accounts for refraction and the spatial extent of the photo-cathode. Thus, it can be used to sample t_{tof} for a realistic measurement. The photon emission time by the LED t_{LED} can be sampled from the measured spectrum and t_{PMT} follows a Gaussian distribution with a width given by the PMTs TTS of 1.5 ns. Since the absolute value of t_0 is not important for this study, t_{elec} is also sampled from a Gaussian distribution centered around zero with $\sigma = 1$ ns. Figure 8.15 shows the resulting distribution of t_0 for 10^4 SPE events for one PMT. The mean value is determined by fitting a Gaussian to the peak area. Repeating the procedure for 10^4 toy experiments, the distribution of the extracted t_0 is plotted in Figure 8.16. It shows that with this procedure and 10^4 events per PMT, the individual time offset t_0 can be determined with an uncertainty of $\sim$0.08 ns. Thus, the total timing resolution for position reconstruction is dominated by the innate PMT time uncertainty from its TTS with $\sigma = 1.5$ ns.

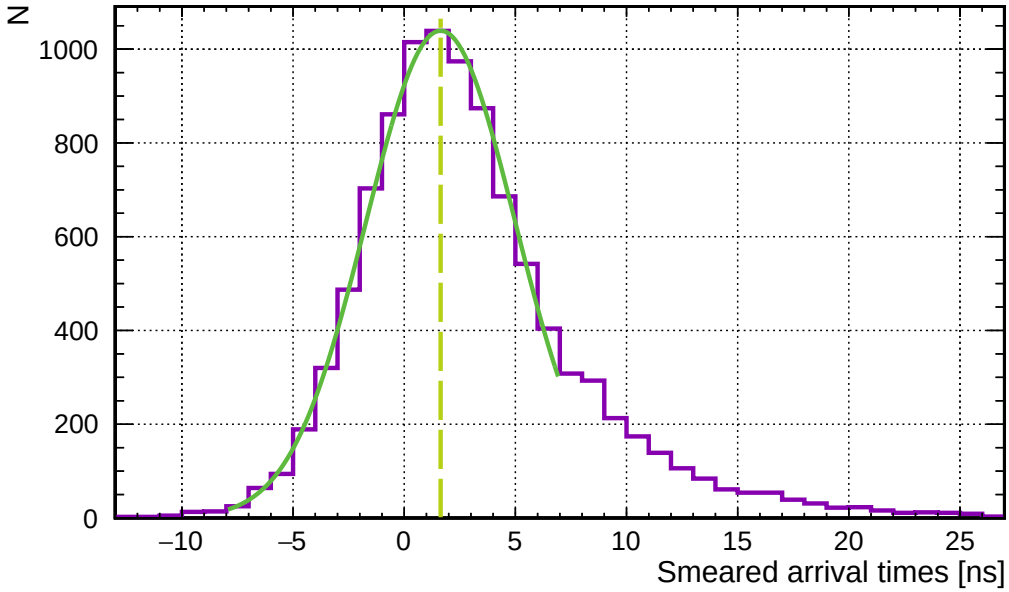

Figure 8.15 – Simulated arrival times of photons emitted by the calibration LED at $\rho = 120\,\text{cm}$ and $z = 0\,\text{cm}$. The constant offsets were subtracted and the mean (dashed green line) was determined by a Gaussian fit to the corresponding region. The main shape is governed by the LED emission time spectrum. Details about the included uncertainties are given in the text. The data for this plot was provided by A.G.

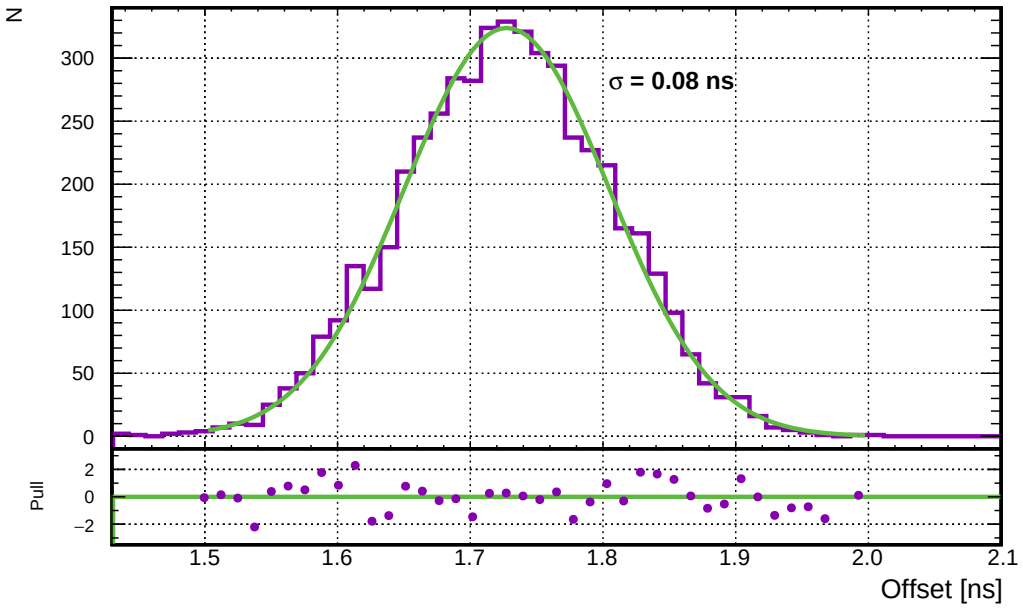

Figure 8.16 – Accuracy of the PMT timing calibration estimated from 10^4 experiments. The offset introduced by all elements mentioned in the text, can be determined with an uncertainty of $\sim$0.08 ns, if 10^4 SPE events are recorded in the calibration. The data for this plot was provided by A.G.

8.4 Calibration campaign

Based on the hardware considerations and simulation studies, a general calibration strategy was designed and proposed.
It was shown that one axis at $\rho = 120\,\text{cm}$ is sufficient for the purpose of OSIRIS. The high variation along this axis gives a strong handle to verify and tune the MC simulation. At the same time, the γ leakage is sufficiently small to provide an energy scale with only 1% uncertainty over the observed energy range.
The ACU provided by Daya Bay is perfectly suited for this application and will be integrated into OSIRIS. It can be mounted on top of the steel tank to provide the needed calibration axis. In addition, it is able to deploy a second capsule and a LIS based on a LED. Its control software can be adapted from the existing code and only needs new interfaces for communication with the other OSIRIS systems like the DAQ and run-control.
The combination of ^{137}Cs, ^{65}Zn, and ^{60}Co in one capsule for deployment by the ACU along the calibration axis can yield a sufficient energy calibration in a short time. The three peaks are well separated and cover the energy range of 0.5 - 5 MeV.
Furthermore, the second position of the ACU turntable can be used for an online-calibration. Given its low natural activity and clearly peaked spectrum, ^{40}K would be ideal for the purpose. A capsule containing an amount of potassium with a total activity of $\sim$0.1 Bq could be deployed permanently close the AV edge. Since it should not interfere with the measurement of Bi-Po-coincidences, it has to be placed outside the FV. In this setup, a change in light yield of 1% could be identified within one day. The deployment is controlled by the ACU, so that no other holding structure has to be introduced into the LS and the source can be pulled back into the ACU housing whenever needed.
Regarding the LIS, it would be ideal to implement both available systems. They do not interfere and can be used independently to cross-check each other. The LED injection via the third ACU turntable position can be used in the scope of a full calibration campaign before the start of data taking. In addition the faster laser system from the *Universität Tübingen* could be used on a daily or weekly basis for fine-tuning and stability monitoring of the time alignment.

Chapter 9

Conclusion and Outlook

The effect of flavor oscillations has been a focus in the field of neutrino physics in the last decades. With several experiments independently reporting results, that can be explain with flavor oscillations [5, 7, 14, 78, 148], it was widely accepted in the field. This minimal extension to the SM brings up the question about the ordering the three neutrino mass states. With the measurement of the non-zero mixing angle θ_{13} [20], the determination of the *neutrino mass ordering* (MO) through the vacuum oscillation of reactor anti-neutrinos became accessible. As a next-generation, 20 kton neutrino detector, JUNO was proposed to exploit this feature and measure the MO on a 53 km baseline. Large *research and development* (R&D) efforts in JUNO push the boundaries of PMT and LS performances to achieve its design goal. The LS mixture will be prepared and purified to feature a total attenuation length of more than 25 m. This enables the enormous size of a spherical LS vessel with 35.7 m diameter while maintaining an event topology, that allows for accurate position reconstruction and particle identification. Combined with an array of ∼18000 20-inch PMTs with a detection efficiency of close to 30%, the CD can claim an unprecedented energy resolution of $3\%/\sqrt{\mathrm{E[MeV]}}$. A secondary array of 3-inch PMTs provides an independent readout with a complimentary system to tackle systematic uncertainties and very large signals, that might saturate the large modules.

The first major focus of this thesis is the track reconstruction of muon events in the JUNO CD. In order to determine the MO, JUNO will make a precision measurement of the electron anti-neutrino spectrum from nuclear reactors. They are detected through the IBD reaction. Due JUNO's shallow depth, a high muon rate creates a large correlated background for the IBD measurement. Without any muon veto, the signal-to-background ratio is ∼1:1. A good knowledge of the muon tracks by a precise reconstruction can be used to define a veto cylinder around the track to remove those events. Thus, accurate muon tracking is paramount for JUNO, in order to achieve a favorable signal-to-background ratio of ∼16:1 [30]. Based on the time evolution of the first hits signal created by a traversing muon through the CD, I developed a novel tracking algorithm using a geometric approach. Instead of using hit times directly, it models the intersection of the first-light

cone with the PMT array and optimizes the track parameters with regard to the expected opening-angle of the cone. The model was then refined further to include additional effects like a spherical light emission at the bottom of the cone and Cherenkov light for the path when the muon exits the LS and enters the water-buffer. This likelihood fit was implemented in the JUNO *offline* software framework and its performance determined with use of the official `Geant4` MC simulation. Under consideration of both PMT arrays individually and their combination, with and without the simulation of electronics effects, the best results are achieved when the systems are combined. In this case, the muon track's distance from the detector center ΔD can be determined with an uncertainty of 5 cm and its direction with 0.3 °. Furthermore, I developed a muon veto simulation to quantify the impact of the tracking's imperfection on the detector deadtime. The `C++` code evaluates the vetoed volume around muon tracks under consideration of parameterized biases and resolutions introduced by the reconstruction. It was shown, that the herein presented algorithm reduces the detector's exposure only by 4% in comparison to a prefect tracking. The algorithm can be applied to other LS detectors and a comprehensive report was published in the *Journal of Instrumentation* [111].

In the second part of this work, the *Online Scintillator Internal Radioactivity Investigation System* (OSIRIS) is studied. It is a standalone 20 ton LS detector, that will monitor the radiopurity of the LS, while it is filled into the JUNO CD. As a sub-project of JUNO, its further goals are of a supportive nature, to aid in the commissioning of the LS purification plants and to undertake long-time LS measurements.
As the first step in the design of an experiment, a full detector simulation based on `C++` and `Geant4` was developed in this thesis. In close collaboration with *Sebastian Lorenz*, the software was designed to be easy to use for physics studies and accessible for developers. Thus, it features different simulation modes, which are tailored to a certain physics case and are customizable through *macro* files. Furthermore, I implemented a dedicated mode for *geometric importance sampling*, to increase the simulation efficiency of external background. This *biasing method* copies or removes tracked particles, in order to increase the number of events in the region of interest. Other key features of the simulation are a sophisticated optical model with an implementation of a custom scintillation process and a detector geometry, that includes all influential structural details.
Then, I used the simulation to estimate the detector's sensitivity to its main physics goal: monitoring the contamination of ^{238}U and ^{232}Th in the LS. The analysis follows a statistical approach, in which all relevant background spectra for internal and external backgrounds are build from events created with the detector simulation. They are then scaled with the corresponding volume's specific activity and total mass. Furthermore, out-of-equilibrium contamination for ^{210}Bi and ^{210}Po in the LS is considered and an increased Radon rate in the water-shield by emanation from the surrounding materials. The signals are coincidence decays of ^{214}Bi and ^{214}Po for ^{238}U and of ^{212}Bi and ^{212}Po for ^{232}Th. The event selection is based on a set four cuts. After defining a *fiducial volume*, only events in the energy regions for Bi and Po are selected. In addition, the timing between both events is considered as well as the spatial distance in the detector. Due to correlation of the efficiencies, the cuts were optimized for best sensitivity, using a

grid search algorithm. In the course of the development of the detector, different setups regarding the number and placement of PMTs were studied. The best setup yields a 90% CL sensitivity of $2.8 \times 10^{-16}\,\mathrm{g/g}$ for ^{238}U and $7.3 \times 10^{-16}\,\mathrm{g/g}$ for ^{232}Th within a 24 h measurement in the monitoring mode. Thus, OSIRIS can reach its goal to monitor both decay chains to a limit of $1 \times 10^{-15}\,\mathrm{g/g}$ within a few hours. Confirming a LS cleanliness of $1 \times 10^{-16}\,\mathrm{g/g}$, which is needed for the study of solar neutrinos in JUNO, a measurement longer than one day has to be averaged for several batches of LS. This study proved critical to the definition of key features in the detector design, since the sensitivity to Bi-Po identification is its main goal.
Finally, I explored strategies to calibrate the OSIRIS detector. Based on different hardware limitations, the decision was made to re-purpose an *automated calibration unit* (ACU) from the Daya Bay collaboration. The device can deploy three different cables with sources along one vertical axis in the detector. Since the central axis is not accessible, as it is used for continuous filling, the ideal position of this vertical axis was determined to be at a radial distance $\rho = 120\,\mathrm{cm}$. At this position, the shift from γ-leakage of the measured peak with regard to the full absorption peak is below 2%. Simultaneously, it allows to probe the largest variation in the detector's uniformity of ∼10%. The choice of gamma-emitters as calibration sources is based on availability and achievable activity. In order to minimize the calibration time, one source capsule with three isotopes will be used for energy calibration. The range between 0.5 MeV and 3 MeV will be calibrated with ^{137}Cs, ^{65}Zn, and ^{60}Co, as their spectra do not overlap and, thus, can be be fitted accurately. The second source position of the ACU is foreseen to be used as a constant, low-activity ^{40}K source, deployed at the edge of the detector to monitor changes over time. For the third source in the ACU, a light injection system based on a 430 nm LED was investigated. According to the presented simulation, it can be used for time alignment of the PMTs with an accuracy better than 0.1 ns. In combination, this configuration of the ACU allows for a comprehensive calibration strategy for OSIRIS.

In the scope of this thesis, I was able to explore and influence to development of a next-generation LS neutrino detector from several different angles. A low-level reconstruction algorithm, like the presented muon tracking, warrants a good understanding of the available readout systems and capabilities of the hardware. For the estimation of its impact on the physics goal of JUNO to determine the MO, also the many different sources and topologies of backgrounds were studied. In addition, the simulation and analysis of a detector with ∼42000 channels lead to many insights about the design of efficient software with regard to data handling. In the future, when a baseline for event reconstruction is defined, the presented algorithm is likely to be improved and combined with other reconstructions to work on real data.
The studies on the OSIRIS pre-detector, dedicated to verifying the cleanliness of the JUNO LS, were even more comprehensive. As a part of a smaller sub-group from the start of the project, I could further improve my coding capabilities in the development of a modern, standalone detector simulation software from scratch. Using this tool, I was able to get experience with a high-level physics analysis by studying the sensitivity to Bi-Po coincidences. In the future, the simulation and this study will be updated to the

final detector design and extended to account for even more effects.
While the work on the calibration campaign for the detector started on the base of simulations, it was crucial to consider aspects of the hardware as well. Only the hands-on investigation of the ACU and the factors that lead to the decision to use it in OSIRIS could be presented in this thesis. Nevertheless, the next steps include preparation of the unit with new deployment cables, calibration of its wheel's diameters, and defining a cleaning procedure for the system. In parallel, the control software to automatically deploy sources and monitor the unit's state is developed.

Appendix A

Inputs for the OSIRIS detector simulation

The OSIRIS detector simulation uses input spectra for the simulation of external background in the `BkgEdep` mode. For all volumes outside the acrylic vessel, only gammas are considered, since α and β particles cannot penetrate the vessel to reach the LS. When generating primary gammas, the simulation samples the energies from the given input spectra. The decay chains of ^{238}U and ^{232}Th are shown in Figures 6.1 and 6.2, respectively. The information about the accompanying γ-emissions from excited states of the daughter isotope are taken from Ref. [124]. In the spectra, only gammas energies larger than 250 keV are considered. The fact that several gammas can be emitted along the chain is accounted for in the subsequent analysis and scaling of the high-statistics spectra.

For the simulation of additional Radon the water shield of OSIRIS, only the parts of the decay chains after Radon have to be considered. Thus, the spectra are built accordingly.

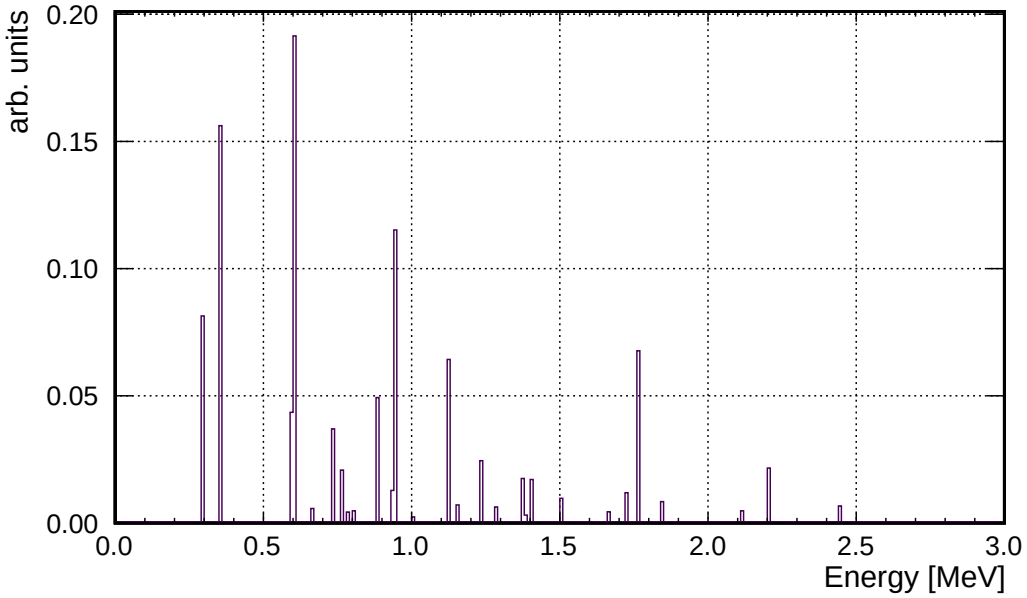

Figure A.1 – Input γ spectrum of the ^{238}U chain for external backgrounds in the OSIRIS detector simulation.

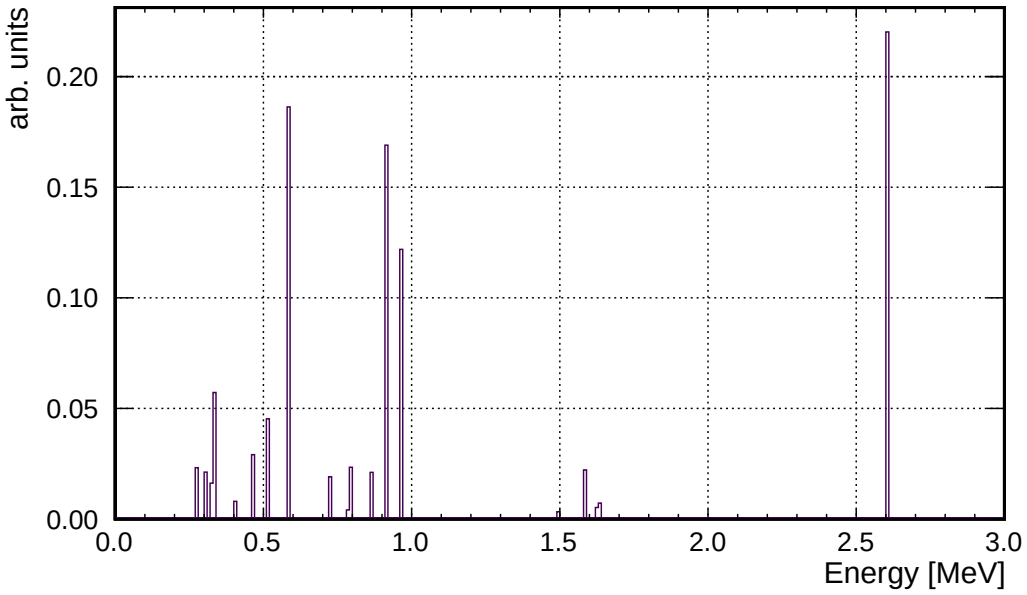

Figure A.2 – Input γ spectrum of the ^{232}Th chain for external backgrounds in the OSIRIS detector simulation.

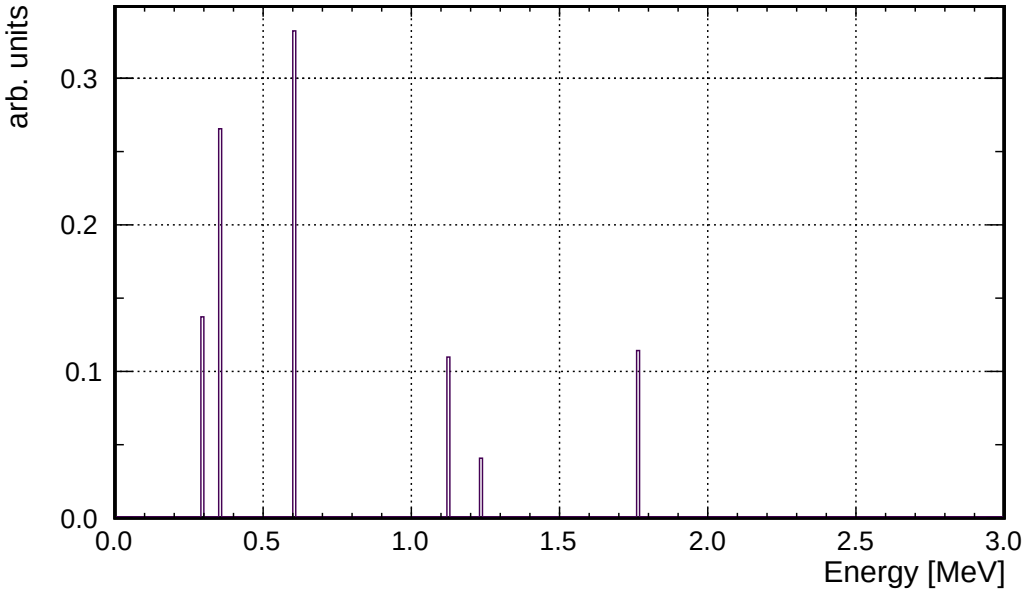

Figure A.3 – Input γ spectrum of the ^{222}Rn chain for Radon contamination of the water shield in the OSIRIS detector simulation.

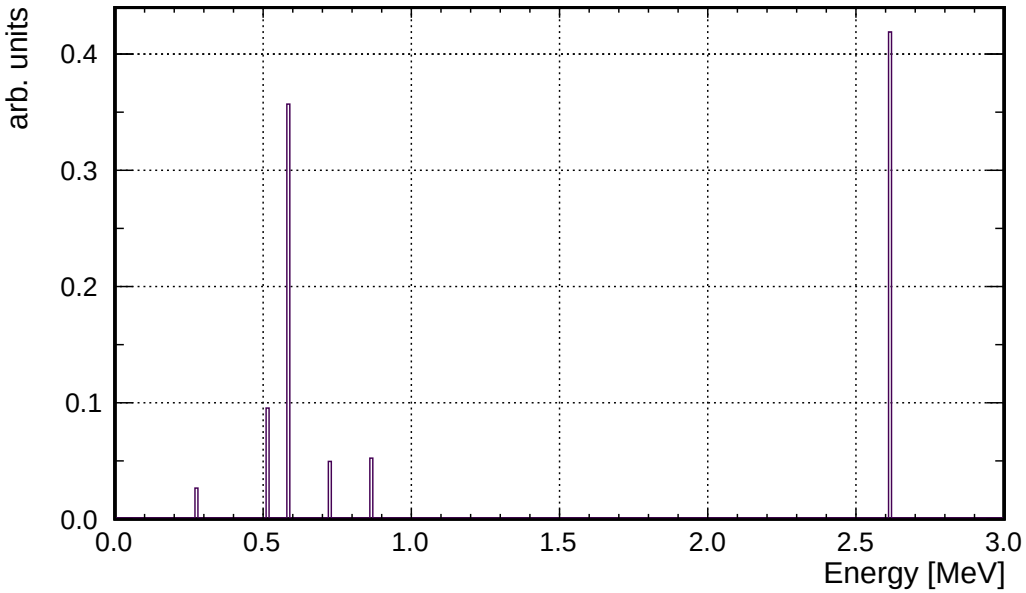

Figure A.4 – Input γ spectrum of the ^{220}Rn chain for Radon contamination of the water shield in the OSIRIS detector simulation.

Appendix B

Radon emanation into the OSIRIS water shield

As described in Section 7.4, the increased total singles rate of background events involve a new set of optimized selection cuts for the Bi-Po-coincidence. While Table 7.5 gives the exact values, the changed energy windows in comparison to the total rate is shown in Figure B.1.

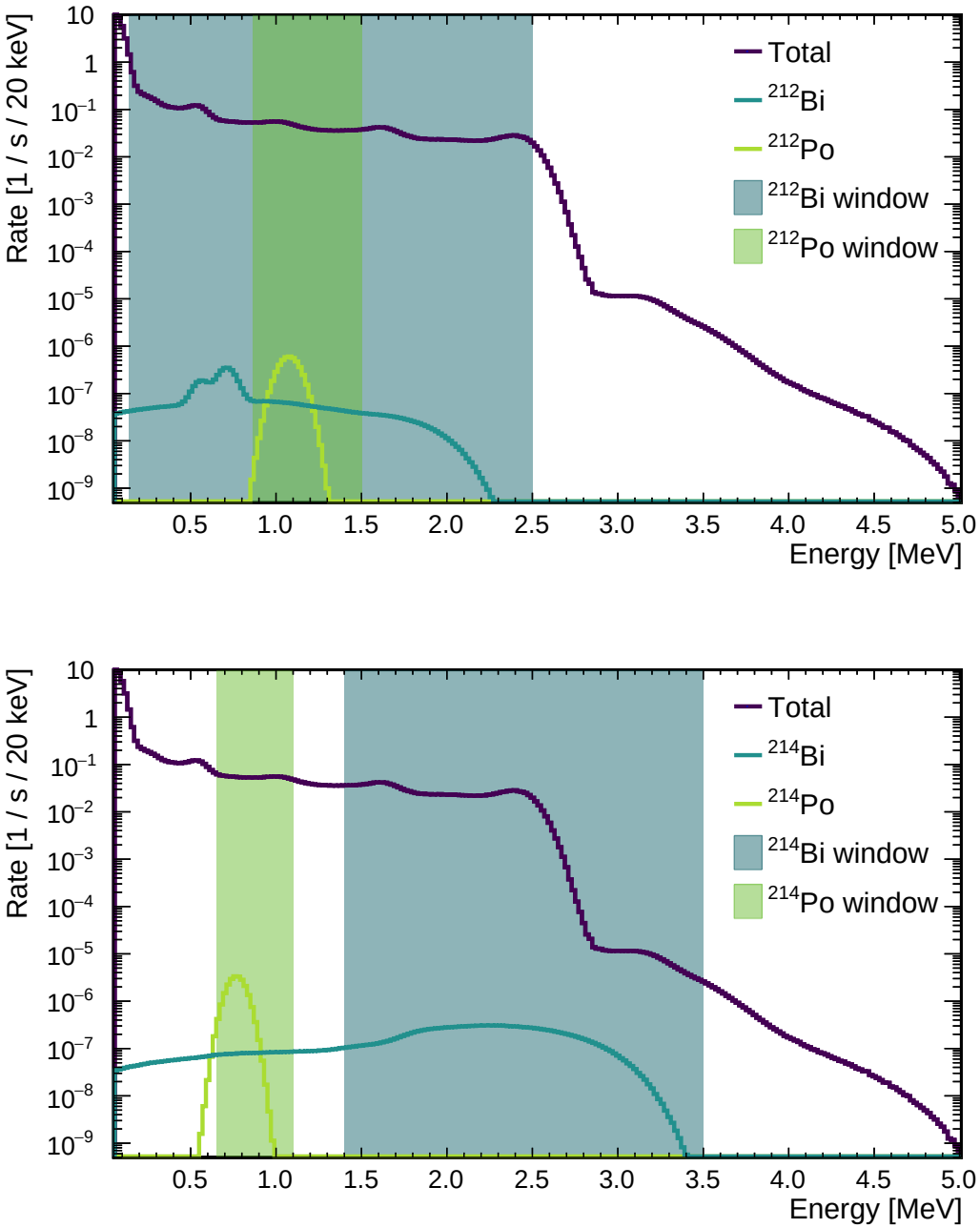

Figure B.1 – Energy spectra of the ^{212}Bi-^{212}Po (*top*) and ^{214}Bi-^{214}Po (*bottom*) decays in comparison to the total singles rate. An additional Radon contamination in the water of 550 $^{\mathrm{mBq}}/_{\mathrm{m}^3}$ for ^{222}Rn and 3.9 $^{\mathrm{mBq}}/_{\mathrm{m}^3}$ for ^{220}Rn was assumed. The optimized energy cut windows are drawn in green for the α decay of Po and in blue for the β spectrum of Bi.

List of Figures

List of Tables

Bibliography

[1] M. Tanabashi et al. “Review of Particle Physics”. In: *Phys. Rev. D* 98 (3 Aug. 2018), p. 030001. DOI: 10.1103/PhysRevD.98.030001. URL: https://link.aps.org/doi/10.1103/PhysRevD.98.030001.

[2] John N. Bahcall and R. Davis. “Solar Neutrinos - a Scientific Puzzle”. In: *Science* 191 (1976). [,141(1976)], pp. 264–267. DOI: 10.1126/science.191.4224.264.

[3] B. T. Cleveland et al. “Measurement of the solar electron neutrino flux with the Homestake chlorine detector”. In: *Astrophys. J.* 496 (1998), pp. 505–526. DOI: 10.1086/305343.

[4] John N. Bahcall. “Solar models: An Historical overview”. In: *AAPPS Bull.* 12.4 (2002). [Int. J. Mod. Phys.A18,3761(2003)], pp. 12–19. DOI: 10.1016/S0920-5632(03)01306-9. arXiv: astro-ph/0209080 [astro-ph].

[5] K. Abe et al. “Evidence of Electron Neutrino Appearance in a Muon Neutrino Beam”. In: *Phys. Rev.* D88.3 (2013), p. 032002. DOI: 10.1103/PhysRevD.88.032002. arXiv: 1304.0841 [hep-ex].

[6] J. Boger et al. “The Sudbury neutrino observatory”. In: *Nucl. Instrum. Meth.* A449 (2000), pp. 172–207. DOI: 10.1016/S0168-9002(99)01469-2. arXiv: nucl-ex/9910016 [nucl-ex].

[7] Q. R. Ahmad et al. “Direct Evidence for Neutrino Flavor Transformation from Neutral-Current Interactions in the Sudbury Neutrino Observatory”. In: *Phys. Rev. Lett.* 89 (1 June 2002), p. 011301. DOI: 10.1103/PhysRevLett.89.011301. URL: https://link.aps.org/doi/10.1103/PhysRevLett.89.011301.

[8] Y. Fukuda et al. “The Super-Kamiokande detector”. In: *Nucl. Instrum. Meth.* A501 (2003), pp. 418–462. DOI: 10.1016/S0168-9002(03)00425-X.

[9] S. Fukuda et al. “Solar B-8 and hep neutrino measurements from 1258 days of Super-Kamiokande data”. In: *Phys. Rev. Lett.* 86 (2001), pp. 5651–5655. DOI: 10.1103/PhysRevLett.86.5651. arXiv: hep-ex/0103032 [hep-ex].

[10] Masami Nakagawa, Shoichi Sakata, and Ziro Maki. “Remarks on the Unified Model of Elementary Particles”. In: *Progress of Theoretical Physics* 28.5 (Nov. 1962), pp. 870–880. ISSN: 0033-068X. DOI: 10.1143/PTP.28.870. eprint: http://oup.prod.sis.lan/ptp/article-pdf/28/5/870/5258750/28-5-870.pdf. URL: https://dx.doi.org/10.1143/PTP.28.870.

[11] B. Pontecorvo. "Neutrino Experiments and the Problem of Conservation of Leptonic Charge". In: *Sov. Phys. JETP* 26 (1968). [Zh. Eksp. Teor. Fiz.53,1717(1967)], pp. 984–988.

[12] Michael Soiron. "The sensitivity of liquid scintillator detectorsfor the measurement of the neutrino masshierarchy with atmospheric neutrinosVeröffentlicht auf dem Publikationsserver der RWTH Aachen University". Veröffentlicht auf dem Publikationsserver der RWTH Aachen University; Dissertation, RWTH Aachen University, 2017. Dissertation. Aachen: RWTH Aachen University, 2017. DOI: 10.18154/RWTH-2017-07139. URL: https://publications.rwth-aachen.de/record/697535.

[13] P. Alivisatos et al. "KamLAND: A Liquid scintillator anti-neutrino detector at the Kamioka site". In: (1998).

[14] Y. Fukuda et al. "Evidence for oscillation of atmospheric neutrinos". In: *Phys. Rev. Lett.* 81 (1998), pp. 1562–1567. DOI: 10.1103/PhysRevLett.81.1562. arXiv: hep-ex/9807003 [hep-ex].

[15] K. Abe et al. "The T2K Experiment". In: *Nucl. Instrum. Meth.* A659 (2011), pp. 106–135. DOI: 10.1016/j.nima.2011.06.067. arXiv: 1106.1238 [physics.ins-det].

[16] P. Adamson et al. "A Study of Muon Neutrino Disappearance Using the Fermilab Main Injector Neutrino Beam". In: *Phys. Rev.* D77 (2008), p. 072002. DOI: 10.1103/PhysRevD.77.072002. arXiv: 0711.0769 [hep-ex].

[17] Xinheng Guo et al. "A Precision measurement of the neutrino mixing angle θ_{13} using reactor antineutrinos at Daya-Bay". In: (2007). arXiv: hep-ex/0701029 [hep-ex].

[18] F. Ardellier et al. "Double Chooz: A Search for the neutrino mixing angle theta(13)". In: (2006). arXiv: hep-ex/0606025 [hep-ex].

[19] J. K. Ahn et al. "RENO: An Experiment for Neutrino Oscillation Parameter θ_{13} Using Reactor Neutrinos at Yonggwang". In: (2010). arXiv: 1003.1391 [hep-ex].

[20] F. P. An et al. "Observation of electron-antineutrino disappearance at Daya Bay". In: *Phys. Rev. Lett.* 108 (2012), p. 171803. DOI: 10.1103/PhysRevLett.108.171803. arXiv: 1203.1669 [hep-ex].

[21] D. S. Ayres et al. "NOvA: Proposal to build a 30 kiloton off-axis detector to study nu(mu) —> nu(e) oscillations in the NuMI beamline". In: (2004). arXiv: hep-ex/0503053 [hep-ex].

[22] K. N. Deepthi, Soumya C, and R. Mohanta. "Revisiting the sensitivity studies for leptonic CP-violation and mass hierarchy with T2K, NOnuA and LBNE experiments". In: *New J. Phys.* 17.2 (2015), p. 023035. DOI: 10.1088/1367-2630/17/2/023035. arXiv: 1409.2343 [hep-ph].

[23] R. Acciarri et al. "Long-Baseline Neutrino Facility (LBNF) and Deep Underground Neutrino Experiment (DUNE)". In: (2016). arXiv: 1601.02984 [physics.ins-det].

[24] R. Acciarri et al. "Long-Baseline Neutrino Facility (LBNF) and Deep Underground Neutrino Experiment (DUNE)". In: (2015). arXiv: 1512.06148 [physics.ins-det].

[25] Veronique Van Elewyck. "ORCA: measuring the neutrino mass hierarchy with atmospheric neutrinos in the Mediterranean". In: *J. Phys. Conf. Ser.* 598.1 (2015), p. 012033. DOI: 10.1088/1742-6596/598/1/012033.

[26] M. G. Aartsen et al. "Letter of Intent: The Precision IceCube Next Generation Upgrade (PINGU)". In: (2014). arXiv: 1401.2046 [physics.ins-det].

[27] K. Abe et al. "A Long Baseline Neutrino Oscillation Experiment Using J-PARC Neutrino Beam and Hyper-Kamiokande". In: 2014. arXiv: 1412.4673 [physics.ins-det]. URL: http://inspirehep.net/record/1334360/files/arXiv:1412.4673.pdf.

[28] K. Abe et al. "Measurement of neutrino and antineutrino oscillations by the T2K experiment including a new additional sample of ν_e interactions at the far detector". In: *Phys. Rev.* D96.9 (2017). [Erratum: Phys. Rev.D98,no.1,019902(2018)], p. 092006. DOI: 10.1103/PhysRevD.96.092006,10.1103/PhysRevD.98.019902. arXiv: 1707.01048 [hep-ex].

[29] M. A. Acero et al. "New constraints on oscillation parameters from ν_e appearance and ν_μ disappearance in the NOvA experiment". In: *Phys. Rev.* D98 (2018), p. 032012. DOI: 10.1103/PhysRevD.98.032012. arXiv: 1806.00096 [hep-ex].

[30] Fengpeng An et al. "Neutrino Physics with JUNO". In: (2015). arXiv: 1507.05613 [physics.ins-det].

[31] Ivan Esteban et al. "Global analysis of three-flavour neutrino oscillations: synergies and tensions in the determination of $\theta_2 3, \delta_C P$, and the mass ordering". In: *JHEP* 01 (2019), p. 106. DOI: 10.1007/JHEP01(2019)106. arXiv: 1811.05487 [hep-ph].

[32] J. A. Formaggio and G. P. Zeller. "From eV to EeV: Neutrino Cross Sections Across Energy Scales". In: *Rev. Mod. Phys.* 84 (2012), pp. 1307–1341. DOI: 10.1103/RevModPhys.84.1307. arXiv: 1305.7513 [hep-ex].

[33] John F. Beacom, Will M. Farr, and Petr Vogel. "Detection of supernova neutrinos by neutrino proton elastic scattering". In: *Phys. Rev.* D66 (2002), p. 033001. DOI: 10.1103/PhysRevD.66.033001. arXiv: hep-ph/0205220 [hep-ph].

[34] K. Zuber. *Neutrino Physics, Second Edition (Series in High Energy Physics, Cosmology and Gravitation)*. CRC Press, 2011.

[35] P. Vogel and J. F. Beacom. "Angular distribution of neutron inverse beta decay, $\overline{\nu}_e + \overrightarrow{p} \; e^+ + n$". In: *Phys. Rev. D* 60 (5 July 1999), p. 053003. DOI: 10.1103/PhysRevD.60.053003. URL: https://link.aps.org/doi/10.1103/PhysRevD.60.053003.

[36] Soo-Bong Kim, Thierry Lasserre, and Yifang Wang. "Reactor neutrinos". In: *Adv. High Energy Phys.* 2013 (2013), p. 453816. DOI: 10.1155/2013/453816.

[37] Philipp Soldin. "Improved measurement of the neutrino mixing angle theta13 with the Double Chooz experiment". RWTH Aachen University, July 2017. URL: %7Bhttp://www.institut3b.physik.rwth-aachen.de/global/show_document.asp?id=aaaaaaaaaaxulrt%7D.

[38] M. Agostini et al. “Comprehensive measurement of *pp*-chain solar neutrinos”. In: *Nature* 562.7728 (2018), pp. 505–510. DOI: 10.1038/s41586-018-0624-y.

[39] M. G. Aartsen et al. “Evidence for High-Energy Extraterrestrial Neutrinos at the IceCube Detector”. In: *Science* 342 (2013), p. 1242856. DOI: 10.1126/science.1242856. arXiv: 1311.5238 [astro-ph.HE].

[40] Patrick Huber and Thomas Schwetz. “Precision spectroscopy with reactor antineutrinos”. In: *Phys. Rev. D* 70 (5 Sept. 2004), p. 053011. DOI: 10.1103/PhysRevD.70.053011. URL: https://link.aps.org/doi/10.1103/PhysRevD.70.053011.

[41] Liang Zhan et al. “Determination of the Neutrino Mass Hierarchy at an Intermediate Baseline”. In: *Phys. Rev.* D78 (2008), p. 111103. DOI: 10.1103/PhysRevD.78.111103. arXiv: 0807.3203 [hep-ex].

[42] Patrick Huber. “Determination of antineutrino spectra from nuclear reactors”. In: *Phys. Rev. C* 84 (2 Aug. 2011), p. 024617. DOI: 10.1103/PhysRevC.84.024617. URL: https://link.aps.org/doi/10.1103/PhysRevC.84.024617.

[43] Th. A. Mueller et al. “Improved Predictions of Reactor Antineutrino Spectra”. In: *Phys. Rev.* C83 (2011), p. 054615. DOI: 10.1103/PhysRevC.83.054615. arXiv: 1101.2663 [hep-ex].

[44] G. Mention et al. “The Reactor Antineutrino Anomaly”. In: *Phys. Rev.* D83 (2011), p. 073006. DOI: 10.1103/PhysRevD.83.073006. arXiv: 1101.2755 [hep-ex].

[45] Naumov, Dmitry V. “Recent results from Daya Bay experiment”. In: *EPJ Web of Conferences* 95 (2015), p. 04043. DOI: 10.1051/epjconf/20149504043. URL: https://doi.org/10.1051/epjconf/20149504043.

[46] J. I. Crespo-Anadón. “Double Chooz: Latest results”. In: *Nucl. Part. Phys. Proc.* 265-266 (2015), pp. 99–104. DOI: 10.1016/j.nuclphysbps.2015.06.025. arXiv: 1412.3698 [hep-ex].

[47] Seon-Hee Seo. “New Results from RENO and The 5 MeV Excess”. In: *AIP Conf. Proc.* 1666 (2015), p. 080002. DOI: 10.1063/1.4915563. arXiv: 1410.7987 [hep-ex].

[48] Feng Peng An et al. “Measurement of the Reactor Antineutrino Flux and Spectrum at Daya Bay”. In: *Phys. Rev. Lett.* 116.6 (2016). [Erratum: Phys. Rev. Lett.118,no.9,099902(2017)], p. 061801. DOI: 10.1103/PhysRevLett.116.061801, 10.1103/PhysRevLett.118.099902. arXiv: 1508.04233 [hep-ex].

[49] D. A. Dwyer and T. J. Langford. “Spectral Structure of Electron Antineutrinos from Nuclear Reactors”. In: *Phys. Rev. Lett.* 114.1 (2015), p. 012502. DOI: 10.1103/PhysRevLett.114.012502. arXiv: 1407.1281 [nucl-ex].

[50] David V. Forero, Rebekah Hawkins, and Patrick Huber. “The benefits of a near detector for JUNO”. In: (2017). arXiv: 1710.07378 [hep-ph].

[51] Liang Zhan. *Proposal of a Near Detector for JUNO Experiment*. June 2018. DOI: 10.5281/zenodo.1314423. URL: https://doi.org/10.5281/zenodo.1314423.

[52] P. A. R. Ade et al. “Planck 2015 results. XIII. Cosmological parameters”. In: *Astron. Astrophys.* 594 (2016), A13. DOI: 10.1051/0004-6361/201525830. arXiv: 1502.01589 [astro-ph.CO].

[53] Christian Weinheimer and Kai Zuber. “Neutrino Masses”. In: *Annalen Phys.* 525.8-9 (2013), pp. 565–575. DOI: 10.1002/andp.201300063. arXiv: 1307.3518 [hep-ex].

[54] Stefano Dell’Oro, Simone Marcocci, and Francesco Vissani. “New expectations and uncertainties on neutrinoless double beta decay”. In: *Phys. Rev.* D90.3 (2014), p. 033005. DOI: 10.1103/PhysRevD.90.033005. arXiv: 1404.2616 [hep-ph].

[55] Ch. Kraus et al. “Final results from phase II of the Mainz neutrino mass search in tritium beta decay”. In: *Eur. Phys. J.* C40 (2005), pp. 447–468. DOI: 10.1140/epjc/s2005-02139-7. arXiv: hep-ex/0412056 [hep-ex].

[56] V. N. Aseev et al. “An upper limit on electron antineutrino mass from Troitsk experiment”. In: *Phys. Rev.* D84 (2011), p. 112003. DOI: 10.1103/PhysRevD.84.112003. arXiv: 1108.5034 [hep-ex].

[57] J. Angrik et al. “KATRIN design report 2004”. In: (2005).

[58] Ali Ashtari Esfahani et al. “Determining the neutrino mass with cyclotron radiation emission spectroscopy—Project 8”. In: *J. Phys.* G44.5 (2017), p. 054004. DOI: 10.1088/1361-6471/aa5b4f. arXiv: 1703.02037 [physics.ins-det].

[59] A. Nucciotti et al. “Status of the HOLMES Experiment to Directly Measure the Neutrino Mass”. In: *J. Low. Temp. Phys.* 193.5-6 (2018), pp. 1137–1145. DOI: 10.1007/s10909-018-2025-x. arXiv: 1807.09269 [physics.ins-det].

[60] Janet M. Conrad, William C. Louis, and Michael H. Shaevitz. “The LSND and MiniBooNE Oscillation Searches at High Δm^2”. In: *Ann. Rev. Nucl. Part. Sci.* 63 (2013), pp. 45–67. DOI: 10.1146/annurev-nucl-102711-094957. arXiv: 1306.6494 [hep-ex].

[61] F. Kaether et al. “Reanalysis of the GALLEX solar neutrino flux and source experiments”. In: *Phys. Lett.* B685 (2010), pp. 47–54. DOI: 10.1016/j.physletb.2010.01.030. arXiv: 1001.2731 [hep-ex].

[62] J. N. Abdurashitov et al. “Measurement of the response of the Russian-American gallium experiment to neutrinos from a Cr-51 source”. In: *Phys. Rev.* C59 (1999), pp. 2246–2263. DOI: 10.1103/PhysRevC.59.2246. arXiv: hep-ph/9803418 [hep-ph].

[63] J. N. Abdurashitov et al. “Measurement of the response of a Ga solar neutrino experiment to neutrinos from an Ar-37 source”. In: *Phys. Rev.* C73 (2006), p. 045805. DOI: 10.1103/PhysRevC.73.045805. arXiv: nucl-ex/0512041 [nucl-ex].

[64] Carlo Giunti and Marco Laveder. “Statistical Significance of the Gallium Anomaly”. In: *Phys. Rev.* C83 (2011), p. 065504. DOI: 10.1103/PhysRevC.83.065504. arXiv: 1006.3244 [hep-ph].

[65] G. Bellini et al. “SOX: Short distance neutrino Oscillations with BoreXino”. In: *JHEP* 08 (2013), p. 038. DOI: 10.1007/JHEP08(2013)038. arXiv: 1304.7721 [physics.ins-det].

[66] Mikhail Danilov. “Searches for sterile neutrinos at very short baseline reactor experiments”. In: *4th International Conference on Particle Physics and Astrophysics (ICPPA 2018) Moscow, Russia, October 22-26, 2018*. 2018. arXiv: 1812.04085 [hep-ex].

[67] William R. Leo. *Techniques for Nuclear and Particle Physics Experiments - A How-to Approach*. Springer-Verlag Berlin Heidelberg, 1994. DOI: 10.1007/978-3-642-57920-2.

[68] J.B. Birks. *The Theory and Practice of Scintillation Counting*. International Series of Monographs in Electronics and Instrumentation. Pergamon, 1964. DOI: 10.1016/C2013-0-01791-4.

[69] G. Ranucci, A. Goretti, and P. Lombardi. “Pulse-shape discrimination of liquid scintillators”. In: *Nucl. Instrum. Meth.* A412 (1998), pp. 374–386. DOI: 10.1016/S0168-9002(98)00456-2.

[70] J D Jackson. *Klassische Elektrodynamik*. Berlin, New York: Walter de Gruyter, 1983.

[71] J. R. Alonso et al. “Advanced Scintillator Detector Concept (ASDC): A Concept Paper on the Physics Potential of Water-Based Liquid Scintillator”. In: (2014). arXiv: 1409.5864 [physics.ins-det].

[72] Vincent Fischer. “Theia: A multi-purpose water-based liquid scintillator detector”. In: *13th Conference on the Intersections of Particle and Nuclear Physics (CIPANP 2018) Palm Springs, California, USA, May 29-June 3, 2018*. 2018. arXiv: 1809.05987 [physics.ins-det].

[73] Michael Wurm et al. “Optical Scattering Lengths in Large Liquid-Scintillator Neutrino Detectors”. In: *Rev. Sci. Instrum.* 81 (2010), p. 053301. DOI: 10.1063/1.3397322. arXiv: 1004.0811 [physics.ins-det].

[74] *Photomultiplier Tubes - Basics and Applications*. 3a. Hamamatsu Photonics K. K. 2007. URL: https://www.hamamatsu.com/resources/pdf/etd/PMT_handbook_v3aE.pdf.

[75] Hamamatsu Photonics K.K. URL: %7Bhttps://www.hamamatsu.com/eu/en/product/optical-sensors/pmt/about_pmts/index.html%7D (visited on 03/19/2019).

[76] R. S. Vallery, P. W. Zitzewitz, and D. W. Gidley. “Resolution of the Orthopositronium-Lifetime Puzzle”. In: *Phys. Rev. Lett.* 90 (20 May 2003), p. 203402. DOI: 10.1103/PhysRevLett.90.203402. URL: https://link.aps.org/doi/10.1103/PhysRevLett.90.203402.

[77] F. Reines and C. L. Cowan. "Detection of the Free Neutrino". In: *Phys. Rev.* 92 (3 Nov. 1953), pp. 830–831. DOI: 10.1103/PhysRev.92.830. URL: https://link.aps.org/doi/10.1103/PhysRev.92.830.

[78] K. Eguchi et al. "First results from KamLAND: Evidence for reactor antineutrino disappearance". In: *Phys. Rev. Lett.* 90 (2003), p. 021802. DOI: 10.1103/PhysRevLett.90.021802. arXiv: hep-ex/0212021 [hep-ex].

[79] G. Bellini et al. "Final results of Borexino Phase-I on low energy solar neutrino spectroscopy". In: *Phys. Rev.* D89.11 (2014), p. 112007. DOI: 10.1103/PhysRevD.89.112007. arXiv: 1308.0443 [hep-ex].

[80] S. Andringa et al. "Current Status and Future Prospects of the SNO+ Experiment". In: *Adv. High Energy Phys.* 2016 (2016), p. 6194250. DOI: 10.1155/2016/6194250. arXiv: 1508.05759 [physics.ins-det].

[81] Michael Wurm et al. "The next-generation liquid-scintillator neutrino observatory LENA". In: *Astropart. Phys.* 35 (2012), pp. 685–732. DOI: 10.1016/j.astropartphys.2012.02.011. arXiv: 1104.5620 [astro-ph.IM].

[82] Zelimir Djurcic et al. "JUNO Conceptual Design Report". In: (2015). arXiv: 1508.07166 [physics.ins-det].

[83] De-Wen Cao et al. "Light Absorption Properties of the High Quality Linear Alkylbenzene for the JUNO Experiment". In: *Nucl. Instrum. Meth.* A927 (2019), pp. 230–235. DOI: 10.1016/j.nima.2019.01.077. arXiv: 1801.08363 [physics.ins-det].

[84] P. Lombardi et al. "Distillation and stripping pilot plants for the JUNO neutrino detector: Design, operations and reliability". In: *Nuclear Instruments and Methods in Physics Research Section A: Accelerators, Spectrometers, Detectors and Associated Equipment* 925 (2019), pp. 6–17. ISSN: 0168-9002. DOI: https://doi.org/10.1016/j.nima.2019.01.071. URL: http://www.sciencedirect.com/science/article/pii/S0168900219301299.

[85] Miao He. "Double Calorimetry System in JUNO". In: *Proceedings of International Conference on Technology and Instrumentation in Particle Physics 2017 (TIPP2017), Beijing, China, May 22-26, 2017*. 2017. arXiv: 1706.08761 [physics.ins-det].

[86] N. Anfimov. "Large photocathode 20-inch PMT testing methods for the JUNO experiment". In: *JINST* 12.06 (2017), p. C06017. DOI: 10.1088/1748-0221/12/06/C06017. arXiv: 1705.05012 [physics.ins-det].

[87] Alexander TIETZSCH. *The PMT Mass Testing System for JUNO*. June 2018. DOI: 10.5281/zenodo.1300494. URL: https://doi.org/10.5281/zenodo.1300494.

[88] Liangjian Wen. *Characterization of the 20-inch Photomultiplier Tubes for the JUNO Central Detector*. July 2018. URL: https://pos.sissa.it/340/.

[89] M Güler et al. *An appearance experiment to search for $\nu_\mu\nu_\tau$ oscillations in the CNGS beam: experimental proposal*. Tech. rep. CERN-SPSC-2000-028. LNGS-2000-25. SPSC-P-318. Geneva: CERN, July 2000. URL: https://cds.cern.ch/record/456523.

[90] T. Adam et al. "The OPERA experiment Target Tracker". In: *Nucl.Instrum.Meth.* A577 (2007), pp. 523–539. arXiv: physics/0701153.

[91] G. Ranucci and E. Meroni. "Counting test facility for the Borexino experiment". In: *International Journal of Modern Physics A* 29.16 (2014), p. 1442001. DOI: 10.1142/S0217751X14420019. eprint: https://doi.org/10.1142/S0217751X14420019. URL: https://doi.org/10.1142/S0217751X14420019.

[92] R. Brun and F. Rademakers. "ROOT: An object oriented data analysis framework". In: *Nucl. Instrum. Meth.* A389 (1997), pp. 81–86. DOI: 10.1016/S0168-9002(97)00048-X.

[93] BOOST C++ libraries. URL: http://www.boost.org.

[94] S. Agostinelli et al. "GEANT4: A Simulation toolkit". In: *Nucl. Instrum. Meth.* A506 (2003), pp. 250–303. DOI: 10.1016/S0168-9002(03)01368-8.

[95] Jiang Zhu et al. "A method of detector and event visualization with Unity in JUNO". In: *JINST* 14.01 (2019), T01007. DOI: 10.1088/1748-0221/14/01/T01007. arXiv: 1812.05304 [physics.ins-det].

[96] Blyth Simon C. "Opticks : GPU Optical Photon Simulation for Particle Physics using NVIDIA® OptiX™". In: *Journal of Physics: Conference Series* 898 (Oct. 2017), p. 042001. DOI: 10.1088/1742-6596/898/4/042001. URL: https://doi.org/10.1088%2F1742-6596%2F898%2F4%2F042001.

[97] Kaijie Li et al. "GDML based geometry management system for offline software in JUNO". In: *Nuclear Instruments and Methods in Physics Research Section A: Accelerators, Spectrometers, Detectors and Associated Equipment* 908 (2018), pp. 43–48. ISSN: 0168-9002. DOI: https://doi.org/10.1016/j.nima.2018.08.008. URL: http://www.sciencedirect.com/science/article/pii/S0168900218309537.

[98] Teng Li et al. "Design and Development of JUNO Event Data Model". In: *Chin. Phys.* C41.6 (2017), p. 066201. DOI: 10.1088/1674-1137/41/6/066201. arXiv: 1702.04100 [physics.ins-det].

[99] R. N. Cahn et al. "White Paper: Measuring the Neutrino Mass Hierarchy". In: *Community Summer Study 2013: Snowmass on the Mississippi (CSS2013) Minneapolis, MN, USA, July 29-August 6, 2013*. 2013. arXiv: 1307.5487 [hep-ex]. URL: http://inspirehep.net/record/1243859/files/arXiv:1307.5487.pdf.

[100] Hisakazu Minakata et al. "Determination of the neutrino mass hierarchy via the phase of the disappearance oscillation probability with a monochromatic anti-electron-neutrino source". In: *Phys. Rev.* D76 (2007). [Erratum: Phys. Rev.D76,079901(2007)], p. 053004. DOI: 10.1103/PhysRevD.76.053004,10.1103/PhysRevD.76.079901. arXiv: hep-ph/0701151 [hep-ph].

[101] Yu-Feng Li et al. “Unambiguous Determination of the Neutrino Mass Hierarchy Using Reactor Neutrinos”. In: *Phys. Rev.* D88 (2013), p. 013008. DOI: 10.1103/PhysRevD.88.013008. arXiv: 1303.6733 [hep-ex].

[102] K. Abe et al. “Updated T2K measurements of muon neutrino and antineutrino disappearance using 1.5×10^{21} protons on target”. In: *Phys. Rev.* D96.1 (2017), p. 011102. DOI: 10.1103/PhysRevD.96.011102. arXiv: 1704.06409 [hep-ex].

[103] F. P. An et al. “Improved Measurement of Electron Antineutrino Disappearance at Daya Bay”. In: *Chin. Phys.* C37 (2013), p. 011001. DOI: 10.1088/1674-1137/37/1/011001. arXiv: 1210.6327 [hep-ex].

[104] Marco Grassi et al. “Showering Cosmogenic Muons in A Large Liquid Scintillator”. In: *JHEP* 09 (2014), p. 049. DOI: 10.1007/JHEP09(2014)049. arXiv: 1401.7796 [physics.ins-det].

[105] H. de Kerret et al. “Yields and production rates of cosmogenic ^{9}Li and ^{8}He measured with the Double Chooz near and far detectors”. In: *JHEP* 11 (2018), p. 053. DOI: 10.1007/JHEP11(2018)053. arXiv: 1802.08048 [hep-ex].

[106] S. Abe et al. “Production of Radioactive Isotopes through Cosmic Muon Spallation in KamLAND”. In: *Phys. Rev.* C81 (2010), p. 025807. DOI: 10.1103/PhysRevC.81.025807. arXiv: 0907.0066 [hep-ex].

[107] L. Wolfenstein. “Neutrino Oscillations in Matter”. In: *Phys. Rev.* D17 (1978). [,294(1977)], pp. 2369–2374. DOI: 10.1103/PhysRevD.17.2369.

[108] S. P. Mikheyev and A. Y. Smirnov. “Resonance Amplification of Oscillations in Matter and Spectroscopy of Solar Neutrinos”. In: *Sov. J. Nucl. Phys.* 42 (1985). [,305(1986)], pp. 913–917.

[109] Francesco L. Villante et al. “The Chemical Composition of the Sun from Helioseismic and Solar Neutrino Data”. In: 787.1, 13 (May 2014), p. 13. DOI: 10.1088/0004-637X/787/1/13. arXiv: 1312.3885 [astro-ph.SR].

[110] Maria Bergemann and Aldo Serenelli. “Solar Abundance Problem”. In: *Determination of Atmospheric Parameters of B-, A-, F- and G-Type Stars. Series: GeoPlanet: Earth and Planetary Sciences, ISBN: 978-3-319-06955-5. Springer International Publishing (Cham), Edited by Ewa Niemczura, Barry Smalley and Wojtek Pych, pp. 245-258*. 2014, pp. 245–258. DOI: 10.1007/978-3-319-06956-2_21.

[111] C. Genster et al. “Muon reconstruction with a geometrical model in JUNO”. In: *Journal of Instrumentation* 13.03 (Mar. 2018), T03003–T03003. DOI: 10.1088/1748-0221/13/03/t03003. arXiv: 1906.01912 [physics.inst-det]. URL: https://doi.org/10.1088%2F1748-0221%2F13%2F03%2Ft03003.

[112] Kun Zhang et al. “Muon Tracking with the fastest light in the JUNO Central Detector”. In: (2018). DOI: 10.1007/s41605-018-0040-8. arXiv: 1803.10407 [physics.ins-det].

[113] Björn S. Wonsak et al. “Topological track reconstruction in unsegmented, large-volume liquid scintillator detectors”. In: *JINST* 13.07 (2018), P07005. DOI: 10.1088/1748-0221/13/07/P07005. arXiv: 1803.08802 [physics.ins-det].

[114] B. S. Wonsak et al. “3D topological reconstruction in liquid scintillator detectors”. In: *Solar Neutrinos*, pp. 445–463. DOI: 10.1142/9789811204296_0028. eprint: https://www.worldscientific.com/doi/pdf/10.1142/9789811204296_0028. URL: https://www.worldscientific.com/doi/abs/10.1142/9789811204296_0028.

[115] Y. Abe et al. “Precision Muon Reconstruction in Double Chooz”. In: *Nucl. Instrum. Meth.* A764 (2014), pp. 330–339. DOI: 10.1016/j.nima.2014.07.058. arXiv: 1405.6227 [physics.ins-det].

[116] G Bellini et al. “Muon and cosmogenic neutron detection in Borexino”. In: *Journal of Instrumentation* 6.05 (2011), P05005. URL: http://stacks.iop.org/1748-0221/6/i=05/a=P05005.

[117] F. James and M. Roos. “Minuit: A System for Function Minimization and Analysis of the Parameter Errors and Correlations”. In: *Comput. Phys. Commun.* 10 (1975), pp. 343–367. DOI: 10.1016/0010-4655(75)90039-9.

[118] D. W. Scott. *Multivariate Density Estimation: Theory, Practice, and Visualization.* John Wiley, 1992.

[119] S. Agostinelli et al. “Geant4—a simulation toolkit”. In: *Nuclear Instruments and Methods in Physics Research Section A: Accelerators, Spectrometers, Detectors and Associated Equipment* 506.3 (2003), pp. 250–303. ISSN: 0168-9002. DOI: https://doi.org/10.1016/S0168-9002(03)01368-8. URL: %7Bhttp://www.sciencedirect.com/science/article/pii/S0168900203013688%7D.

[120] Sören Jetter et al. “PMT waveform modeling at the Daya Bay experiment”. In: *Chinese Physics C* 36.8 (2012), p. 733. URL: http://stacks.iop.org/1674-1137/36/i=8/a=009.

[121] Michael Wurm et al. “The next-generation liquid-scintillator neutrino observatory LENA”. In: *Astroparticle Physics* 35.11 (2012), pp. 685–732. ISSN: 0927-6505. DOI: https://doi.org/10.1016/j.astropartphys.2012.02.011. URL: http://www.sciencedirect.com/science/article/pii/S0927650512000503.

[122] Dominikus Hellgartner. “Advanced Event Reconstruction in LENA and Precision Attenuation-Length Measurements in Liquid Scintillators”. Dissertation. München: Technische Universität München, 2015.

[123] J. Allison et al. “Recent developments in Geant4”. In: *Nuclear Instruments and Methods in Physics Research Section A: Accelerators, Spectrometers, Detectors and Associated Equipment* 835 (2016), pp. 186–225. ISSN: 0168-9002. DOI: https://doi.org/10.1016/j.nima.2016.06.125. URL: %7Bhttp://www.sciencedirect.com/science/article/pii/S0168900216306957%7D.

[124] R.B. Firestone et al. *The 8th edition of the Table of Isotopes*. John Wiley and Sons, Inc, 1997.

[125] Steffen Hauf et al. "Radioactive Decays in Geant4". In: *IEEE Trans. Nucl. Sci.* 60.4 (2013), pp. 2966–2983. DOI: 10.1109/TNS.2013.2270894. arXiv: 1307.0996 [physics.comp-ph].

[126] Jagdish K. Tuli. "Evaluated Nuclear Structure Data File (ENSDF)". In: (). URL: %7Bhttps://www.nndc.bnl.gov/ensdf/ensdf%7D.

[127] Florian Kiel. "Design and test of a power board for an intelligent PMT for the JUNO-detector". Veröffentlicht auf dem Publikationsserver der RWTH Aachen University; Dissertation, RWTH Aachen University, 2019. Dissertation. Aachen: RWTH Aachen University, 2019, 1 Online–Ressource (xiii, 109 Seiten) : Illustrationen, Diagramme. DOI: 10.18154/RWTH-2019-01597. URL: http://publications.rwth-aachen.de/record/755091.

[128] Tobias Richard Sterr. "PMT Array Timing Calibration with a Pulsed Light Source". Eberhard Karls Universität Tübingen, Nov. 2018.

[129] Y. Abe et al. "Reactor electron antineutrino disappearance in the Double Chooz experiment". In: *Phys. Rev.* D86 (2012), p. 052008. DOI: 10.1103/PhysRevD.86.052008. arXiv: 1207.6632 [hep-ex].

[130] Kitware Inc. URL: %7Bhttps://cmake.org/%7D.

[131] P. Antonioli et al. "A Three-dimensional code for muon propagation through the rock: Music". In: *Astropart. Phys.* 7 (1997), pp. 357–368. DOI: 10.1016/S0927-6505(97)00035-2. arXiv: hep-ph/9705408 [hep-ph].

[132] Sebastian Lorenz. "Topological Track Reconstruction in Liquid Scintillator and LENA as a Far-Detector in an LBNO Experiment". PhD thesis. Hamburg: U. Hamburg, Dept. Phys., 2016. DOI: 10.3204/PUBDB-2016-06366.

[133] M Dressel. *Geometrical importance sampling in Geant4: from design to verification*. Tech. rep. CERN-OPEN-2003-048. Geneva: CERN, Sept. 2003. URL: %7Bhttp://cds.cern.ch/record/642987%7D.

[134] Simone Marcocci. "Precision measurement of solar neutrino fluxes with Borexino and prospects for 0 nu beta beta search with 136Xe-loaded liquid scintillators". PhD thesis. GSSI, Aquila, 2016. URL: %7Bhttp://borex.lngs.infn.it/Thesis/Simone_Marcocci_PhD_Thesis.pdf%7D.

[135] M. Agostini et al. "The Monte Carlo simulation of the Borexino detector". In: *Astropart. Phys.* 97 (2018), pp. 136–159. DOI: 10.1016/j.astropartphys.2017.10.003. arXiv: 1704.02291 [physics.ins-det].

[136] Randolph Mollenberg. "Monte Carlo Study of Solar ^{8}B Neutrinos and the Diffuse Supernova Neutrino Background in LENA". PhD thesis. Munich, Tech. U., 2013. URL: %7Bhttps://mediatum.ub.tum.de/doc/1175550/1175550.pdf%7D.

[137] JUNO Collaboration. "JUNO Material Radioactivity Database". password-protected. July 2017. URL: http://junodb.ihep.ac.cn.

[138] M. Balata et al. “The water purification system for the low background counting test facility of the Borexino experiment at Gran Sasso”. In: *Nucl. Instr. and Meth. in Phys. Res. A* 370.2 (1996), pp. 605–608. ISSN: 0168-9002. DOI: https://doi.org/10.1016/0168-9002(95)00862-4. URL: %7Bhttp://www.sciencedirect.com/science/article/pii/0168900295008624%7D.

[139] Michael Wurm. “OSIRIS Update on Liquid Handling System”. password-protected. May 2019. URL: https://juno.ihep.ac.cn/cgi-bin/Dev_DocDB/ShowDocument?docid=4615.

[140] Gary J. Feldman and Robert D. Cousins. “A Unified approach to the classical statistical analysis of small signals”. In: *Phys. Rev.* D57 (1998), pp. 3873–3889. DOI: 10.1103/PhysRevD.57.3873. arXiv: physics/9711021 [physics.data-an].

[141] J. J. Gomez-Cadenas et al. “Sense and sensitivity of double beta decay experiments”. In: *JCAP* 1106 (2011), p. 007. DOI: 10.1088/1475-7516/2011/06/007. arXiv: 1010.5112 [hep-ex].

[142] Philipp Kampmann. *private communication*. 2019.

[143] H Back et al. “Borexino calibrations: hardware, methods, and results”. In: *Journal of Instrumentation* 7.10 (Oct. 2012), P10018–P10018. DOI: 10.1088/1748-0221/7/10/p10018. URL: https://doi.org/10.1088%2F1748-0221%2F7%2F10%2Fp10018.

[144] J. Liu et al. “Automated calibration system for a high-precision measurement of neutrino mixing angle θ_{13} with the Daya Bay antineutrino detectors”. In: *Nucl. Instrum. Meth.* A750 (2014), pp. 19–37. DOI: 10.1016/j.nima.2014.02.049. arXiv: 1305.2248 [physics.ins-det].

[145] K. J. R. Rosman and P. D. P. Taylor. “Isotopic Compositions of the Elements 1997”. In: *Journal of Physical and Chemical Reference Data* 27.6 (1998), pp. 1275–1287. DOI: 10.1063/1.556031. eprint: https://doi.org/10.1063/1.556031. URL: https://doi.org/10.1063/1.556031.

[146] Y. Abe et al. “Improved measurements of the neutrino mixing angle θ_{13} with the Double Chooz detector”. In: *JHEP* 10 (2014). [Erratum: JHEP02,074(2015)], p. 086. DOI: 10.1007/JHEP02(2015)074,10.1007/JHEP10(2014)086. arXiv: 1406.7763 [hep-ex].

[147] Brite-LED Optoelectronics, Inc. URL: %7Bhttp://sinogerman.brinkster.net/brite-led/PDF/BL-LBVB5N15C%20series%20datasheet.pdf%7D (visited on 04/24/2019).

[148] D. G. Michael et al. “Observation of muon neutrino disappearance with the MINOS detectors and the NuMI neutrino beam”. In: *Phys. Rev. Lett.* 97 (2006), p. 191801. DOI: 10.1103/PhysRevLett.97.191801. arXiv: hep-ex/0607088 [hep-ex].

Eidesstattliche Erklärung

Ich, Christoph Genster

erkläre hiermit, dass diese Dissertation und die darin dargelegten Inhalte die eigenen sind und selbstständig, als Ergebnis der eigenen originären Forschung, generiert wurden.

Hiermit erkläre ich an Eides statt

1. Diese Arbeit wurde vollständig oder größtenteils in der Phase als Doktorand dieser Fakultät und Universität angefertigt;
2. Sofern irgendein Bestandteil dieser Dissertation zuvor für einen akademischen Abschluss oder eine andere Qualifikation an dieser oder einer anderen Institution verwendet wurde, wurde dies klar angezeigt;
3. Wenn immer andere eigene- oder Veröffentlichungen Dritter herangezogen wurden, wurden diese klar benannt;
4. Wenn aus anderen eigenen- oder Veröffentlichungen Dritter zitiert wurde, wurde stets die Quelle hierfür angegeben. Diese Dissertation ist vollständig meine eigene Arbeit, mit der Ausnahme solcher Zitate;
5. Alle wesentlichen Quellen von Unterstützung wurden benannt;
6. Wenn immer ein Teil dieser Dissertation auf der Zusammenarbeit mit anderen basiert, wurde von mir klar gekennzeichnet, was von anderen und was von mir selbst erarbeitet wurde;
7. Ein Teil oder Teile dieser Arbeit wurden zuvor veröffentlicht und zwar in:
   - C. Genster et al. “Muon reconstruction with a geometrical model in JUNO”. In: *Journal of Instrumentation* 13.03 (Mar. 2018), T03003. doi: 10.1088/1748-0221/13/03/t03003

Aachen, den 3. Dezember 2019
Ort, Datum

Christoph Genster

Acknowledgements / Danksagung

This work would not have been possible without the support and guidance of several different people. In addition, I met and worked with many colleagues, that made the last three and a half years a great experience.

First of all, I generally want to thank my *neutrino group* at the *Nuclear Physics Institute* of *Forschungszentrum Jülich* for many interesting discussions in group meetings, coffee breaks or lunches and exciting trips to conferences and collaboration meetings.
Especially, I want to express my gratitude to Prof. Dr. *Livia Ludhova* for giving me the opportunity to do my PhD studies in her group. Being the first member of her then newly formed working group, I could not only learn about the development of LS neutrino detectors, but also the evolution of a diverse and fun working group. With her enthusiasm for neutrino physics, she guided me towards a more comprehensive understanding of neutrino detectors than I had imagined - including aspects of software and hardware. Most notably, she gave me the possibility to attend meetings and conferences in many places around the world, for which I am very thankful. Those experiences did not only help to build connections in the scientific community, but also expanded my personal horizon.
Furthermore, I want to thank Prof. Dr. *Achim Stahl*, Prof. Dr. *Christopher Wiebusch*, and the whole LAND group from *III. Physikalisches Institut B* for their continuous feedback and suggestions in all topics of my work. In our weekly meetings and occasional lunches, their ideas often opened up new perspectives on the problems at hand.
Einen ganz besonderen Dank möchte ich Dr. *Sebastian Lorenz* aussprechen, mit dem ich die Ehre hatte für einige Monate gemeinsam Software zu entwicklen. Seine strukturierte Herangehensweise an wissenschaftliche Fragestellungen, aber auch an die Vermittlung von Wissen, ist für mich ein Vorbild. Abseits der Arbeit bin ich dankbar für spannende gemeinsame (Dienst-)Reisen – ob mit dem Auto nach Tübingen oder mit dem Maglev durch Shanghai.
Während der Entwicklung meines Rekonstruktionsansatzes konnte ich mich immer auf hilfreiche, neue Anstöße von Dr. *Björn Wonsak* verlassen. Für die immerzu optimistischen Ideen und Hilfestellungen möchte ich mich hier bedanken.
Prof. Dr. *Michael Wurm* gilt meine Dankbarkeit für die Möglichkeit vom Begin des

Projektes bei OSIRIS mitzuwirken, das entgegengebrachte Vertrauen und die herzliche Art und Weise das Projekt zu leiten.

Bei *Michaela Schever* möchte ich mich bedanken für die gute Unterhaltung während des täglichen Pendelns, hitzige Diskussionen über mathematische Probleme und das Ertragen meiner Späße, sowohl im Büro, als auch im Flugzeug oder beim Wandern entlang der Chinesischen Mauer.
Darüber hinaus bedanke ich mich bei *Philipp Kampmann* und *Alexandre Göttel* für anregende Diskussionen über verschiedenste, relevante und weniger relevante wissenschaftliche Themen, Serien & Filme und Nerf-Duelle. Auch unsere Reisen waren mir ein großes Vergnügen.
Darüber hinaus bin ich auch meiner wunderbaren JUNO *Forschergruppe* dankbar, insbesondere: *Alexander Tietzsch*, *Axel Müller*, *David Blum*, *David Meyhöfer*, *Henning Rebber*, *Heike Enzmann*, *Paul Hackspacher*, *Wilfried Depnering* und *Hans Steiger*. Ich freue mich jedes mal auf unsere gemeinsamen Meetings und erinnere mich gerne an die einzigartigen Tage und Nächte, in denen wir (chinesische) Städte erkundet haben.

Selbstverständlich gilt mein Dank auch den Menschen, die mich außerhalb des Arbeitsumfeld stets tatkräftig unterstützt haben. Ich danke meinen langjährigen Freunden *Sadi Kamar*, *Phil Imhausen*, *Johannes Kniprath* und *Lisa Schumacher* dafür, sich stets meine neusten Errungenschaften angehört zu haben, selbst wenn die Begeisterung dafür selten auf sie übergreifen konnte. Ganz besonders möchte ich mich bei meiner Freundin *Nele Ulmer* bedanken für die Unterstützung insbesondere im letzten halben Jahr, die nicht nur aus motivierendem Zuspruch bestand, sondern auch aus einer Grundversorgung an Energy-Drinks. Abschließend bedanke ich mich bei meiner Mama *Petra Genster*, die es mir überhaupt erst ermöglicht hat Physik zu studieren und ohne die ich heute diesen Text nicht hätte schreiben können.